SYNTHESIS AND PROPERTIES OF METALLIZED CELLULOSE NANOMATERIALS

A Dissertation
Presented to
The Academic Faculty

by

Nikolay Semenikhin

In Partial Fulfillment
of the Requirements for the Degree
Doctor in Philosophy in Materials Science and Engineering

Georgia Institute of Technology
May 2019

SYNTHESIS AND PROPERTIES OF METALLIZED CELLULOSE NANOMATERIALS

Approved by:

Dr. Kenneth H. Sandhage, Advisor
School of Materials Science and Engineering
Georgia Institute of Technology

Dr. John Zhang
School of Chemistry and Biochemistry
Georgia Institute of Technology

Dr. Robert J. Moon
School of Materials Science and Engineering
Georgia Institute of Technology

Dr. Bernard J. Kippelen
School of Electrical and Computer Engineering
Georgia Institute of Technology

Dr. Michael A. Filler
School of Chemical & Biomolecular Engineering
Georgia Institute of Technology

Date Approved: January 8, 2019

To my parents, Irina and Sergey Semenikhin,
your love and tremendous sacrifice made this accomplishment possible.

ACKNOWLEDGEMENTS

I would like to first thank my advisors, Dr. Kenneth H. Sandhage and Robert J. Moon, for giving me an opportunity to explore the fascinating world of nanotechnology.

Dr. Sandhage, your passion for rigorous scientific research has encouraged me to develop critical analysis skills that have not only helped me meet goals that at times I thought were impossible but will continue to serve me throughout my career.

Robert, your optimism and easy-going nature made for many refreshing brainstorming and discussion sessions, and your unwavering belief in Murphy's law always brought a sense of realism to my research, but never limited my curiosity.

I would like to acknowledge the board of the Renewable Bioproducts Institute, for their sponsorship and all the wonderful social events they have hosted over the years. I am also grateful to have had the opportunity to interact with so many RBI industry members, who have provided invaluable insight into the realm of the renewable products industry and into the commercial future of cellulose nanomaterials.

I would like to extend a special thank you to Dr. Joseph Perry and Dr. Meilin Liu, who provided me with critical laboratory and administrative resources during my tenure. It was a pleasure to be an "honorary" member of your groups and to have had the opportunity to work with your students and research scientists. I would also like to thank my committee members, Dr. John Zhang, Dr. Michael Filler, and Dr. Bernard Kippelen for their constructive criticism and their time spent evaluating my work.

To the administrators and support staff for making my graduate school experience a seamless one. Thanks to Mechelle Kitchings, Keia Dodd, and Ebere Lima for their help in the gamut of administrative tasks. A big thank you to Eric Woods, Yolande Berta, and Todd Walters for the many equipment training lessons and for their dedication to tool maintenance that made my research possible.

I have been fortunate to have met and have been surrounded by many supportive people whose encouragement grew my curiosity and led me to pursue a graduate degree in Materials Science and Engineering. To my high school trigonometry teacher Mrs. May, for connecting me with Cynthia Marvel, who introduced me to the most generous, patient, and supportive people I have ever met, Dean and Teresa DeLamar. Dean and Teresa, the support and guidance you offered me years ago still influence my life today, and I am eternally grateful to have met you.

To my fellow graduate students, for the endless discussions on research, hobbies, politics, and general geek stuff. Ben Deglee, for being a consistent coffee buddy and for being an excellent scientist, whose advice is always appreciated. Dr. Philip Brooke, for the many laughs and for being the lab's personal trainer; I look forward to working with you again shortly. Dr. Luke Johnstone, for understanding the frustrations and difficulties of nanomaterial research and for sharing his acquired wisdom. Sunghwan Hwang, for all the beautiful TEM images, including the ones in this thesis. Kai Chi, for providing suspensions of bacterial cellulose nanocrystals, vital to my research. Ryan Murphy, for keeping the Liu lab stocked and up to code. To Dr. Jeffery Luo, for the fruitful collaborations and for bringing a little rambunctiousness to the graduate student life.

To my high school friends, Joshua Sample, Tyler and Becky Gose, and Mark DeAlva, for staying in touch and for our bi-yearly vacations that always seem too short.

I would like to thank my wonderful surgeons, Dr. Tariq Javed and Dr. Jennifer Tirino. Let my quick recovery, be a testament to their caring personalities, professionalism, and supreme skill. I would also like to thank all the surgery support staff and all the nurses, who took such wonderful care of me during my short stay at Kennethstone. Megan Spence, thank you for being an awesome physical therapist and helping me get back to it in no time.

To my parents, who immigrated to the United States and sacrificed their established lives in Kyrgyzstan to provide their children with a better opportunity for success. Your love, wisdom, and guidance has shaped us into the successful people we are today. To my brothers Igor and Vitaliy, thank you for letting me be the weird middle child. To Alan and Nancy Fu, for accepting me into their family and for all the much-needed and delicious homecooked meals. And to the love of my life, Clarissa Fu, thank you for embracing my child-like curiosity and for sticking by me all these years. I couldn't have made it this far without your love and support.

TABLE OF CONTENTS

LIST OF TABLES

LIST OF FIGURES

LIST OF SYMBOLS AND ABBREVIATIONS

1-D	One Dimensional
a-CNCs	Aminated Cellulose Nanocrystals
AgNWs	Silver Nanowires
AGU	Anhydrous Glucose Unit
aminosilane	N1-(3-trimethoxylsilylpropyl)diethylenetriamine
AR	Aspect Ratio
AuNS-BCNCs	Gold Nanoshell-Bearing Bacterial Cellulose Nanocrystals
BC	Bacterial Cellulose
BCNCs	Bacterial Cellulose Nanocrystals
BEM	Boundary Element Method
Boc	tert-Butylcarbonyl protecting group
CCD	Charge Coupled Device
cm	Centimeter
cm^{-1}	Wavenumber
CNCs	Cellulose Nanocrystals
CNF	Cellulose Nanofibrils
CNTs	Carbon Nanotubes
D_2O	Deuterium Oxide (Heavy Water)
DDA	Discrete Dipole Approximation
Desulfonated	Cellulose without sulfate half-ester groups
DI	Deionized
DLS	Dynamic Light Scattering
EDS	Electron Dispersive Spectroscopy
emu/g	Electromagnetic Unit per gram
*e*R	Simplified Shape Factor
FDTD	Finite Difference Time Domain
FFT	Fast Fourier Transform
FOM	Figure of Merit
FPL	Forest Products Laboratory
FTIR	Fourier-Transform Infrared Spectroscopy
FWHM	Full Width at Half Maximum
H_c	Coercive Field
HRTEM	High-Resolution Transmission Electron Microscopy

HS	Hestrin-Schram
IR	Infrared
ITO	Indium Tin Oxide
K	Kelvin
keV	Kiloelectron Volt
kOe	Kilo oersted
kV	Kilovolt
kX	Magnification 1000 X
LED	Light Emitting Diode
LSPR	Longitudinal Surface Plasmon Resonance
M	Molar
MCC	Microcrystalline Cellulose
MCF	Microfibrilated Cellulose
meV	Milli Electron Volts
mg	Milligram
min.	Minute
mL	Milliliter
mM	Millimolar
mm	Millimeter
$mmolg^{-1}$	Millimoles per Gram
MPa	Megapascal
M_r	Remnant Magnetization
M_s	Saturation Magnetization
mV	Millivolt
Mw	Molecular Weight
MWCO	Molecular Weight Cut Off
n	Refractive Index
NA	Numerical Aperture
Nanorice	Hematite Spindles Coated with Gold or Silver
NiNS-BCNCs	Nickel Nanoshell-Bearing Bacterial Cellulose Nanocrystals
NIR	Near-Infrared
NMR	Nuclear Magnetic Resonance
Oe	Oersted
P	Perimeter of a binarized image of a particle
P_{cir}	Perimeter of a circle with an area equivalent to the analyzed particle area
PES	Polyether Sulfone

Pt-BCNCs	Platinum Decorated Bacterial Cellulose Nanocrystals
PVP	Polyvinylpyrrolidone
μm	Micrometer
RCF	Relative Centrifugal Force
RI	Refractive Index
RIS	Refractive Index Sensitivity
RIU	Refractive Index Unit
ROI	Region of Interest
s	Seconds
Scm^{-1}	Siemens per centimeter
SD	Standard Deviation
SEM	Scanning Electron Microscopy
SPR	Surface Plasmon Resonance
SQUID	Super Conducting Quantum Interference Device
Super	Supernatant
SWIR	Short-Wave Infrared
TEM	Transmission Electron Microscopy
TEMPO	(2,2,6,6-tetramethylpiperidin-1-yl)oxidanyl
THCP	Tetrakis(hydroxymethyl)phosphonium chloride
UV	Ultraviolet
VINIR	Visible to Near-Infrared
Vis	Visible to Near-Infrared
wt.%	Weight Percent
XRD	X-ray Diffraction
ε	Dielectric Constant
ε_m	Dielectric Constant of Medium
λ_{max}	Wavelength of Maximum Intensity

SUMMARY

Considerable interest in cellulose nanomaterials is driven by their sustainable worldwide availability, biodegradability, and versatility. Their extraordinary physical (optical, rheological, thermal, etc.) and mechanical properties (tensile strength, stiffness) make them promising engineering materials of the future. Additionally, cellulose nanomaterials possess a high aspect ratio, rod/fiber-like morphology with easily modifiable surfaces, which make them attractive for template assisted synthesis of functional 1-D nanoparticles. Anisotropic nanomaterials are of great scientific interest because, using directed self-assembly, their individual nanoscale direction dependent properties can be translated to macroscopic materials; such materials have the potential to stimulate breakthroughs in many modern technologies. Unfortunately, numerous state-of-the-art synthesis methods for direct fabrication of 1-D nanomaterials involve the use of complex chemistries and expensive reagents that complicate large scale implementation, and many of these methods are not applicable across material chemistries. Therefore, this research is focused on generating functional nanomaterials through application of conformal coatings of tailorable composition onto high aspect ratio cellulose nanomaterial templates as well as exploring the physical properties of these organic/inorganic hybrid nanomaterials.

This work is divided into four specific research thrusts. First, a wet chemical surface modification process is developed to generate stable suspensions of individually dispersed cationic cellulose nanocrystals. Second, a wet chemical electroless deposition method for applying thin, conformal, and continuous gold coatings onto the surface-modified cellulose nanocrystals is used to produce gold nanoshell-bearing CNCs with tailorable plasmonic properties. Third, correlated single-particle spectroscopy is used to gain further

understanding of how size, surface roughness, and surrounding environment affect the plasmonic properties of gold nanoshell-bearing bacterial cellulose nanocrystals (AuNS-BCNCs); this data is then used to establish structure-property relationships. Finally, the versatility of the methods developed in the first two thrusts is demonstrated by extending these techniques to two new material systems, nickel and silver, which produced magnetic and electrically conductive 1-D nanoparticles, respectively.

CHAPTER 1: SURFACE MODIFICATION OF CELLULOSE NANOCRYSTALS

1.1 Summary

Cellulose nanocrystals are attractive materials for the generation of lightweight nanocomposites as well as functional organic/inorganic nanoparticles, given their fine sizes, aspected shapes, intrinsic strength, and sustainable worldwide availability in abundant quantities. However, their native surface chemistry is incompatible with many material systems. Thus, there is a need for the development of chemical processes that preserve the unique physical properties of CNCs, while making their surfaces compatible with a variety of materials systems and applications. For the first time, stable suspensions of individually dispersed positively charged CNCs have been generated from commercially available sulfate-bearing CNCs, using a wet chemical process. The stability of CNC suspensions was maintained through careful consideration of surface functional group interactions. A process was developed to remove the native negatively charged sulfate half-ester groups, yielding structurally unchanged and nearly charge free CNCs, ready for surface modification. Sodium meta-periodate oxidation coupled with reductive amination were then used to graft positively charged primary amines onto the surfaces of the uncharged CNCs. Cross-linking and agglomeration were prevented by the use of a protected diamine molecule (i.e. ethylenediamine), which allowed for the precise control over surface chemistry and charge. The resulting aminated CNCs were shown to be dispersible down to the individual particle level.

1.2 Introduction

1.2.1 Cellulose Nanocrystals

Cellulose is Earth's most abundant polymer, consisting of D-glucose molecules connected by β (1-4) glycosidic linkages in a linear fashion (**Figure 1**). It is one of the main building blocks of all plant species and can also be found in algae, animals (e.g. tunicates), and bacterial colonies. Each organism produces cellulose with a unique set of attributes (i.e. molecular weight, crystallinity, purity) tailored to its needs.[1] The cellulose chains are typically packed into larger, fibril-like structures, consisting of crystalline and amorphous regions held together by hydrogen bonds and secondary compounds (e.g. lignin, hemicellulose) arranged in a hierarchical morphology.

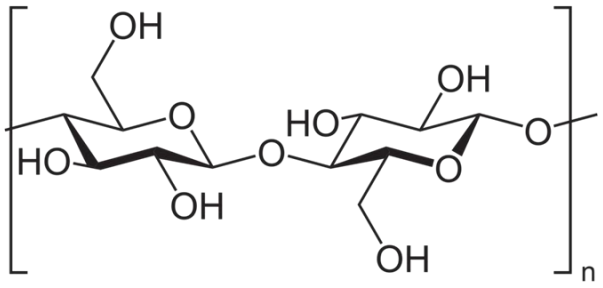

Figure 1. Schematic of cellulose building block.

Cellulose nanocrystals are extracted from raw cellulose-bearing material first, by source specific purification methods that result in a product that is typically >96wt.% cellulose, then an acid hydrolysis step, which preferentially dissolves the amorphous regions of the cellulose fibrils, leaving behind the crystalline sections (i.e. CNCs).[1] The resulting rod-like CNCs have dimensions (5-20 nm wide and 25-3000 nm long), crystallinity (≈60%-90%), and surface chemistries that greatly depend on the cellulose

source as well as the processing conditions.[1-2] Examples of such morphological variety are presented in **Figure 2** and a list of cellulosic nanomaterials derived from different sources along with their dimensions is presented in **Table 1**.

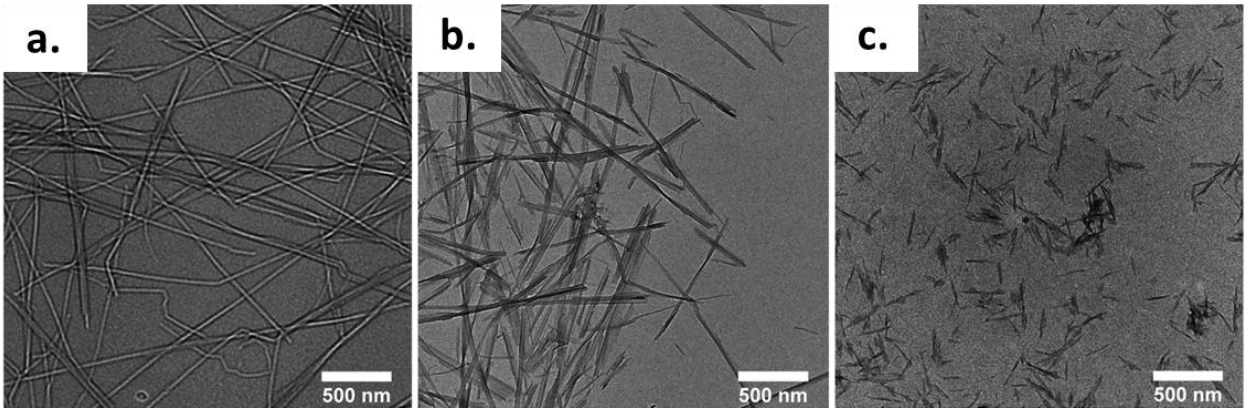

Figure 2. TEM images of CNCs derived from different sources: (a) tunicates, (b) bacteria, and (c). Adapted from Moon, et al.[2]

Table 1. Selected examples of length (L) and width (w) of cellulose nanomaterials obtained from different sources. Adapted from Habibi, et al.[3]

Source	L(nm)	w (nm)
Bacterial	100-1000	10-50
Cotton	70-300	5-10
Cotton Linter	25-320	6-30
Ramie	150-250	6-8
Sisal	100-500	3-5
Tunicate	500-300	10-30
Valonia	>1000	10-20
Soft Wood	100-200	3-5
Hard Wood	140-150	4-5

1.2.2 Surface Functionalization

The importance of cellulose in our society is evident by the vast amount of scientific literature spanning all aspects of its utilization and modification.[4] Recently, an interest in cellulosic nanomaterials has prompted many researchers to revisit the rich chemistry of cellulose functionalization to tailor materials for new high-performance applications.[2-3, 5-7] In recent reviews Eyley[8] and Moon[2] highlight some common approaches to surface modification, such as ion exchange, adsorption, and surface derivatization (i.e. hydrolysis, oxidation, esterification, amidation, carbamation, and etherification), which represent the diverse toolbox of available methods for adding new functionality to CNCs. The range of existing techniques is represented by the variety of chemical pathways shown in **Figure 3**.

Thiols and primary amines are well known for their ability to coordinate and form robust covalent bonds with noble metal surfaces;[9] Oldenburg, et al. showed that primary surface amine groups on silica nanospheres could serve as excellent anchor sites for small gold nanoparticles that could subsequently be grown into thin gold nanoshells.[10] Similarly, by implementing a dendritic amine amplification approach, Fang, et al. showed that even the most intricate features of silica diatom frustules could be replicated with thin metallic coatings.[11-12] Shi et al. showed that the approach of functionalizing surfaces with gold anchor sites could be extended to organic templates by synthesizing polystyrene cores coated with thin gold shells.[13]

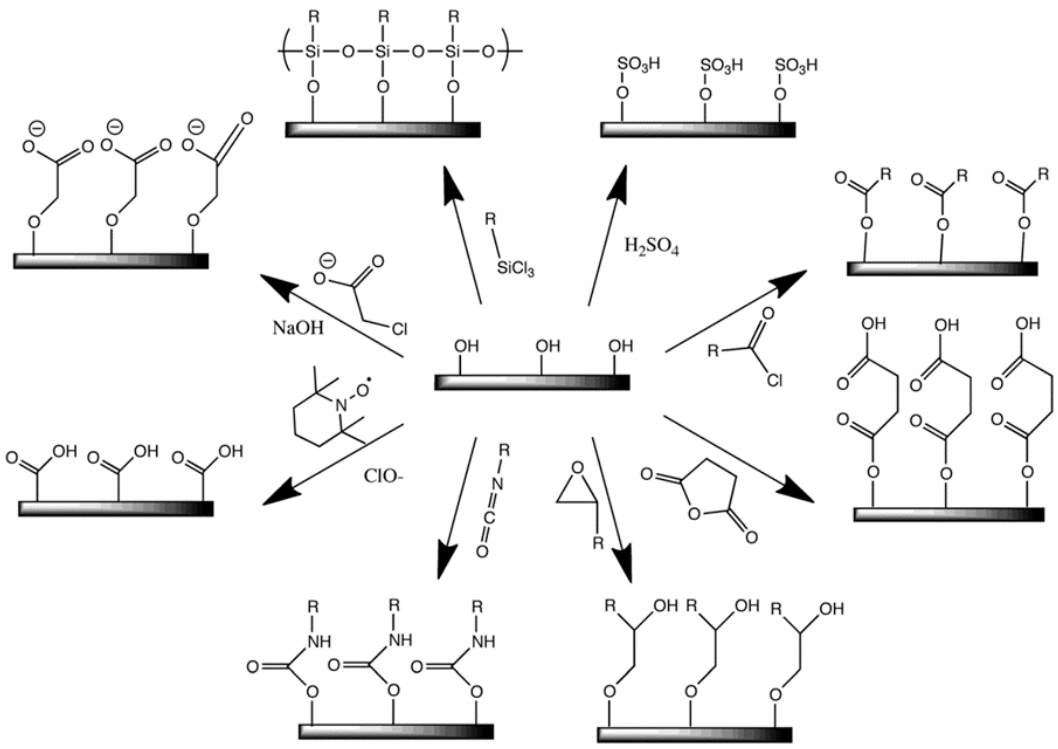

Figure 3. Common modification chemistries of cellulose nanomaterial surfaces: (clockwise from top-right) sulfuric acid treatment provides sulfate esters, carboxylic acid halides create ester linkages, acid anhydrides create ester linkages, epoxides create ether linkages, isocyanates create urethane linkages, TEMPO mediated hypochlorite oxidation creates carboxylic acids, halogenated acetic acids create carboxymethyl surfaces, and chlorosilanes create an oligomeric silylated layer. Adapted from Moon, et al.[2]

The first attempt at creating core-shell structures using CNCs as templates was reported by Gruber, et al.[14] Their work involved mineralizing CNCs with silica, then functionalizing and subsequently coating the silica nanowires with gold nanoparticles. Their analysis revealed a material consisting of interconnected rod-like silica shells, decorated with small gold nanoparticles (**Figure 4**) and the optical absorption spectrum resembled that of agglomerated gold nanoparticles (**Figure 5**).

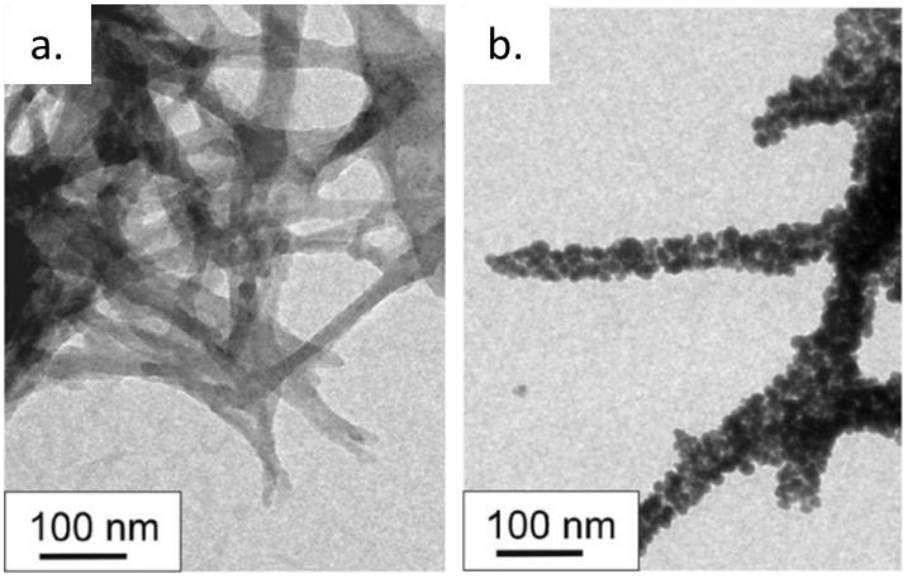

Figure 4. TEM images of silica coated CNCs (a) and gold coated silica nanowires (b) Adapted from Gruber, et al.[14]

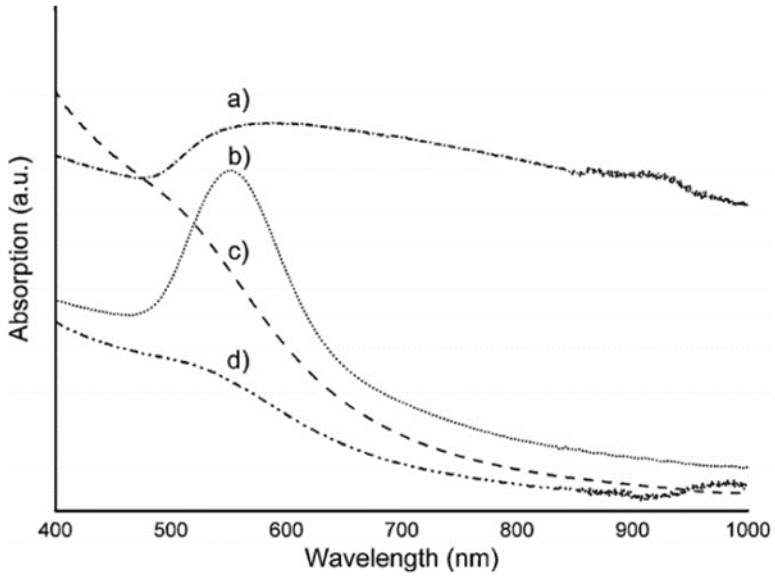

Figure 5. Absorption spectra of (a) gold-coated silica-cellulose nanowires treated with 3 mL coating solution, (b) 1 mL coating solution, (c) gold nanoparticles synthesized via reduction of $HAuCl_4$ with Tetrakis(hydroxymethyl)phosphonium chloride (THCP) and (d) THPC-decorated seeded silica nanowire. Adapted from Gruber, et al.[14]

Building on these examples, the work detailed below aims to develop a surface functionalization scheme that yields cationic CNCs with a high surface amine density. The role of amine groups is two-fold: one, to provide suspension stability through electrostatic repulsion, and two, to impart the CNCs with an affinity towards gold nanoparticles which will serve as preferential nucleation sites for the electroless deposition of thin, continuous, and conformal gold coatings onto individually dispersed CNCs.

There are several reported methods for introducing primary amine groups directly onto the surface of cellulose nanocrystals: Way, et al. used a combination of (2,2,6,6-tetramethylpiperidin-1-yl)oxidanyl (TEMPO) mediated oxidation and peptide coupling to introduce free amines onto HCl hydrolysed tunicate CNCs and showed that hydrogels made with amine-modified CNCs had pH responsive mechanical properties.[15] Even though Way, et al. reported successful amidation of CNCs, they did not report the resulting CNC suspension stability and gave no evidence of a well-dispersed system. Hermaz, et al. used a similar approach to Way, et al. and showed that peptide coupling of amines onto H_2SO_4 hydrolysed CNCs also resulted in amine bearing CNCs.[16] They used zeta (ζ)-potential analysis to assess the surface charge, which revealed that the (ζ)-potential increased from -58.2 ± 0.5 mV to -28.7 ± 0.5 mV after amidation. The reduced surface charge can be attributed to the screening effect of oppositely charged surface moieties: negative sulfate half-esters and positive primary amines. With sufficient amine loading, a surface charge reversal would be expected, but the results of Hemraz, et al. show this not to be the case; in actuality reduced surface charge lead to CNC agglomeration as evidenced by the increase in hydrodynamic radii after surface functionalization.[16] The data provided in these

publications suggests that peptide coupling is not efficient enough to yield highly cationic CNCs that are stable in suspension.

Several other groups have since explored alternate means of introducing amine groups onto CNCs, such as periodate oxidation in combination with reductive amination. Periodate oxidation primarily cleaves the C2-C3 glycosidic bonds of the cellulose ring, resulting in the formation of two highly reactive aldehyde groups as demonstrated in **Figure 6**.[17-18]

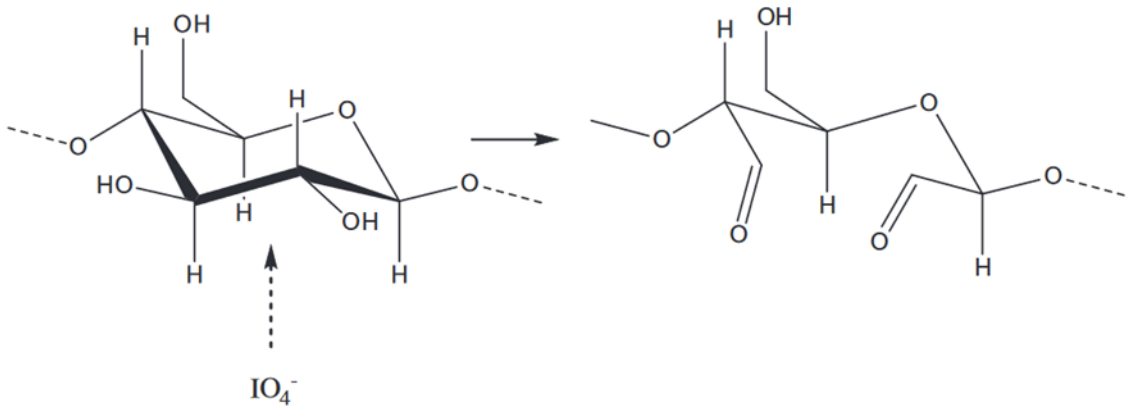

Figure 6. Schematic of periodate oxidation of polysaccharides illustrated by β(1-4) glycosidic residues: double oxidation between C2 and C3 resulting in a dialdehyde functional group.[17]

These dialdehyde moieties can be subsequently reacted with a variety of functional groups including primary amines.[18] Dash, et al. implemented this approach to graft alkyl amines to the surface of CNCs, rendering them more hydrophobic.[19] Their findings showed that this method was an effective way of introducing various amine-bearing compounds to the surfaces of CNCs without drastically altering the CNC morphology and crystallinity. Using a very similar approach, Jin, et al. were able to graft primary amine groups onto sulfuric acid derived CNCs using diamine moieties; the resulting aminated CNCs had a higher

affinity for dye adsorption in acidic conditions making them an attractive bio-renewable and environmentally friendly option for removing dyes from recycled paper wastewater streams.[20] However, their report did not elucidate the effect this surface modification had on the CNCs' surface charge, which is important for dispersability and suspension stability.

Since periodate oxidation attacks the cellulose backbone, there is a potential that the reaction can proceed non-uniformly and destroy the starting particle morphology. Kim, et al. investigated periodate oxidation of *Cladophora*-derived CNCs, which have lengths of several microns, and reported that after periodate oxidation, the algal CNCs were less rigid, showing kinks and bends when imaged using TEM.[18] They supported this claim by reacting the aldehyde groups on the oxidized CNCs with a Schiff-base containing a thiol moiety. The grafted thiol was then used as an anchor site for gold nanoparticles. Based on the spotty coverage of gold nanoparticles and the flexible nature of the oxidized CNCs, Kim, et al. concluded that periodate oxidation must not proceed uniformly along the surface, but in a more localized manner.[18] Conversely, Azzam, et al. later showed, using nuclear magnetic resonance (NMR) and dynamic light scattering (DLS), that periodate oxidation of cotton derived CNCs proceeds uniformly from the surface to the core, and reported that only extended reaction times result in the disruption of the cellulose crystalline structure.[21] A possible explanation of the results obtained by Kim, et al. could be attributed to the extremely long length of the Cladophora-derived CNCs. It is accepted that amorphous regions of cellulose are more reactive[22] than their tightly packed crystalline counterparts, and thus, it is possible that the long Cladophora-derived CNCs used in Kim's study still contained alternating amorphous and crystalline regions along their length. Upon oxidation, the amorphous regions would be preferentially oxidized and become highly

disrupted, acting like hinges which allow the structure to become less rigid as reported by Kim. The low gold nanoparticle coverage is more difficult to explain with certainty because it is subject to many variables (e.g., extent of Schiff-base reaction, gold nanoparticle size, gold surface chemistry, the gold particle concentration, incubation time, etc.) and the authors do not provide details of their gold nanoparticle attachment protocol. The results reported by Azzam, et al. are more aligned with the proposed research because cotton CNCs are similar to wood based CNCs in size, crystallinity, and surface chemistry. Their results indicate that a high number of functional groups can be easily and uniformly introduced onto the surface of short CNCs. The high surface modification efficiency of periodate oxidation can be rationalized considering the reactive site this method exploits. For example, TEMPO mediated oxidation mainly targets the C6 hydroxyls, which cover about 50% of the cellulose crystal surface, resulting in carboxylic acid groups that can be further reacted with amine molecules.[8] On the other hand, periodate oxidation targets the C2-C3 bond, and each oxidized bond produces two reactive dialdehydes, doubling the amount of functional groups, making periodate oxidation a relatively attractive route to CNC surface modification.

1.3 Experimental Procedures

1.3.1 Bio-organic Templates

Wood derived CNCs were produced at the USDA Forest Products Laboratory and were purchased through the Process Development Center at the University of Maine. The production of CNCs involves the hydrolysis of Kraft rayon-grade dissolving pulp (typically ≥ 96% cellulose) with 64 wt.% sulfuric acid at 45°C. The resulting hydrolysate is

neutralized with sodium hydroxide and then purified by diafiltration to a resistivity value of ≥0.02 MΩ, before being concentrated.[1] The final product is obtained as an 11.8 wt.% slurry with a sulfur content of ≈1 wt.%, as was determined by elemental analysis. The morphology of the resulting particles is rod-like with tapered ends **(Figure 7**).

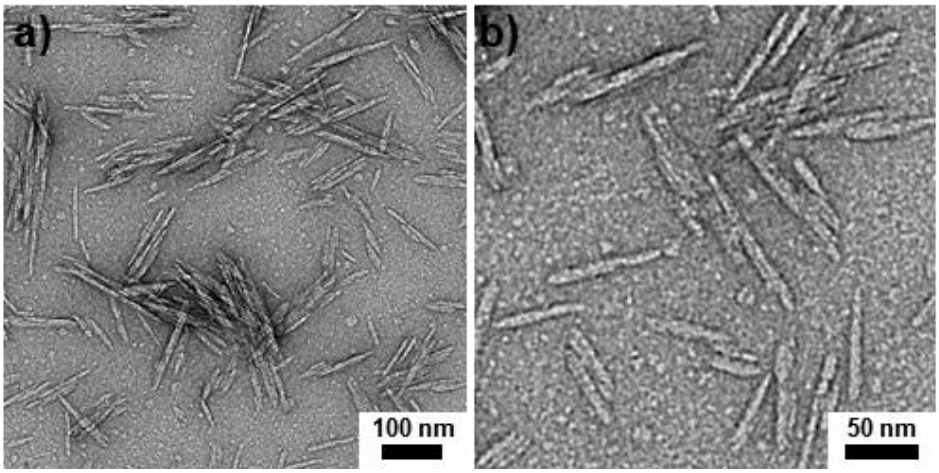

Figure 7. TEM images of as-received wood CNCs showing needle-like particle morphology. Sample stained with 2 wt.% aqueous uranyl acetate solution which was allowed to remain in contact with the deposited CNCs for 3 minutes.

Bacterial cellulose nanocrystals were obtained from Jeff Catchmark's group at Pennsylvania State University. The bacterial pellicles were grown in their lab using the bacterial strain *Komagataeibacter hansenii,* which was obtained from the bio-resource centre of American Type Culture Collection. *K. hanseii* cells were statically cultured in a standard Hestrin-Schramm (HS) medium containing 2% (w/v) glucose, 0.5% (w/v) yeast extract, 0.27% (w/v) Na_2HPO_4 and 0.12% (w/v) citric acid at a temperature of 30°C and a pH of 5.[23] After a 2-day cultivation period, a bacterial cellulose (BC) pellicle was formed on the air-medium interface. The BC pellicle was removed from the growth medium and purified by heating in an aqueous sodium hydroxide solution (0.1M) at 80^{o} C for 14 hours,

followed by rinsing with ultra-pure water (Millipore Milli-Q UF Plus) until a pH of 7 was achieved. The purification and rinsing treatments remove impurities such as *K. hanseii* cells, HS medium components, proteins, and other freely associated polysaccharides. The purified BC was lyophilized (Freezone 18 lyophilizer, Labconco, Kansas City, MO) prior to sulfuric acid hydrolysis.

The method described by Hirai, et al. [24] was used to prepare bacterial cellulose nanocrystals (BCNCs) with some minor modifications. Briefly, the lyophilized BC was treated with 60 wt.% sulfuric acid using an acid-to-cellulose ratio of 70 ml/g at a temperature of 45 °C for 2 hours. The resulting suspensions were then diluted 10-fold to stop the reaction. The dilute suspensions were centrifuged (10,000 RCF for 10 minutes) to sediment the produced BCNCs; the collected BCNCs were washed repeatedly by re-suspending in deionized water followed by centrifugation. The washing process was repeated (4-5 cycles) until the supernatant remained turbid after centrifugation. At this point, the suspension was transferred into dialysis bags (3.5 K MWCO) and dialyzed against deionized water until the pH of the dialysis water became constant (≈6.5, as measured with pH strips). The dialyzed suspension was then ultrasonically processed (Branson Model 5510, Danbury) for 10 minutes to break apart large aggregates. The suspension was once again centrifuged at 4550 g for 15 minutes to sediment any remaining agglomerates, and the supernatant containing dispersed BCNCs was collected and stored at 4°C until use.

1.3.2 Removal of Sulfate Half-Ester Groups

An aqueous CNC slurry (11.8 wt.% CNCs, Lot#: 2014-FPL-CNC-064, produced at USDA Forest Products Laboratory, Madison, WI) obtained from the Process Development Center at the University of Maine (Orono, ME) and the bacterial cellulose produced by the Catchmark group were used as the starting material. Sulfate half-ester groups present on the as-received CNCs were removed by acid hydrolysis. A 1.0 wt.% stock CNC suspension was prepared by diluting the obtained CNC suspensions with deionized (DI) water (Nanopure, Barnstead International, Dubuque, IA). Hydrochloric acid (37 wt.%) was added to 300 mL of the 1.0 wt.% suspensions to achieve a concentration of 250 mM. The acidified suspensions were heated under reflux at 100^{o}C with magnetic stirring (250 rpm, magnetic stirring hot plate, Cimarec, Barnstead International, Dubuque, IA) for 24 hr in a 500 mL round bottom flask. After cooling, the CNCs were washed by repeated centrifugation (Relative Centrifugal Force, RCF, of 8000, 5 min) and dispersion in DI water (5 cycles) using a vortexer (Vortex Genie 2T, Bohemia, NY) until the pH of the supernatant reached a value of 6. The CNCs were then dispersed in 200 mL of DI water using the vortexer, and the suspension was probe sonicated (Misonix 3000, Misonix Inc., Farmingdale, NY) at 30% of the peak amplitude for 5 minutes to break up agglomerates. The sonicated suspensions were transferred to dialysis bags (14,000 MWCO, Ward's Science, Rochester, NY) and dialyzed against DI water to a neutral pH. The resulting opaque, milky suspensions of desulfonated CNCs were diluted with additional DI water to yield a solid content of 0.25 wt.% and were stored at 4°C.

1.3.3 Periodate Oxidation of CNCs

Dialdehyde groups were generated on CNC surfaces by sodium periodate oxidation. Sodium (meta)periodate ($NaIO_4$, 4.0 g, 99% purity, Sigma Aldrich, St. Louis, MO) was added to a suspension of desulfonated CNCs (200 mL, 0.25 wt.% CNC loading). After adjusting the pH of the suspension to 3.5 using glacial acetic acid (99.9% purity, Fisher Scientific, Hampton, NH), the suspension was transferred to a jacketed beaker heated to 45°C. The beaker was covered with aluminum foil (to avoid light induced decomposition of the periodate ion) and the suspension was magnetically stirred (350 rpm) for 2.5 h in a darkened fume hood. Ethylene glycol (10 mL, 99% purity, BDH VWR Analytical, Radnor, PA) was then added to decompose any remaining periodate to iodate and, after 5 minutes, the suspension was cooled to room temperature. The suspension was subjected to five cycles of centrifugation (8000 RCF, 5 min) and dispersion in DI water (using a vortexer) to remove excess reagents. After dialysis against DI water (as described above) for 3 days, the resulting dialdehyde-bearing CNC suspensions (0.187 wt.% CNCs) were stored at 4°C.

1.3.4 Reductive Amination of Oxidized CNCs

A suspension of dialdehyde-bearing CNCs (80.2 mL, 0.187 wt.%) was diluted with 80 mL of phosphate buffer (0.2 M, pH 6.0) in a 250 mL round bottom flask. N-Boc-ethylenediamine (1.0 g, 98% purity, Alfa Aesar, Haverhill, MA) and $NaBH_3CN$ (0.4 g, 95% purity, Alfa Aesar, Haverhill, MA) were added to the suspension, which was then magnetically stirred (350 RPM) for 5 days at room temperature. After the allotted time, the suspension was exposed to five cycles of centrifugation (8000 RCF, 5 min) and

redispersion in DI water (using a vortexer) to remove excess reagents. After the final centrifugation step, the CNCs were suspended in a 4 M HCl solution and magnetically stirred (350 RPM) for 24 hours at room temperature to cleave off the Boc protecting group. The CNCs were once again washed by repeated centrifugation and dispersion in DI water (five or more washing cycles) until the supernatant remained turbid from suspended CNCs. After dialysis against DI water to achieve a neutral pH, the amine-bearing CNC (a-CNC) suspension (0.60 wt.% a-CNCs) was stored at 4°C.

1.3.5 Dispersal of Aminated CNCs

The suspension of aminated CNCs was diluted (from 0.60 wt.% to 0.11 wt.% a-CNCs) with DI water and then placed in an ice/water bath for sonication. The a-CNC suspension was sonicated using a 5 mm probe (Misonix 3000, Misonix Inc., Farmingdale, NY) operating in pulse mode (on/off times of 10 s/5 s) at an amplitude of ≈90 μm (power setting of 3) for 2 hours (note: further sonication beyond 2 hours did not result in a change in the hydrodynamic radius of the a-CNCs, as determined by DLS).

1.3.6 Chemical Analysis

FTIR analysis was conducted with an Equinox 55 Fourier transform infrared spectrometer (Bruker, Billerica, MA). Cellulose suspensions (0.01 wt.%) were frozen at -80°C and then freeze-dried (Freezone 18 lyophilizer, Labconco, Kansas City, MO) for 24 hours. The dried samples were mixed with KBr powder (Spectroscopic Grade, Graseby Specac, Orpington, UK) at a concentration of 1 wt.% (total mass of 150 mg) and ground into a fine powder mixture in an agate mortar. The KBr-CNC powder mixture was uniaxially pressed into 13.5 mm diameter disks at a peak stress of 550 MPa. The spectral

analysis for each sample was obtained as an average of 64 scans conducted in the range of 4000 cm^{-1} to 400 cm^{-1} with a resolution of 4 cm^{-1}.

1.3.7 Zeta Potential and Dispersity Analyses

Zeta (ζ) potential analyses of CNC-bearing suspensions were conducted at 25°C (NanoZS Zetasizer, Malvern Instruments, Malvern, UK). Prior to such analyses, the suspensions were diluted to a CNC concentration of 0.1 wt.% via addition of an aqueous NaCl (1 mM), pH 7 solution. For each suspension, 5 measurements were used to obtain an average zeta potential value. Dynamic light scattering (DLS) analysis was performed to monitor the state of CNC dispersion in solution using the DLS capabilities of the NanoZS instrument. A backscatter detector set at a fixed collection angle of 178° was used and the average of 5 measurements are reported.

1.3.8 Shape/Morphology Analysis

Transmission electron microscopy (TEM) analyses of the as-received CNCs were conducted with a field emission gun instrument (Hitachi HT7700 microscope, Hitachi, Tokyo, Japan) using an accelerating voltage of 120 KV. Dilute CNC suspensions (0.001 wt.%) were deposited onto carbon-coated TEM grids (CF300-Cu, Electron Microscopy Sciences, Hatfield, PA) and the water was evaporated at room temperature. TEM samples were stained by exposing the grids to an aqueous solution of uranyl acetate (2 wt.%) for 3 minutes. Excess liquid was wicked from the surface of the TEM grid with a tissue (Kimwipes).

1.3.9 Elemental Analyses

Elemental analyses were conducted to determine the sulfur content in the as-received and desulfonated CNC samples (LECO CHNS-932 analyzer, Atlantic Microlabs Inc., Norcross, GA) and the nitrogen content of aminated CNCs (Carlo Erba 1108 elemental analyzer, Atlantic Microlabs Inc.). The CNC specimens were lyophilized (Freezone 18 lyophilizer, Labconco, Kansas City, MO) and then vacuum dried at 60°C for 24 hours prior to analysis.

1.3.10 Phase and Crystallinity Analysis

X-ray diffraction was used to evaluate changes in CNC crystallinity before and after desulfonation using an X-pert Pro Alpha 1 diffractometer (PANalytical, Almelo, Netherlands) equipped with a Xcelerator linear detector.

1.4 Results and Discussion

1.4.1 Development of CNC Surface Functionalization Process

Previous work towards the creation of CNCs with high surface amine loadings for subsequent metallization has led to the development of a protocol seen in **Figure 8**. Early attempts at functionalization included the use of amino-silanes, the use of which for modification of hydroxylated silica substrates is well documented,[11-12, 25] which resulted in the agglomeration of CNCs into large networks that could not be individually dispersed as shown in **Figure 9**. Attempts at implementing TEMPO oxidation followed by a peptide coupling protocol as described by Way, et al.[15] resulted in some primary amine presence, but the amine loading remained low and was not sufficient to impart colloidal stability to

the nanoparticles, resulting in CNC agglomerates similar to the results reported by Hermaz.[16] Therefore, the method shown in **Figure 8** was developed to overcome the pitfalls of earlier attempts and is based around periodate oxidation and reductive amination of cellulose nanocrystals.

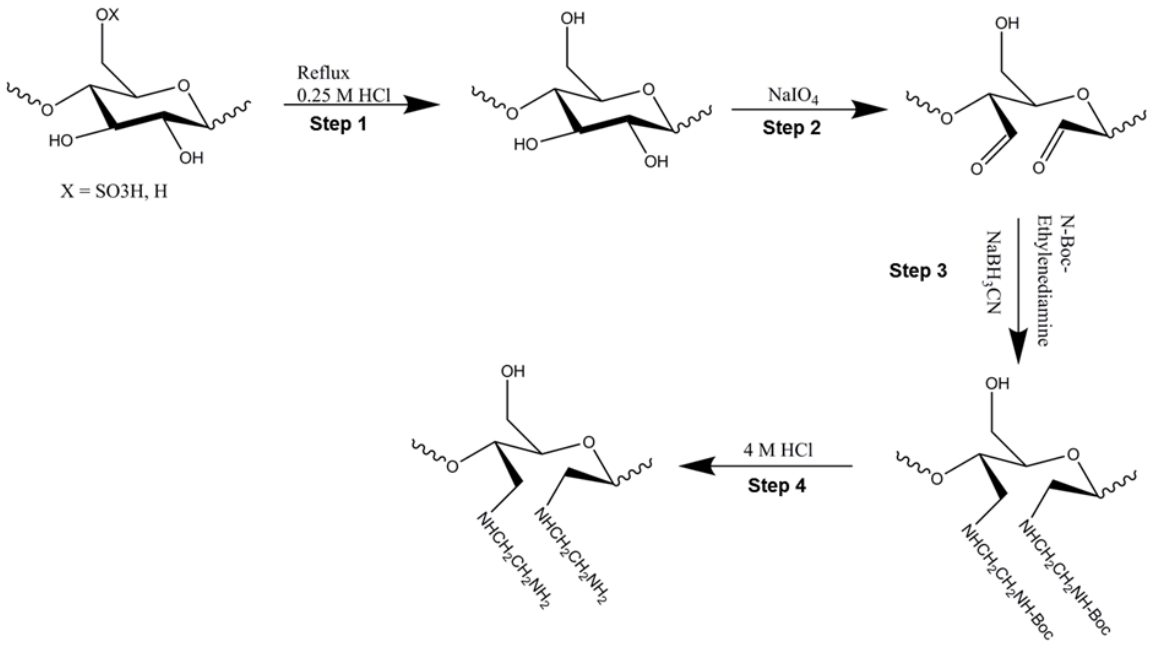

Figure 8. Schematic of CNC surface functionalization method developed in this work. (Step 1) Sulfate ester removal. (Step 2) Periodate oxidation. (Step 3) Reductive Amination (Step 4) Cleavage of Boc protecting group.

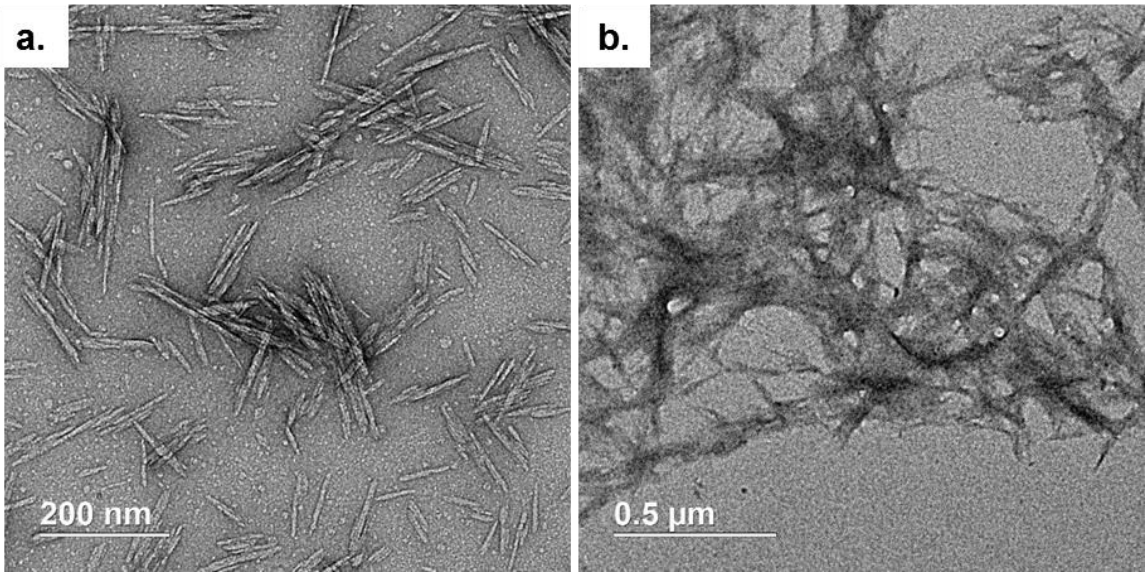

Figure 9. a) TEM image of as-received CNCs and b) TEM image of CNCs after aminosilane treatment, showing CNCs in an agglomerated state.

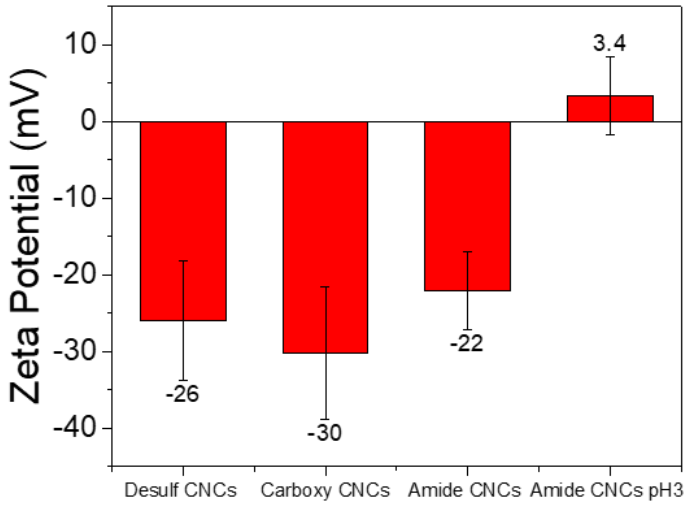

Figure 10. Zeta potential values of CNCs at various stages of amidation reaction showing diminished surface charge of amidated CNCs. (Measurements taken at a pH of 7 unless otherwise stated)

1.4.2 Desulfonation

The first obstacle to overcome when functionalizing CNCs with amines, is the surface charge neutralization and flocculation that occur upon modification. The as-received CNCs are produced through sulfuric acid hydrolysis, resulting in sulfate half-ester-bearing CNCs that have a highly negative surface charge characterized by a ζ-potential of -40 ± 11 mV. Upon addition of free amine groups to the surface, which are positively charged, the ζ-potential is expected to increase due to a screening effect of the two oppositely charged moieties. ζ-potential values below ±30 mV indicate unstable colloidal suspensions, which tend to flocculate into larger aggregates. To overcome this charge neutralization, the sulfate half-ester groups were first removed through mild hydrochloric acid hydrolysis, which has been shown to be non-derivatizing and used to produce CNCs with low surface charge.[26] The protocol for sulfate half-ester removal was adapted from the work by Rees, and consisted of refluxing a 1 wt.% CNC suspension in aqueous hydrochloric acid (0.25 M) at 100°C.[27] The progress of desulfonation was monitored by ζ-potential analysis as shown in **Figure 11.** The ζ-potential dropped to about -6 ± 3.6 mV after 24 hours of refluxing, indicating that most of the sulfate half-ester groups were removed. A 24-hour hydrolysed sample along with an untreated sample were sent out for elemental sulfur analysis (Atlantic Microlabs Inc.) and the results showed 0 ± 0.3 wt.% and 0.95 ± 0.3 wt.% sulfur respectively, confirming the successful removal of sulfate half-esters.

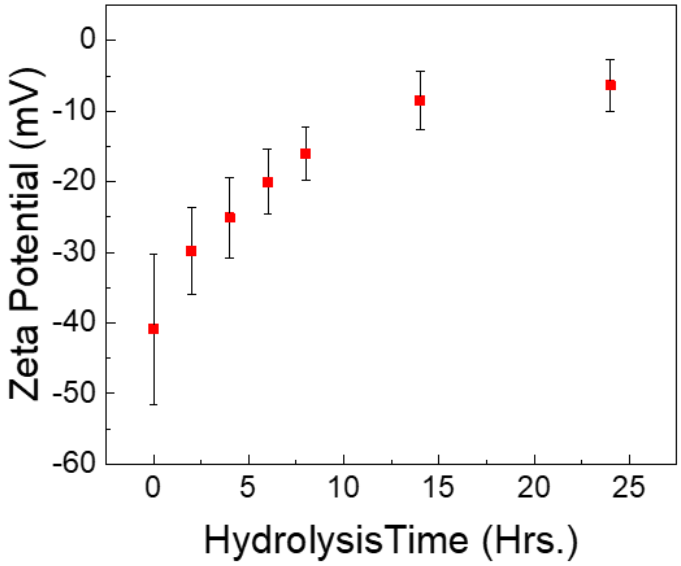

Figure 11. ζ-potential values of CNCs obtained after hydrochloric acid hydrolysis for varying lengths of time (measured in 10 mM aqueous NaCl solution at pH 7).

FTIR was used to further analyse changes to the chemical structure before and after removal of the sulfate half-ester groups, as shown **Figure 12a, b**. Gu, et al. have shown that FTIR absorbance located around 1250 cm^{-1} correspond to the asymmetrical S=O vibrations and the absorbance band located around 815 cm^{-1} is associated with the C-O-S symmetrical vibration.[28] After mild hydrochloric acid hydrolysis (**Step 1, Figure 8**), the band located around 815 cm^{-1} disappeared and a relative decrease (≈ 35%) in absorbance around 1250 cm^{-} was observed, supporting the successful removal of sulfate half-ester groups.

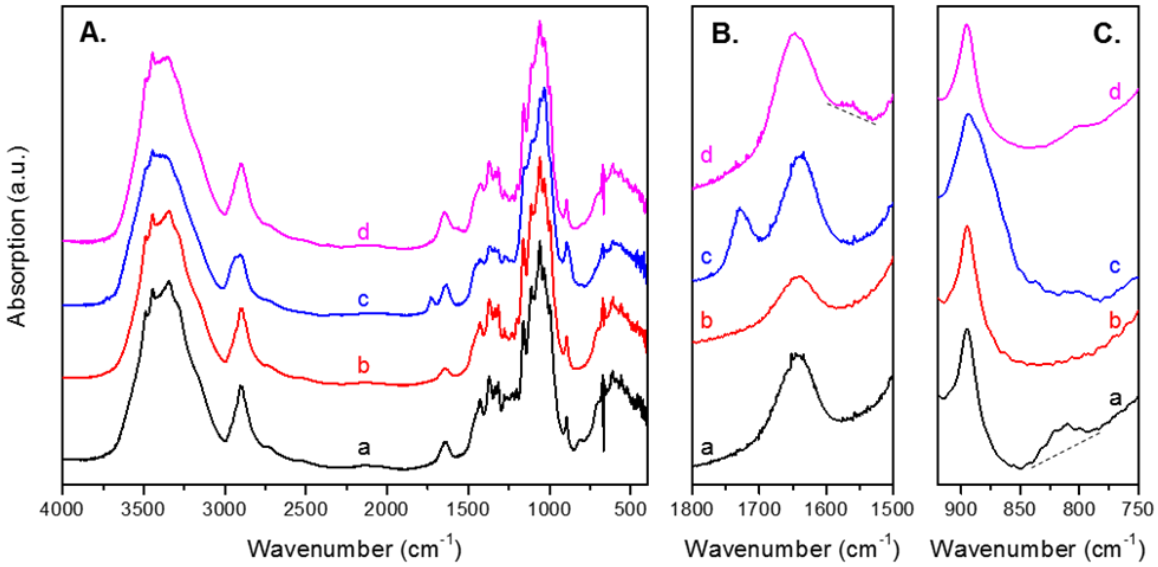

Figure 12. FTIR spectra of CNCs after each functionalization step: (a) As-received CNCs, (b) Desulfonated CNCs, (c) Dialdehyde-bearing CNCs, (d) Aminated CNCs (a-CNCs). Full wavenumber range (A) and two selected ranges (B, C)

X-ray diffraction analysis was performed on the hydrolysed samples to determine if the treatment was detrimental to CNC crystallinity. The XRD patterns seen in **Figure 13** give an indication of crystallinity before and after removal of sulfate ester groups. There is a slight increase in the crystallinity index of the material after HCl hydrolysis through a comparison made between the intensity ratio of the 002 (22.6°) peak and the minimum at 18.3°, which is taken to be the maximum intensity of the amorphous cellulose as suggested by Segal, et al.[29] Apart from this, there is no significant change to the overall crystallinity of the CNCs, suggesting that the sulfate ester removal conditions are mild enough to preserve the CNC structure. It is also evident from the XRD patterns that the CNCs manufactured by FPL contain both cellulose I and cellulose II (**Figure 14**).

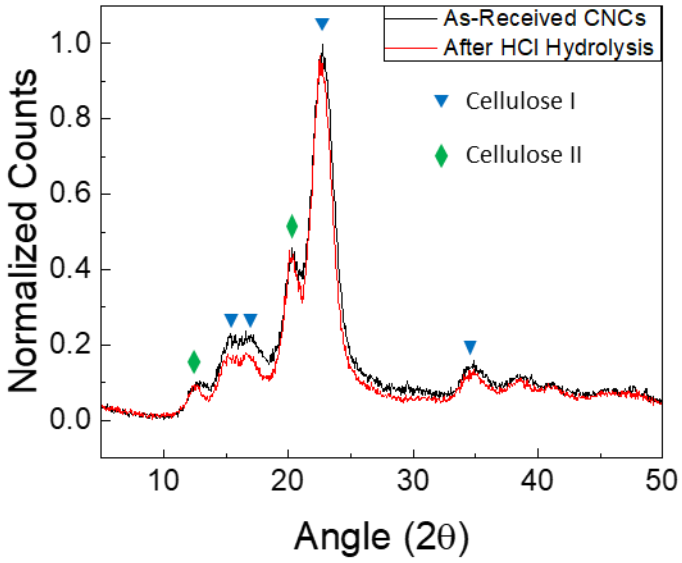

Figure 13. XRD patterns of as-received CNCs and CNCs that have been hydrolyzed with 0.25M HCl for 23 hours to remove sulfate ester groups. Cellulose I and II peak positioned referenced from Nam, et al.[30]

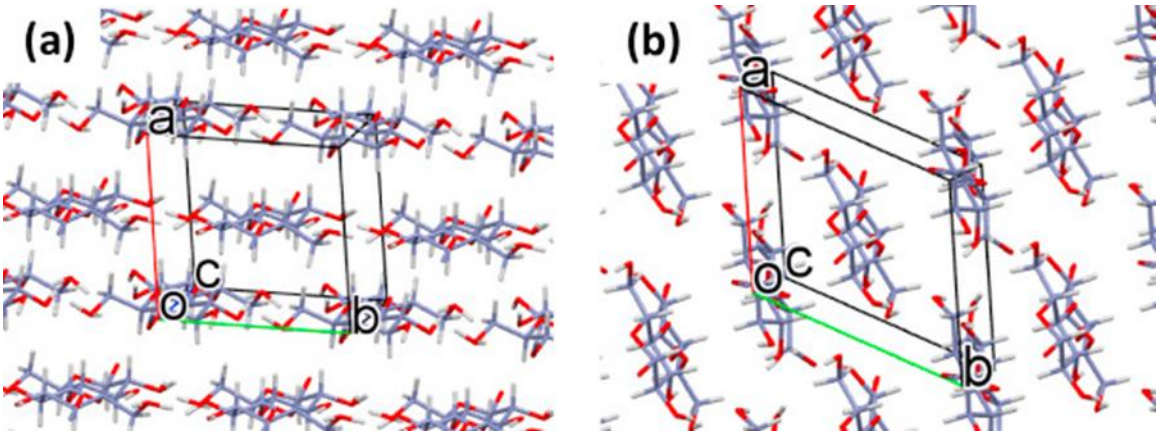

Figure 14. Crystals of (a) cellulose Iβ with lattice parameters a = 7.784 Å, b = 8.201 Å, c = 10.380 Å, γ = 96.55° and (b) cellulose II with a = 8.10 Å, b = 9.03 Å, c = 10.31 Å and γ =117.10°. Image reproduced from reference 31.

Natural samples of cellulose are exclusively cellulose I type. Since, these CNCs are produced from highly processed dissolving pulp, which is treated with strong solutions of sodium hydroxide during purification, it is possible that some cellulose chains undergo an

irreversible phase transformation to cellulose II, which is implicated to have a higher chemical reactivity towards derivatization.[31]

1.4.3 Periodate Oxidation

Fang, et al. have shown that a high surface amine content is necessary to form conformal and continuous gold coatings on (Bio)silica templates.[11] Previous works have shown that periodate oxidation leads to a much higher functional group content in cellulosic samples (>8 $mmolg^{-1}$) when compared to TEMPO (2,2,6,6-Tetramethyl-1-piperidinyloxy) mediated oxidation using NaClO (<2 $mmolg^{-1}$).[20, 32] This large difference is due to the selective nature of TEMPO mediated oxidation, which has been shown to target only the surface C6 hydroxyls, and thus, the total number of functional groups is dictated by the crystalline packing of cellulose chains.[8] On the other hand, periodate oxidation, which targets the C2-C3 glycosidic linkages in the cellulose chain, has been shown to likely proceed evenly across the surface of crystalline cellulose and the functional group content is limited only by the total availability of surface anhydrous glucose units (AGU).[21]

In this work, periodate oxidation (**Step 2, Figure 8**) was carried out in a similar manner as that described by Jin, et al. with minor modification.[20] The resulting dialdehyde CNCs were characterized by FTIR and their corresponding spectrum can be seen in **Figure 12c**. After periodate oxidation, the appearance of a new absorption band at 1730 cm^{-1} (C=O, stretching) indicates the presence of carbonyl groups of aldehydes. Also, the band around 895 cm^{-} broadened after oxidation, which can be attributed to the formation of hemiacetal bonds between the newly formed aldehyde groups.[20] Both characteristic changes in

infrared (IR) absorption confirm that periodate oxidation successfully introduced aldehyde groups to the surface of CNCs. The dialdehyde CNC suspension was further characterized by ζ-potential measurements (**Figure 15)** and was found to have similar ζ-potential values to desulfonated CNCs (-4 ± 5 mV). This result is not surprising because aldehyde groups are not capable of producing charged species in solution, but this raises the concern that the subsequent amination step may lead to crosslinking of the dialdehyde-bearing CNCs, since they cannot be individually dispersed.

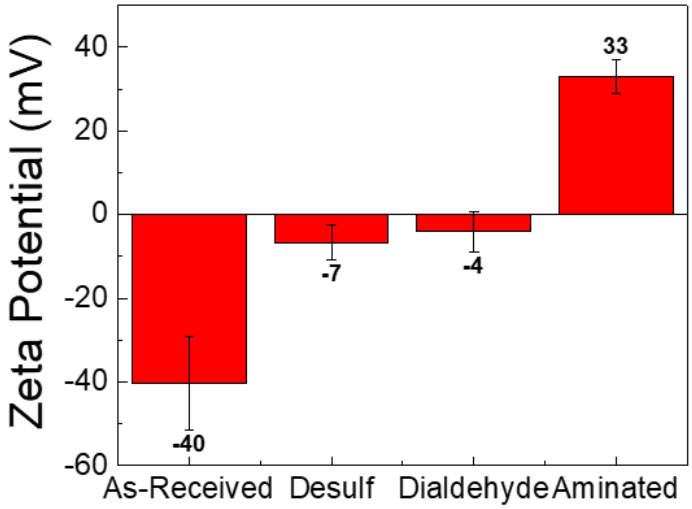

Figure 15. ζ-potential values for CNCs at each step of CNC surface functionalization. (measured in 1 mM NaCl at pH 7).

1.4.4 Reductive Amination

There are several methods of performing reductive aminations. The method employed by Jin, et al. and Dash, et al. involved using a large excess of an amine precursor to push the equilibrium imine formation further to the right before quickly reducing the metastable imines with sodium borohydride.[19-20] To be able to have free amines on the

CNC surface, a diamine must be employed in this reaction. This gives rise to the possibility of both ends of the molecule reacting with aldehyde groups and can result in the crosslinking of adjacent CNCs, which would lead to the reduction of available free amines on the surface and possibly crosslinked CNC agglomerates. The dialdehyde CNCs produced in this work do not disperse well due to their low surface charge, and thus, employing the reaction scheme described above would likely result in crosslinking. Since the aim of this work is to create gold coatings on individualized CNCs, the use of tert-Butyloxycarbonyl (Boc) protected ethylenediamine (**Step 3, Figure 8**) ensured that only one end of the diamine molecule was available for reaction during amination. Sodium cyanoborohydride was used as an in situ reductant to reduce metastable imines as they formed, guaranteeing the reaction progresses towards completion and yields the maximum number of amine groups on the CNC surface (**Figure 16**). The Boc-protecting group was selectively cleaved after amination using an aqueous HCl solution (4M). The use of a protecting group during reductive amination was an innovative development that ensured that CNCs did not become crosslinked during amination and guaranteed that after deprotection, the CNCs surfaces were decorated with free surface amine groups that could bind gold particles as well as electrostatically stabilize the CNCs in suspension.

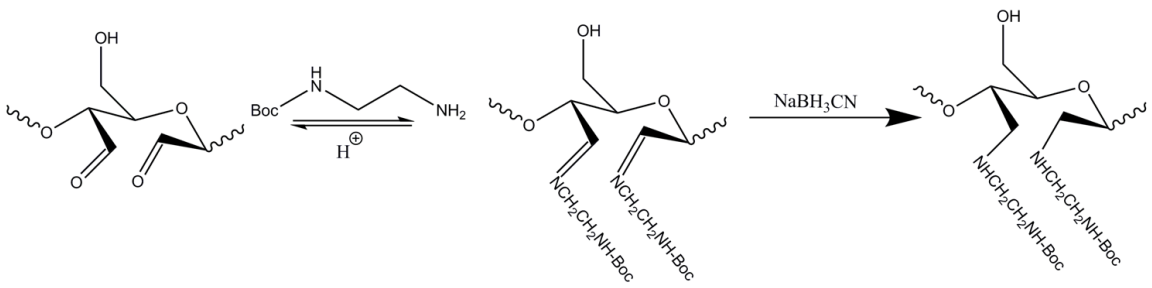

Figure 16. Reaction schematic showing the formation of metastable imines and their subsequent reduction by sodium cyanoborohydride.

The success of amination was characterized by FTIR, ζ-potential measurements, and elemental analysis. FTIR results (**Figure 12d**) show that after reductive amination, the carbonyl band at 1730 cm^{-1} disappears. Since $NaNH_3CN$ is highly selective toward the reduction of imines[33], unlike $NaBH_4$, the disappearance of the 1730 cm^{-1} band indicates that the majority of available aldehyde groups have reacted. The broadened band around 895 cm^{-} of the aldehyde CNCs becomes much sharper after amination, suggesting that hemiacetal bonds of dialdehyde CNCs are no longer present. The small increase in IR absorbance at 1560 cm^{-1} can be attributed to the N-H bending mode and reaffirms the presence of amine groups.[19] The broadening of the absorption band at 1646 cm^{-1} can also be attributed to the formation of amine bonds, but the signal is convoluted by the presence of bound water and is not as conclusive. The ζ-potential of amine bearing CNCs was +33 ± 4 mV at pH 7. This ζ-potential represents a charge reversal from the starting material and the associated charge magnitude is characteristic of stable suspensions. Elemental analyses were conducted on aminated CNCs and the as-received CNCs to quantify the nitrogen content, which was found to be 1.7 wt.% (±0.3%) and 0.0 wt.% (±0.3%), respectively.

1.4.5 CNC Dispersal

To insure the a-CNCs were individually dispersed, a 0.11 wt.% suspension was processed using an ultrasonic probe to break up any agglomerates. The state of dispersion was assessed by dynamic light scattering (DLS). It has been shown by Chang, et al. that similarly sourced, individually dispersed CNCs have hydrodynamic radii ranging between 22 to 27 nm.[34] Ultrasonication was continued until no further improvement in the hydrodynamic radius was observed, which was 36 nm for amine-bearing CNCs. This value is comparable to those reported by Chang. These individually dispersed amine-bearing CNCs served as the starting material for synthesis of gold-coated CNCs.

1.5 Conclusions

This work demonstrates the development of a wet chemical process that enabled the production of individually dispersible cationic CNCs, having surfaces uniformly modified with primary amines. It was found necessary to remove the native anionic CNC sulfate half-ester moieties due to their charge neutralizing effect on grafted cationic primary amines. The rate and extent of sulfate half-ester removal by dilute hydrochloric acid hydrolysis was monitored by ζ-potential analysis, which revealed a monotonic decrease in potential with increasing hydrolysis time. After 15 hours of reaction, the ζ-potential remained constant (-6± 3.6 mV). FTIR analysis of 24 hour hydrolyzed samples revealed a 35% decrease in absorption at ≈1250 cm^{-1} and a complete disappearance of the 815 cm^{-1} absorption band, which are associated with S=O and C-O-S vibration modes, respectively. Complete sulfur half-ester removal was confirmed by elemental analysis, which revealed a sulfur content of 0.0 ± 0.3% after the acid hydrolysis treatment. XRD analysis of the

hydrolyzed samples revealed a minor increase in CNC crystallinity, suggesting that the structure of the as-received CNCs was largely unaffected.

Sodium meta-periodate was used to oxidize CNCs because of its ability to uniformly modify the surfaces of highly crystalline CNCs with reactive dialdehyde functional groups. The success of this reaction was confirmed with FTIR, which revealed the presence of a new absorption band at 1730 cm^{-1} and a broadening of the 895 cm^{-1} absorption band after oxidation, which are associated with the presence of carbonyl groups of aldehydes and hemiacetal bonds between aldehyde groups and cellulose hydroxyls, respectively. The dialdehyde-bearing CNCs were reductively aminated utilizing a one-pot approach with an in situ reducing agent (i.e. $NaBH_3CN$) and a Boc-protected diamine (i.e. Boc-ethylenediamine). The use of a protected diamine insured that the uncharged poorly dispersed dialdehyde CNCs would not cross-link during amination and was selectively removed after amination with a hydrochloric acid treatment. FTIR analysis of the aminated products, revealed the disappearance of the carbonyl absorption band (1730 cm^{-1}) coupled with a narrowing of the hemiacetal absorption signal (895 cm^{-1}). An increase in absorption at 1560 cm^{-1} was attributed to N-H bending mode of the grafted primary amines. The extent of amination was quantified with elemental analysis, which revealed a nitrogen content of 1.7 wt.% (±0.3%). The success of the surface modification process was assessed by ζ-potential and DLS analysis of the final aminated product, which revealed a ζ-potential of +33 mV and a hydrodynamic radius of 36 nm, consistent with electrostatically stabilized individually dispersed CNCs.

Although the surface modification process developed in this work has focused primarily on generating stable cationic wood derived CNCs, it may be applied to a variety

of cellulose nanomaterials (e.g., MFC, CNFs, BCNCs, etc.) and is not limited to primary amine functionality. However, the developed surface functionalization method is novel in the fact that it prevents agglomerated and uncharged CNCs from crosslinking together using a Boc-protected amine molecule. This novel functionalization approach can be highly attractive for applications where CNC agglomerates are detrimental to the material performance (e.g., chiral nematic films, liquid crystals, and polymer composites). The introduced dialdehyde group functionality provides a convenient means for surface modification because dialdehydes can be reacted with a host of molecules containing at least a single primary amine moiety. Thus, this functionalization method may be particularly attractive for compatibilization of cellulose nanocrystal with non-polar polymeric matrices, which is an active area of research for CNC based nanocomposites. For example, grafting alkyl amines or other non-polar molecules onto periodate oxidized cellulose nanomaterials has the potential to improve CNC dispersion in polymer matrices, which can provide realization of CNC intrinsic strengths that will lead to strong, lightweight, and environmentally friendly nanocomposites.

1.6 References

[1] Postek, M. T.; Moon, R. J.; Rudie, A. W.; Bilodeau, M. A., *Production and applications of cellulose*. Tappi Press. Peachtree Corners: 2013.

[2] Moon, R. J.; Martini, A.; Nairn, J.; Simonsen, J.; Youngblood, J., Cellulose nanomaterials review: structure, properties and nanocomposites. *Chemical Society Reviews* **2011,** *40* (7), 3941-3994.

[3] Habibi, Y.; Lucia, L. A.; Rojas, O. J., Cellulose Nanocrystals: Chemistry, Self-Assembly, and Applications. *Chemical Reviews* **2010,** *110* (6), 3479-3500.

[4] Hon, D. N.-S., Cellulose: a random walk along its historical path. *Cellulose* **1994,** *1* (1), 1-25.

[5] Habibi, Y., Key advances in the chemical modification of nanocelluloses. *Chemical Society Reviews* **2014,** *43* (5), 1519-1542.

[6] Moon, R. J.; Schueneman, G. T.; Simonsen, J., Overview of Cellulose Nanomaterials, Their Capabilities and Applications. *JOM* **2016,** *68* (9), 2383-2394.

[7] Hubbe, M. A.; Rojas, O. J.; Lucia, L. A.; Sain, M., *CELLULOSIC NANOCOMPOSITES: A REVIEW*. 2008; Vol. 3.

[8] Eyley, S.; Thielemans, W., Surface modification of cellulose nanocrystals. *Nanoscale* **2014,** *6* (14), 7764-7779.

[9] Neouze, M.-A.; Schubert, U., Surface Modification and Functionalization of Metal and Metal Oxide Nanoparticles by Organic Ligands. *Monatshefte für Chemie - Chemical Monthly* **2008,** *139* (3), 183-195.

[10] Oldenburg, S. J.; Averitt, R. D.; Westcott, S. L.; Halas, N. J., Nanoengineering of optical resonances. *Chemical Physics Letters* **1998,** *288* (2–4), 243-247.

[11] Fang, Y.; Chen, V. W.; Cai, Y.; Berrigan, J. D.; Marder, S. R.; Perry, J. W.; Sandhage, K. H., Biologically Enabled Syntheses of Freestanding Metallic Structures Possessing Subwavelength Pore Arrays for Extraordinary (Surface Plasmon-Mediated) Infrared Transmission. *Advanced Functional Materials* **2012,** *22* (12), 2550-2559.

[12] Fang, Y.; Berrigan, J. D.; Cai, Y.; Marder, S. R.; Sandhage, K. H., Syntheses of nanostructured Cu- and Ni-based micro-assemblies with selectable 3-D hierarchical biogenic morphologies. *Journal of Materials Chemistry* **2012,** *22* (4), 1305-1312.

[13] Shi, W.; Sahoo, Y.; Swihart, M. T.; Prasad, P. N., Gold Nanoshells on Polystyrene Cores for Control of Surface Plasmon Resonance. *Langmuir* **2005,** *21* (4), 1610-1617.

[14] Gruber, S.; Taylor, R. N. K.; Scheel, H.; Greil, P.; Zollfrank, C., Cellulose-biotemplated silica nanowires coated with a dense gold nanoparticle layer. *Materials Chemistry and Physics* **2011,** *129* (1–2), 19-22.

[15] Way, A. E.; Hsu, L.; Shanmuganathan, K.; Weder, C.; Rowan, S. J., pH-Responsive Cellulose Nanocrystal Gels and Nanocomposites. *ACS Macro Letters* **2012,** *1* (8), 1001-1006.

[16] Hemraz, U. D.; Boluk, Y.; Sunasee, R., Amine-decorated nanocrystalline cellulose surfaces: synthesis, characterization, and surface properties. *Canadian Journal of Chemistry* **2013,** *91* (10), 974-981.

[17] Kristiansen, K. A.; Potthast, A.; Christensen, B. E., Periodate oxidation of polysaccharides for modification of chemical and physical properties. *Carbohydrate Research* **2010,** *345* (10), 1264-1271.

[18] Kim, U.-J.; Kuga, S.; Wada, M.; Okano, T.; Kondo, T., Periodate Oxidation of Crystalline Cellulose. *Biomacromolecules* **2000,** *1* (3), 488-492.

[19] Dash, R.; Elder, T.; Ragauskas, A. J., Grafting of model primary amine compounds to cellulose nanowhiskers through periodate oxidation. *Cellulose* **2012,** *19* (6), 2069-2079.

[20] Jin, L.; Li, W.; Xu, Q.; Sun, Q., Amino-functionalized nanocrystalline cellulose as an adsorbent for anionic dyes. *Cellulose* **2015,** *22* (4), 2443-2456.

[21] Azzam, F.; Galliot, M.; Putaux, J.-L.; Heux, L.; Jean, B., Surface peeling of cellulose nanocrystals resulting from periodate oxidation and reductive amination with water-soluble polymers. *Cellulose* **2015,** *22* (6), 3701-3714.

[22] Ciolacu, D.; Ciolacu, F.; Popa, V., *Amorphous cellulose - Structure and characterization*. 2011; Vol. 45, p 13-21.

[23] Schramm, M.; Hestrin, S., Factors affecting Production of Cellulose at the Air/ Liquid Interface of a Culture of Acetobacter xylinum. *Microbiology* **1954,** *11* (1), 123-129.

[24] Hirai, A.; Inui, O.; Horii, F.; Tsuji, M., Phase separation behavior in aqueous suspensions of bacterial cellulose nanocrystals prepared by sulfuric acid treatment. *Langmuir* **2008,** *25* (1), 497-502.

[25] Wang, G.; Fang, Y.; Kim, P.; Hayek, A.; Weatherspoon, M. R.; Perry, J. W.; Sandhage, K. H.; Marder, S. R.; Jones, S. C., Layer-By-Layer Dendritic Growth of Hyperbranched Thin Films for Surface Sol–Gel Syntheses of Conformal, Functional, Nanocrystalline Oxide Coatings on Complex 3D (Bio)silica Templates. *Advanced Functional Materials* **2009,** *19* (17), 2768-2776.

[26] Yu, H.; Qin, Z.; Liang, B.; Liu, N.; Zhou, Z.; Chen, L., Facile extraction of thermally stable cellulose nanocrystals with a high yield of 93% through hydrochloric acid hydrolysis under hydrothermal conditions. *Journal of Materials Chemistry A* **2013,** *1* (12), 3938-3944.

[27] Rees, D., A note on the characterization of carbohydrate sulphates by acid hydrolysis. *Biochemical Journal* **1963,** *88* (2), 343.

[28] Gu, J.; Catchmark, J. M.; Kaiser, E. Q.; Archibald, D. D., Quantification of cellulose nanowhiskers sulfate esterification levels. *Carbohydrate Polymers* **2013,** *92* (2), 1809-1816.

[29] Segal, L.; Creely, J. J.; A.E. Martin, J.; Conrad, C. M., An Empirical Method for Estimating the Degree of Crystallinity of Native Cellulose Using the X-Ray Diffractometer. *Textile Research Journal* **1959,** *29* (10), 786-794.

[30] Nam, S.; French, A. D.; Condon, B. D.; Concha, M., Segal crystallinity index revisited by the simulation of X-ray diffraction patterns of cotton cellulose Iβ and cellulose II. *Carbohydrate Polymers* **2016,** *135*, 1-9.

[31] da Silva Perez, D.; Montanari, S.; Vignon, M. R., TEMPO-Mediated Oxidation of Cellulose III. *Biomacromolecules* **2003,** *4* (5), 1417-1425.

[32] Shinoda, R.; Saito, T.; Okita, Y.; Isogai, A., Relationship between Length and Degree of Polymerization of TEMPO-Oxidized Cellulose Nanofibrils. *Biomacromolecules* **2012,** *13* (3), 842-849.

[33] Lane, C. F., Sodium Cyanoborohydride - A Highly Selective Reducing Agent for Organic Functional Groups. *Synthesis* **1975,** *1975* (03), 135-146.

[34] Chang, H.; Luo, J.; Bakhtiary Davijani, A. A.; Chien, A.-T.; Wang, P.-H.; Liu, H. C.; Kumar, S., Individually Dispersed Wood-Based Cellulose Nanocrystals. *ACS Applied Materials & Interfaces* **2016,** *8* (9), 5768-5771.

CHAPTER 2: SYNTHESIS AND PROPETIES OF INDIVIDUALLY DISPERSED GOLD NANOSHELL-BEARING CELLULOSE NANOCRYSTALS

2.1 Summary

Individually dispersed CNCs having thin, continuous and conformal coatings of gold have been generated using the amine-bearing CNCs developed in the previous chapter. Gold coatings/shells were deposited onto the aminated CNCs by first decorating their surfaces with many fine gold nuclei, which then served as preferential heterogeneous nucleation sites for electroless gold deposition. Gold nanoshell-bearing CNCs (AuNS-CNCs) were found to have size dependent optical properties, characterized by two surface plasmon resonance extinction bands, corresponding to plasmon resonances along the transverse and longitudinal directions. The wavelength maximum position of the longitudinal surface plasmon resonance band (λ_{max} LSPR) was found to be sensitive to the thickness of the deposited gold shell as well as to the length of the aminated CNC templates. The position of the λ_{max} LSPR was observed to blue-shift with increasing gold shell thickness and could be tuned from 1300 to 1000 nm. Viscosity gradient centrifugation revealed that the variety of CNC lengths contributed to the inhomogeneous broadening of the near-infrared LSPR band, demonstrating that size fractionation of AuNS-CNCs can yield particles having LSPR extinction bands with narrower linewidths at desired wavelengths.

2.2 Introduction

2.2.1 Gold Nanoparticles

Gold's luster and lack of tarnish has been valued since antiquity. Its ductile and malleable nature lent itself to being shaped into intricate jewelry and artworks that are still prized today. Perhaps one of the most intriguing uses of gold by early artisans is exemplified in the Lycurgus Cup (**Figure 17**), where color changing properties are a result of colloidal gold. Over the centuries, gold's allure has not waned, and it continues to be used in jewelry and art as well as in a host of high-tech modern applications.

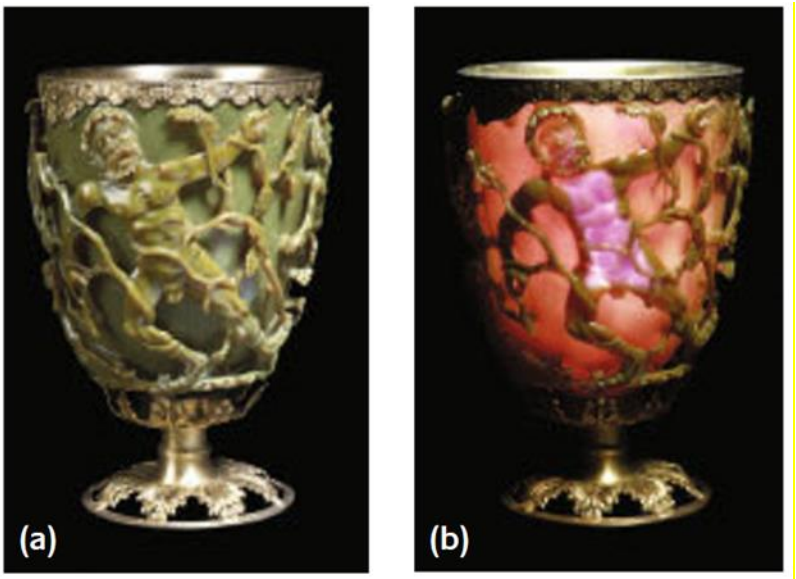

Figure 17. The Lycurgus cup in reflected (a) and transmitted (b) light. [1]

Today, we understand that nano-sized gold particles exhibit properties different from their bulk counterpart, and have found nano-sized gold particles useful in applications ranging from optics, sensors, biological imaging, cancer therapy, and catalysis.[2-8]

The unique optical properties of gold nanoparticles arise from the collective oscillation of electron clouds that are set into motion when the nanosized metal encounters a traveling electromagnetic wave.[9] This collective electron motion is termed "surface plasmon resonance" (SPR) and gives rise to unique extinction bands that are indicative of the particle geometry.[9] The position of these absorption and scattering bands is dictated by the particle's size, shape, and environment. Mie first modeled this phenomenon by solving Maxwell's equations for metallic spheres interacting with an electromagnetic field.[10] Mie's equation for polarizability of a metallic sphere can be seen in **Equation 1** (where, α is polarizability, a is particle radius, ε is the dielectric function of the metal, and ε_m is the dielectric function of the medium).[11] The plasmon resonance condition can be determined by analyzing the extrema of polarizability, which occur when the denominator of **Equation 1** is at a minimum.[9-10] Since the dielectric constant of gold varies with wavelength, the resonant condition occurs when the real component of the dielectric function is equal to twice that of the medium dielectric function ($\mathrm{Re}[\varepsilon(\omega)] = -2\varepsilon_m$, Fröhlich condition).[9] This resonance condition results in the cooperative oscillation of electrons and is termed "localized surface plasmon resonance."

$$\alpha = 4\pi a^3 \left[\frac{\varepsilon - \varepsilon_m}{\varepsilon + 2\varepsilon_m}\right] \quad (1)$$

The cross-sections for scattering (C_{sca}) and absorption (C_{abs}) are obtained from the scattering field radiated by the resonating dipole (electron cloud/plasma) as shown in **Equation 2** (eR) and **3**, where k is the wave vector ($k = \frac{2\pi}{\lambda}$).[9]

$$C_{sca} = \frac{8\pi}{3} k^4 a^6 \left[\frac{\varepsilon - \varepsilon_m}{\varepsilon + 2\varepsilon_m}\right]^2 \quad (2)$$

$$C_{abs} = 4\pi k a^3 \left[\frac{\varepsilon - \varepsilon_m}{\varepsilon + 2\varepsilon_m}\right] \quad (3)$$

From the above equations and the graph presented in **Figure 18**, it is evident that the extinction of small particles tends to be dominated by absorption processes, but as size increases (>85 nm), scattering becomes the dominant extinction mechanism.

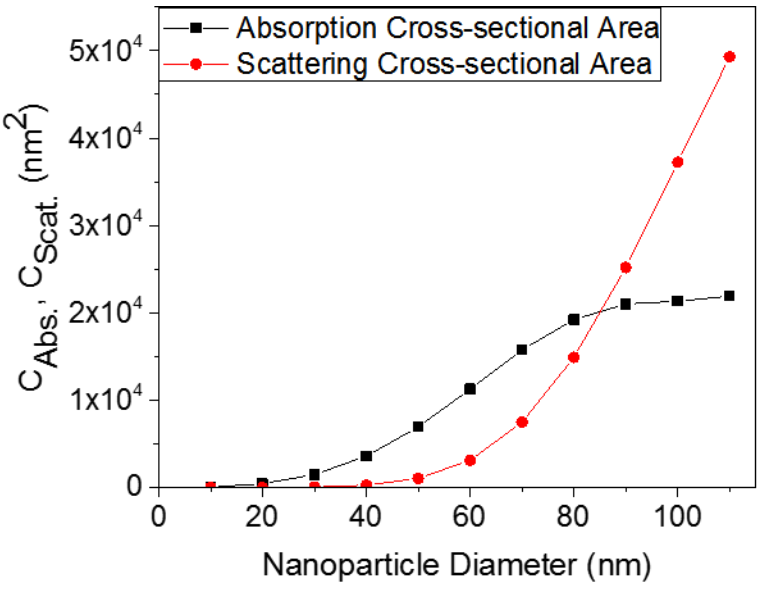

Figure 18. Graph showing how the cross-sectional area for absorption and scattering varies with increasing gold nanoparticle diameter. Scattering processes become more efficient with increasing size and dominate optical extinction for spherical particles of >85 nm.

These findings serve as guidelines for nanoparticle design and synthesis. However, they do not describe the effects of particle anisotropy and potential electromagnetic phase

retardation, which become important when dealing with non-spherical particles and those of large size (>30 nm).

For example, gold nanorods having aspect ratios >1 exhibit two plasmon extinction bands that correspond to surface plasmon resonance modes parallel and perpendicular to the long axis.[12] The oscillations in the transverse mode (the short axis) tend to exhibit plasmon resonances around 520-550 nm depending on the diameter of the rod, while the longitudinal mode (the long axis) is observed at longer wavelengths and is a function of aspect ratio. El-Sayed, et al. have shown that for small gold nanorods (diameter < 30 nm) increasing the particle aspect ratio while holding the diameter constant linearly shifts the longitudinal plasmon band towards infrared wavelengths, and for particles suspended in water (ε_m=1.77), the band maximum (λ_{max}) can be approximated by **Equation 4** where AR is the particle aspect ratio.[13]

$$\lambda_{max} = 96.9(AR) + 385 \quad (4)$$

Recently, there has been a growing interest in designer plasmonic particles having highly tunable plasmon resonance bands.[14-18] The first example of such a particle was demonstrated by Oldenburg, et al., who coated dielectric silica microspheres with a thin layer of gold, producing gold nanoshells with enhanced extinction cross-sections and extinction bands that could be easily tuned across a wide spectral range.[18] Since the dielectric environment is different at the interior and exterior surfaces of the gold shell, the observed optical extinction band is the result of surface plasmon mode hybridization as demonstrated in **Figure 19**.[14, 19] This phenomenon allows for fine tuning of the plasmon resonance band maximum simply by changing the thickness of the gold shell which

modulates the extent of surface plasmon coupling between the two gold surfaces.[14, 19] This new particle architecture has sparked much interest and has been investigated for a variety of applications ranging from photothermal cancer therapy,[20-21] to single-particle sensors.[16, 22]

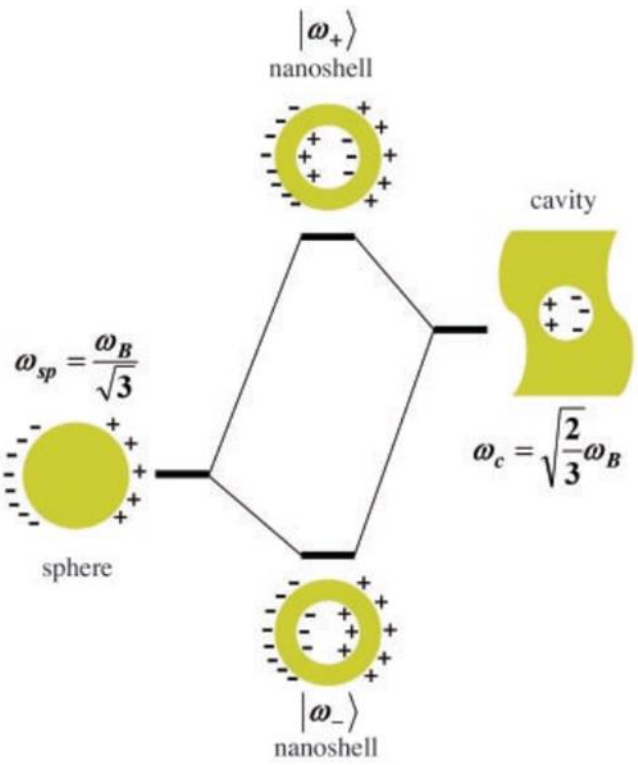

Figure 19. An energy-level diagram describing the plasmon hybridization in metal nanoshells resulting from the interaction between the outer shell and cavity plasmons. The two nanoshell plasmons are an anti-symmetrically coupled (antibonding) ω_+ plasmon mode and a symmetrically couple (bonding) ω_- plasmon mode. Reproduced from Prodan, et al.[19]

More recently, a novel core-shell nanoparticle architecture was developed that consists of hematite spindles coated with a thin layer of gold (Nanorice).[14] The elongated shape of the spindles gives rise to two plasmon modes similar to gold nanorods, but in the case of nanorice, the thickness of the gold shell plays a main role in tuning the longitudinal plasmon band position, as shown in **Figure 20**. Increasing the gold coating thickness blue-

shifts the longitudinal plasmon band due to the increased distance between the inner and outer surfaces, which weakens plasmon mode coupling between them and thus the plasmon energy shifts from the hybridized bonding mode towards that of just the outer shell (i.e., higher energy), see **Figure 19** for clarification.

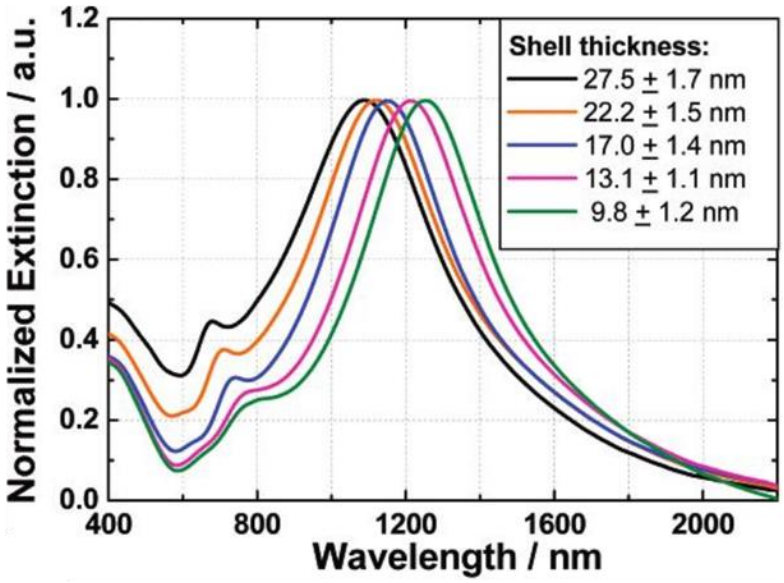

Figure 20. Extinction spectra of gold coated hematite nanorice with different coating thicknesses. Graph reproduced from Wang, et al. [14]

Using calculations and experimental data, Prodan, et al. showed that if the separation distance between the inner and outer surface becomes large enough, the inner and outer plasmon modes decouple and the optical response becomes dominated by the plasmon resonance of the outer surface only.[19] For the case of elongated structures such as nanorice, this suggests that at a particular coating thickness the structure's optical response will become similar to that of gold nanorods, where the diameter and aspect ratio of the particle become the key shape parameters. Wang, et al. also demonstrated that structures with hybridized plasmon modes have significantly increased geometric sensitivity due to the relationship between shell thickness and hybrid plasmon mode coupling strength, which

allows for the tuning of longitudinal plasmon bands across a broader spectral range than their solid gold counterparts (nanorods).[14] Wang, et al. also determined that the core-shell architecture of nanorice showed unprecedented sensitivity towards the surrounding dielectric medium due to its unique core-shell structure; with sensitivities measured as high as 801 nm per refractive index unit (RIU), these novel particles could be beneficial for fabrication of extremely sensitive optical sensors.[14, 23] The above examples illustrate the exceptional ability of template synthesis to produce nanoparticles with unique and useful optical properties. Thus, the work described below aims to expand the template synthesis tool box with the addition of naturally occurring, bio-renewable, and chemically amenable cellulose nanocrystal templates.

2.3 Experimental Procedures

2.3.1 Preparation of Chloroauric Acid Solutions

A 25 mM stock solution of chloroauric acid ($HAuCl_4$, 99.99% trace metals, Sigma Aldrich, St. Louis, MO) was prepared using DI water. The solution was aged without stirring in a dark cabinet for a minimum of 3 days before use. The stock solution could be stored in the dark and used for nanoparticle synthesis for up to a month.

2.3.2 Preparation of Electroless Au Plating Solution

A chloroauric acid-based electroless gold plating solution was prepared as per the method of Brinson, et al.[17] Briefly, the $HAuCl_4$ stock solution (3.0 mL) was mixed with an aqueous solution (200 mL, 1.8 mM) of K_2CO_3 (99% purity, Sigma Aldrich, St. Louis, MO). The solution was magnetically stirred (350 RPM) for 30 minutes in a container covered

with aluminum foil (to avoid exposure to light). The solution was then aged without stirring in a dark cabinet for a minimum of 24 hours before use. The resulting solution could be used electroless deposition trials for up to 6 weeks after initial preparation.

2.3.3 Synthesis of 1-3 nm Diameter Gold Particles

A suspension of 1-3 nm diameter gold particles was prepared as per the method of Duff, et al.[24] An aqueous solution of NaOH (0.3 mL, 1 M, ACS Grade, Sigma Aldrich, St. Louis, MO) was diluted with DI water (47 mL) in a 200 mL beaker. An aqueous solution of tetrakis(hydroxymethyl)phosphonium chloride (12 μL, 80% THPC, Sigma Aldrich, St. Louis, MO) was diluted with DI water (1 mL), and then added to the NaOH solution with magnetic stirring (350 RPM). After 5 minutes, the stirring speed was increased to 1200 RPM, and the aged stock $HAuCl_4$ solution (1.9 mL, 25 mM) was quickly injected into the THPC-NaOH solution from a pipet (with the aid of a full pipet bulb). The solution quickly turned dark brown indicating the formation of colloidal gold particles. After stirring at 1200 RPM for an additional 5 minutes, the suspension of gold nanoparticles was passed through a 0.1 μm syringe filter into a clean glass bottle (cleaned with Aqua Regia and thoroughly rinsed with DI water). The gold nanoparticle suspension was stored at 4°C for a minimum of two weeks before use. The shelf-life of these particles has been reported to be ≈6 months.[17]

2.3.4 Preparation of Gold Nanoparticle-Decorated a-CNCs

A 15 μL aliquot of aminated CNC (a-CNCs) suspension (0.11 wt.% a-CNCs) was diluted to 1 mL with DI water. The diluted a-CNCs suspension was sonicated for 5 minutes (Branson 2510 ultrasonic bath, Branson Ultrasonic Corp., St. Louis, MO). The 1-3 nm gold

nanoparticle suspension (4 mL) was added to a scintillation vial (20 mL, Cat No. 66022-065, VWR Analytical, Radnor, PA) and was placed into the ultrasonic bath (Branson 2510 ultrasonic bath, Branson Ultrasonic Corp., St. Louis, MO). A pipet was used to gradually add the diluted a-CNC suspension (1 mL), at a rate of ≈0.1 mL per minute, to the gold nanoparticle suspension. The vial was capped and stored in the dark for 14 hours. Gold-decorated a-CNCs were then separated from loose gold nanoparticles by centrifugation. The contents of the scintillation vial were transferred into several 2 mL centrifuge vials and centrifuged at 20,000 RCF for 30 min. After careful removal of the supernatant, the resulting film of gold-decorated a-CNCs was dispersed in DI water for further centrifugation (15,000 RCF) for 30 min. The DI water dispersal and centrifugation (15,000 RCF) treatment was repeated three more times. The gold-decorated a-CNCs were then diluted with DI water to yield an absorbance value of 0.06 at 490 nm as measured through 1 cm wide cuvette using a UV-vis spectrometer (UV-3101PC, Shimadzu, Kyoto, Japan). This suspension was ultrasonically processed (Branson 2510 ultrasonic bath, Branson Ultrasonic Corp., St. Louis, MO) for 1 hour to ensure particles were dispersed. The suspension of gold nanoparticle-decorated a-CNCs (≈0.006 wt.% a-CNC loading) was stored at 4°C until use. The particle suspensions were found to be remain viable for electroless gold deposition for several (2-3) months.

2.3.5 Carbon Monoxide Generation

Carbon monoxide was generated and used as a reducing agent during electroless gold deposition. Given the odorless, colorless, and toxic nature of carbon monoxide, such carbon monoxide generation and use were conducted entirely within a fume hood. Carbon monoxide was generated in small quantities (500 mL) via the dehydration of 5 mL of

formic acid (97% purity, Alfa Aesar, Haverhill, MA) by reaction with 10 mL of sulfuric acid (ACS Grade 95-98% purity, BDH VWR Analytical, Radnor, PA). The gas was collected and contained in a 3-neck round bottom 500 mL flask fitted with a rubber septum. Once the flask was filled with CO gas, the remaining formic acid/sulfuric acid solution was poured into 200 mL of cold water to stop the dehydration reaction. The gas generator construction and operation are detailed in **Appendix A**.

2.3.6 Synthesis of Gold-Coated a-CNCs

Electroless deposition was used to apply additional gold onto the gold nanoparticle-decorated a-CNCs to generate continuous gold shells (i.e., gold nanoshell-bearing CNCs). A suspension of gold nanoparticle-decorated a-CNCs (200 μL, ≈0.006 a-CNC wt.% loading) was placed in a 10 mL vial along with a controlled volume (0.1 mL to 2.75 mL) of the electroless gold plating solution. DI water was then added to adjust the total suspension volume to 3 mL, and the vial was sealed with a rubber septum. A syringe was used to pull a slight vacuum in the vial to help keep the septum in place during subsequent gold ion reduction, and the contents were briefly mixed with a lab vortexer (Vortex Genie 2T, Bohemia, NY). A hypodermic needle was then used to inject 1 mL of CO gas just above the suspension within the vial. The vial was quickly placed back on the vortexer and the contents were mixed at the highest speed setting for 1 min. During such mixing, the colorless solution developed a deep purple color, which was consistent with the formation of gold nanoshells. The suspension was then centrifuged at 500 RCF for 10 minutes to remove freely nucleated particles (i.e., gold particles not attached to CNCs). After careful removal of the supernatant, the remaining gold-nanoshell CNCs (AuNS-CNCs) were dispersed in DI water.

2.3.7 Mass Based Fractionation of Gold Coated a-CNCs

Differential viscosity gradient centrifugation was employed to allow for size/mass-based separation of the AuNS-CNCs. Aqueous solutions of 50 wt.%, 40 wt.%, 30 wt.%, 20 wt.%, and 10 wt.% glycerol, were sequentially placed (layer by layer) in a 5mL centrifuge vial by carefully pipetting solutions of lower glycerol content (lower density) on top of solutions of higher glycerol content (higher density). Each glycerol layer (0.9 mL thick) could be distinguished from neighboring layers due to refractive index differences of the layers. The dilute AuNS-CNC suspension was centrifuged down at 500 RCF for 15 min and then dispersed in 100 μL of DI water. This concentrated suspension (≈0.13 wt.% AuNS-CNCs) of gold-coated CNCs was then placed on the top (10 wt.%) glycerol solution layer, and the vial was centrifuged (300 RCF) for 20 minutes. Two distinct AuNS-CNCs fractions were recovered. Each fraction was washed (to remove glycerol) using 5 cycles of centrifugation (1000 RCF, 5 min) and dispersion in DI water. The washed AuNS-CNCs were dispersed in 1 mL of DI water using an ultrasonic bath for 5 minutes prior to optical analysis.

2.3.8 Optical Analysis

Visible-Near Infrared extinction analyses were conducted with a spectrophotometer (UV-3101PC, Shimadzu, Kyoto, Japan) operating in the range of 400 nm to 1300 nm. Spectra of aqueous suspensions were collected over a 1 cm path length using quartz cuvettes (108-QS, Hellma Analytics, Muellheim Germany).

2.3.9 Size, Shape and Morphology Analyses

Scanning electron microscopy (SEM) was conducted with a scanning electron microscope equipped with a field emission gun (Ultra 60 FE-SEM, Carl Ziess, Oberkochen, Germany). Images were collected at an accelerating voltage of 5 kV. Samples were prepared for imaging by depositing ~2 μL of dilute AuNS-CNC suspensions onto ozone-cleaned, platinum-coated silicon wafer substrates and allowing the water to evaporate at room temperature.

TEM analyses of individual AuNS-CNCs were conducted using a transmission electron microscope equipped with a LaB_6 filament (Tecnai T20, FEI, Hillsboro, Oregon). Images were collected at an accelerating voltage of 200 kV. Samples were prepared by depositing 1 μL of dilute (≈0.004 wt.%) AuNS-CNC suspensions onto carbon-coated copper TEM grids followed by water evaporation at room temperature.

2.4 Results and Discussion

Although several methods[25-27] for creating conformal gold coatings on silica and polymeric microspheres have been developed over the years the methods investigated in this work for depositing gold coatings onto aminated CNCs were similar to those reported by Oldenburg, et al.[17-18] Suspensions of aminated CNCs and 1-3 nm diameter gold particles were mixed to allow for adsorption of gold nanoparticles onto the CNC surfaces through weak covalent bonding.[28] The CNC-bound gold nanoparticles then served as heterogeneous nucleation sites for subsequent electroless gold deposition. With sufficient electroless deposition, the gold nanoparticles became interconnected to yield continuous nanocrystalline gold shells around the aminated CNCs. A schematic illustration of this

process is shown in **Figure 21a**. TEM analysis of the as-received CNCs (**Figure 21b**) revealed rod-like particles with a wide distribution of lengths. The optical extinction of the as-received CNC suspensions (**Figure 21b**) followed a monotonically decaying curve with increasing wavelength, which is characteristic of particles exhibiting Rayleigh scattering.[11] Suspensions of 1-3 nm diameter gold particles whose extinction is dominated by absorption also exhibit a monotonically decaying extinction profile with increasing wavelength (**Figure 21c**).[24] The small shoulder seen at 520 nm in the gold nanoparticle extinction spectrum was consistent with plasmon absorption associated with particle growth during aging.[24] This plasmon shoulder (**Figure 21c**) was much more pronounced in the extinction spectrum of gold-decorated CNCs, which is attributed to plasmon coupling between closely spaced gold nanoparticles on the surface of CNCs. TEM images of CNCs after gold nanoparticle attachment (**Figure 21c**) confirmed the presence of dense rod-like assemblies containing fine gold particles.

To enhance the interconnection of the fine gold nanoparticles along the length of the aminated CNCs and to generate complete gold shells, additional gold was applied via electroless deposition using carbon monoxide (CO) as the reducing agent. Prior work by Brinson, et al. has revealed that the use of CO during such electroless gold deposition enhanced the continuity and uniformity of the resulting gold shells.[17] Heterogeneous gold nucleation during CO-enhanced electroless deposition resulted in the coarsening of gold nanoparticles on the CNC surfaces (**Figure 21d**). After 1 minute of exposure to a modest volume of gold electroless solution (0.25 mL), however, significant gaps were still detected between the gold particles on the CNC surfaces. Exposure for the same time to a larger volume (>2.0 mL) of gold electroless solution resulted in enhanced gold interconnectivity

(**Figure 21e**) to yield CNCs possessing complete gold nanoshells (AuNS-CNCs). These fully encapsulated AuNS-CNCs possessed a zeta potential of -20 ± 4 mV, which is consistent with reports for uncapped gold nanoparticles, whose charge is a result of the accumulation of hydroxide ions on their surface.[29-31] The extinction spectrum of the AuNS-CNCs exhibited two distinct bands (**Figure 21e**), with one band located in the visible range (around 550 nm) and the other broader band located in the near-infrared range. These visible and near-infrared bands were consistent with plasmon resonance through the nanoshell thickness (transverse) and along the nanoshell length (longitudinal), respectively. The broad nature of the near-infrared band in **Figure 21e** was consistent with reported optical response of nanorice[14] which has a similar core-shell structure. As expected, the position of the near-infrared plasmon peak was highly red-shifted relative to reported longitudinal plasmon resonance peaks for shorter gold nanorods of similar aspect ratio ranging from ≈750 nm to ≈980 nm for nanorods with aspect ratios of 2.8 and 4.9, respectively.[13, 32] Since, such longer/wider gold particles with a core-shell architecture fall outside of the quasi-static dipole approximation range, they are subject to phase retardation, plasmon dampening, and plasmon hybridization effects, which can cause a significant redshift of the longitudinal plasmon band.[19, 33-34]

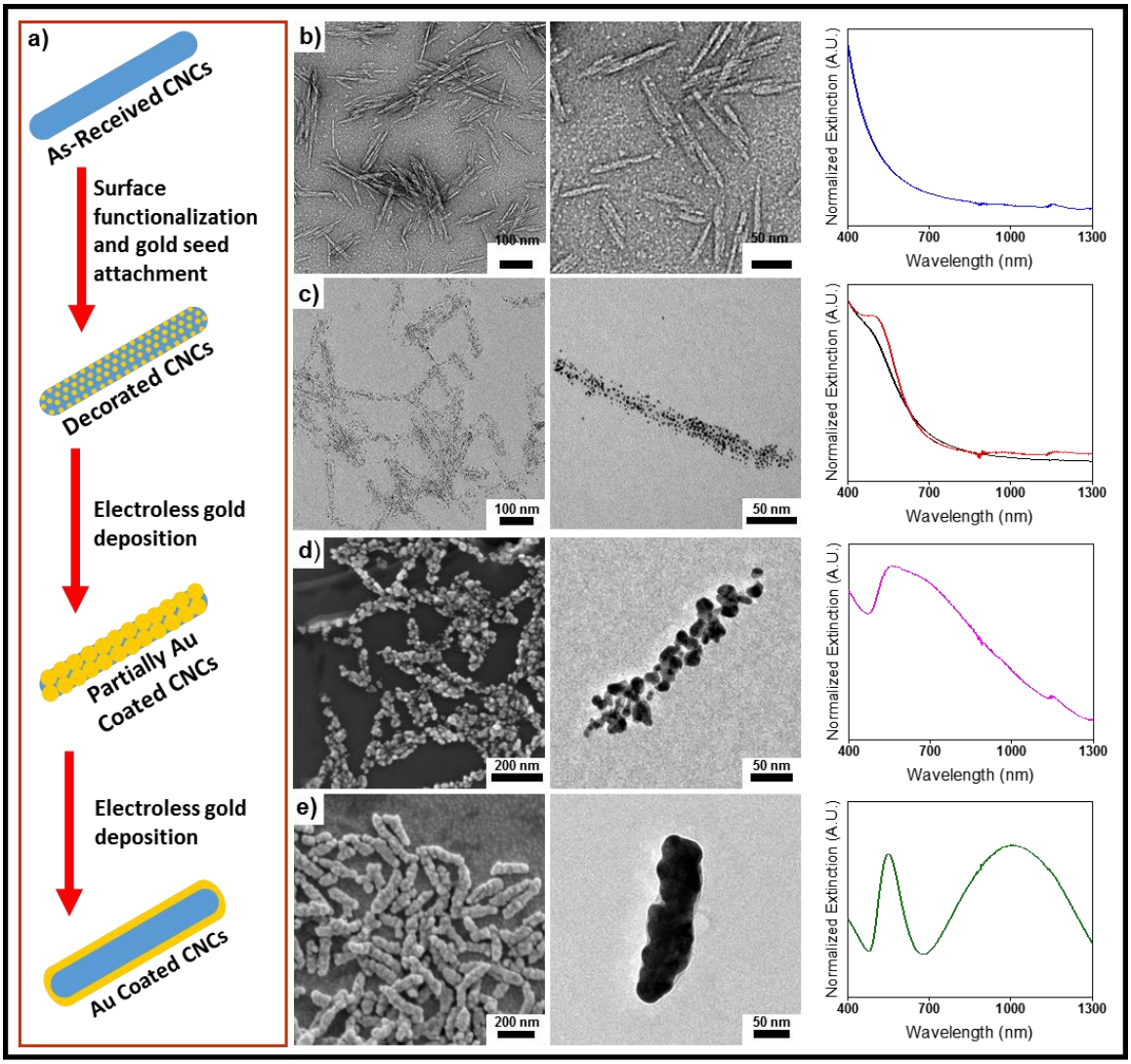

Figure 21. (a) Schematic illustration of the gold coating process. (b) As-received CNCs: TEM images and optical extinction spectrum. (c) Gold-decorated a-CNCs: TEM images and optical extinction spectra of 1-3 nm gold nanoparticles [black] and gold-decorated a-CNCs [red]. (d) Partially gold-coated CNCs: SEM and TEM images of CNCs with partial gold coatings (using 0.25 mL of gold plating solution) and the extinction spectrum. (e) Gold nanoshell-bearing CNCs (AuNS-CNCs): SEM and TEM images of CNCs with complete and continuous gold coatings (using 2.75 mL of gold plating solution) and the extinction spectrum.

To investigate the influence of the gold nanoshell thickness on the tunability of the longitudinal plasmon band, the amount of deposited gold was increased by exposing gold nanoparticle-decorated a-CNC suspensions of similar concentration and volume (200 µL,

≈0.006 wt.% loading) to increasing volumes (2.0 mL to 2.75 mL) of electroless gold solution. Particle width analyses were then conducted using SEM images of 200 individual particles for each volume of electroless gold solution used. A general increase was observed in the mean AuNS-CNC particle width upon exposure to an increasing volume of electroless gold solution as shown in **Figure 22**.

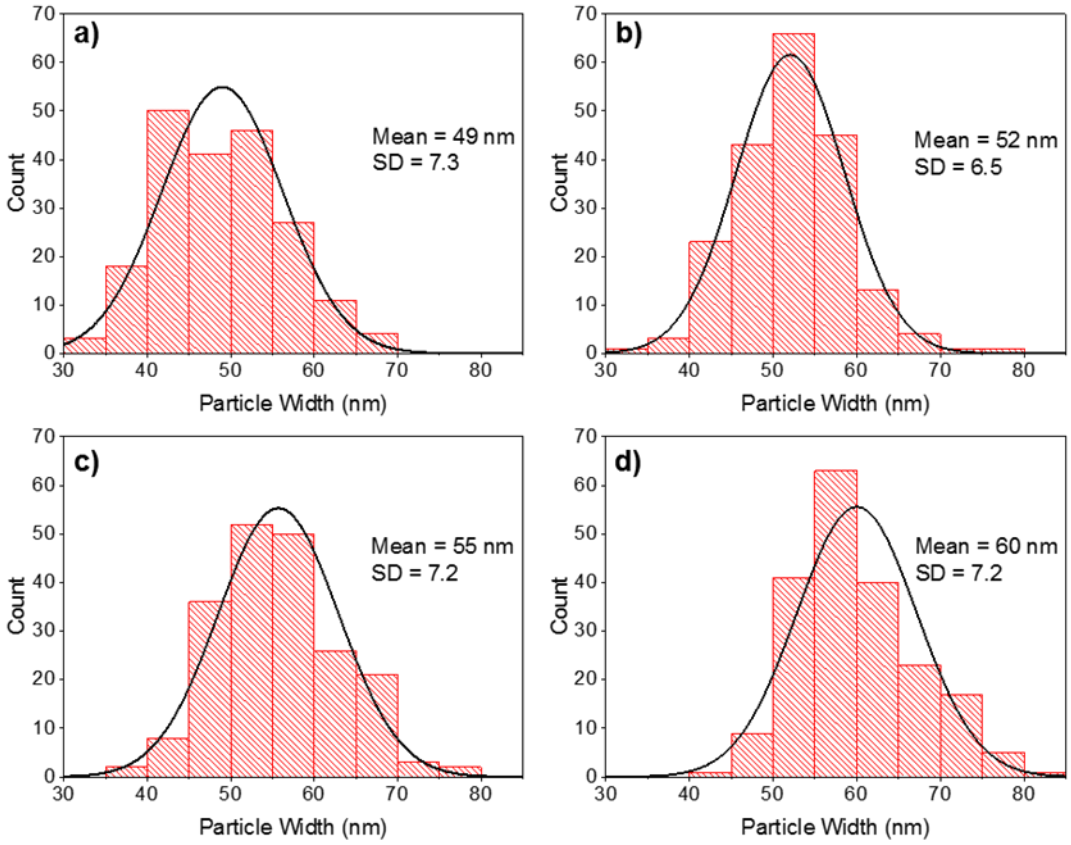

Figure 22. Particle widths of AuNS-CNCs synthesized by exposure to increasing volumes of electroless gold solution: (a) 2.0 mL, (b) 2.125 mL, (c) 2.5 mL, and (d) 2.75 mL.

Student's t-test analysis confirmed, within 95% confidence, that the values of the mean particle width obtained upon exposure to an increasing volume of electroless solution were statistically different (i.e., p values obtained by comparing pairs of data sets were well

below 0.001). The values of the average gold nanoshell thickness were determined by subtracting the average CNC cross-sectional width value of 7 ± 2 nm (for wood-derived CNCs synthesized via sulfuric acid hydrolysis[35]) from the mean width values shown in **Figure 22** and dividing by two.

Exposure to an increasing volume of the electroless gold solution (from 2.0 mL to 2.75 mL) resulted in a monotonic increase in the average thickness of the gold nanoshells (from 21 nm to 26.5 nm) and, in turn, a monotonic blueshift in the peak (maximum extinction) location of the longitudinal plasmon band from about 1300 nm to about 1000 nm as shown in **Figure 23**. The width of the longitudinal band also decreased with an increase in the mean gold nanoshell thickness. Similar shifts in plasmon resonance with increasing shell thickness have been reported for gold nanoshells[18] as well as gold nanorice[14, 36] and are attributed to the change in the extent of plasmon mode hybridization[19] between the inner and outer surface plasmon modes of the gold nanoshells. Tuning the longitudinal band outside of the range presented here was not investigated, but it's anticipated that thinner coatings would push the longitudinal plasmon resonance band further towards the infrared wavelengths, which would require a more transparent solvent (e.g. deuterium oxide), while thicker coatings would reduce the aspect ratio further and produce particles with both extinction bands in the visible wavelength region. A more detailed analysis of AuNS-CNC optical properties is provided in **Chapter 3**.

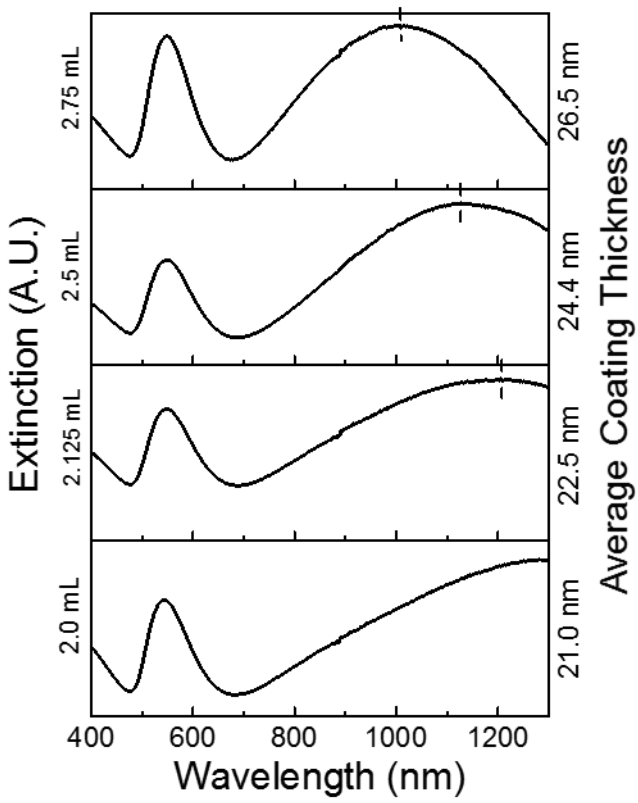

Figure 23. Extinction spectra of gold coated CNCs showing the effect of increasing amount of electroless growth solution / average coating thickness (Y-axis).

To evaluate the influence of the average gold nanoshell length on optical behavior, viscosity gradient fractionation was used to obtain populations of AuNS-CNCs with different average lengths. A dispersion of AuNS-CNCs prepared with the use of 2.5 mL of electroless gold solution was separated into two fractions, with the population possessing longer AuNS-CNC particles settling at a faster rate. Particle length analyses were conducted using SEM imaging of 100 individual particles from each fraction. The particle length distributions of the two populations are shown in **Figure 24a**, **c**. The average lengths of the two AuNS-CNC populations were 207 nm (± 46 nm) and 231 nm (± 63 nm), respectively. A student t-test revealed that the two populations were statistically different

with a p-value of 0.0024. Although the difference in the average particle length was less than 30 nm, a blue shift of about 100 nm in the longitudinal plasmon band was detected for the AuNS-CNC population with the shorter average particle length.

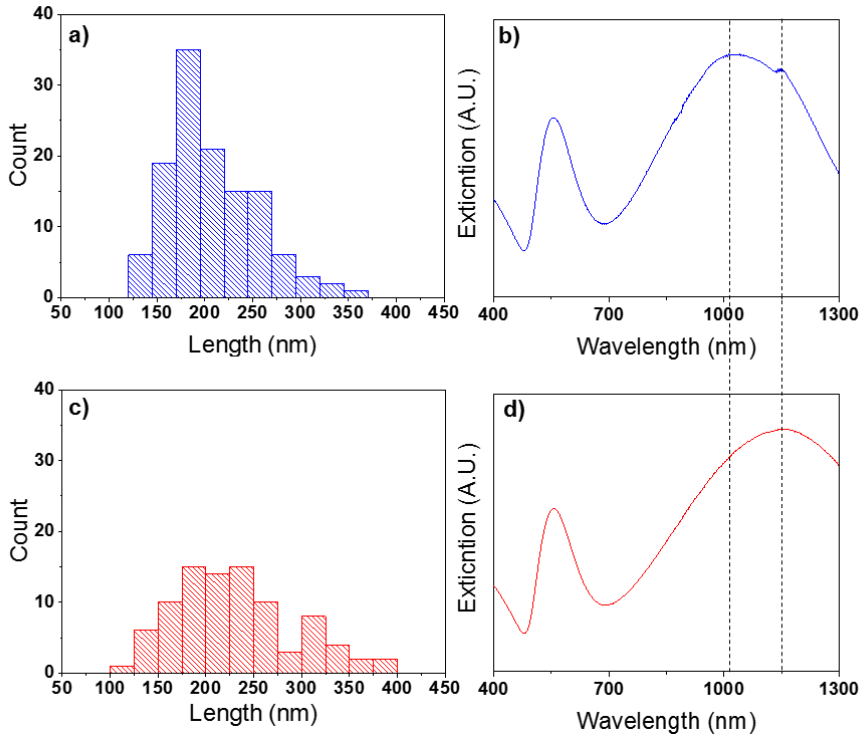

Figure 24. (a, c) Histograms of particle length distributions of the relatively short and long AuNS-CNC fractions, respectively. (b, d) Extinction spectra of the relatively short (blue) and long (red) AuNS-CNC fractions.

Gold coated bacterial cellulose nanocrystals, whose lengths can range from 300 nm to 1000nm (**Figure 25a, b)** were used to further investigate the effect of particle length on the optical response of AuNS-CNCs. Gold-coated BCNCs were also fractionated and their resulting optical spectra are shown in **Figure 25c**. Like the spectrum of gold-coated wood derived CNCs, the spectrum of the gold-coated BCNCs showed two extinction bands, but the longitudinal surface plasmon resonance band was shifted further into the NIR wavelengths (≈1350 nm) as would be expected for longer particles. After density gradient

centrifugation, the two recovered fractions contained particles whose longitudinal plasmon resonance bands were shifted away from that of the unfractionated sample. The resonance band of bottom fraction containing longer/heavier particles red-shifted to about 1470 nm, while the resonance band of the fraction containing shorter/lighter particles blue-shifted to about 1130 nm and became less broad. These results confirmed that the optical extinction of the AuNS-CNCs is highly sensitive to the length distribution of starting template material (i.e. wood CNCs, BCNCs) and the location of the longitudinal plasmon resonance band can be used to roughly estimate the average particle length in suspension. The effect of length on the longitudinal plasmon resonance behavior is analyzed in greater detail in **Chapter 3**.

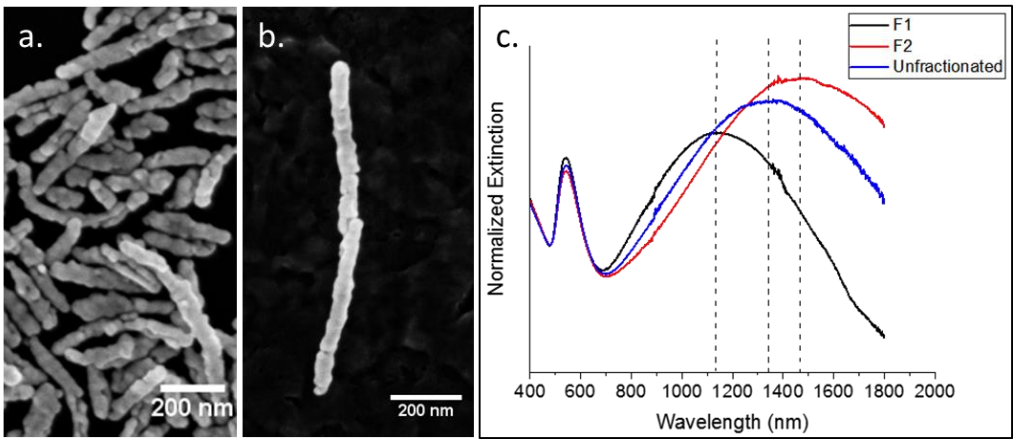

Figure 25. a, b) SEM images showing gold coated BCNCs. c) Extinction spectra of gold coated BCNCs (blue) and the spectra of two fractions recovered after density gradient centrifugation. Spectra were normalized to the minimum at 479 nm to show clarity in trends.

2.5 Conclusions

For the first time, individual gold nanoshell-bearing CNCs have been fabricated using a scalable, surfactant free, wet chemical process. Small (< 3 nm) gold nanoparticles were adsorbed onto the surfaces of aminated CNCs through weak covalent interactions between amines and metal. A dense assembly of gold nanoparticles on CNCs surfaces was indicated by the development of a plasmon extinction band at 520 nm, characteristic of plasmon coupling between closely spaced or agglomerated gold particles. TEM analysis confirmed the presence of individual rod-like assemblies of fine gold particles. Using electroless deposition, the fine gold nanoparticles were enlarged until they formed continuous and conformal coatings around the aminated CNCs. Optical extinction measurements were used to track the progress of the gold coating growth. Upon the formation of a continuous shell, the optical extinction spectrum developed two individual extinction bands associated with surface plasmon resonance in the transverse and longitudinal directions, similar to other elongated gold nanoparticles (e.g., nanorods). The position of the longitudinal plasmon band could be tuned over a range of wavelengths (1000 nm to 1300 nm) by changing the thickness of the gold shell which was achieved by increasing the ratio of electroless gold plating solution to gold nuclei decorated CNCs. The observed blue shift in extinction with increasing shell thickness was found to be consistent with reports of similar core-shell nanoparticles, which stems from plasmon mode hybridization between the inner and outer gold surfaces.[19] The effect of CNC template length on the optical extinction of AuNS-CNCs was investigated by fractionating gold coated CNCs via viscosity gradient centrifugation. The extinction spectra of the resulting fractions were shifted from one another. Fractions with shorter CNCs λ_{max} LSPR that was

blue-shifted in comparison with fractions containing longer CNCs. Identical results were observed upon fractionation of longer gold coated BCNCs, which confirmed that the variation in CNC length was a major contributor to the considerable broadening of the longitudinal plasmon resonance band.

Although the process developed here has been focused on generating gold coatings on individually dispersed aminated CNCs and BCNCs, it should be noted that the developed process is likely compatible with a wide variety of other aminated cellulose nanomaterials, as well as with structures self-assembled from them (hydrogels, chiral nematic films, etc.) The general techniques for the deposition of thin, conformal, and continuous gold coatings developed here can be extended to other material systems and examples of which can be found in later chapters (**Chapter 4** and **Chapter 5**).

2.6 References

[1] Freestone, I.; Meeks, N.; Sax, M.; Higgitt, C., The Lycurgus Cup — A Roman nanotechnology. *Gold Bulletin* **2007,** *40* (4), 270-277.

[2] Eustis, S.; El-Sayed, M. A., Why gold nanoparticles are more precious than pretty gold: Noble metal surface plasmon resonance and its enhancement of the radiative and nonradiative properties of nanocrystals of different shapes. *Chemical Society Reviews* **2006,** *35* (3), 209-217.

[3] Huang, X.; El-Sayed, I. H.; Qian, W.; El-Sayed, M. A., Cancer cell imaging and photothermal therapy in the near-infrared region by using gold nanorods. *Journal of the American Chemical Society* **2006,** *128* (6), 2115-2120.

[4] Betzer, O.; Meir, R.; Dreifuss, T.; Shamalov, K.; Motiei, M.; Shwartz, A.; Baranes, K.; Cohen, C. J.; Shraga-Heled, N.; Ofir, R.; Yadid, G.; Popovtzer, R., In-vitro Optimization of Nanoparticle-Cell Labeling Protocols for In-vivo Cell Tracking Applications. **2015,** *5*, 15400.

[5] Ye, S.; Marston, G.; McLaughlan, J. R.; Sigle, D. O.; Ingram, N.; Freear, S.; Baumberg, J. J.; Bushby, R. J.; Markham, A. F.; Critchley, K.; Coletta, P. L.; Evans, S. D., Engineering Gold Nanotubes with Controlled Length and Near-Infrared Absorption for Theranostic Applications. *Advanced Functional Materials* **2015,** *25* (14), 2117-2127.

[6] Fang, Y.; Sun, M., Nanoplasmonic waveguides: towards applications in integrated nanophotonic circuits. *Light: Science &Amp; Applications* **2015,** *4*, e294.

[7] Pérez-Juste, J.; Rodríguez-González, B.; Mulvaney, P.; Liz-Marzán, L. M., Optical Control and Patterning of Gold-Nanorod–Poly(vinyl alcohol) Nanocomposite Films. *Advanced Functional Materials* **2005,** *15* (7), 1065-1071.

[8] Huang, X.; Jain, P. K.; El-Sayed, I. H.; El-Sayed, M. A., Plasmonic photothermal therapy (PPTT) using gold nanoparticles. *Lasers in Medical Science* **2007,** *23* (3), 217.

[9] Sharma, V.; Park, K.; Srinivasarao, M., Colloidal dispersion of gold nanorods: Historical background, optical properties, seed-mediated synthesis, shape separation and self-assembly. *Materials Science and Engineering: R: Reports* **2009,** *65* (1), 1-38.

[10] Fan, X.; Zheng, W.; Singh, D. J., Light scattering and surface plasmons on small spherical particles. *Light: Science &Amp; Applications* **2014,** *3*, e179.

[11] Bohren, C. F.; Huffman, D. R., Absorption and Scattering by an Arbitrary Particle. In *Absorption and Scattering of Light by Small Particles*, Wiley-VCH Verlag GmbH: 2007; pp 57-81.

[12] Link, S.; Mohamed, M.; El-Sayed, M., Simulation of the optical absorption spectra of gold nanorods as a function of their aspect ratio and the effect of the medium dielectric constant. *The Journal of Physical Chemistry B* **1999,** *103* (16), 3073-3077.

[13] Eustis, S.; El-Sayed, M. A., Determination of the aspect ratio statistical distribution of gold nanorods in solution from a theoretical fit of the observed inhomogeneously broadened longitudinal plasmon resonance absorption spectrum. *Journal of Applied Physics* **2006,** *100* (4), 044324.

[14] Wang, H.; Brandl, D. W.; Le, F.; Nordlander, P.; Halas, N. J., Nanorice: A Hybrid Plasmonic Nanostructure. *Nano Letters* **2006,** *6* (4), 827-832.

[15] Liang, H.; Zhao, H.; Rossouw, D.; Wang, W.; Xu, H.; Botton, G. A.; Ma, D., Silver Nanorice Structures: Oriented Attachment-Dominated Growth, High Environmental Sensitivity, and Real-Space Visualization of Multipolar Resonances. *Chemistry of Materials* **2012,** *24* (12), 2339-2346.

[16] Bukasov, R.; Shumaker-Parry, J. S., Highly Tunable Infrared Extinction Properties of Gold Nanocrescents. *Nano Letters* **2007,** *7* (5), 1113-1118.

[17] Brinson, B. E.; Lassiter, J. B.; Levin, C. S.; Bardhan, R.; Mirin, N.; Halas, N. J., Nanoshells Made Easy: Improving Au Layer Growth on Nanoparticle Surfaces. *Langmuir* **2008,** *24* (24), 14166-14171.

[18] Oldenburg, S. J.; Averitt, R. D.; Westcott, S. L.; Halas, N. J., Nanoengineering of optical resonances. *Chemical Physics Letters* **1998,** *288* (2–4), 243-247.

[19] Prodan, E.; Radloff, C.; Halas, N. J.; Nordlander, P., A Hybridization Model for the Plasmon Response of Complex Nanostructures. *Science* **2003,** *302* (5644), 419-422.

[20] Lal, S.; Clare, S. E.; Halas, N. J., Nanoshell-Enabled Photothermal Cancer Therapy: Impending Clinical Impact. *Accounts of Chemical Research* **2008,** *41* (12), 1842-1851.

[21] Lal, S.; Link, S.; Halas, N. J., Nano-optics from sensing to waveguiding. *Nature Photonics* **2007,** *1*, 641.

[22] Raschke, G.; Brogl, S.; Susha, A. S.; Rogach, A. L.; Klar, T. A.; Feldmann, J.; Fieres, B.; Petkov, N.; Bein, T.; Nichtl, A.; Kürzinger, K., Gold Nanoshells Improve Single Nanoparticle Molecular Sensors. *Nano Letters* **2004,** *4* (10), 1853-1857.

[23] Stewart, M. E.; Anderton, C. R.; Thompson, L. B.; Maria, J.; Gray, S. K.; Rogers, J. A.; Nuzzo, R. G., Nanostructured Plasmonic Sensors. *Chemical Reviews* **2008,** *108* (2), 494-521.

[24] Duff, D. G.; Baiker, A.; Edwards, P. P., A new hydrosol of gold clusters. 1. Formation and particle size variation. *Langmuir* **1993,** *9* (9), 2301-2309.

[25] Priyam, A.; Idris, N. M.; Zhang, Y., Gold nanoshell coated NaYF4 nanoparticles for simultaneously enhanced upconversion fluorescence and darkfield imaging. *Journal of Materials Chemistry* **2012,** *22* (3), 960-965.

[26] Brito-Silva, A. M.; Sobral-Filho, R. G.; Barbosa-Silva, R.; de Araújo, C. B.; Galembeck, A.; Brolo, A. G., Improved Synthesis of Gold and Silver Nanoshells. *Langmuir* **2013,** *29* (13), 4366-4372.

[27] Watanabe, S.; Hiratsuka, T.; Asahi, Y.; Tanaka, A.; Mae, K.; Miyahara, M. T., Flow Synthesis of Plasmonic Gold Nanoshells via a Microreactor. *Particle & Particle Systems Characterization* **2015,** *32* (2), 234-242.

[28] Leff, D. V.; Brandt, L.; Heath, J. R., Synthesis and characterization of hydrophobic, organically-soluble gold nanocrystals functionalized with primary amines. *Langmuir* **1996,** *12* (20), 4723-4730.

[29] Csapó, E.; Sebők, D.; Makrai Babić, J.; Šupljika, F.; Bohus, G.; Dékány, I.; Kallay, N.; Preočanin, T., Surface and Structural Properties of Gold Nanoparticles and Their Biofunctionalized Derivatives in Aqueous Electrolytes Solution. *Journal of Dispersion Science and Technology* **2014,** *35* (6), 815-825.

[30] Verwey, E. J. W.; de Boer, J. H., Surface oxide films. *Recueil des Travaux Chimiques des Pays-Bas* **1936,** *55* (8), 675-687.

[31] Pfeiffer, C.; Rehbock, C.; Hühn, D.; Carrillo-Carrion, C.; de Aberasturi, D. J.; Merk, V.; Barcikowski, S.; Parak, W. J., Interaction of colloidal nanoparticles with their local environment: the (ionic) nanoenvironment around nanoparticles is different from bulk and determines the physico-chemical properties of the nanoparticles. *Journal of The Royal Society Interface* **2014,** *11* (96).

[32] Link, S.; Mohamed, M. B.; El-Sayed, M. A., Simulation of the Optical Absorption Spectra of Gold Nanorods as a Function of Their Aspect Ratio and the Effect of the Medium Dielectric Constant. *The Journal of Physical Chemistry B* **1999,** *103* (16), 3073-3077.

[33] Encina, E. R.; Coronado, E. A., Resonance Conditions for Multipole Plasmon Excitations in Noble Metal Nanorods. *The Journal of Physical Chemistry C* **2007,** *111* (45), 16796-16801.

[34] Slaughter, L. S.; Chang, W.-S.; Swanglap, P.; Tcherniak, A.; Khanal, B. P.; Zubarev, E. R.; Link, S., Single-Particle Spectroscopy of Gold Nanorods beyond the Quasi-Static Limit: Varying the Width at Constant Aspect Ratio. *The Journal of Physical Chemistry C* **2010,** *114* (11), 4934-4938.

[35] Reid, M. S.; Villalobos, M.; Cranston, E. D., Benchmarking Cellulose Nanocrystals: From the Laboratory to Industrial Production. *Langmuir* **2017,** *33* (7), 1583-1598.

[36] Wei, H.; Reyes-Coronado, A.; Nordlander, P.; Aizpurua, J.; Xu, H., Multipolar Plasmon Resonances in Individual Ag Nanorice. *ACS Nano* **2010,** *4* (5), 2649-2654.

CHAPTER 3: CORRELATED SINGLE-PARTICLE SPECTROSCOPY OF GOLD-NANOSHELL BEARING BACTERIAL CELLULOSE NANOCRYSTALS

3.1 Summary

In this chapter, size dependent surface plasmon resonance behavior of AuNS-BCNCs was evaluated by correlated single-particle spectroscopy. Single-particle spectra were collected using a dark-field hyperspectral microscope coupled with a short wave near-infrared (SWIR) spectrometer and detector (CytoViva). The use of a patterned ITO coated glass microscope slide as a substrate made it possible to collect the scattering spectra and high-resolution SEM images from the same particles. A total of 52 individual particles were investigated, and correlations between data sets (particle morphology and dipolar λ_{max} LSPR position) were derived by application of several analytical methods. Analyses revealed that the plasmonic behavior of AuNS-BCNCs is well described by Encina's and Coronado's model, which was derived for large gold nanorods. The use of "plasmon length" analysis revealed a strong linear relationship between the AuNS-BCNC length and λ_{max} LSPR, which can be used to guide the synthesis of AuNS-BCNCs with plasmon resonances in desired spectral windows. The surrounding environment sensing capabilities of the AuNS-BCNCs were evaluated through correlated refractive-index sensitivity measurements; the sensitivity of AuNS-BCNCs was found to be comparable to other gold nanoparticles of similar size (305-566 nm/RIU). A calculated figure of merit revealed that improvement in sensing performance can be realized by modifying the synthesis process to yield AuNS-BCNCs with smoother surfaces, which would increase sensitivity by reducing the LSPR band width.

3.2 Introduction

It is well known that the plasmonic properties of noble metal nanoparticles are highly sensitive to size, shape, and environment. Over the years, researchers have developed a multitude of synthesis techniques[1] that yield particles of a specific shape with improved size uniformity, and localized surface plasmon resonance (LSPR) bands that can be tuned from visible to near infrared (NIR) wavelengths. However, synthesis techniques often produce particles through nucleation and growth in solutions, which tend to produce some degree of variation in size and shape. The resulting particle size/shape dispersion leads to the observed inhomogeneous plasmon band broadening of ensemble-averaged spectra. Since most applications for plasmonic nanoparticles require precise tuning of plasmon bands into specific spectral bands, developing a robust understanding of how size and shape effect the plasmonic response is paramount. Correlated single-particle spectroscopy techniques allow for the measurement of wavelength-dependent phenomena (absorption, scattering, and electric field enhancement) of individual particles, and can be accompanied by detailed morphological information obtained through electron microscopy (TEM and SEM). Consequently, such measurements remove any inhomogeneous broadening and help unravel the effects of particle geometry on LSPR.

A commonly-used single-particle spectroscopy technique is dark-field microscopy, which measures the scattered light emanating from nanoparticles. Single particle light scattering was first observed by Zsigmondy, who received the 1925 Nobel Prize in Chemistry for his studies of colloids.[2] This technique has since become a popular tool for plasmonics research due to its simplicity and minimal equipment requirements, consisting of only a dark-field microscope coupled to a spectrophotometer. Integrated systems have

recently become widely available, and researchers are taking advantage of these benefits to analyze a large variety of nanoparticles with different geometries.[3-18] Other techniques, such as photothermal imaging,[19-20] spatial modulation spectroscopy,[21-22] electron energy loss spectroscopy,[23] typically require highly specialized, and often custom-built setups and, consequently, are encountered less frequently in literature.

Mie's solutions[24] to Maxwell's equations have been found to precisely describe the interaction of light with small metallic particles and are commonly used to predict the plasmonic behavior of spherical particles. A few years later, Gans extended Mie's solutions to particles of elongated geometries (ellipsoids).[25] More recently, these solutions have been shown to correctly predict the plasmonic behavior of metallic nanorods with diameters below 30 nm.[26-27] Unfortunately, many nanoparticles have at least one dimension that is larger than the wavelength of light, causing the quasi-static approximations of Mie-Gans theory to be non-applicable due to retardation effects. To overcome this limitation, numerical methods (DDA,[28] BEM,[17] FDTD,[29] T-Matrix[30-31]) have been used to simulate light-matter interactions and predict plasmonic behavior of particles with arbitrary geometry and size. The most widely used of these numerical methods is the discrete dipole approximation (DDA). DDA is capable of simulating light-matter interactions by breaking arbitrary particle geometries into a point cloud of discrete dipoles. Computing power is then used to solve Maxwell's equations for each individual dipole sequentially as the light wave propagates through the material. Such simulations have resulted in surprisingly accurate predictions of plasmonic behavior and have been used to develop semi-empirical models based on their results.[18, 28, 32] An example of a useful application of such simulations was reported by Encina and Coronado, who used DDA simulations to develop a semi-

empirical model to predict multipolar plasmon resonance of large gold nanorods (diameters ≤ 40 nm).[28] The developed model has proved critical for developing an understanding of size effects for particles beyond the quasi-static approximation limit and has paved the way for new applications such as, nanoantennae,[33] which can be used to harvest light. Since then, there have been a multitude of studies that have implemented correlated dark field single-particle spectroscopy and confirmed the validity of their model while advancing the field of single-particle spectroscopy.[18, 34-35]

3.3 Experimental Procedures

3.3.1 Bioorganic Template

Bacterial cellulose nanocrystals were chosen as organic templates for single particle optical analyses because of their broader particle length distribution (compared to wood derived CNCs), that allowed for a more robust analysis of structure-property relationships.

3.3.2 Gold Coating of Bacterial Cellulose Nanocrystals

Bacterial cellulose nanocrystals obtained from the Catchmark group (Pennsylvania State University, State College, PA) were surface functionalized and then coated with a thin layer of gold using electroless deposition.[36-38] Briefly, the as-received sulfuric acid hydrolyzed BCNCs were desulfonated using mild acid hydrolysis. Afterwards, their surfaces were functionalized through periodate oxidation, followed by reductive amination, leaving the surfaces of BCNCs rich in cationic primary amines. The surface primary amines served as anchor sites for small (1-3 nm) gold nuclei. The gold nuclei seeded BCNCs were then subjected to an electroless gold deposition process, which

resulted in a thin continuous layer of gold on the particles' surface. These gold nanoshell-bearing BCNCs (AuNS-BCNCs) were used for corelated single-particle spectroscopy.

3.3.3 Fabrication of Patterned Substrates for Optical Measurements

To perform correlated single-particle spectroscopy, individual particles had to be easily located and positively identified in both optical and scanning electron microscopy. This stipulation imposed several requirements on the substrate of choice: 1) the substrate had to contain easily identifiable features that could be used to navigate and locate individual particles in optical and electron microscopes, 2) the substrate had to be optically transparent to allow for transmission mode illumination and collection of scattering spectra from individual particles, 3) the substrate had to be electrically conductive to avoid charge build up during electron microscopy, and finally, 4) the refractive index of the substrate had to be low enough as not to shift the dipolar LSPR bands of interest out of the measurable range (400-1700 nm).

Indium tin oxide (ITO) coated microscope slides (Delta Technologies, Stillwater, MN) were chosen as the ideal substrate for these measurements for their high optical transparency, low surface resistance ($R_s \leq 100\ \Omega$), and a low effective refractive index (η_{eff} =1.25).[34] To easily identify regions of interest (ROI) on the substrate, the ITO coated microscope slides were patterned by sputtering a thin layer of platinum through an alpha numeric shadow mask, as shown in **Figure 26**.

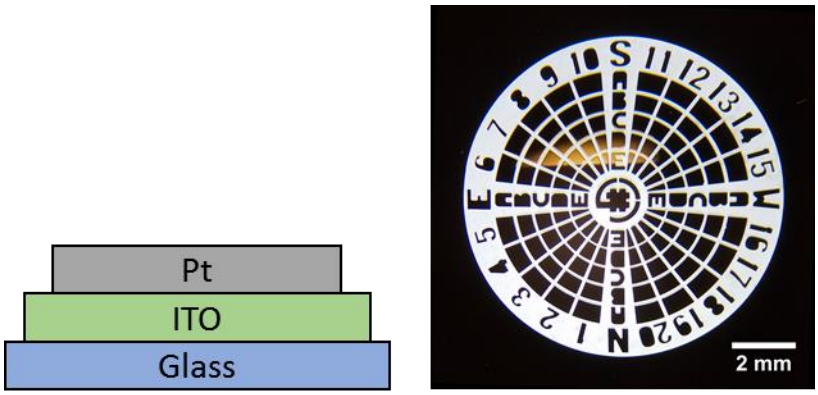

Figure 26. Left, schematic showing the stack up of coatings on the glass slide. Right, optical image of the patterned region of the substrate. (note: dark regions are Pt, light regions are ITO coated glass)

Prior to sputtering, the microscope slides were thoroughly cleaned by first sonicating (Branson 2510 ultrasonic bath, Branson Ultrasonic Corp., St. Louis, MO) in a 2 vol.% cleaning solution (micro-90, Burlington, NJ) for 10 minutes followed by rinsing with DI water and sonicating an additional 10 minutes in clean DI water. After drying with compressed air, the microscope slides were further treated by a 10-minute plasma cleaning cycle (Harrick Plasma, Ithica, NY) to remove any residual traces of surface contaminants. Alpha numeric copper SEM grids (80101-CU, Electron Microscopy Sciences, Hatfield, PA) were used as shadow masks and placed directly onto the ITO side of the cleaned microscope slides. A thin film (≤ 100 nm) of platinum was deposited onto the microscope slides with the help of Nicholas Kane (Liu Group, Georgia Institute of Technology, Atlanta, GA) using a brief (10 minute) DC sputtering cycle (AJA International, Scituate, MA).

To prevent gross agglomeration of gold AuNS-BCNCs on the substrate and to promote particle adhesion the patterned microscope slides were functionalized with a thin

layer of polyvinylpyrrolidone (PVP, Avg. $M_{w.}$ 55,000, Sigma Aldrich Saint Louis, MO). Plasma cleaned patterned microscope slides were immersed in an ethanolic solution of PVP (1 wt.%) for 24 hours. The patterned slides were then rinsed with ethanol and dried with compressed air.

Gold nanoshell-bearing BCNCs were deposited onto the patterned substrate by dropping 5 μL of an aqueous AuNS-BCNC suspension onto the patterned regions of the ITO coated microscope slide. The microscope slide was covered with a polystyrene Petri dish to reduce the evaporation rate and after an allotted time the drop was removed from the microscope slide by rinsing with DI water. The substrate was then gently dried with compressed air and placed into a dust free container for storage. It was found that the best particle density was obtained by allowing the aqueous suspension of AuNS-BCNCs to remain on the PVP functionalized substrate for 5 minutes. Shorter times (<5 minutes) resulted in very few particles while longer times (>10 minutes) resulted in a very high density of particles, which would make collecting scattering spectra from single particles difficult.

3.3.4 Single Particle Optical Scattering Measurements

Scattering spectra of individual AuNS-BCNCs on ITO coated microscope slides were measured with a dark field optical microscope (EX51, Olympus, Shinjuku, Tokyo, Japan) equipped with a motorized microscope stage (Prior Scientific, Rockland, MA). The microscope could be coupled to two spectrophotometer integrated CCDs (VINIR, SWIR, CytoViva, Auburn, AL). The general microscope setup is shown in **Figure 27**.

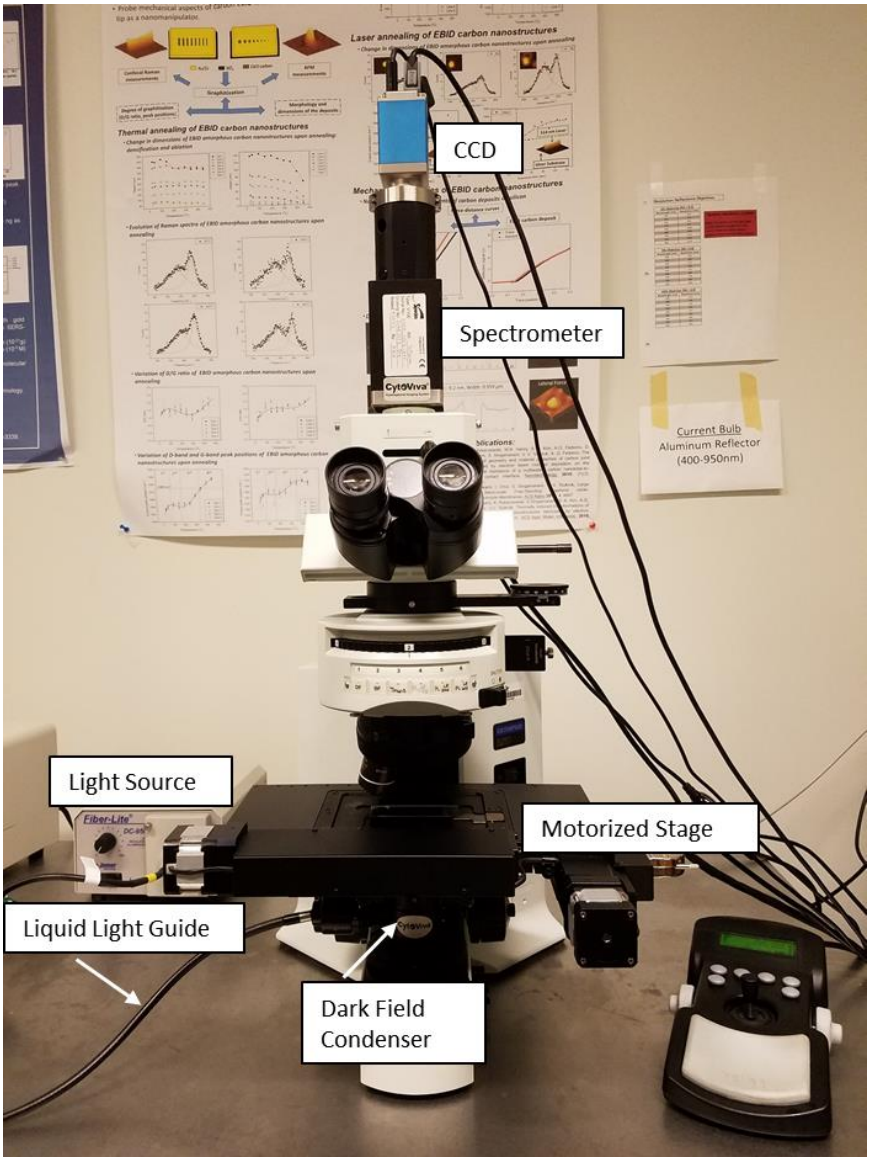

Figure 27. Dark Field optical microscope equipped with a CytoViva dark field condenser and coupled to a spectrophotometer/CCD.

In this technique, white light from a halogen lamp was directed through a high numerical aperture (NA=1.4) enhanced dark-field condenser (CytoViva) to illuminate the sample. The dark-field condenser is fitted with a light stop so that a hollow cone of light illuminates the sample substrate, as shown in **Figure 28**. The scattered light from individual particles was then collected by an oil immersion objective equipped with an iris (adjustable NA),

which is set to an NA just below that of the dark field condenser. Because the definition of numerical aperture is NA=n·sinθ, where n is the refractive index and θ is the half-angle of the cone of light, the difference in NA between condenser and objective means that the angle of the illumination light was higher than what the objective lens could collect insuring that only the light scattered by the nanoparticles was collected.

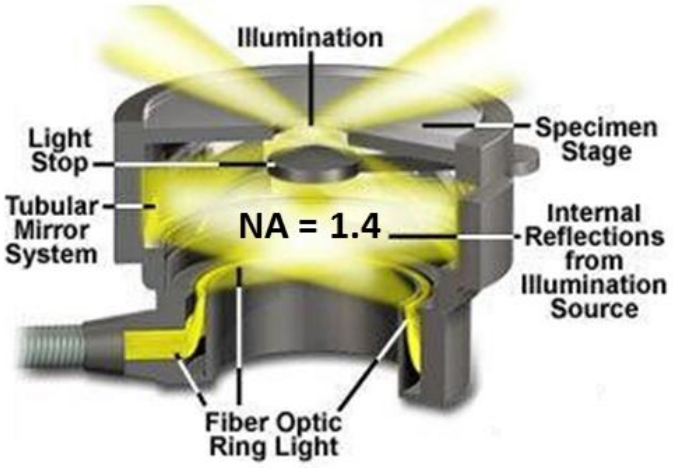

Figure 28. Cross-section of a darkfield condenser showing the formation of a hollow cone of light.

Short wave near-infrared spectra (SWIR) were collected using a transmission grating spectrophotometer (spectral range 900–1700 nm, 5 nm spectral resolution w/30 μm slit) coupled with an InGaAs CCD (resolution 320 X 256 pixels) (Xenics Infrared Solutions, Leuven, Belgium). Dark-field illumination was achieved by directing unpolarized white light from a 150-watt tungsten/halogen bulb equipped with an aluminium reflector (International Light Technologies, Peabody, MA) via a liquid light guide (Fiber-Lite DC-950, Dolan-Jenner, Boxborough, MA) to the enhanced dark-field condenser (CytoViva, Auburn AL). Scattered light from nanoparticles was collected by a 60X immersion objective with the iris set for NA just below 1.4. Immersion oil (Cargile

Laboratories, Cedar Grove, NJ) with a refractive index of 1.515, was used as an index matching liquid between the dark-field condenser, the sample substrate and immersion objective. A thin 0.17 mm thick glass coverslip was used between the sample and immersion objective to protect the sample from accidental contact. Immersion oil was also placed onto the sample itself to produce an environment having a constant refractive index in the spectral measurement range, which maximized the signal-to-noise ratio.

Hyperspectral images were captured using ENVI 4.8 software. Images were collected by line scanning the field of view. A dark image was collected before the start of each scan by diverting illumination light into the eyepiece of the microscope. Images were then collected by scanning one-pixel line at a time and each pixel was recorded as a part of a 3-dimensional data matrix (cube). The image/matrix dimensions (x, y) are set by the resolution of the CCD (SWIR = 320 X 256) and the data cube depth (z) is set by the number of spectral bands (SWIR = 184). Before spectral analysis, each data cube was pre-processed by correcting for the wavelength-dependence of the lamp intensity and background signal. The lamp spectral profile was collected by focusing on an area of the sample without any particles, then the objective iris was opened to allow illumination light to flood the field of view. A partial image of 50 lines was collected with a short exposure time (.05s) to insure the detector was not saturated. The average lamp spectral profile was extracted using the built-in ENVI ROI function and saved for further processing. Background signal was extracted directly from sample images by selecting particle free regions with the built-in ROI tool and averaging the selected spectra. These two spectral profiles (lamp and background) were then used to correct the entire data cube using ENVI spectral math function**.** First, the background signal was subtracted from each spectrum in the data cube

and the resulting data cube was then divided by the normalized lamp profile. An illustration of the spectral processing method is shown in **Figure 29**. Fifty-three individual particle spectra were then extracted from the corrected data cube by averaging the spectra contained in the pixels associated with a single particle using ENVI's ROI tool, as demonstrated in **Figure 30**. Once the spectra were extracted, they were fitted with a Lorentzian line shape using Origin (OrginLab, Northampton, MA, USA) data analysis and graphing software. Each spectrum was fitted using the built in Lorentzian peak fit algorithm. Fitting iterations were continued until a Chi-squared tolerance of $1x10^{-9}$ was reached.

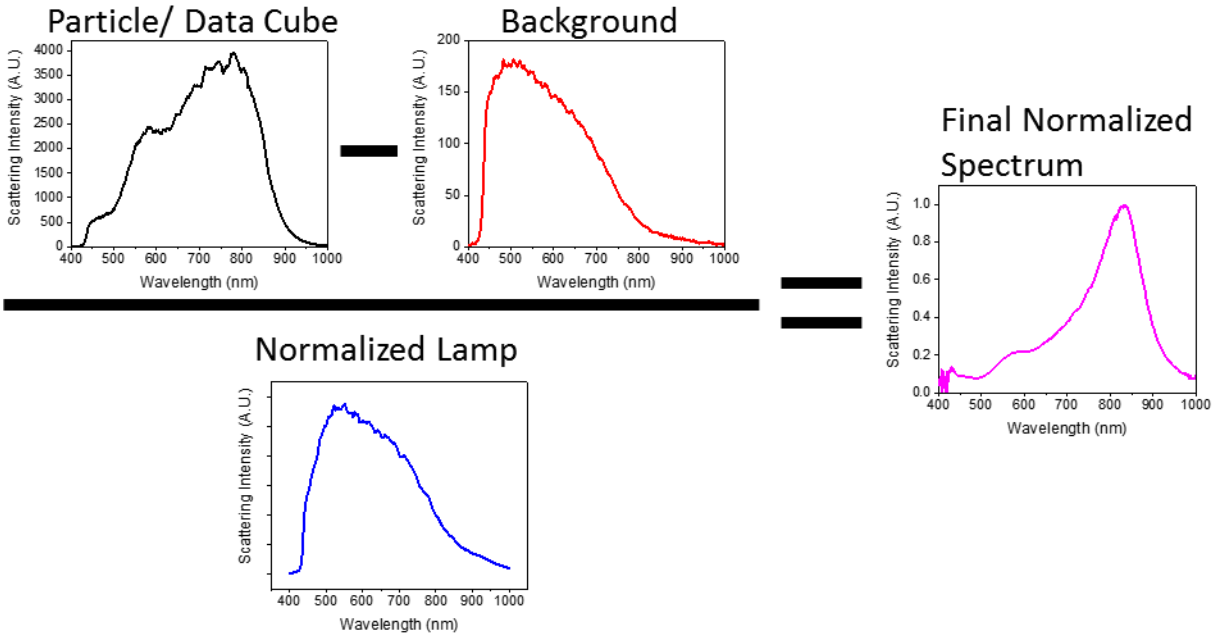

Figure 29. Spectral processing preformed on hyperspectral image data cubes. Note: detector dark current is accounted for at the start of image collection.

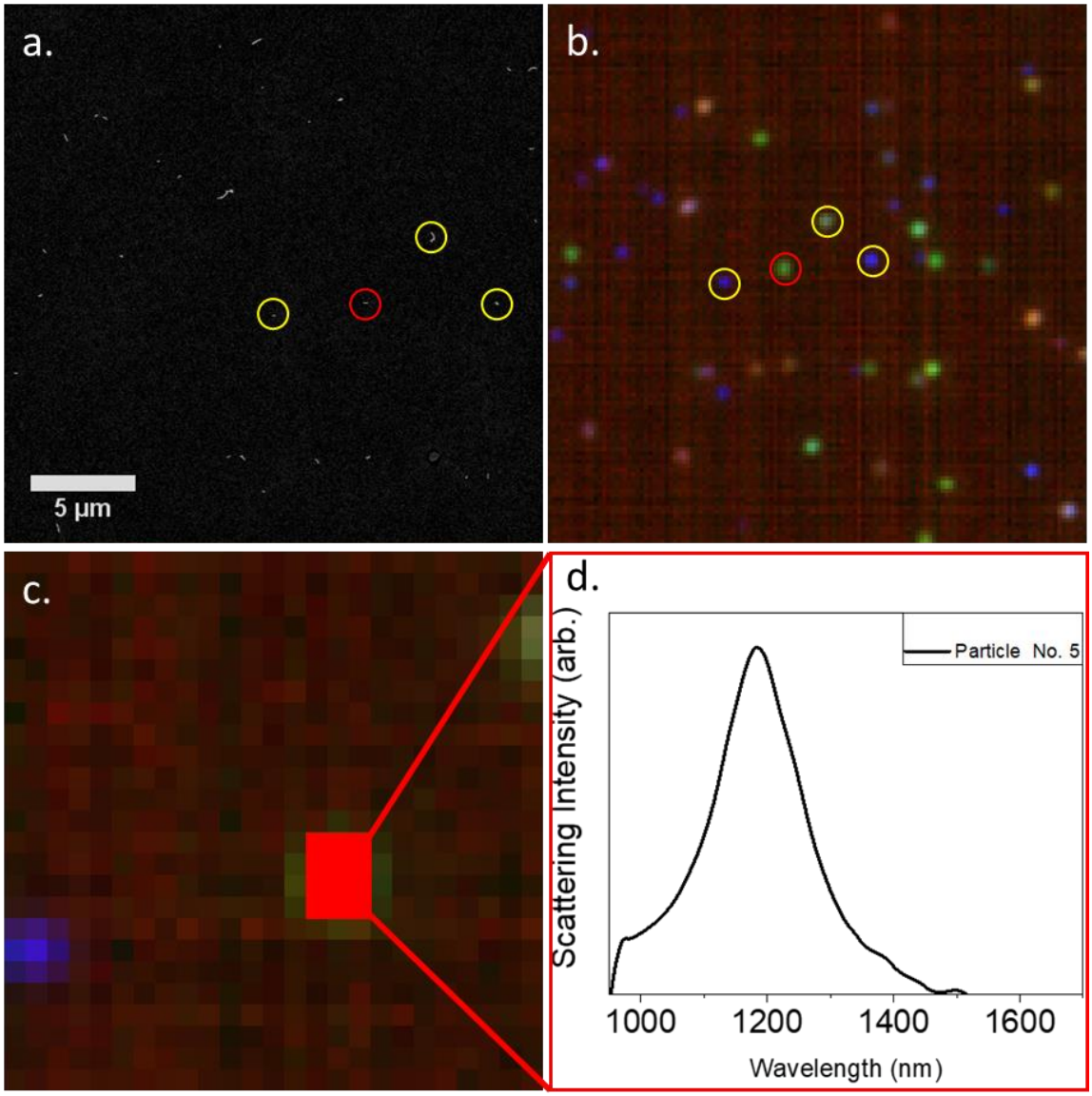

Figure 30. Representative process for extracting spectral data from hyperspectral images using ENVI 4.8 software. (a) SEM image of the region of interest. (b) Hyperspectral image of the same region of interest as in (a). Circles highlight individual particles in both images. (c) Selected pixels corresponding to a single particle. (d) Averaged scattering spectrum of highlighted particle in (c).

3.3.5 Correlated Particle Morphology Analysis

Scanning electron microscopy (Ultra 60 FE-SEM, Carl Ziess, Oberkochen, Germany) was conducted promptly after hyperspectral data collection. The platinum

patterned microscope slides were rinsed with hexanes (Sigma Aldrich, St. Louis, MO) to remove any traces of immersion oil as to prevent contamination of the SEM high vacuum environment. It was found that rinsing with hexanes effectively removed the immersion oil without disturbing the nanoparticles. Optical dark field images of ROIs served as maps for locating the same regions in the SEM as imaged with optical dark-field microscopy so that individual particles could be matched with their spectral profiles, as shown in **Figure 30**. High magnification (100 kX) secondary electron images of individual particles were collected at an acceleration voltage of 5 kV with a typical working distance of 3-4 mm. The contrast settings were adjusted to provide images with a dark background and bright foreground ideal for automated image analysis. A representative SEM image is shown in **Figure 31a.**

Secondary electron images were analyzed using ImageJ (FIJI)[39]. Images were first cropped to isolate a single particle. The cropped images were then binarized using ImageJ's default thresholding algorithm (**Figure 31b**). Any holes resulting from contrast differences in the interior of the particle perimeter were filled in using the *fill holes* function. Missing pixels around the perimeter of the particle were filled in using the *close* function. Dimensions and morphological descriptors were collected using ImageJ's built-in particle analysis functions. Specifically, each particle was analyzed using the *Feret's diameter* function, which sweeps a bounding rectangle around the perimeter of the particle returning the minimum and maximum distance between two parallel sides (analogous to caliper diameter), as shown in **Figure 31**. Each particle was also fitted with an ellipse having the same area as the particle. The lengths of the major and minor axes of this best fit ellipse were recorded along with other parameters such as particle perimeter and area.

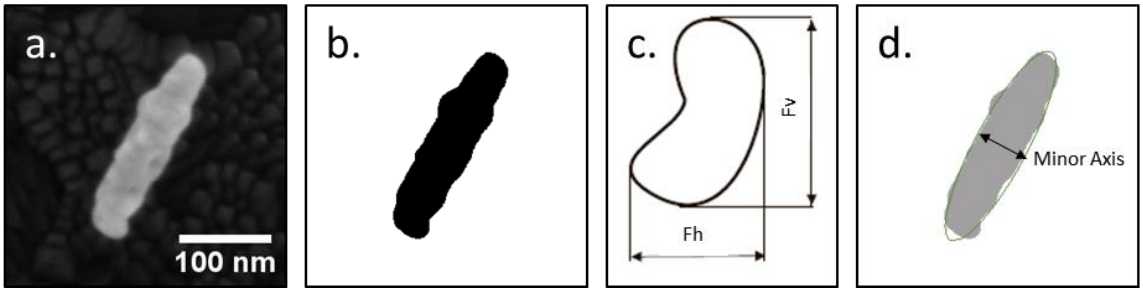

Figure 31. Image processing/analysis of individual particles. (a) SEM image of an individual AuNS-BCNC. (b) Binarized image of (a). (c) Schematic demonstrating the concept of Feret's diameter. (d) Ellipse fit of (b) highlighting the minor axis.

3.3.6 Correlated Refractive Index Sensitivity Measurements

Correlated RIS measurements were performed using the same procedure as describe above, but the immersion oil surrounding the AuNS-BCNCs was replaced with varying concentrations of aqueous glycerol solutions. This allowed for the controlled variation of the refractive index surrounding the AuNS-BCNCs. The refractive index of pure 100% glycerol is 1.47399 (at 20°C)[40] and is sensitive to dilution with water. A series of glycerol solutions (**Table 2**) along with immersion oil (RI = 1.51, value reported by Cargille labs)

were used to study the sensitivity of dipolar LSPR peaks to environmental refractive index changes. A drop of glycerol solution was placed onto the sample and was covered with a 0.17 mm coverslip. A drop of immersion oil was placed on top of the coverslip to couple scattered light to the immersion objectives. The coverslip was carefully removed after each measurement and the substrate was rinsed with DI water and dried before application of the next glycerol solution. The measurement in immersion oil was performed last as to not contaminate the substrate with a non-polar substance.

Table 2. Refractive index of glycerol-water solutions at 20°C, from Hoyt.[40]

Glycerol by Wt. %	Refractive Index $n^{20°C}$
14	1.3498
30	1.3707
51	1.3996
65	1.4204
85	1.4509

3.4 Results and Discussion

The implementation of correlated single-particle spectroscopy is quickly becoming an indispensable tool for plasmonics research. The ensemble-averaged optical response of nanoparticle suspensions is convoluted by the effects of particle size and shape heterogeneity. Much effort has gone into the development of synthesis and purification techniques that improve particle size and shape purity. However, developing a deep understanding of structural, chemical, and environmental effects using bulk measurements remains a difficult task. Unlike bulk suspension measurements, correlated single-particle spectroscopy can decouple many of these variables by allowing the collection of detailed spectral and structural information from individual particles.

In **Chapter 2**, it was shown that gold nanoshell bearing CNCs have size dependent optical properties, i.e., their optical extinction was dominated by a dipolar LSPR band whose peak position was shown to be dependent on the particle size. Similarly, suspensions of AuNS-BCNCs exhibited a broad extinction band in the NIR range **(Figure 32**) that could be split into narrower bands through particle size fractionation (**Figure 25**). However, the broadness of the LSPR bands and the heterogeneity of particle size in the fractionated

samples made it difficult to establish any robust relationships between AuNS-BCNC size and the dipolar LSPR wavelength, limiting the analysis to general trends only.

It is well documented that light interactions with plasmonic metal nanoparticles having diameters below 30 nm are well modeled by the quasi-static (i.e., dipole) approximation of Mie-Gans scattering theory, which assumes a constant electromagnetic phase around the particle.[25] It has been shown that, for such particles, the longitudinal surface plasmon resonance wavelength is solely dependent on the aspect ratio and in fact simple linear relationships between the longitudinal surface plasmon resonance wavelength and aspect ratio have been reported for plasmonic (Au, Ag) nanorods.[26-27]

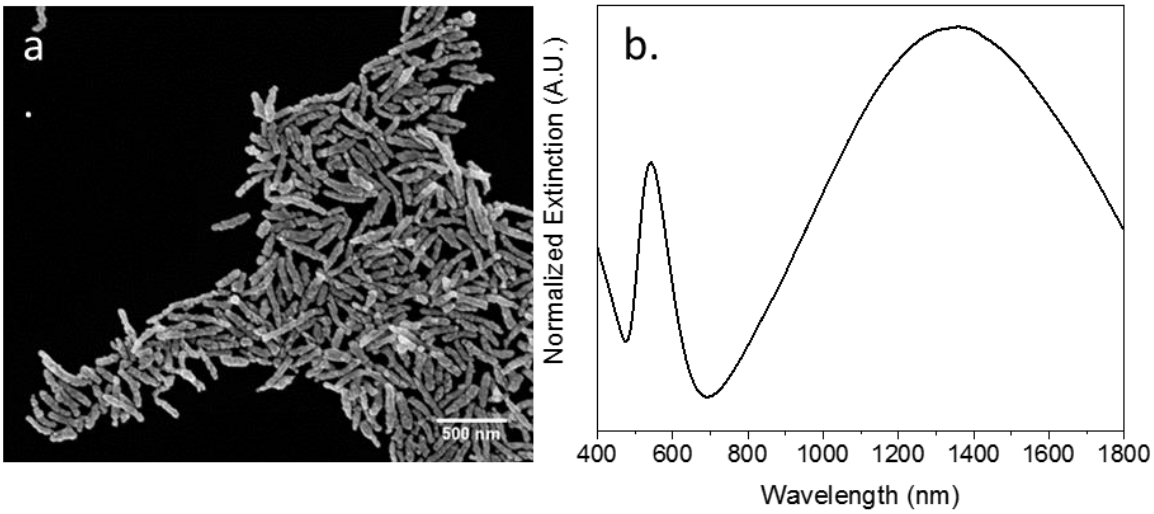

Figure 32. Secondary electron image of AuNS-BCNCs (a) and their bulk extinction spectrum (b).

3.4.1 Size Effects Dipolar LSPR Wavelength

To investigate the effect of gold AuNS-BCNC structure on the longitudinal surface plasmon resonance energy, the influence of AuNS-BCNC size was investigated first. Dark

field hyperspectral and scanning electron microscopy were performed on AuNS-BCNCs deposited onto patterned ITO coated microscope slides. Representative spectra along with corresponding SEM images of individual AuNS-BCNC on ITO are presented in **Figure 33.** A comparison of the bulk and individual particle scattering spectra elucidated that the major contribution to the broadness of the LSPR extinction band observed in the bulk suspension, which had a full-width half max (FWHM) of roughly 1544 nm, was the result of particle size dispersity. As can be seen in **Figure 33**, the spectra from individual particles had much smaller associated linewidths (ranging from 78 nm to 425 nm). However, it is evident that the average of several individual particle spectra would yield a spectrum with a much broader linewidth. It is precisely such ensemble-averaging of spectra that cause the observed inhomogeneous broadening in bulk suspension measurements, evidencing the need for single-particle spectroscopy.

To track size dependent changes in spectral attributes (i.e., the longitudinal surface plasmon resonance wavelength and linewidth), a Lorentzian line shape function was fit to the lowest energy (i.e. longest wavelength) dipolar peak of each particle's spectrum. The dipolar LSPR peak wavelength and FWHM values were obtained from the fitted Lorentzian line shapes. It was observed that the dipolar LSPR wavelengths showed a general red-shift with increasing particle size, which was consistent with the plasmonic behavior of aspected nanoparticles, as has been reported by others.[15-16, 18, 26-28]

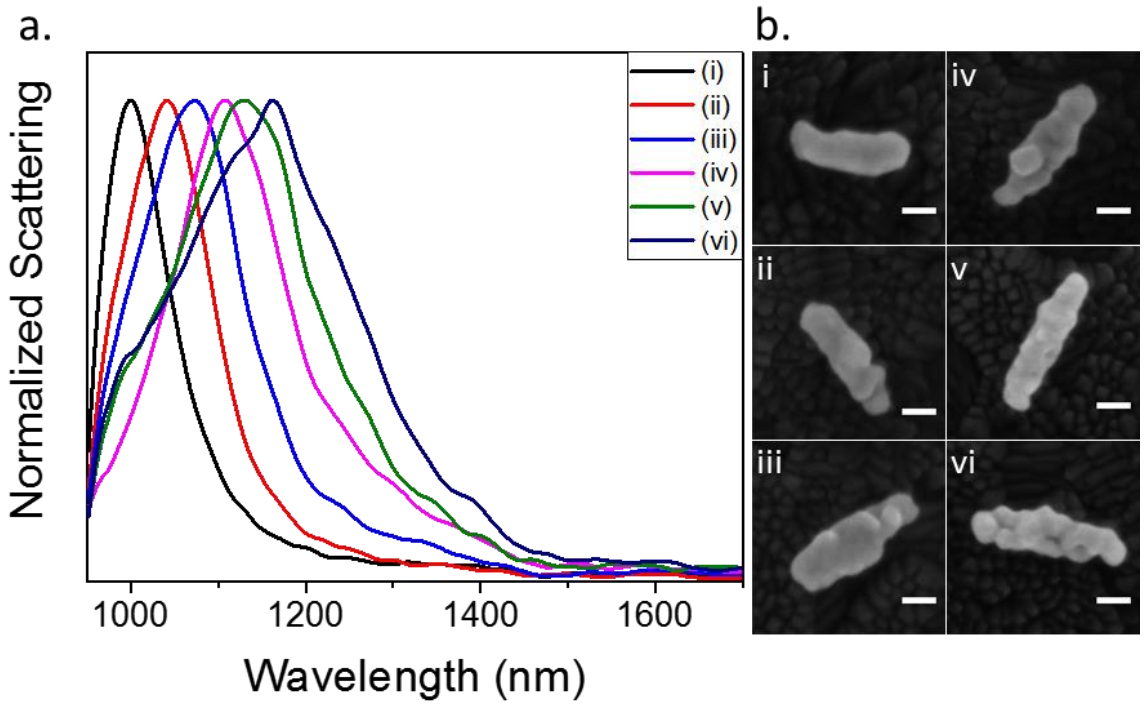

Figure 33. Representative individual particle LSPR spectra (a) and corresponding secondary electron images of AuNS-CNCs on ITO coated glass(b). Scale bars, 50 nm.

As an initial attempt to correlate the size of AuNS-BCNCs to their LSPR wavelength, an effective particle aspect ratio was determined from the principal axes of an ellipse fitted to the binarized SEM images of individual AuNS-BCNCs (**Figure 31d**). The resulting plot of AuNS-BCNC aspect ratio vs. LSPR wavelength (**Figure 34**) clearly shows a general red-shifting of the LSPR wavelength maximum with increasing aspect ratio.

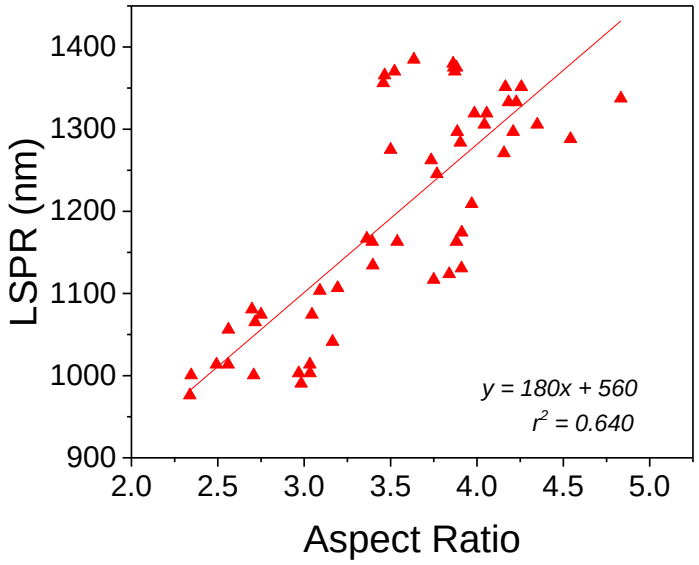

Figure 34. Plot of LSPR wavelength maximum versus AuNS-BCNC aspect ratio.

However, a linear regression of the data, resulted in a line that poorly described the data set (r^2 = 0.64). This result is not surprising, considering the average particle diameter of analyzed AuNS-BCNCs is much greater than 30 nm, which places these particles outside the range where phase retardation and radiative dampening effects can be ignored. Thus, aspect ratio alone is an insufficient descriptor of the size/LSPR wavelength relationship for AuNS-BCNCs. Since AuNS-BCNCs are outside of the static approximation solutions to Mie-Gans theory, a different analysis approach was attempted. One of the more successful models for describing the plasmonic behavior of large gold nanorods was developed by Encina and Coronado, who used discrete dipole approximation (DDA) electrodynamic simulations to develop a semi-empirical mathematical relationship between nanorod dimensions and multipolar LSPR wavelengths.[41] For the dipole mode (l=1), the LSPR λ_{max} is given by

$$\lambda_{max}(\mu m) = \frac{\left[\left(\frac{L^2}{l^2\pi^2}\left(A + \frac{B}{d^2}\right) + C\right)\epsilon_m + \alpha\right]^{\frac{1}{2}}}{\beta} \quad (5)$$

or

$$\lambda_{max}(\mu m) = \frac{\left[\left(\frac{R^2}{l^2\pi^2}(Ad^2 + B) + C\right)\epsilon_m + \alpha\right]^{\frac{1}{2}}}{\beta} \quad (6)$$

where the coefficients A, B, and C were derived from a series of DDA calculations attempting to characterize the non-linear relationships between size parameters (L = length, d = diameter, and R = L/d) and the resonance condition. The relationship was generalized to the above equation assuming that the dielectric function of the metal particles is given by the Drude-Sommerfeld model: $\epsilon_m = \alpha - \beta^2\lambda^2$, where $\alpha = 9.8$ and $\beta = 7.3\ \mu m^{-1}$ for gold. Therefore, to accurately predict the λ_{max} for a given particle using the above equation, one must have knowledge of the particle dimensions (L and d). The task for identifying a particle diameter for AuNS-BCNCs was complicated by their non-uniform surface morphology; thus, a method that yielded an effective diameter was used instead. The effective diameter (d) for AuNS-BCNCs was obtained by fitting an ellipse to the binarized particle image. The length of the minor ellipse axis was used as the effective particle diameter as it tended to yield a value that resembled the average particle diameter and was less sensitive to surface irregularities unlike the values obtained from the minimum Feret

length. Particle length was determined from the maximum Feret diameter, which measured the distance between the two furthest points of the binary particle image (**Figure 31c**). The max Feret diameter was used as the length of the particle in leu of the major axis of a fitted ellipse because it more accurately represented the true length of the particles. Since synthesis of AuNS-BCNCs yielded particles with variable diameters, two bounding curves were calculated using **Equation 6**. The curves shown in **Figure 35**, represent the predicted LSPR wavelengths ($\lambda_{max,\ dipole}$) for particles with average diameters equal to the maximum (88 nm) and minimum (56 nm) observed AuNS-BCNC diameters.

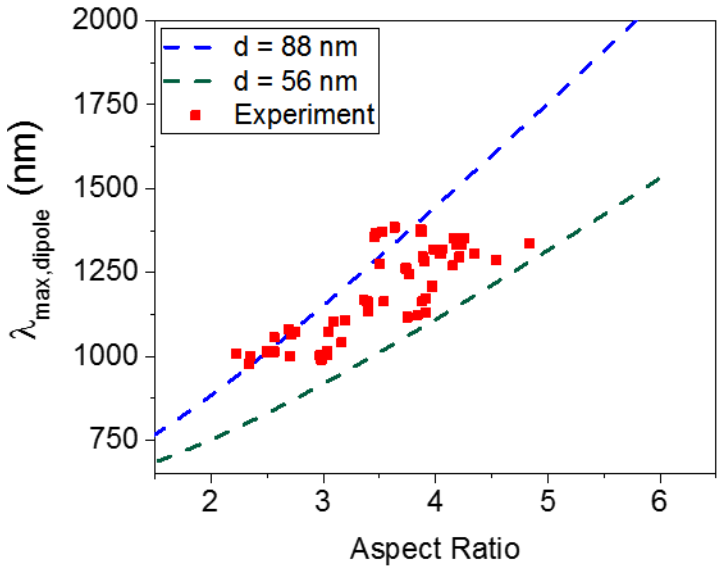

Figure 35. Comparison between experimentally measured $\lambda_{max,\ dipole}$ of AuNS-BCNCs having varying diameters (red squares) and values calculated using Equation 6 for the maximum (88 nm, blue dashed line) and minimum (56 nm, green dashed line) observed AuNS-BCNC diameters. A medium refractive index of 1.51 (Note $\epsilon_m = n^2$) was used for all calculations.

The average diameters were determined from the length of the minor axis of a fitted ellipse and not the minimum Feret diameter because the minor axis of the ellipse tends to average

over the particle surface irregularities, providing a better estimate of the average particle diameter. If **Equation 6** accurately predicts the dipolar plasmon resonance ($\lambda_{max,dipole}$) for AuNS-BCNCs, then the experimental values should fall within the bounds of the two curves. Indeed, without using any adjustable parameters most of the experimental data points fall in-between these upper and lower bounds, with only a few points falling outside of the predicted range. As a further test of the model's ability to predict the dipole LSPR wavelength; LSPR $\lambda_{max,\ dipole}$ values were calculated for individual particles with different aspect ratios and compared against the experimentally measured ones. Selected results of this comparison are presented in **Table 3**, for a complete list of values please see **Table 9** located in **Appendix D**.

Table 3. Comparison of experimentally measured and predicted LSPR $\lambda_{max,dipole}$ values for AuNS-BCNCs with varying diameters and aspect ratios.

Aspect Ratio	Length (nm)	Diam. (nm)	$\lambda_{max,exp}$	$\lambda_{max,\ Encina}$	% Diff.*
2.23	156	70	1008	849	-16%
2.34	159	68	976	861	-12%
3.52	310	88	1370	1303	-5%
3.54	230	65	1163	1095	-6%
4.54	277	61	1288	1277	-1%
4.83	290	60	1337	1330	-1%

$$* \%\ Diff. = \left(\frac{\lambda_{Encina} - \lambda_{Exp.}}{\lambda_{Exp.}}\right) * 100$$

Not only did the model accurately predict the observed red shift of the dipole peak as a function of diameter and aspect ratio, but it yielded values for dipole resonance wavelengths that were within a few percentage points (1-16 %) of the experimental values.

A student t-test comparison between the predicted and observed values of $\lambda_{max,\ dipole}$, resulted in a p-value of 0.021, indicating that the two data sets are statistically different but not to a large degree. The model did however tend to consistently underestimate the plasmon resonance wavelength, which could in part be due to an approximation of the medium refractive index. Since the AuNS-BCNCs are deposited onto the surface of ITO coated glass and surrounded by immersion oil, the effective refractive index may be some linear combination of the two materials. Nevertheless, the agreement between model and experiment for some particles suggested that the true refractive index was not far from that of the immersion oil (n = 1.51), which was used to calculate LSPR $\lambda_{max,\ dipole}$ values. It is worth mentioning that **Equation 6** was derived for solid gold particles with diameters less than 40 nm, but similarly to Slaughter, et al., it was found that **Equation 6** was applicable to particles with diameters greater than 40 nm.[18] However, it was noticed that the agreement between predicted and observed values improved for particles with larger aspect ratios. This observation may in part have been due to the highly irregular morphology of low aspect ratio AuNS-BCNCs, which made the idealized nanorod representation of these particles inadequate. AuNS-BCNCs with higher aspect ratios more closely resembled nanorods since their surface irregularities tended to be spread across longer distances, as revealed in **Figure 36**.

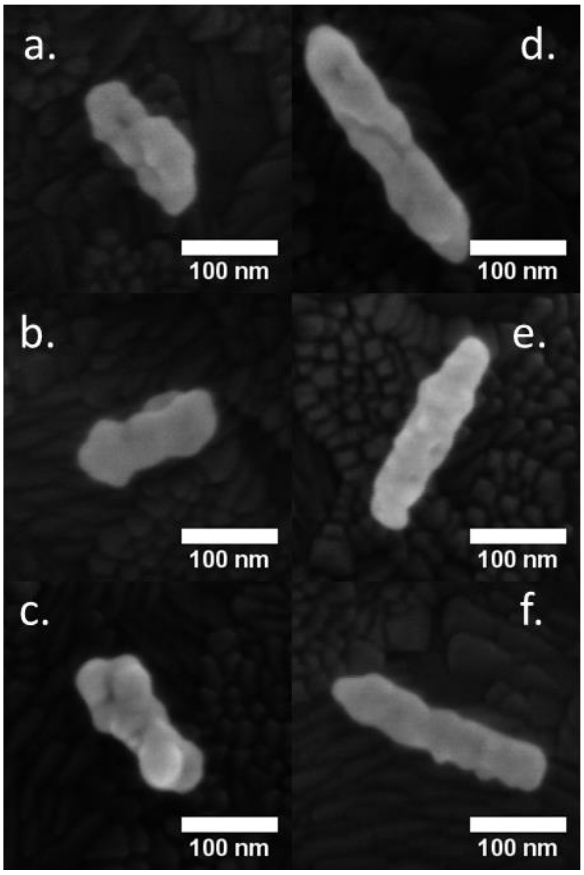

Figure 36. Representative SEM images of low aspect ratio (a-c) and higher aspect ratio (d-f) AuNS-BCNCs showing that surface irregularities tend to be less dramatic for longer AuNS-BCNCs.

Interestingly, even though AuNS-BCNCs have a core-shell structure similar to nanoshells[16, 37-38, 42-43], which have optical responses that are augmented by hybridization of inner and outer surface plasmons, such effects were not observed in this sample of AuNS-BCNCs. This observation can potentially be rationalized by considering plasmon hybridization strength as a function of the inner BCNC aspect ratio. Wang, et al. calculated the effect of the inner core aspect ratio on LSPR energy (**Figure 37**) and showed that plasmon mode hybridization decreases with increasing core aspect ratio.[42] The hybridized plasmon bonding mode becomes indistinguishable from that of a solid spheroidal particle when the aspect ratio of the inner core is large. Considering that the typical aspect ratio of

BCNCs is much higher (>20, see **Figure 38**) than that of AuNS-BCNCs, it is likely that the cellulose core would have a negligible effect on the plasmonic behavior. There is also a possibility that the gold coating thickness had surpassed a critical dimension ($39 < t \leq 236$ nm) at which point the effects of the inner surface plasmon resonance become insignificant, as has been observed by others.[16, 44] These considerations could explain why AuNS-BCNCs behaved like large gold nanorods and not nanoshells.

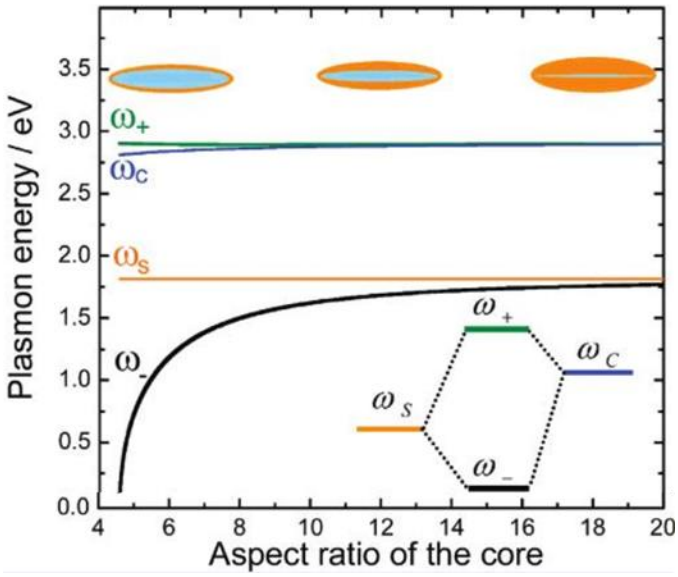

Figure 37. Simulation of the hybridized longitudinal surface plasmon resonance energy as a function of the dielectric core aspect ratio. Values were calculated for silver nanorice with a fixed particle aspect ratio of 4.575. Adapted from Wang, et al.[42]

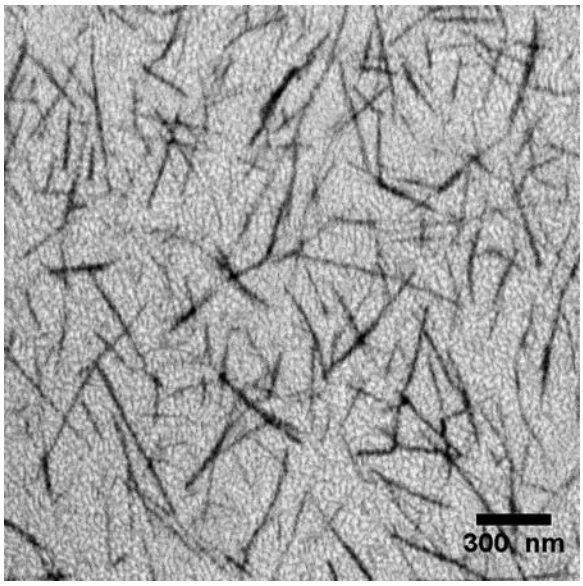

Figure 38. SEM image of aminated BCNCs showing their typical high (>20) aspect ratio morphology.

3.4.2 Plasmon Length Analysis

An additional method for analyzing the size dependent plasmon resonances of large elongated metal nanoparticles, is to consider them analogous to antennas.[16, 28, 41, 45] Hence, an understanding of their optical properties can be gained by considering oscillations of electrons as standing waves along the length (L) of the particle which has a resonance set by a simple geometric condition: $\lambda_{res} = n(2*L)$, where n denotes the number of nodes along the length of the particle. Indeed, evidence of just such standing waves have been predicted and observed in nanowires[2] and nanorice.[17] An example of all possible standing waves in silver nanorice is shown in **Figure 39**. These distinct resonance modes can be observed in single-particle spectroscopy experiments by changing the polarization of incident light. The change in light polarization allows for precise excitation of single plasmon modes, providing a method for deconvoluting the contribution of each mode to the composite spectrum obtained by using non-polarized light. [5, 17, 41]

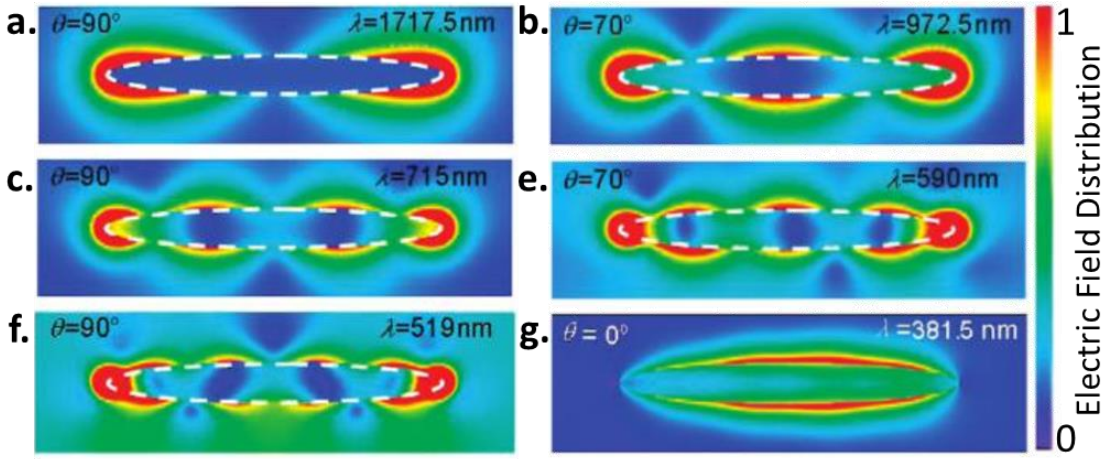

Figure 39. Local electric field distribution induced in Ag nanorice by excitation at different angles (θ) at the resonance wavelengths (λ). Panels (a–f) show multipolar longitudinal resonances (*l* = 1-5). Panel (g) shows the transverse resonance mode. Adapted from Wei, et al. [17]

Building on the idea of charge oscillation, Ringe, et al. proposed that a shape independent universal size parameter for dipolar plasmon resonance exists, and can potentially be described as the distance between two oppositely charged regions created by electron oscillation (i.e., plasmon length).[45] Ringe, et al. showed that the dipolar plasmon resonance energies of particles with arbitrary shapes, but with similar plasmon lengths, indeed had very similar LSPR spectra as can be seen in **Figure 40.** Ringe, et al. claimed that the small variations in dipolar resonance energy that remained after normalization by plasmon length were the result of particle geometry. This implied that the geometrical contributions to dipolar plasmon resonance are real but small when plasmon length is used a descriptor of nanoparticle size. However, their analysis was limited to particles with fixed aspect ratios

having well-formed vertices and minimal corner rounding, which is far from the highly irregular particle geometries found in AuNS-BCNCs.

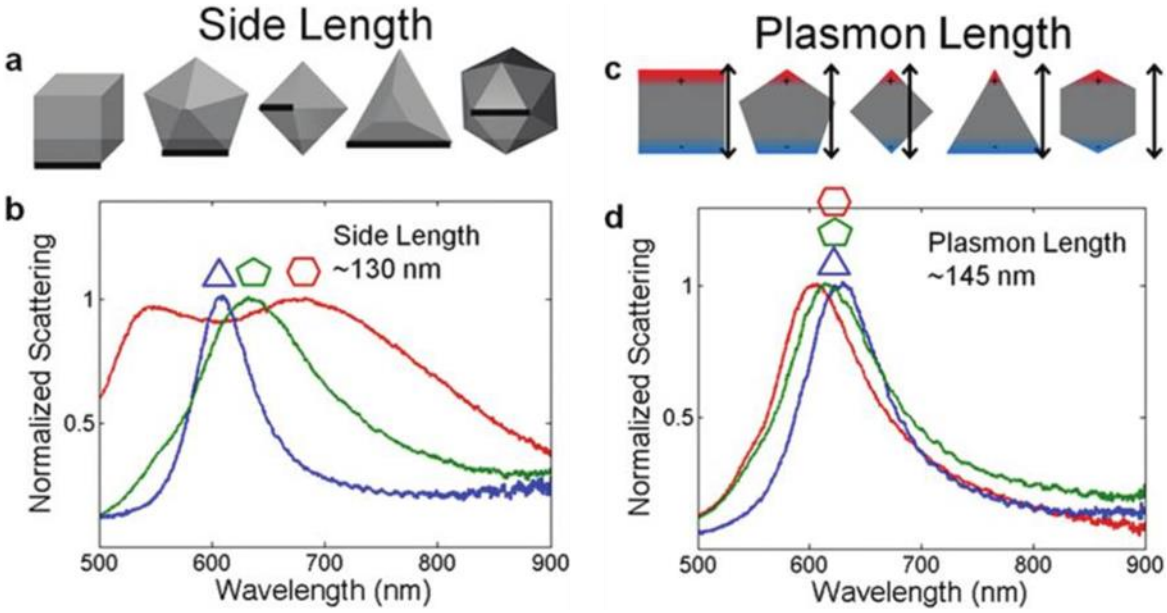

Figure 40. Comparison between side length and plasmon length as descriptors of nanoparticle size. (a) Definition of side length. (c) Definition of plasmon length. (b, d) Representative single-particle spectra for particles having similar side (b) or plasmon length (d). Adapted from Ringe, et al.[45]

Nevertheless, an attempt was made to apply the concept of plasmon length to AuNS-BCNCs. Considering the nanorod-like structure of AuNS-BCNCs, it is easy to visualize how the dipole resonance mode would establish two regions of charge at the opposite ends of the rod (**Figure 39a**) and the plasmon length would then be closely related to the overall length of the particle. If such a hypothesis is valid for rod-like particles, then a plot of nanorod length vs. dipolar plasmon resonance wavelength should yield a linear relationship as suggested by Ringe, et al. Such a plot is presented in **Figure 41** where the length of AuNS-BCNCs was determined by measuring the distance between the two furthest points on binarized SEM images of AuNS-BCNCs (Feret's Diameter). Linear regression analysis

of the data set produced a fit having a r^2 value of 0.969, indicative of a strong correlation between particle length and LSPR wavelength.

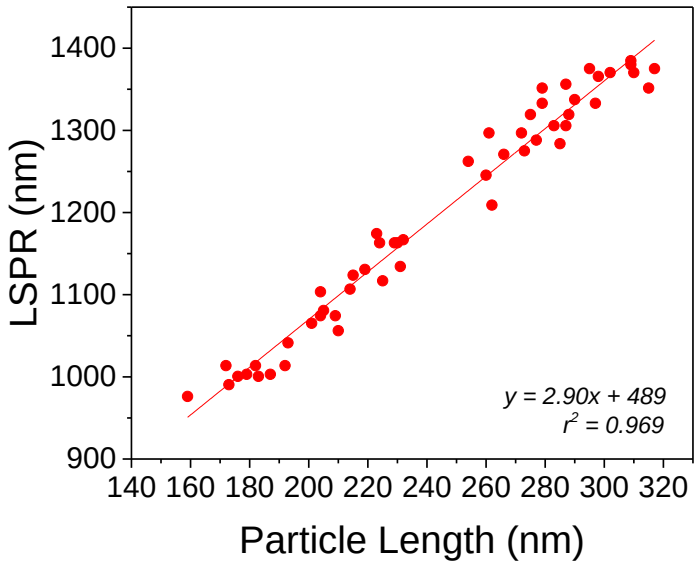

Figure 41. Longitudinal surface plasmon resonance dependence on the particle length of AuNS-BCNCs.

Using variance analysis, Ringe, et al. concluded that, irrespective of the particle shape, the value of the slope of plasmon energy vs. size (plasmon length) was equal to -3.08 meV/nm and the slope of the plasmon linewidth as a function of size was 2.96 meV/nm.[45] This linearity and shape independence was attributed to the linear increase in the distance between regions of opposite oscillation-induced charge separation, which is claimed to be the major contributor to retardation effects.[45] Linear regression analysis of dipolar plasmon energy dependence on AuNS-BCNC length yielded a slope of -2.60 meV/nm (**Figure 42a**) and analysis of linewidth dependence (**Figure 42b**) produced a positive slope of 2.4 meV. The general increase in dipolar plasmon linewidth with increasing size was found to be consistent with the value reported by Ringe (2.96 meV/nm).[35, 45]

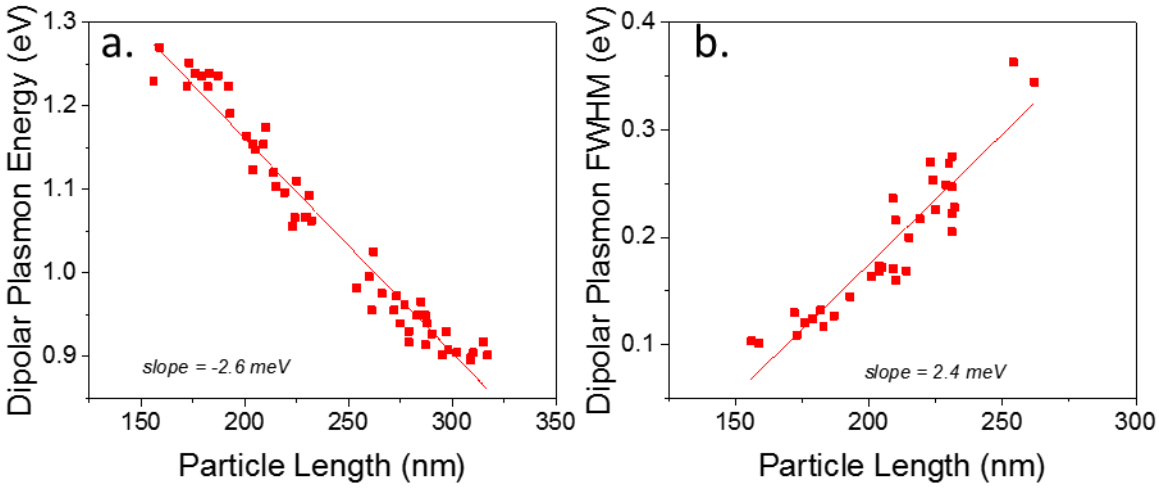

Figure 42. (a) Dipolar plasmon energy dependence on AuNS-BCNC length. (b) Dipolar plasmon linewidth dependence on AuNS-BCNC length.

However, comparison of the obtained slopes to those reported by Ringe, et al. revealed that the dipolar energy and linewidth of AuNS-BCNCs were both less sensitive to changes in particle size. This discrepancy in slopes and the scatter of data points about the fitted line may have been the result of several factors. Since electron charge density can extend slightly beyond a particle's physical dimensions (i.e. near-field), the approximation of plasmon length used in this study may not represent the true plasmon length. Other structural factors such as surface irregularities and ill-formed vertices may also contribute to the observed difference in slopes. Nevertheless, the empirical linear relationship obtained from this analysis could be useful in guiding the future design/synthesis of AuNS-BCNCs with specific plasmon resonance wavelengths and linewidths.

3.4.3 Surface Roughness Effects

A significant point of difference between particles analyzed in the cited literature and those presented here, is particle surface roughness. The single-particle spectroscopy

experiments discussed above have been performed on particles having neat geometrical shapes (cubes, triangles, rods, spheres, etc.). However, AuNS-BCNC used in this study are hybrid materials consisting of a cellulosic core surrounded by a polycrystalline gold shell. During the nucleation and growth of the gold coating, individual gold nanoparticles grow and coalesce into a continuous shell, and the density of gold nanoparticles on a particular seeded BCNC ultimately determines the final surface morphology of the coating. BCNCs having high nanoparticle density tend to form smooth coatings while those with lower nanoparticle density form coatings having a rough undulating morphology. The thickness of the coating also plays an important role in the surface roughness, as thicker coatings tend to fill in spaces between nuclei and smooth over surface irregularities (see **Figure 21d, e** for example).

To investigate the effect of surface roughness on the optical response of AuNS-BCNCs, several particles with increasing surface roughness were analyzed in more detail. To describe the surface roughness, a simplified shape factor[46] (e_R) was calculated for each particle. The simplified shape factor was calculated using **Equation 7**, the area (A), perimeter (P), and the Feret Min. and Max. lengths were obtained from binary AuNS-BCNCs images.

$$e_R = \frac{P_{cir}}{P} - \sqrt{1 - \left(\frac{Feret\ Min}{Feret\ Max}\right)^2} \tag{7}$$

The simplified shape factor considers both the deviation from circularity and surface irregularities. Values for e_R range from -1 to 1, where 1 represents a perfect circle, while smaller values represent particles with increased shape irregularity. Unfortunately, the effect of surface irregularity analysis is complicated for high aspect ratio particles, due in part to the lack of adequate numerical descriptions of their surface roughness. As an example, correlation between dipolar LSPR wavelength and linewidth would be difficult to establish using the simplified shape factor because, the e_R value is a function of both surface irregularity and particle shape, making a straightforward comparison of the surface roughness effect on dipolar LSPR energy difficult. Thus, this type of analysis would be limited only to particles having similar geometries and dimensions.

Fortunately, because of the large variation in AuNS-BCNC size and surface morphology, correlated single-particle spectroscopy of AuNS-BCNCs provides a unique opportunity to analyze such roughness effects. The comparison of particles with almost identical size (length, diameter) but different surface roughness is made possible by examination of many particles. A comparison of three such particles having increasing surface roughness is presented in **Table 4** (Note: a comparison between all similar sized particles measured, is presented in **Table 10** in **Appendix D**). A comparison of particles with similar dimensions is not expected to yield any differences in their dipolar LSPR wavelength and would not be predicted by **Equation 6**. However, it is evident from the results in **Table 4** that even though these particles are of similar size, their spectral responses are very different, showing a general increase in the dipolar LSPR wavelength (1083nm–1127nm) and linewidth (192nm–250nm) with decreasing e_R values (increasing surface roughness). Comparison of the measured LSPR λ_{max} to those pre

231dicted by **Equation 6** reveals that the difference between predicted and measured values increased with particle surface roughness.

Table 4. Comparison of the optical response of similar sized particles but increasing surface roughness.

	Particle Morphology		
			
Particle Length (nm)	231	231	231
Particle Diameter (nm)	68	70	68
Simplified Shape Factor e_R	-0.211	-0.246	-0.274
Measured LSPR (nm)	1083	1098	1127
Difference from Predicted LSPR Energy (**Eq**. **6**)	-0.17%	-1.9%	-4.0%
FWHM (nm)	192	214	250

This evidence strongly suggested that the consistent underestimation of the LSPR wavelengths by Encina's and Coronado's model, presented in **Table 3** and **Table 4**, was due to increased damping and retardation effects, resulting from the highly irregular surface morphology of AuNS-BCNCs. Such a decrease in LSPR energy with increasing roughness has been reported by others and has been attributed to the increase in inductive resistance the polarization current must overcome during resonance. Hence, this has the tendency to reduce the overall resonant energy/frequency.[47-48] The result of surface morphology analysis again reaffirms the validity of **Equation 6** and suggest that smooth AuNS-BCNCs would behave identically to large diameter gold nanorods.

3.4.4 Correlated Refractive Index Sensitivity Measurements

Perhaps one of the most widely suggested uses for plasmonic nanoparticles is for sensing applications where the sensitivity of the LSPR wavelength position to the surrounding environment's refractive index can be exploited to monitor chemical changes.[49-52] The efficiency of such sensors is typically reported as a refractive index sensitivity (RIS) value, which is the magnitude of the LSPR wavelength shift per refractive index unit (RIU). This relationship is linear for typical refractive index ranges of common aqueous and solvent solutions.[53] Typical values of sensitivity for solid gold or silver nanoparticles range from 70 to 500 nm/RIU.[53] However, particles with core-shell structures typically have even higher reported sensitivities arising from the enhanced sensitivity of hybridized plasmon modes to environmental changes. The highest reported RIS values to date are that of nanorice[42] and nanocrescents[8], with reported sensitivities of 801 nm/RIU and 880 nm/RIU, respectively.

To evaluate the potential performance of AuNS-BCNCs in sensing applications, single-particle correlated refractive index sensitivity measurement were performed on AuNS-BCNCs deposited onto ITO coated glass slides. Particles were exposed to aqueous glycerol solutions of varying concentration (**Table 2**) and a total of 5 particles were analyzed. Representative spectra from a single particle and a high-magnification SEM image of the same particle are presented in **Figure 43**. The linear relationship between LSPR wavelength and RI is shown in **Figure 44**.

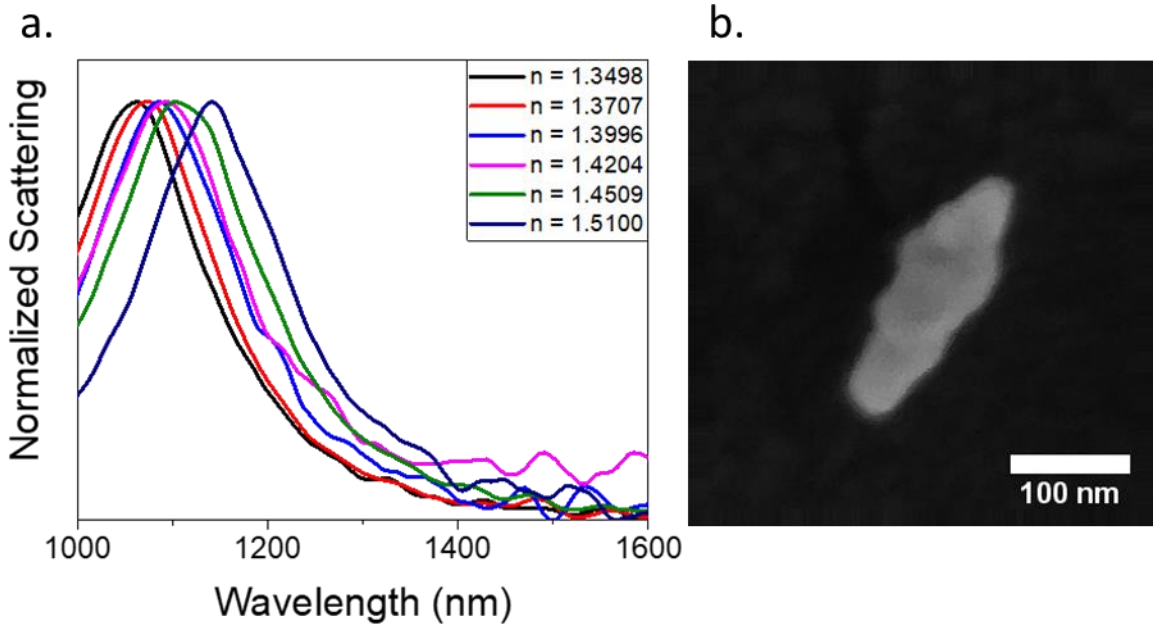

Figure 43. Refractive index sensitivity measurements of a single AuNS-BCNC. LSPR spectra collected in solutions of increasing refractive index (a). SEM image of the corresponding AuNS-BCNC (b).

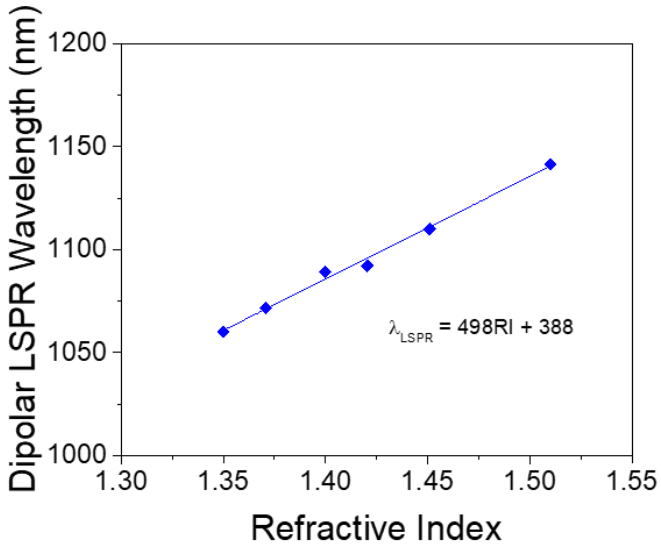

Figure 44. Plot of the maximum dipolar LSPR wavelength versus solution refractive index, as measured for the particle in Figure 43, showing a typical linear relationship with an RIS of 498 nm/RIU.

When considering the use of plasmonic nanoparticles as sensors, the linewidth of the plasmon resonance band must also be considered since sharper linewidths allow for easier detection of changes in peak positions (i.e., refractive index changes). Thus, a figure of merit (FOM) defined as the RIS value divided by the FWHM (**Equation 8)** was calculated to compare the performance of AuNS-BCNCs to the performance of other nanoparticles studied in literature.[14]

$$FOM = \frac{RIS(\frac{eV}{RIU})or(\frac{nm}{RIU})}{FWHM\ (eV)or(nm)} \quad (8)$$

A list of measured RIS and FOM values are presented in **Table 5**. The RIS values for AuNS-BCNCs ranged from 305 to 566 nm/RIU, with FOM values ranging from 2.72 to 3.06. The RIS of the AuNS-BCNCs was found to fall in the range of values reported for monolithic gold nanoparticles, which again suggest that these particles behave like solid gold nanorods and not as nanoshells, that have much higher reported refractive index sensitivities (>800 nm/RIU).[42, 53] The FOM values were found to be similar to values reported for solid, monolithic gold and silver nanoparticles of comparable size (2.6 for rods,[54-55] 5.4 for cubes,[14] 3.0 for triangles,[53] and 2.8 for decahedra[53]).

Table 5. Individual particle RIS and FOM values along with their size and shape descriptors.

Particle	Length (nm)	Diam. (nm)	AR	eR	RIS (nm/RI)	FOM
1	239	77	3.1	-0.190	498	2.72
2	167	61	2.8	-0.150	305	2.97
3	251	60	4.2	-0.301	532	2.74
4	251	62	4.0	-0.295	559	2.74
5	213	71	3.0	-0.191	566	3.06

Even though AuNS-BCNCs had rough surface morphologies and were generally more irregular, their ability to perform as sensors was not decreased. In fact, a reduction of surface roughness through improved synthesis techniques could potentially lead to a significant enhancement in FOM values by reducing line broadening caused by surface irregularities.

It is difficult to draw any conclusion between the size of the AuNS-BCNCs and their respective sensing performance due to the limited data set, but it has been previously shown that larger particles tend to have higher RIS values.[53, 55] However, an increase in particle size also tends to broaden the plasmon bands, which works to negate any gains in FOM values. Nevertheless, the advantage of using large plasmonic particles for sensing comes back to their high light scattering efficiency. The increased light scattering from large particles makes them appear brighter in dark-field microscopy and allows for much easier identification and measurement of single particles. This can be advantageous for biological studies where the dynamics of living organisms stipulate a need for short image collection times.

3.5 Conclusions

To the knowledge of the author, it has been demonstrated for the first time that a hyperspectral microscope equipped with a short-wave infrared detector (SWIR) is capable of capturing hyperspectral images of individual gold nanoshell bearing BCNCs with plasmon resonance bands extending to NIR wavelengths. Using a patterned ITO substrate, correlated spectral data was linked to AuNS-BCNCs size and morphology. It was shown that the model of Encina and Coronado is applicable to AuNS-BCNCs and can predict the

dipolar plasmon resonance wavelength with high accuracy (within 20%). This analysis also revealed that even though AuNS-BCNCs have a core-shell structure similar to other nanoshells, their gold nanorod-like plasmonic behavior suggests that hybridization of plasmon modes had a negligible effect on their optical properties owing to the thin high aspect ratio (>20) cellulose nanocrystal core.

Analysis of correlated Feret length and λ_{max} LSPR data revealed a robust ($r^2 = 0.97$) linear relationship between the dipolar plasmon resonance wavelength and the overall length of AuNS-BCNCs, giving credence to the concept of "plasmon length" as proposed by Ringe et al. However, it was found that other structural factors likely contributed to the plasmonic behavior of AuNS-BCNCs, because the slopes of plasmon energy and linewidth vs. plasmon length were found to be 15.6% and 18.9% lower than the values reported by Ringe. Nevertheless, this analysis resulted in a useful empirical relationship, which can guide future synthesis of particles with dipolar plasmon resonance bands in desired spectral windows.

The observed discrepancies between models and experiment led to the analysis of particle surface roughness and its effect on the plasmonic behavior of AuNS-BCNCs. Using a simplified structure factor, the surface roughness of similarly sized particles was estimated and used to draw conclusions about surface roughness effects. It was found that increased surface roughness corresponded to a red-shift of the dipolar plasmon resonance wavelength and a general broadening of linewidth. Since the AuNS-BCNC synthesis procedure results in particles having an irregular surface morphology, which is not accounted for by the Encina and Coronado model, it is not surprising that the predicted dipolar plasmon resonance wavelengths were consistently lower than experimentally

observed values but tended to deviate less for particles having smoother surfaces. This result reaffirmed the nanorod-like behavior of AuNS-BCNCs and provided useful insight for future improvements in AuNS-BCNCs synthesis techniques.

To investigate the possibility of using AuNS-BCNCs in sensing applications, correlated refractive index sensitivity measurements were performed on individual particles. The refractive index was modulated by surrounding the AuNS-BCNCs with aqueous glycerol solutions of varying concentration. It was found that the RIS for AuNS-BCNCs ranged from 305 to 566 nm/RIU, with an average FOM of 2.85. These values were found to be comparable to values reported in literature for solid, monolithic nanoparticles of similar size. Given the limited collected data set, additional work is needed to establish a correlation between AuNS-BCNC size/roughness and refractive index sensitivity.

3.6 References

[1] Lu, X.; Rycenga, M.; Skrabalak, S. E.; Wiley, B.; Xia, Y., Chemical Synthesis of Novel Plasmonic Nanoparticles. *Annual Review of Physical Chemistry* **2009,** *60* (1), 167-192.

[2] Ringe, E.; Sharma, B.; Henry, A.-I.; Marks, L. D.; Van Duyne, R. P., Single nanoparticle plasmonics. *Physical Chemistry Chemical Physics* **2013,** *15* (12), 4110-4129.

[3] Becker, J.; Schubert, O.; Sönnichsen, C., Gold Nanoparticle Growth Monitored in situ Using a Novel Fast Optical Single-Particle Spectroscopy Method. *Nano Letters* **2007,** *7* (6), 1664-1669.

[4] Slaughter, L.; Chang, W.-S.; Link, S., Characterizing Plasmons in Nanoparticles and Their Assemblies with Single Particle Spectroscopy. *The Journal of Physical Chemistry Letters* **2011,** *2* (16), 2015-2023.

[5] Uwada, T.; Asahi, T.; Masuhara, H.; Ibano, D.; Fujishiro, M.; Tominaga, T., Multipole Resonance Modes in Localized Surface Plasmon of Single Hexagonal/Triangular Gold Nanoplates. *Chemistry Letters* **2007,** *36* (2), 318-319.

[6] Munechika, K.; Smith, J. M.; Chen, Y.; Ginger, D. S., Plasmon Line Widths of Single Silver Nanoprisms as a Function of Particle Size and Plasmon Peak Position. *The Journal of Physical Chemistry C* **2007,** *111* (51), 18906-18911.

[7] Zopf, D.; Jatschka, J.; Dathe, A.; Jahr, N.; Fritzsche, W.; Stranik, O., Hyperspectral imaging of plasmon resonances in metallic nanoparticles. *Biosensors and Bioelectronics* **2016,** *81* (Supplement C), 287-293.

[8] Bukasov, R.; Shumaker-Parry, J. S., Highly Tunable Infrared Extinction Properties of Gold Nanocrescents. *Nano Letters* **2007,** *7* (5), 1113-1118.

[9] Giannini, R.; Hafner, C. V.; Löffler, J. F., Scaling Behavior of Individual Nanoparticle Plasmon Resonances. *The Journal of Physical Chemistry C* **2015,** *119* (11), 6138-6147.

[10] Grasseschi, D.; Lima, F. S.; Nakamura, M.; Toma, H. E., Hyperspectral dark-field microscopy of gold nanodisks. *Micron* **2015,** *69*, 15-20.

[11] Kuwata, H.; Tamaru, H.; Esumi, K.; Miyano, K., Resonant light scattering from metal nanoparticles: Practical analysis beyond Rayleigh approximation. *Applied Physics Letters* **2003,** *83* (22), 4625-4627.

[12] Lombardi, A.; Loumaigne, M.; Crut, A.; Maioli, P.; Del Fatti, N.; Vallée, F.; Spuch-Calvar, M.; Burgin, J.; Majimel, J.; Tréguer-Delapierre, M., Surface Plasmon

Resonance Properties of Single Elongated Nano-objects: Gold Nanobipyramids and Nanorods. *Langmuir* **2012,** *28* (24), 9027-9033.

[13] McMahon, J. M.; Wang, Y.; Sherry, L. J.; Van Duyne, R. P.; Marks, L. D.; Gray, S. K.; Schatz, G. C., Correlating the Structure, Optical Spectra, and Electrodynamics of Single Silver Nanocubes. *The Journal of Physical Chemistry C* **2009,** *113* (7), 2731-2735.

[14] Sherry, L. J.; Chang, S.-H.; Schatz, G. C.; Van Duyne, R. P.; Wiley, B. J.; Xia, Y., Localized Surface Plasmon Resonance Spectroscopy of Single Silver Nanocubes. *Nano Letters* **2005,** *5* (10), 2034-2038.

[15] Zhuo, X.; Yip, H. K.; Ruan, Q.; Zhang, T.; Zhu, X.; Wang, J.; Lin, H.-Q.; Xu, J.-B.; Yang, Z., Broadside Nanoantennas Made of Single Silver Nanorods. *ACS Nano* **2018,** *12* (2), 1720-1731.

[16] Zhuo, X.; Zhu, X.; Li, Q.; Yang, Z.; Wang, J., Gold Nanobipyramid-Directed Growth of Length-Variable Silver Nanorods with Multipolar Plasmon Resonances. *ACS Nano* **2015,** *9* (7), 7523-7535.

[17] Wei, H.; Reyes-Coronado, A.; Nordlander, P.; Aizpurua, J.; Xu, H., Multipolar Plasmon Resonances in Individual Ag Nanorice. *ACS Nano* **2010,** *4* (5), 2649-2654.

[18] Slaughter, L. S.; Chang, W.-S.; Swanglap, P.; Tcherniak, A.; Khanal, B. P.; Zubarev, E. R.; Link, S., Single-Particle Spectroscopy of Gold Nanorods beyond the Quasi-Static Limit: Varying the Width at Constant Aspect Ratio. *The Journal of Physical Chemistry C* **2010,** *114* (11), 4934-4938.

[19] Yorulmaz, M.; Nizzero, S.; Hoggard, A.; Wang, L.-Y.; Cai, Y.-Y.; Su, M.-N.; Chang, W.-S.; Link, S., Single-Particle Absorption Spectroscopy by Photothermal Contrast. *Nano Letters* **2015,** *15* (5), 3041-3047.

[20] Berciaud, S.; Cognet, L.; Blab, G. A.; Lounis, B., Photothermal Heterodyne Imaging of Individual Nonfluorescent Nanoclusters and Nanocrystals. *Physical Review Letters* **2004,** *93* (25), 257402.

[21] Billaud, P.; Marhaba, S.; Grillet, N.; Cottancin, E.; Bonnet, C.; Lermé, J.; Vialle, J.-L.; Broyer, M.; Pellarin, M., Absolute optical extinction measurements of single nano-objects by spatial modulation spectroscopy using a white lamp. *Review of Scientific Instruments* **2010,** *81* (4), 043101.

[22] Devkota, T.; Devadas, M. S.; Brown, A.; Talghader, J.; Hartland, G. V., Spatial modulation spectroscopy imaging of nano-objects of different sizes and shapes. *Appl. Opt.* **2016,** *55* (4), 796-801.

[23] Nicoletti, O.; Wubs, M.; Mortensen, N. A.; Sigle, W.; van Aken, P. A.; Midgley, P. A., Surface plasmon modes of a single silver nanorod: an electron energy loss study. *Opt. Express* **2011,** *19* (16), 15371-15379.

[24] Mie, G., Beiträge zur Optik trüber Medien, speziell kolloidaler Metallösungen. *Annalen der physik* **1908,** *330* (3), 377-445.

[25] Gans, R., Über die Form ultramikroskopischer Goldteilchen. *Annalen der Physik* **1912,** *342* (5), 881-900.

[26] Eustis, S.; El-Sayed, M. A., Determination of the aspect ratio statistical distribution of gold nanorods in solution from a theoretical fit of the observed inhomogeneously broadened longitudinal plasmon resonance absorption spectrum. *Journal of Applied Physics* **2006,** *100* (4), 044324.

[27] Link, S.; Mohamed, M.; El-Sayed, M., Simulation of the optical absorption spectra of gold nanorods as a function of their aspect ratio and the effect of the medium dielectric constant. *The Journal of Physical Chemistry B* **1999,** *103* (16), 3073-3077.

[28] Encina, E. R.; Coronado, E. A., Resonance Conditions for Multipole Plasmon Excitations in Noble Metal Nanorods. *The Journal of Physical Chemistry C* **2007,** *111* (45), 16796-16801.

[29] Slaughter, L. S.; Wu, Y.; Willingham, B. A.; Nordlander, P.; Link, S., Effects of Symmetry Breaking and Conductive Contact on the Plasmon Coupling in Gold Nanorod Dimers. *ACS Nano* **2010,** *4* (8), 4657-4666.

[30] Khlebtsov, B. N.; Khanadeev, V. A.; Khlebtsov, N. G., Extinction and extra-high depolarized light scattering spectra of gold nanorods with improved purity and dimension tunability: direct and inverse problems. *Physical Chemistry Chemical Physics* **2014,** *16* (12), 5710-5722.

[31] Khlebtsov, N. G., T-matrix method in plasmonics: An overview. *Journal of Quantitative Spectroscopy and Radiative Transfer* **2013,** *123*, 184-217.

[32] Constantin, D., Why the aspect ratio? Shape equivalence for the extinction spectra of gold nanoparticles. *The European Physical Journal E* **2015,** *38* (11), 116.

[33] Giannini, V.; Fernández-Domínguez, A. I.; Heck, S. C.; Maier, S. A., Plasmonic Nanoantennas: Fundamentals and Their Use in Controlling the Radiative Properties of Nanoemitters. *Chemical Reviews* **2011,** *111* (6), 3888-3912.

[34] Grubisic, A.; Schweikhard, V.; Baker, T. A.; Nesbitt, D. J., Multiphoton photoelectron emission microscopy of single Au nanorods: combined experimental and theoretical study of rod morphology and dielectric environment on localized surface plasmon resonances. *Physical Chemistry Chemical Physics* **2013,** *15* (26), 10616-10627.

[35] Schmucker, A. L.; Harris, N.; Banholzer, M. J.; Blaber, M. G.; Osberg, K. D.; Schatz, G. C.; Mirkin, C. A., Correlating Nanorod Structure with Experimentally

Measured and Theoretically Predicted Surface Plasmon Resonance. *ACS Nano* **2010,** *4* (9), 5453-5463.

[36] Semenikhin, N. S.; Kadasala, N. R.; Moon, R. J.; Perry, J. W.; Sandhage, K. H., Individually Dispersed Gold Nanoshell-Bearing Cellulose Nanocrystals with Tailorable Plasmon Resonance. *Langmuir* **2018,** *34* (15), 4427-4436.

[37] Oldenburg, S. J.; Averitt, R. D.; Westcott, S. L.; Halas, N. J., Nanoengineering of optical resonances. *Chemical Physics Letters* **1998,** *288* (2–4), 243-247.

[38] Brinson, B. E.; Lassiter, J. B.; Levin, C. S.; Bardhan, R.; Mirin, N.; Halas, N. J., Nanoshells Made Easy: Improving Au Layer Growth on Nanoparticle Surfaces. *Langmuir* **2008,** *24* (24), 14166-14171.

[39] Schindelin, J.; Arganda-Carreras, I.; Frise, E.; Kaynig, V.; Longair, M.; Pietzsch, T.; Preibisch, S.; Rueden, C.; Saalfeld, S.; Schmid, B.; Tinevez, J.-Y.; White, D. J.; Hartenstein, V.; Eliceiri, K.; Tomancak, P.; Cardona, A., Fiji: an open-source platform for biological-image analysis. *Nature Methods* **2012,** *9*, 676.

[40] Hoyt, L. F., New Table of the Refractive Index of Pure Glycerol at 20°C. *Industrial & Engineering Chemistry* **1934,** *26* (3), 329-332.

[41] Encina, E. R.; Coronado, E. A., Plasmonic Nanoantennas: Angular Scattering Properties of Multipole Resonances in Noble Metal Nanorods. *The Journal of Physical Chemistry C* **2008,** *112* (26), 9586-9594.

[42] Wang, H.; Brandl, D. W.; Le, F.; Nordlander, P.; Halas, N. J., Nanorice: A Hybrid Plasmonic Nanostructure. *Nano Letters* **2006,** *6* (4), 827-832.

[43] Shi, W.; Sahoo, Y.; Swihart, M. T.; Prasad, P. N., Gold Nanoshells on Polystyrene Cores for Control of Surface Plasmon Resonance. *Langmuir* **2005,** *21* (4), 1610-1617.

[44] Prodan, E.; Radloff, C.; Halas, N. J.; Nordlander, P., A Hybridization Model for the Plasmon Response of Complex Nanostructures. *Science* **2003,** *302* (5644), 419-422.

[45] Ringe, E.; Langille, M. R.; Sohn, K.; Zhang, J.; Huang, J.; Mirkin, C. A.; Van Duyne, R. P.; Marks, L. D., Plasmon Length: A Universal Parameter to Describe Size Effects in Gold Nanoparticles. *The Journal of Physical Chemistry Letters* **2012,** *3* (11), 1479-1483.

[46] Pourghahramani, P.; Forssberg, E., REVIEW OF APPLIED PARTICLE SHAPE DESCRIPTORS AND PRODUCED PARTICLE SHAPES IN GRINDING ENVIRONMENTS. PART I: PARTICLE SHAPE DESCRIPTORS. *Mineral Processing and Extractive Metallurgy Review* **2005,** *26* (2), 145-166.

[47] Wang, H.; Goodrich, G. P.; Tam, F.; Oubre, C.; Nordlander, P.; Halas, N. J., Controlled Texturing Modifies the Surface Topography and Plasmonic Properties of Au Nanoshells. *The Journal of Physical Chemistry B* **2005,** *109* (22), 11083-11087.

[48] García-Vidal, F. J.; Pendry, J. B., Collective Theory for Surface Enhanced Raman Scattering. *Physical Review Letters* **1996,** *77* (6), 1163-1166.

[49] ANKER, J. N.; HALL, W. P.; LYANDRES, O.; SHAH, N. C.; ZHAO, J.; DUYNE, R. P. V., Biosensing with plasmonic nanosensors. In *Nanoscience and Technology*, pp 308-319.

[50] Willets, K. A.; Duyne, R. P. V., Localized Surface Plasmon Resonance Spectroscopy and Sensing. *Annual Review of Physical Chemistry* **2007,** *58* (1), 267-297.

[51] Saha, K.; Agasti, S. S.; Kim, C.; Li, X.; Rotello, V. M., Gold Nanoparticles in Chemical and Biological Sensing. *Chemical Reviews* **2012,** *112* (5), 2739-2779.

[52] Mayer, K. M.; Hafner, J. H., Localized Surface Plasmon Resonance Sensors. *Chemical Reviews* **2011,** *111* (6), 3828-3857.

[53] Ringe, E. Building the Nanoplasmonics Toolbox Through Shape Modeling and Single Particle Optical

Studies. NORTHWESTERN UNIVERSITY, 2012.

[54] Becker, J.; Trügler, A.; Jakab, A.; Hohenester, U.; Sönnichsen, C., The Optimal Aspect Ratio of Gold Nanorods for Plasmonic Bio-sensing. *Plasmonics* **2010,** *5* (2), 161-167.

[55] Yong, Z.; Lei, D. Y.; Lam, C. H.; Wang, Y., Ultrahigh refractive index sensing performance of plasmonic quadrupole resonances in gold nanoparticles. *Nanoscale research letters* **2014,** *9* (1), 187-187.

CHAPTER 4: SYNTHESIS OF MAGNETIC NICKEL-COATED BACTERIAL CELLULOSE NANOCRYSTALS

4.1 Summary

Magnetic nickel nanoshell-bearing BCNCs have been generated using functionalization and electroless deposition methods developed in **Chapters 1-2**. It has been shown that aminated BCNCs have potential to be versatile metallic nanoparticle supports as was demonstrated by the efficient adsorption of Pt particles onto their aminated surfaces. The platinum decorated BCNC, were then coated with a layer of Ni, using electroless deposition. The coating morphology and thickness was controlled through adjustment of the electroless plating bath Ni^{2+} ion concentration. The deposited Ni coatings were found to be composed of nanocrystalline Ni nanoparticles, with some grains showing the presence of NiO. The magnetic properties of the NiNS-BCNCs were evaluated using a SQUID magnetometer. The ferromagnetic NiNS-BCNCs exhibited controllable magnetic field-induced self-assembly into long Ni nanowire like structures. The magnetic field-induced self-assembly was shown to be sensitive to process parameters (i.e., magnetic field strength, orientation, and NiNS-BCNC concentration), which allowed for control over the self-assembly process.

4.2 Introduction

Magnetic nanoparticles are being actively researched for their expected performance in applications such as data storage,[1-4] magnetic sensing,[1] catalysis,[2] bio-separation,[5-6] environmental remediation,[7-8] and in medicine as drug delivery vehicles[9] and magnetic resonance imaging (MRI) contrast agents.[10] Each application requires specific control over

particle size and shape as well as a suitable magnetic response for desired performance. Although synthesis protocols for monodispersed magnetic nanoparticles are common in the literature, these methods typically are limited to particles having isotropic morphologies with a narrow size range and are not applicable across material systems. The implementation of templated synthesis techniques allows for greater control over particle geometry and provides a convenient means of tailoring the magnetic properties. However, there are only a handful of reports describing the synthesis of such magnetic core-shell particles, and of those, the majority are limited to the use of silica and polymeric microspheres for the creation of spherical magnetic nanoshells.[2] These templated particles are usually synthesized by electroless deposition of thin layers of metallic Ni, NiP, or mixed alloys (e.g. CoNiP, NiFeP, CoFeP) onto micron-sized spheres.[2]

Due to the direction dependant magnetic properties of anisotropic particles, there is much interest in developing methods to synthesize such particles in bulk, which can be used for the construction of large colloidal assemblies that would exhibit the anisotropic magnetic behavior at the macro-scale. A recent demonstration of this has been reported by Hoffelner, et al., who used magnetic fields to orient and arrange weakly ferromagnetic hematite spindles into ordered macroscopic assemblies that exhibited direction dependant magnetic response.[11] Another potential use of magnetism and anisotropy was demonstrated by Grzelczak, et al., who coated gold nanorods with thin layers of Ni.[12] The resulting Ni coated gold nanorods retained their characteristic anisotropic optical properties, but their optical response could be modulated by an external magnetic field. Such magnetically addressable optical properties could be useful for optomagnetic sensing applications.[12] Unfortunately, such examples are few due to the lack of robust chemical synthesis methods

for highly anisotropic ferromagnetic nanoparticles (e.g., high aspect ratio nanorods, nanowires, etc.).[1] Additionally, many of the existing bottom-up synthesis methods are not applicable across material systems. Thus, a common method for synthesizing 1-D nanostructures is through a hard template approach. Anodic alumina membranes have been used to create a host of metallic 1-D nanomaterials (e.g. Au, Ag, Cu, Ni, Co, etc.) through pulsed electrodeposition of metal into membrane pores. However, the high associated costs of alumina template production and low scalability potential, limit this technique to laboratory scale fabrication. Nevertheless, such experiments have demonstrated that control of magnetic properties can be achieved by manipulating nanoparticle size/aspect ratio.[13-15]

4.3 Experimental Procedures

4.3.1 Synthesis of Pt seed particles

Platinum nanoparticles with an average size of 2.6 ± 0.63 nm were synthesised as described by Rioux, et al.[16] Briefly, in a 500 mL Erlenmeyer flask, 133 mg of PVP (Mw = 55,000, Sigma Aldrich, St. Louis, MO) was dissolved in a mixture of 6.22 mL of a $H_2PtCl_6 \cdot 6H_2O$ (19.3 mM, ACS Reagent, Sigma Aldrich, St. Louis, MO) aqueous solution and 194 mL of ethanol (200 proof, KOPTEC, King of Prussia, PA). The mixture was heated to 80°C and refluxed for 3 hours without stirring. The dark brown solution was cooled to room temperature and stored at 4°C until use. No particle agglomeration or deactivation were observed in suspensions for up to 3 months.

4.3.2 Preparation of Pt decorated BCNCs

Platinum nanoparticles were attached onto the aminated BCNC surfaces by slowly adding (dropwise) 1 mL of a 0.1 wt.% a-BCNCs suspension into 20 mL of a Pt seed particle suspension, which was magnetically stirred (1200 RPM). After the addition of a-BCNCs, the mixture was stirred for 2 hours and was then centrifuged (10,000 RCF, 30 minutes) to separate the Pt-decorated BCNCs from the unbound Pt particles. The supernatant was removed, and the Pt-decorated particles were suspended in 10 mL of fresh Pt nanoparticle suspension via brief (10 min.) sonication (Branson 2510 ultrasonic bath, Branson Ultrasonic Corp., St. Louis, MO). After 2 hours, the particles were once again separated by centrifugation and the supernatant was removed. The absorbance spectrum of the supernatant was compared to that of the fresh Pt seed particle suspension to determine the change in particle concentration. The above procedure was repeated (4 cycles) until the collected supernatant's absorbance was identical to the fresh Pt seed particle suspension. At this point, the BCNCs were suspended in ethanol via brief sonication (10 min) and the suspension was centrifuged (10,000 RCF, 60 min) to sediment the Pt-decorated BCNCs. The pale brown supernatant was removed, and the washing procedure was repeated until the supernatant remained colorless (typically 2 wash cycles). The washed Pt-decorated BCNCs were diluted with DI water until the absorbance (10 mm optical path length) value at 670 nm was equal to 0.08 (or a multiple of this value 2-4x). The diluted Pt-decorated BCNCs were stored at 4°C until use. The Pt-decorated BCNCs were found to remain suitable for electroless Ni deposition for over 6 months.

4.3.3 Synthesis of Ni Coated BCNCs

Nickel coatings were deposited onto the Pt-decorated BCNCs from an electroless Ni-hydrazine plating solution. In a typical procedure, 75 μL of a 0.25 M $NiCl_2$ (98% purity, Alfa Aesar, Haverhill, MA) solution was mixed with 540 μL of 2.5M hydrazine monohydrate (98+% purity, Alfa Aesar, Haverhill, MA). This solution was then diluted to 13.5 mL with DI water in a 20 mL glass vial. To this electroless plating solution, 1.5 mL of the Pt-decorated BCNCs was added. The mixture was probe sonicated using a 5 mm probe (Misonix 3000, Misonix Inc., Farmingdale, NY) operating in pulse mode (on/off times of 10 s/10 s) at an amplitude of ≈90 μm (power setting of 3) for 5 minutes to mix the precursors. After sonication, the vial was placed into a hot water bath (80°C) and allowed to react for 10 minutes under vigorous agitation, which was provided by a small magnetic stir bar (3.5 mm x 12.7 mm, 1500 RPM)

4.3.4 Magnetic Alignment of Ni Coated BCNCs

Ni coated BCNCs were magnetically aligned by depositing known volumes of Ni-BCNC suspensions onto cleaned substrates placed in a magnetic field, and then allowed to dry at room temperature. A uniform magnetic field was established by positioning two neodymium magnets (6.35 mm x 6.35 mm x 25.4 mm, McMaster-Carr, Elmhurst, IL) with their opposite poles facing each other. The magnets were retained in a custom machined PVC plate that could hold the magnets at several fixed distances, which allowed for the variation of the magnetic field strength between the poles. The magnetic alignment fixture is shown in **Figure 45**.

Figure 45. Magnetic alignment fixture used to vary the magnetic field strength by increasing the distance between the magnetic poles of two neodymium magnets.

4.3.5 Morphological Analyses

Transmission electron microscopy (TEM) was used to analyse the size of synthesized Pt nanoparticles as well as the distribution of Pt nanoparticle on the surface of Pt decorated BCNCs using a Hitachi HT7700 TEM (Hitachi, Tokyo, Japan) operating at an acceleration voltage of 120 kV. Scanning electron microscopy was performed on Ni coated BCNCs using a Zeiss Ultra 60 field-emission SEM (Carl Zeiss, Oberkochen, Germany) operating at an accelerating voltage of 2-3 kV and a working distance range of 3-4 mm. A reduced voltage was found to be necessary for Ni-BCNCs due to charge artifacts caused by the electron beam interacting with the magnetic particles. Diced silicon wafer pieces were used as substrates for SEM imaging. The substrates were cleaned prior to use by sonication in a 2 wt.% cleaning solution (micro-90, Burlington, NJ) for 10 minutes followed by rinsing with DI water and sonicating an additional 10 minutes in clean DI water. The washed substrates were stored in DI water until use. Before depositing Ni-BCNCs suspensions, the

substrates were treated with a 10-minute plasma cleaning cycle (Harrick Plasma, Ithica, NY) to remove any residual traces of surface contaminants and render the surface hydrophilic, which aided in spreading particles across the substrate surface as can be seen in **Figure 46**.

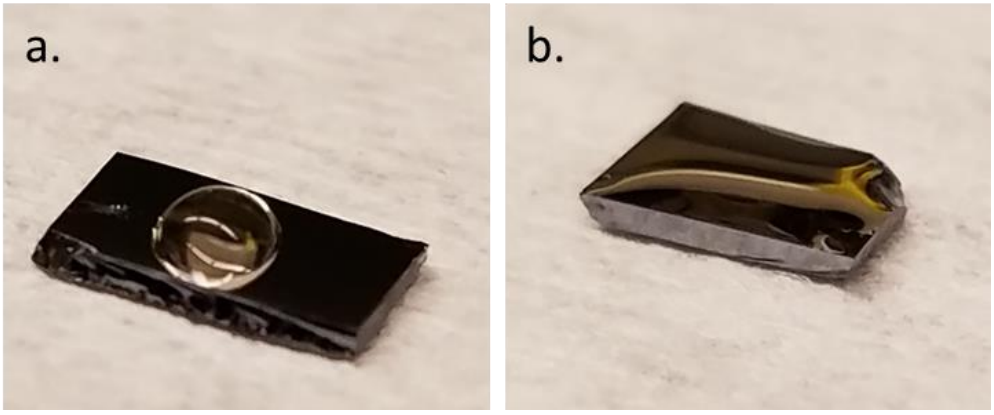

Figure 46. Effect of plasma cleaning on the contact angle between a Si wafer substrate and sample droplet. (a) Si wafer before plasma cleaning. (b) Silicon wafer after a 10-minute plasma cleaning cycle.

4.3.6 Magnetic Property Characterization

The magnetic properties (i.e., remnant magnetization, coercivity, and saturation) of nickel-coated BCNCs were analysed using a superconducting quantum interference device (SQUID) magnetometer with the help of Dr. Zhang's group (Georgia Institute of Technology, Atlanta, GA). Magnetic measurements were conducted at 5 Kelvin by sweeping the magnetic field strength from -50 kOe to 50 kOe.

4.4 Results and Discussion

4.4.1 Pt decorated BCNCs

The approach for depositing nickel coatings onto aminated BCNCs was similar to the methods used to synthesis AuNS-CNCs, where many small metallic nanoparticles were first deposited onto the surface of the cellulose nanocrystals, which served as preferential heterogeneous nucleation sites for subsequent electroless metal deposition. However, it was found that small gold nanoparticles were ineffective as heterogeneous nucleation sites for nickel. Trials revealed that gold nanoparticles did not cause any significant decomposition of the electroless nickel precursor, which was evidenced by the absence of a change in color after heating the solution for an extended time (>20 mins). Similar findings have also been reported in the literature.[12] A representative experiment is shown in **Figure 47a,** which is compared to a parallel trial conducted with Pt decorated BCNCs (as will be discussed below). A more active metal nucleating agent capable of catalyzing electroless nickel deposition from a nickel hydrazine bath was sought. Two of the most common catalytic metals that are cited in the literature for conformal electroless nickel deposition are platinum and palladium.[17] Palladium is typically utilized to sensitize inert substrates, such as plastics and ceramics, by first incubating the substrate in a solution of a palladium chloride followed by immersion of the substrate in a solution of stannous chloride, which reduces the palladium ions into small metallic particles.[18-19] It is also possible to sensitize materials by reducing palladium ions to colloidal Pd nanoparticles that can sensitize substrates by adsorbing onto them from a single solution.[20]

Figure 47. Electroless deposition trials using gold decorated BCNCs(left) and platinum decorated BCNCs (right). Gold decorated BCNCs did not produce an observable color change after heating for 20 minutes at 80°C.

Although these processes have been found to be effective for large templates/substrates, both methods tend to yield solutions that quickly age and become deactivated over time.[18] These methods also tend to produce colloidal particles that are relatively large (4-10 nm) in comparison to the cross-section of BCNCs (5-20 nm), which can limit the amount of surface covered by the catalytic particles. To eliminate the issue of solution aging, minimize the use of costly reagents, and to increase catalyst surface coverage, a colloidal suspension of Pt nanoparticles was chosen as the ideal sensitizing solution. Platinum particles with an average diameter of 2.7 nm were synthesized by refluxing an ethanolic solution of chloroplatinic acid in the presence of PVP (55,000 MW).[16] A representative TEM image of the synthesized Pt nanoparticles and their particle size distribution as measured from TEM images are shown in **Figure 48** and **Figure 49,** respectively.

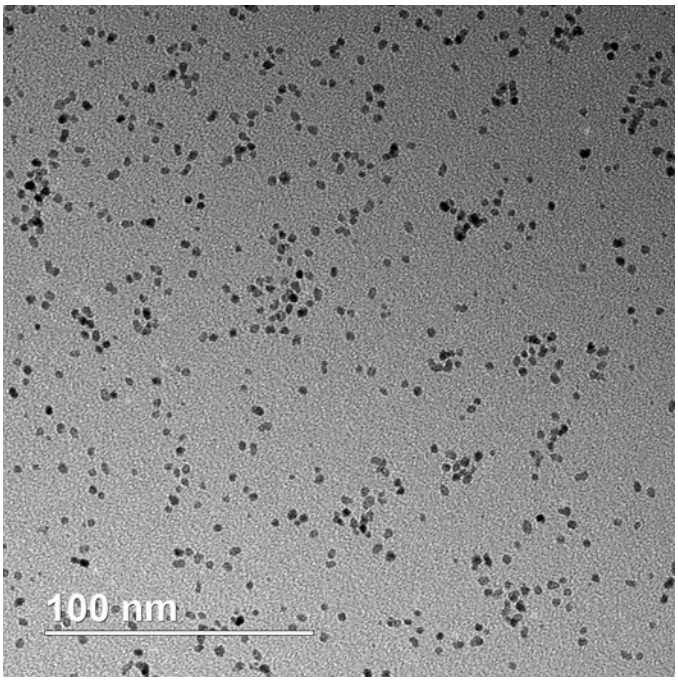

Figure 48. Representative TEM image of PVP stabilized Pt nanoparticles.

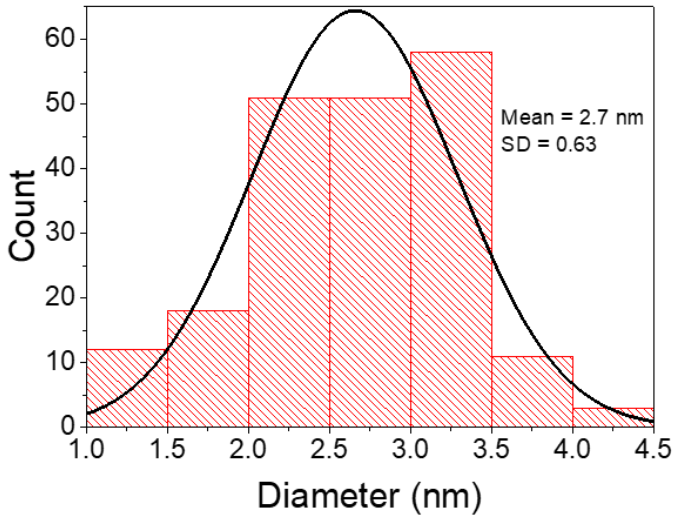

Figure 49. Particle size distribution of PVP stabilized Pt nanoparticles. The fit to a normal distribution curve (Mean = 2.7 nm, SD = 0.63) is shown.

It was found that colloidal suspensions of PVP stabilized Pt nanoparticles were stable for over 6 months and retained their activity towards electroless Ni deposition during this time.

Aminated BCNCs were seeded/sensitized with Pt nanoparticles by dropwise addition of aminated BCNCs suspension to the Pt nanoparticle suspension with strong mixing (a well-formed vortex). After mixing of the two suspensions, the Pt nanoparticles quickly adsorbed onto the surfaces of aminated BCNCs, which was evidenced by the formation of large brown flocs, which settled out of suspension and left behind a colorless solution. The flocculated particles were separated from the solution by centrifugation and were dispersed in a fresh aliquot of Pt nanoparticle suspension and was left stirring (500 RPM) for 1 hour to allow for the adsorption of additional Pt nanoparticles to saturate the amine anchor sites present on the surface of aminated BCNCs. The incubation and centrifugation cycles were repeated several times until the extinction spectrum of the supernatant was matched the spectrum of as-synthesized Pt nanoparticle suspension. It was found, that after three incubation cycles, the absorbance spectrum of the supernatant closely matched that of the synthesized Pt nanoparticle suspension. No appreciable gain in absorbance was seen with an additional incubation cycle as shown in **Figure 50**. The extinction spectrum of the Pt decorated BCNCs was compared to the spectrum of the as-synthesized Pt nanoparticles, as shown in **Figure 51**.

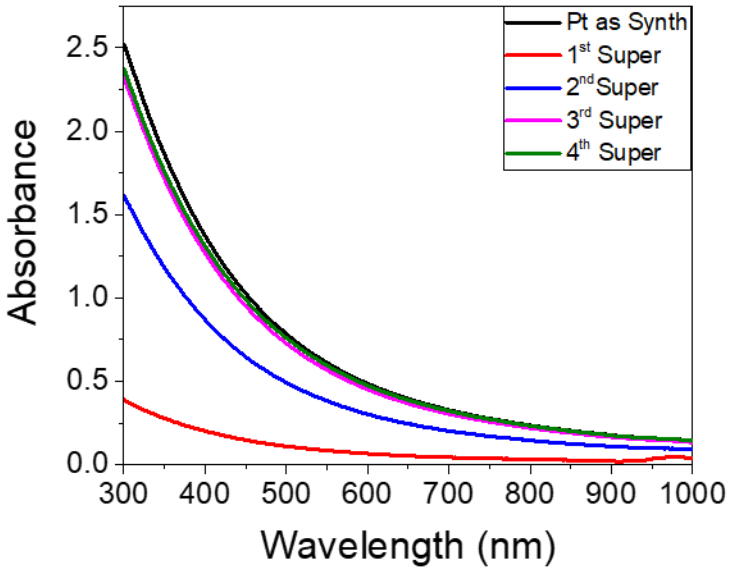

Figure 50. Ultraviolet-visible extinction spectra of the supernatant after incubation of aminated BCNCs with Pt nanoparticles (in order of increasing incubation cycle). (Pt as synth) spectrum is of the as-synthesized Pt nanoparticle suspension.

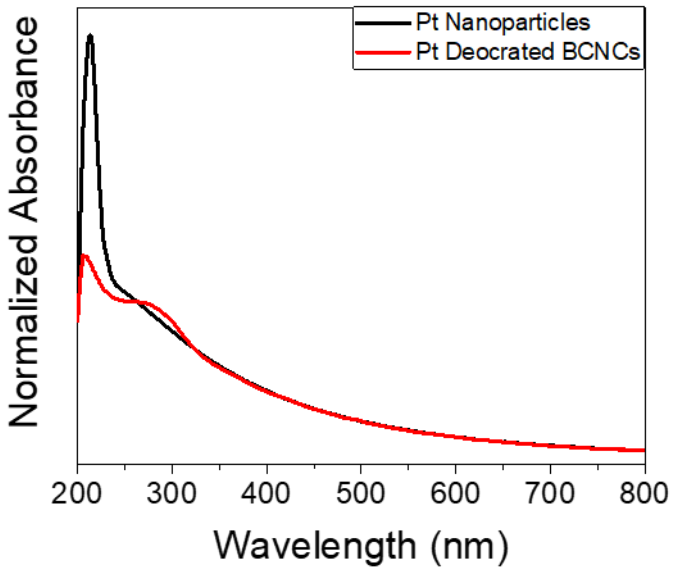

Figure 51. Ultraviolet-visible spectra of the as synthesized Pt nanoparticles and Pt decorated BCNCs.

Analysis of the spectra revealed that the peak at 213 nm, which is attributed to Pt electron intra-band transitions, is dampened, and the shoulder at 300 nm became more pronounced

in the Pt decorated BCNC sample. The change in these features has been attributed to the increase of Pt nanoparticle size or the agglomeration of small Pt particles.[21-22] Since the sequential incubation procedure is expected to saturate the surfaces of the aminated BCNCs with Pt particles, the observed changes in the extinction spectra suggests that Pt particles existed in proximity to each other on the aminated BCNCs surfaces. Transmission electron microscopy performed on the Pt decorated BCNCs confirmed that the observed changes in the extinction spectrum as the result of desired Pt particle surface coverage and not from particle agglomeration. Representative TEM images of this analysis are shown in **Figure 52**. TEM images revealed rod-like assemblies of fine Pt nanoparticles.

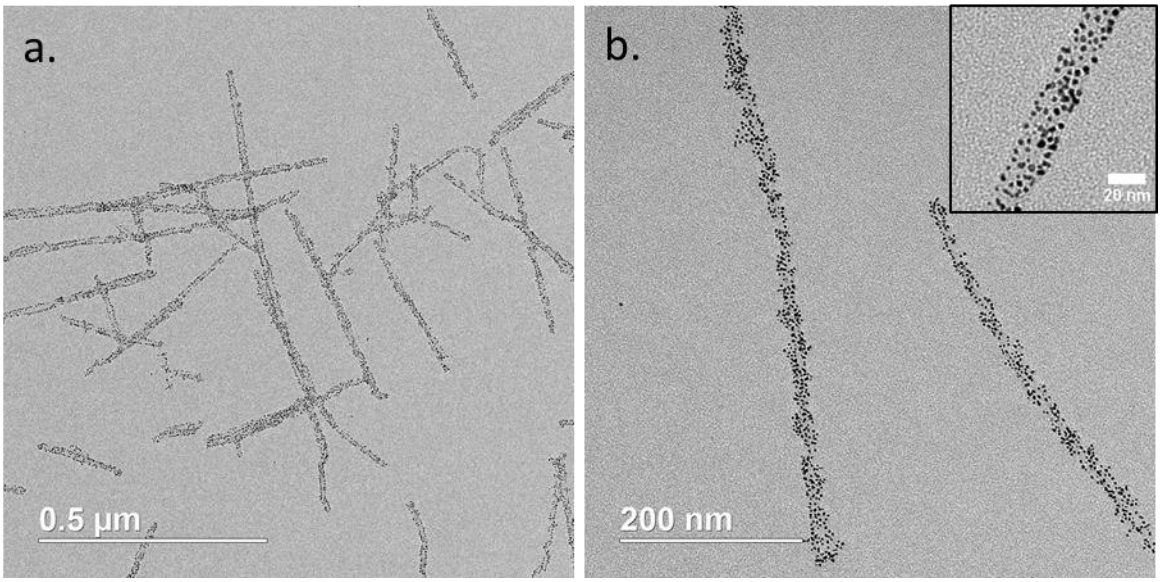

Figure 52. TEM images of Pt decorated BCNCs. (a) Low magnification image showing Pt on BCNCs. (b) Higher magnification image of Pt decorated BCNCs (inset) detailed view of the Pt particle spacing along the surface of a BCNC. Aminated BCNCs were subjected to a total of 4 incubation cycles.

Although, cellulose nanocrystals could not be directly observed due to their electron transparency, the length of Pt nanoparticle assemblies was consistent with the typical length and length distribution of BCNCs. High magnification images revealed that Pt

nanoparticles remained as discrete particles but were densely populated along BCNC surfaces. Not only did these results confirm that the sequential incubation procedure was successful at creating aminated BCNCs densely decorated with Pt nanoparticles, but they also verified the uniformity of the surface modification reactions, developed in **Chapter 1** as each Pt particle along the BCNC surface must correspond to at least one amine moiety. The high surface amine density and, in turn, Pt nanoparticle coverage proved to be advantageous for creating conformal Ni coatings, as will be discussed below, but also demonstrated that aminated BCNCs can potentially be used as high-surface-area catalyst supports, which serve to stabilize catalytic nanoparticles in suspension and can keep them from agglomerating over time.

4.4.2 Electroless Ni Deposition

To impart magnetic qualities to BCNCs, nickel nanoshells were grown around the Pt decorated BCNCs using electroless deposition. Nickel (Ni) was chosen as the transition metal of choice due to its ferromagnetism and increased oxidation resistance in comparison to iron and cobalt. Reports of successful aqueous synthesis of air stable pure Ni nanoparticles without the need of an inert atmosphere via the catalytic reduction of $NiCl_2$ by hydrazine in the presence of a stabilizing agent served as the basis of the process used in this study.[23-25] This approach has been recently used to create Ni nanoshells on gold nanorods[12] as well as silica microspheres,[2] demonstrating the versatility of this method.

It has been reported that the ratio of Ni^{2+} ions to hydrazine monohydrate plays an important role in controlling the size of synthesized nanoparticles, with higher ratios yielding smaller Ni nanoparticles.[23-24] This effect has been attributed to the enhancement

of Ni^{2+} reduction and Ni nucleation rate. However, it was found that above a certain ratio (12 to 20), no additional reduction in size is observed, which stems from the maximization of the nucleation rate.[23, 25] Since the formation of small Ni nuclei on the surface of BCNCs is desirable for the formation of conformal coatings, the hydrazine to Ni^{2+} ratio was kept above 20 for all Ni nanoshell synthesis trials. Temperature has also been shown to affect the formation of Ni particles from Ni-hydrazine solutions. Increasing temperatures lead to shorter reaction times and are associated with an acceleration of the Ni particle growth rate.[26] A temperature of 80°C was found to give short reactions times (10-20 minutes) and was used for all trials discussed below.

Sanels-Sobrido, et al. recently demonstrated that Ni-hydrazine solutions can be used to synthesize Ni nanoshells on silica spheres without the use of capping agents.[2] Their X-ray electron spectroscopy (XPS) analysis showed that the aqueous reduction of a Ni-hydrazine complex resulted in Ni coatings that consisted of metallic Ni covered by a thin layer of protective oxide, which, they claim, helped prevent further oxidation of the coating. Thus, initial synthesis trials of Ni nanoshell-bearing BCNCs (NiNS-BCNCs) were performed without the addition of stabilizing/capping agents and in unstirred solutions. Unfortunately, these trials yielded agglomerated particles composed of several BCNCs fused together by the deposited Ni metal, as shown in **Figure 53**.

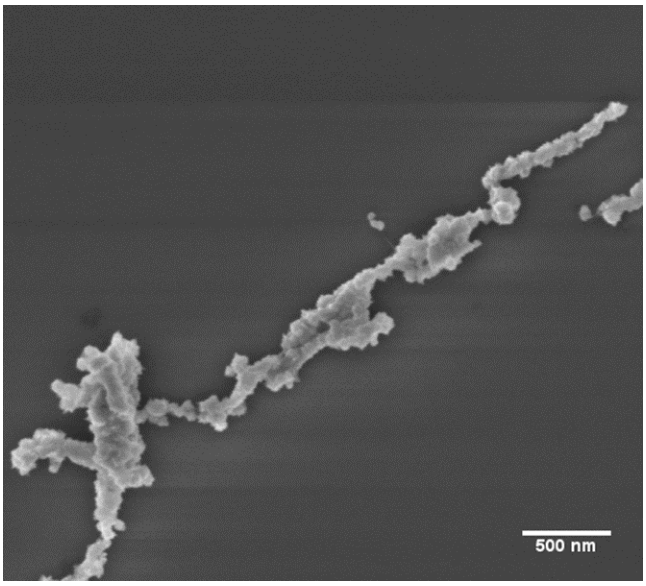

Figure 53. Representative SEM image of Ni nanoshell-bearing BCNCs synthesized in a quiescent solution without the presence of a stabilizing agent.

The observed agglomeration could be due to the greater potential of particles to link together and form networks in quiescent solutions, where only Brownian motion, convection, and gravity influence particle motion. To alleviate the issue of particle agglomeration, polyvinylpyrrolidone (PVP) was added to the electroless plating solution to act as a stabilizing agent. PVP is known to adsorb onto metallic surfaces and has been extensively used in the synthesis of silver nanowires and nanotriangles, where it not only directs particle growth but serves to stabilize the particles in suspension;[27-28] that is, the addition of PVP with a large molecular weight (1.3 million) could increase the steric hindrance between growing NiNS-BCNCs. **Figure 54** shows Ni coated BCNCs synthesized in the presence of 1.3 million molecular weight PVP.

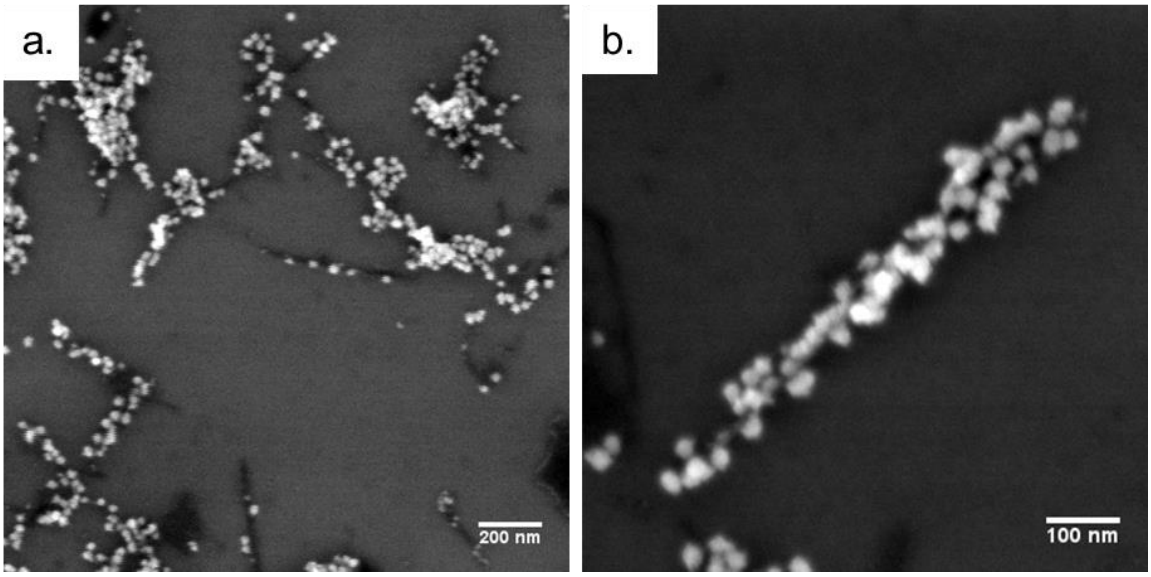

Figure 54. Representative SEM image of NiNS-BCNCs synthesized in the presence of PVP stabilizing agent in a quiescent solution.

As determined from SEM analysis, the resulting particles were better dispersed, but had varying levels of patchy Ni coverage. The observed non-uniformity in Ni coatings was attributed to either an insufficient Ni^{2+} to Pt-BCNCs ratio or to an inhomogeneous distribution of precursor ions during reduction. Experiments were conducted to determine the effect of each. Firstly, the effect of increasing Pt-BCNCs concentration on the morphology of the Ni coatings was studied conducted. The compositions of electroless plating solutions for these trials are presented in **Table 6**.

Table 6. Composition of electroless plating solutions for trials 1-3

Trial	$NiCl_2$ (µL)	N_2H_4 (µL)	PVP (µL)	H_2O (mL)	Pt-BCNCs (µL)
1	12	90	250	2.00	125
2	12	90	250	1.75	250
3	12	90	250	1.50	500

Representative images of Ni coated bacterial cellulose particles synthesized with increasing amounts of Pt-BCNCs as shown in **Table 6** are presented in **Figure 55.** All trials resulted in Ni deposition onto Pt-BCNCs. Ni coverage was found to comparable between trials 1 and 2, with particles from trial 2 having generally thinner coatings. However, variation in coating thickness was observed in both trials and coatings were composed of many distinct Ni nanoparticles covering the surfaces of BCNCs. Upon increasing the amount of Pt-BCNCs to 500 µL, Ni coverage became more non-uniform across Pt-BCNC particles. Some Pt-BCNCs showed extremely thick Ni coatings while others were found to have only a few Ni particles along their length (**Figure 55e, f**), suggesting that the amount of Pt-BCNCs was greater than the amount of Ni particles that could be uniformly nucleated from solution under present conditions. The results of these trials suggested that the amount of the Pt-BCNC suspension used must below 500 µL and that mixing of the electroless plating solution is likely required to achieve Ni coatings of a uniform thickness. An additional issue identified in the course of these trials was the difficulty of removing excess PVP from the synthesized particles. Even though PVP is a water-soluble polymer, extensive washing and centrifugation cycles were needed to remove the residual PVP. If not removed, the residual PVP obscured Ni coated BCNCs during SEM observations.

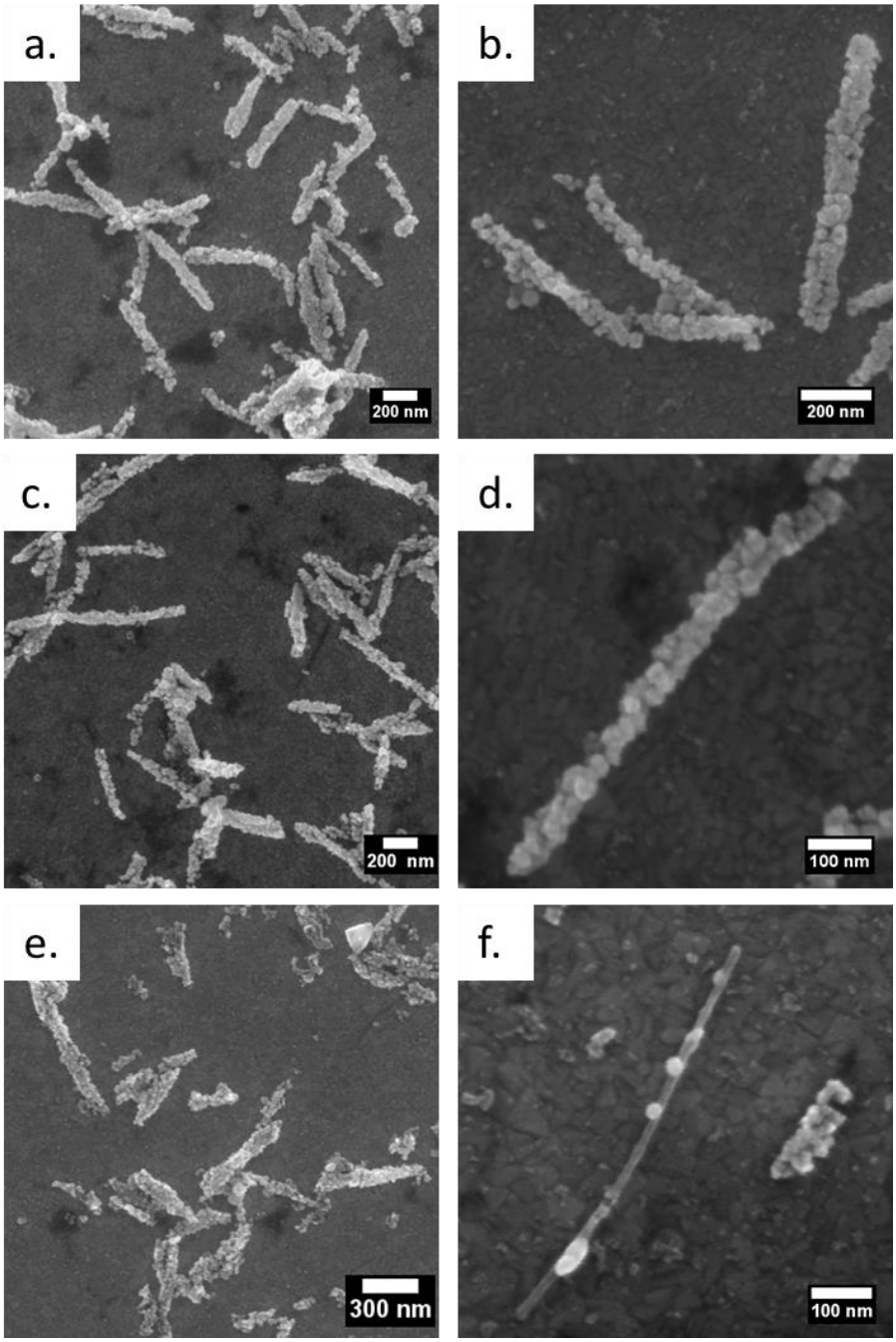

Figure 55. Representative images of NiNS-BCNCs resulting from the synthesis trials listed in Table 6: (a, b) trial 1, (c, d) trial 2, and (e, f) trial 3.

Thus, subsequent trials described below were conducted without the addition of PVP, but with vigorous solution agitation provided by a magnetic stir bar.

The effects of $NiCl_2$ concentration on Ni coating morphology were studied in trials 4-6, with the plating solution compositions detailed in **Table 7**.

Table 7. Compositions of electroless plating solutions for trials 4-6

Trial	$NiCl_2$ (µL)	N_2H_4 (µL)	H_2O (mL)	Pt-BCNCs (mL)
4	40	540	12.92	1.50
5	60	540	12.90	1.50
6	80	540	12.88	1.50

SEM images of NiNS-BCNCs synthesized with 40 µL, 60 µL, and 80 µL of Ni_2Cl are presented in **Figure 56**. The NiNS-BCNCs remained dispersed during these synthesis trials, which proved that stirring of the plating solution during reduction is sufficient to prevent gross particle agglomeration. Ni coverage of the BCNCs increased with $NiCl_2$ concentration and the coatings became thicker. Although the coatings had rough surfaces, coating uniformity was found to be more consistent across NiNS-BCNCs synthesized with magnetic stirring. This suggested that a homogeneous distribution of Ni precursor ions is essential for uniform Ni deposition. No adverse effects, such as agglomeration and uneven Ni deposition, were observed to be caused by the rotating magnetic field of the stir plate magnet; this was likely due to the short reaction times and the relationship between the magnetic moment of individual NiNS-BCNCs increasing with the coating thickness. The agitation provided by the magnetic stir bar may have also helped counteract any magnetic attraction of particles towards the stir plate and the stir bar.

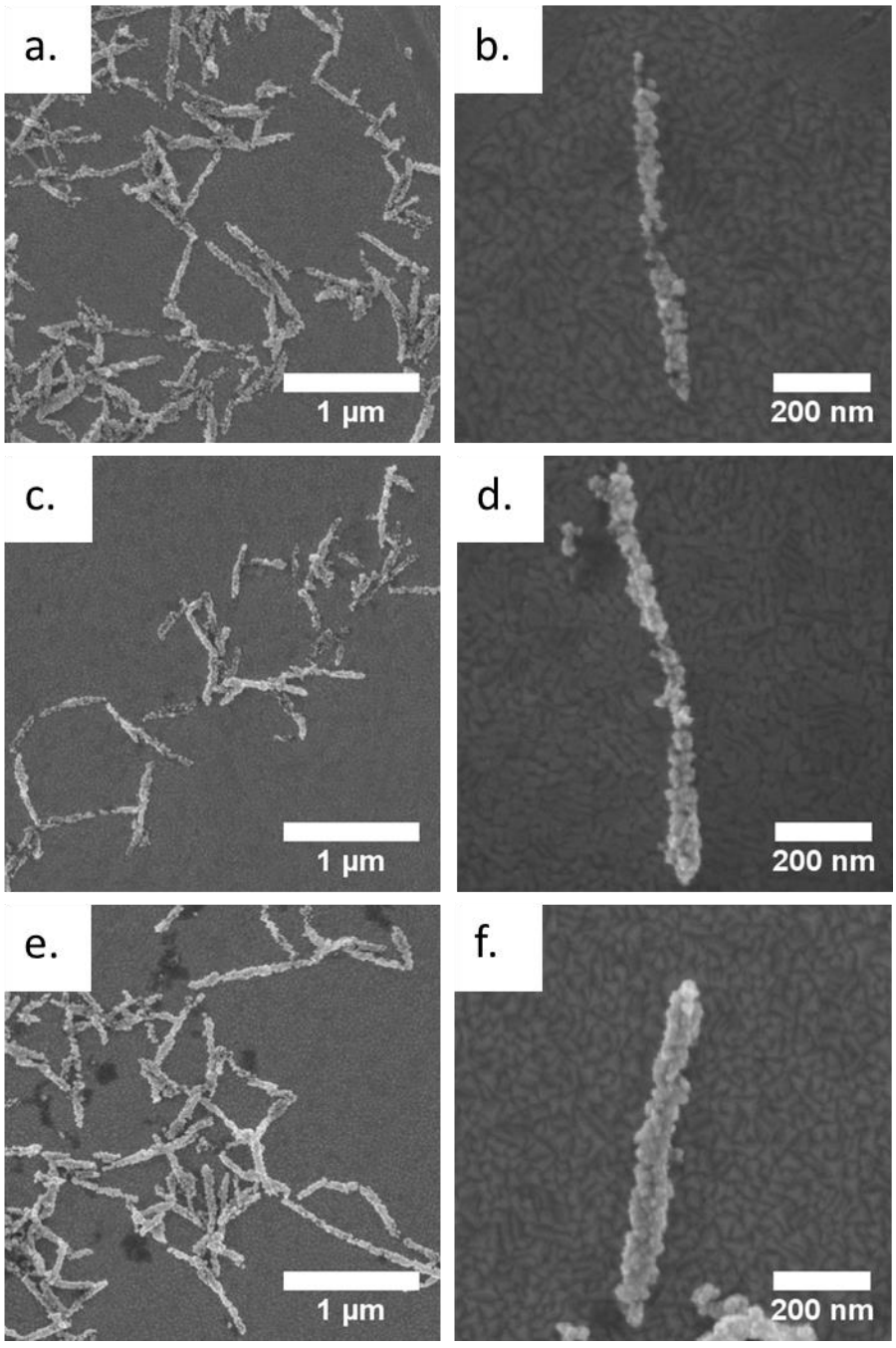

Figure 56. Representative images of NiNS-BCNCs resulting from the synthesis trials listed in Table 7. (a, b) trial 4, (c, d) trial 5 (e, f) trial 6. All samples were reacted at 80°C for 10 minutes in a stirred solution.

The morphology and nanostructure of a Ni coating grown from a solution containing 70 uL of $NiCl_2$ was analyzed with high resolution transmission electron microscopy (HRTEM). A representative image of this analysis is presented in **Figure 57**.

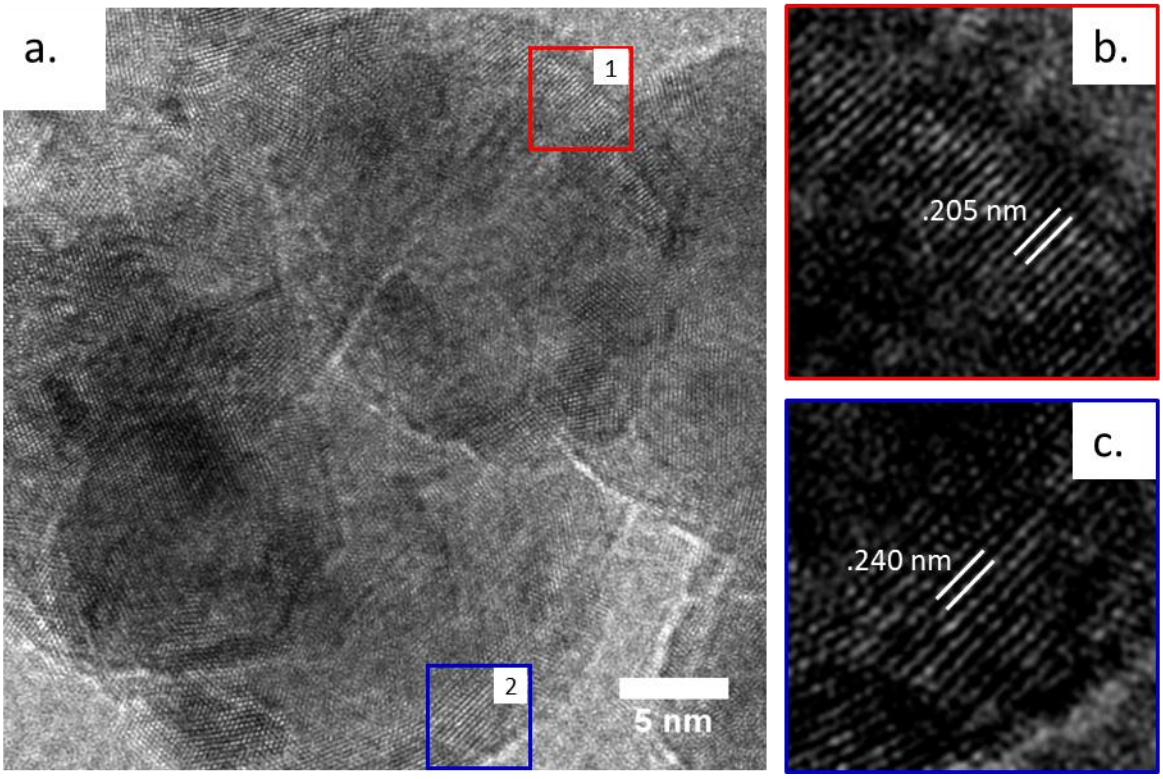

Figure 57. HRTEM analysis of Ni coating grown on Pt-BCNCs using 70 uL of $NiCl_2$. Magnified and FFT filtered images of areas 1 and 2 in (a) were identified as FCC lattices of Ni (b) and NiO (c) from their interplanar spacings of 0.205 nm and 0.240 nm respectively, which corresponds to the spacing between (111) planes in both lattices.

The nickel coating was found to consist of many Ni nanoparticles with an average diameter of ≈20 nm and individual Ni nanoparticles consisted of several nanograins as evidenced by observed lattice fringes with varying orientations, confirming the polycrystalline nature of the coating. The grain size was estimated to be roughly 5 nm. In **Figure 57b, c**, fast Fourier transform (FFT) filtered images of areas 1 and 2 allowed for the measurement of lattice

spacing, with a value of 0.205 nm for area 1 (**Figure 57b**) and 0.240 nm for area 2 (**Figure 57c**), corresponding to distances between the (111) planes of Ni and NiO, respectively. The presence of NiO grains indicated that the NiNS-BCNCs were likely oxidized during synthesis and washing steps. Since NiO is antiferromagnetic, extensive oxidation would greatly reduce the net magnetic moment of NiNS-BCNCs, and future syntheses should either incorporate capping/coating agents or be carried out in an organic solvent, such as ethylene glycol, to slow and prevent oxidation of the Ni coatings.

Since the NiNS-BCNC particles are bimetallic in nature, electron dispersive spectroscopy (EDS) analysis was conducted to estimate the Ni/Pt ratio. Analysis of particles with complete Ni coatings (those synthesized with 75 µL of $NiCl_2$) (**Figure 58**) yielded an average Ni/Pt mass ratio of 13.3 ± 1.0. Carbon and oxygen were also detected and attributed largely to BCNCs and the graphite substrate, although some of the oxygen signal possibly originated from a thin NiO passivation layer as was detected in HRTEM. However, this cannot be confirmed with certainty since the electron beam penetration depth would also sample the bacterial cellulose nanocrystals.

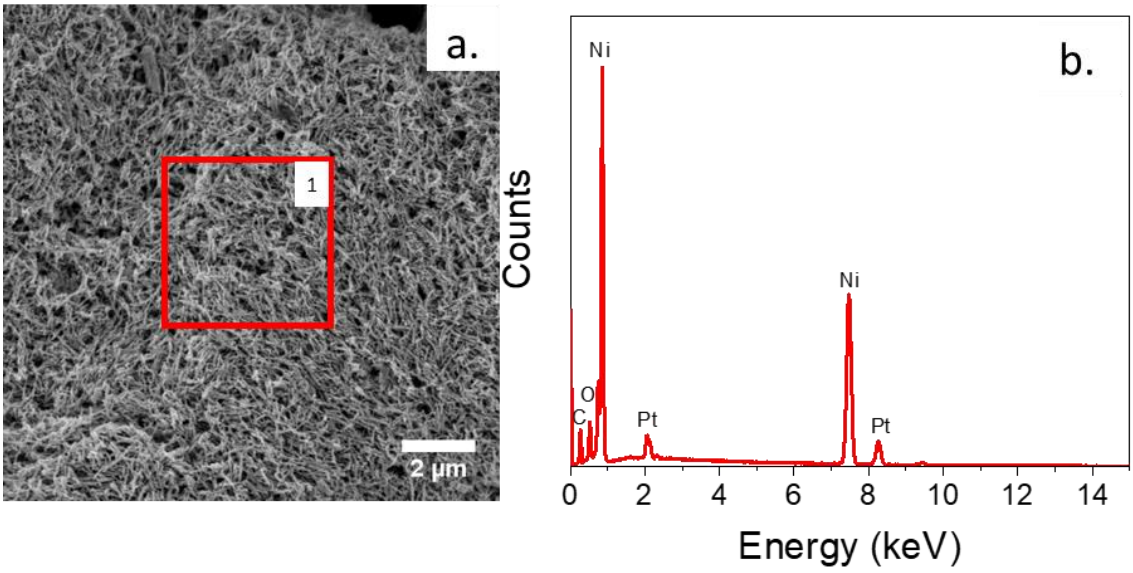

Figure 58. EDS analysis of NiNS-BCNCs synthesized with 75 µL of $NiCl_2$. (a) SEM image of a large agglomeration of NiNS-BCNCs (b) EDS spectrum collected from area 1 in (a).

It is useful to note that the Ni/Pt ratio can also be easily tuned by adjusting the coating thickness/coverage, which could be found beneficial for catalysis applications where the synergistic effects of bimetallic Ni-Pt nanoparticles can be exploited.[29] Interestingly, the porous structure of the NiNS-BCNC agglomerates were reminiscent of cellulose nanocrystal aerogels, having a high surface and highly interconnected porosity. Such porous Ni foams are of great interest for energy storage applications including Li-ion batteries[30] and supercapacitors,[31] and future work is needed to investigate the potential for magnetic assembly of NiNS-BCNC foams for use as active material supports in energy storage applications.

4.4.3 Magnetic Properties

The strong magnetic response of the NiNS-BCNCs was apparent from visual observation of the attraction of NiNS-BCNCs, dispersed in water, to a permanent magnet

as demonstrated in **Figure 59**. Suspended NiNS-BCNCs collected near the permanent magnet within minutes, leaving behind a clear solution.

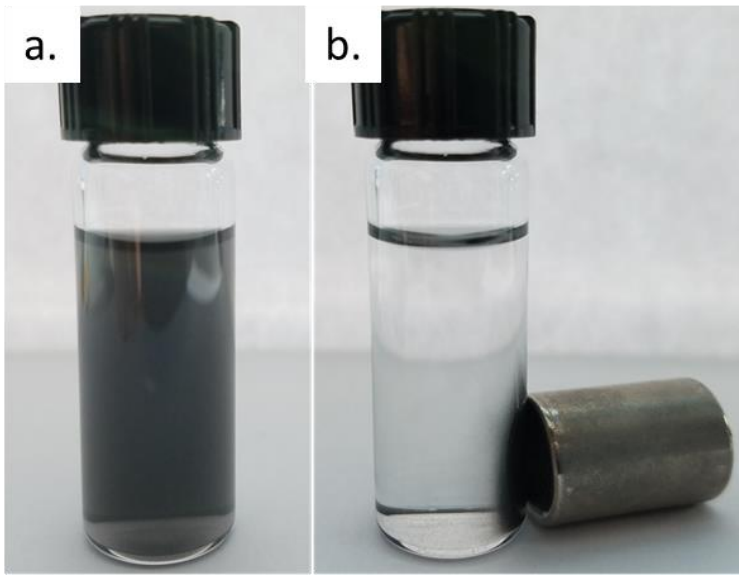

Figure 59. NiNS-BCNCs dispersed in water before (a) and after (b) the introduction of a permanent magnet.

The magnetic behavior of these NiNS-BCNCs was measured using a superconducting quantum interference device (SQUID) magnetometer at 5 K. The measurements were conducted with the help of Eric Drew (Zhang Group, Georgia Institute of Technology, Atlanta, GA). Magnetization versus magnetic field plots (i.e., M-H hysteresis loops) for NiNS-BCNCs grown with 75 µL of $NiCl_2$ are shown in **Figure 60**. At 5 K, the saturation magnetization (M_s) reached 42 emu/g at 50 kOe, corresponding to an effective moment of 0.44 μ_B per Ni atom. This value is 27% lower than the reported bulk value of 0.602 μ_B per Ni atom at 300K.[1] The remnant magnetization (M_r) and coercivity (H_c) values were 13.6 emu/g and 703 Oe. These magnetic measurements were attained by normalizing the magnetization values by the mass of the sample which included the Ni coatings, Pt nanoparticles, and the BCNCs. The inclusion of the mass of nonmagnetic components can

lead to underestimation M_s and M_r values. However, in this case, the expected effect is likely to be marginal, due the much higher density of Ni (8.9 g/cm^3) compared to cellulose (1.5 g/cm^3) and the small amount of Pt, shown to be roughly 13 times lower than Ni as determined from EDS analysis. Consequently, the reported values were directly compared to values reported in literature for similar Ni nanostructures in literature and are listed in **Table 8**.

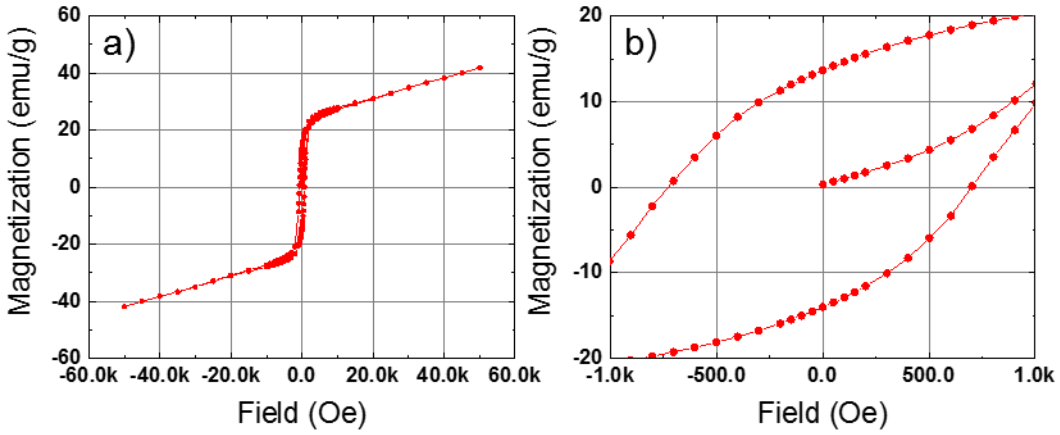

Figure 60. (a) Magnetization versus field plot for NiNS-BCNCs (75 µL $NiCl_2$) at 5 K. (b) Enlargement of plot in (a) around the origin.

Table 8. Saturation magnetization and coercivity values for various Ni nanoparticles measured at 5 K.

Particle	Diam. (nm)	Ms (emu/g)	Hc (Oe)
NiNS-BCNCs	65	42	703
Ni Nanochains[32]	75	49	305
Ni Nanowires[33]	70	45	382
Ni Nanorods[1]	4	60	275

The value for M_s of NiNS-BCNCs was found to be similar in magnitude to those reported for Ni nanochains and nanowires but was much lower than that of bulk Ni and small single crystalline Ni nanorods (M_s = 60 emu/g). However, the coercivity of NiNS-BCNCs was found to be nearly double the highest reported coercivity. The dependence of coercivity on grain size and Ni nanowire diameter has been studied by others,[14, 34-35] and the coercivity of anisotropic Ni nanowires have been shown to increase dramatically (up to 950 Oe[35]) with decreasing nanowire diameter.[14] This observation has been attributed to the tendency of fine-grained anisotropic nanoparticles to behave as single magnetic domains. Thus, the perceived coercivity enhancement in NiNS-BCNCs can be attributed to the unique synthesis method, which promoted the formation of many small Ni nanoparticles, along highly anisotropic BCNCs that quickly grew and impinged on their neighbors, limiting their final size.

The nanorod-like geometry of NiNS-BCNCs lends itself towards magnetic field induced self-assembly. Assemblies of similar shape-anisotropic magnetic nanoparticles have been shown to result in materials with direction dependent magnetic properties.[11, 36] As has been observed for other elongated nanoparticles,[37] NiNS-BCNCs dispersed in suspension tended to align with their longitudinal axis parallel to the external magnetic field. Such behavior is attributed to the magnetization of domains along a particles' easy axis, typically the long axis for nanowires and nanorods.[1, 13, 38] An example of this is shown in **Figure 61a-b**, where NiNS-BCNCs were deposited onto a Si substrate in the presence of a magnetic field. The NiNS-BCNCs were observed to preferentially orient themselves along the direction of the magnetic field lines. In contrast, NiNS-BCNCs deposited in the

absence of a magnetic field **Figure 61c-d** showed no preferred orientation and were randomly distributed on the substrate.

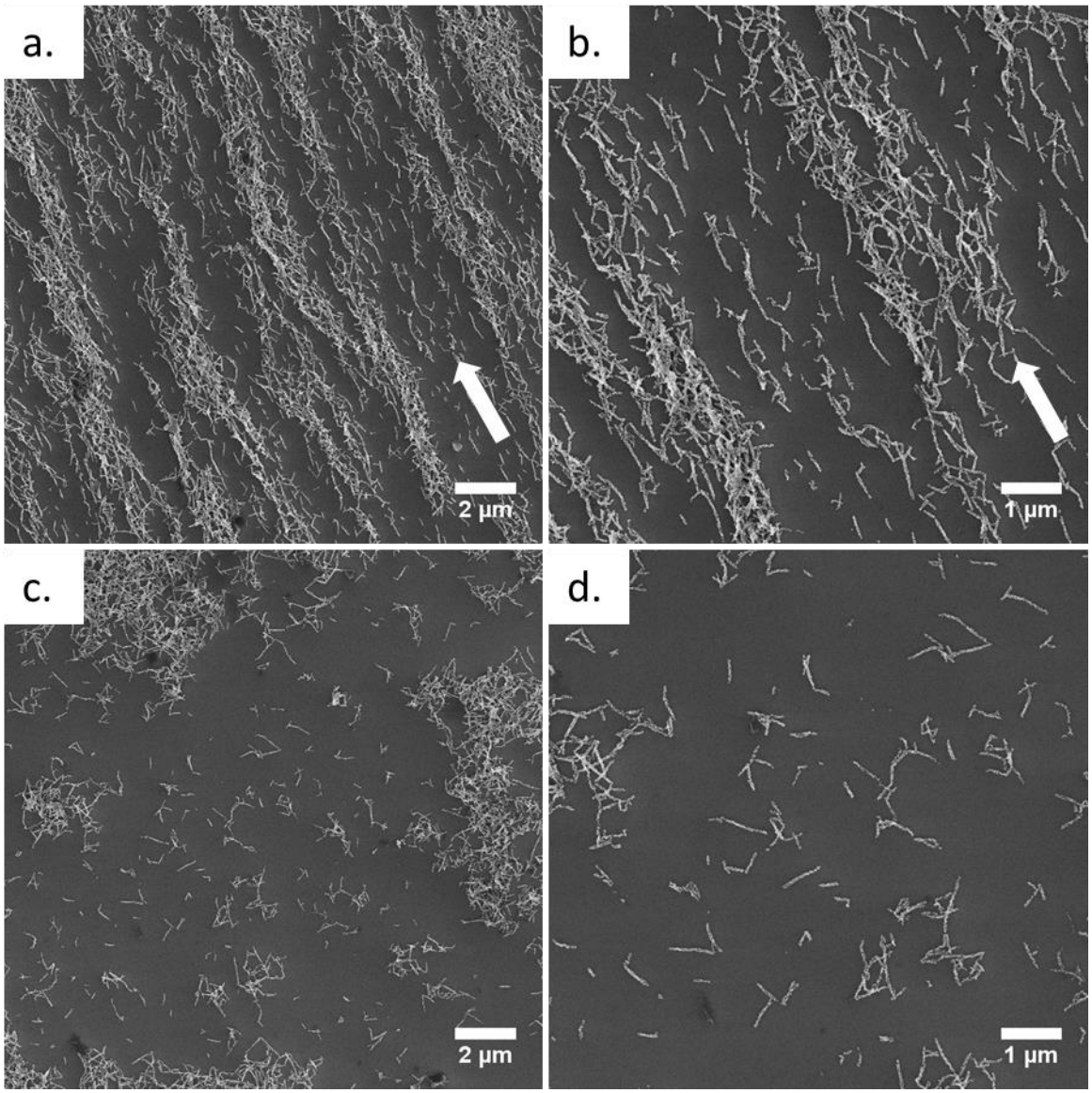

Figure 61. (a-b) Alignment of NiNS-BCNCs deposited onto a Si substrate in the presence of an external magnetic field (white arrow designates magnetic field direction, distance between magnet faces was 35 mm) (c-d) Random orientation of NiNS-BCNCs deposited in the absence of an external magnetic field.

The alignment of magnetic domains along the length of NiNS-BCNCs causes particles to behave as individual magnets with a north and south pole. Deposition of particles from

dilute suspensions, made it evident that these small magnets preferentially seek out and connect to their neighbors in a head-to-tail arrangement (**Figure 62a**).This resulted in the self-assembly of long NiNS-BCNCs chains, resembling Ni nanowires that were tens of micrometers in length, as shown in **Figure 62b**. It was also found that the diameter of such nanowires could be tuned by adjusting the strength of the external magnetic field as well as the concentration of NiNS-BCNC suspensions. Weaker magnetic fields, which are characterized by low magnetic flux line density, resulted in the assembly of thin nanowires that covered a larger surface area of the substrate, while stronger fields resulted in wider nanowires that spanned longer distances as demonstrated in **Figure 63**. Similar effects were observed by increasing the concentration of NiNS-BCNC suspensions as demonstrated in **Figure 64a, b**.

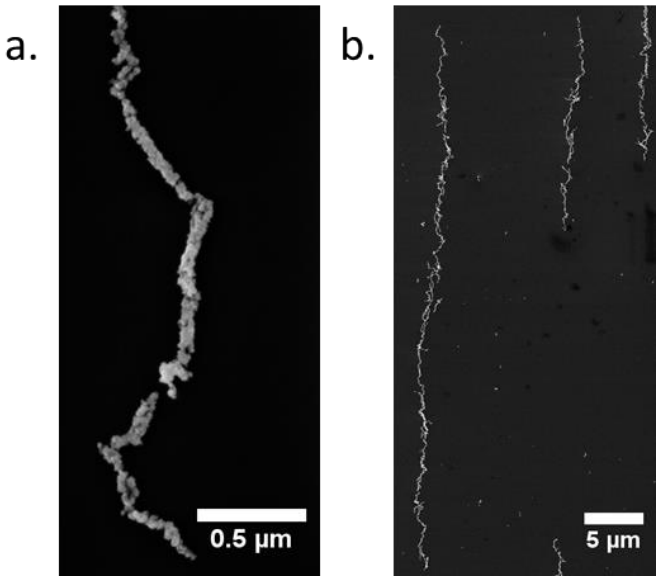

Figure 62. SEM images of NiNS-BCNCs deposited from dilute suspensions showing head-to-tail alignment in the presence of an external magnetic field. (a) Detailed view, (b) self-assembled Ni nanowires.

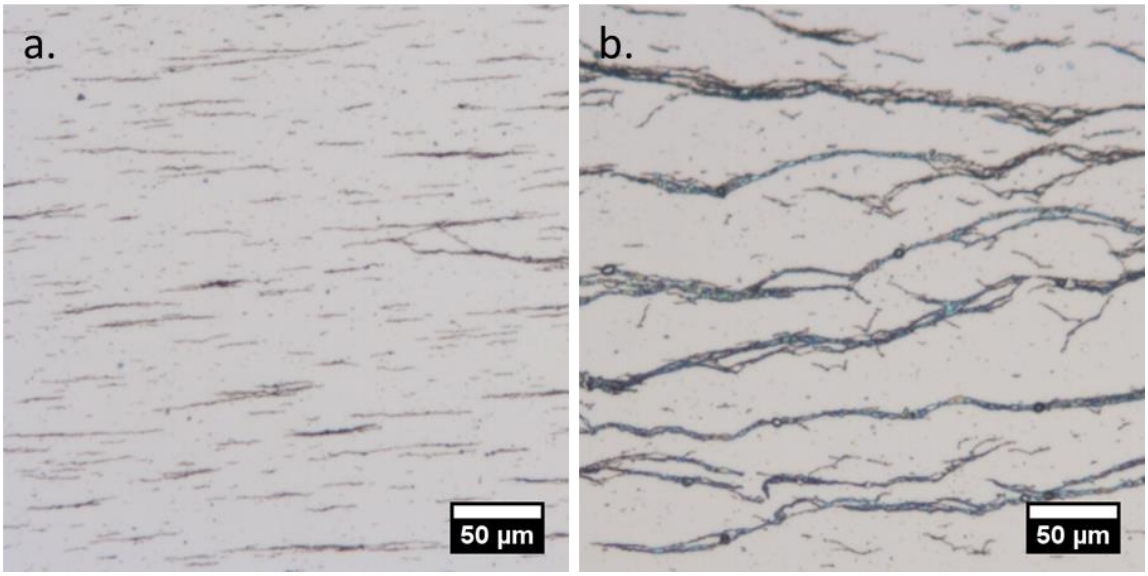

Figure 63. Optical images of NiNS-BCNC nanowires self-assembled in the presence of an external magnetic field of varying strength. The magnetic field strength was modified by changing the spacing between two neodymium magnets. The spacing in (a) was 45 mm and in (b) 35 mm.

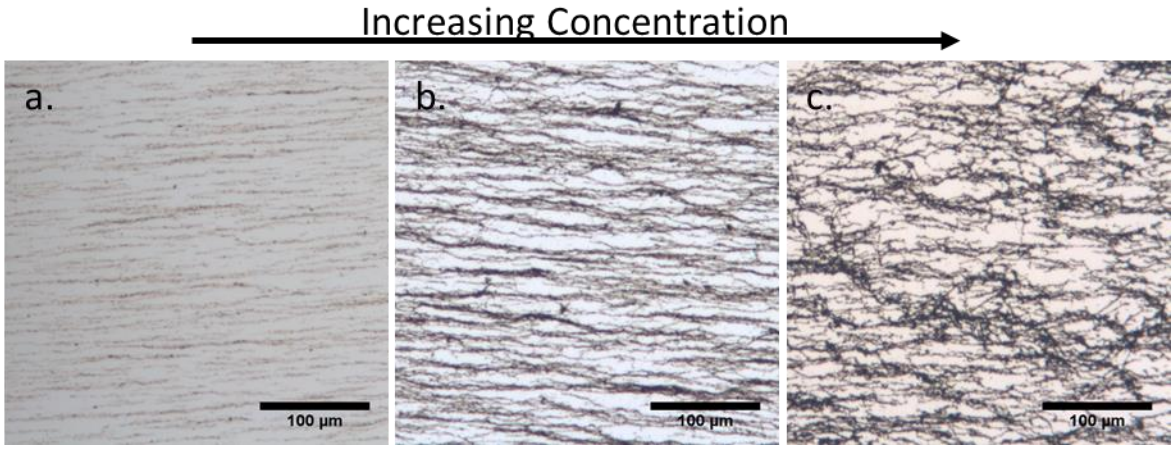

Figure 64. Optical images of NiNS-BCNCs aligned in a constant magnetic field (magnet separation of 35 mm) but deposited from increasingly concentrated NiNS-BCNC suspensions (a) 0.1 mg/mL (b) 0.5 mg/mL and (c) 1 mg/mL.

However, the extent of alignment decreased with increasing concentration due to an increase in interparticle interactions that hindered the mobility of individual NiNS-BCNCs. For samples deposited from highly concentrated NiNS-BCNC suspensions, particle

interactions led to the formation of partially aligned networks (**Figure 64c)** instead of nanowires.

To demonstrate the versatility of magnetic alignment, NiNS-BCNCs were arranged into an intersecting grid pattern by rotating the substrate 90° between two sequential NiNS-BCNC depositions, as illustrated in **Figure 65**. As shown in **Figure 66**, this sequential deposition resulted in NiNS-BCNCs chains of varying diameters intersecting each other at approximately 90° angles. The controlled deposition of NiNS-BCNCs into ordered grid patterns could potentially be useful for fabrication of thin electrodes on flexible substrates as has been recently demonstrated for Ag nanowires.[39]

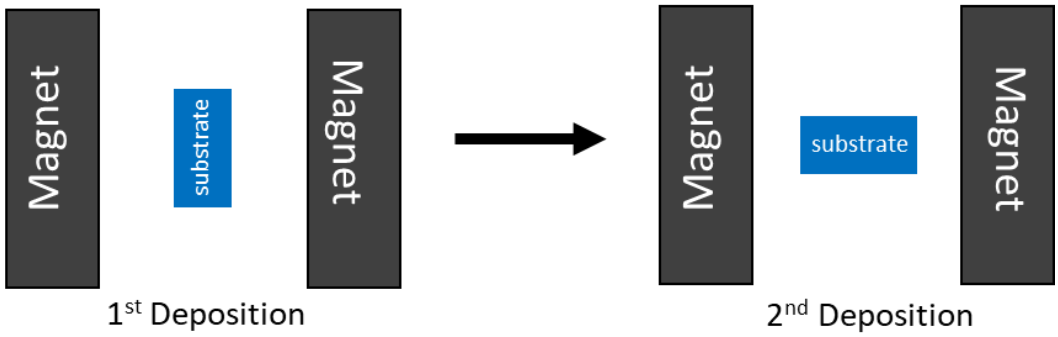

Figure 65. Schematic illustrating the method for used to direct the self-assembly of NiNS-BCNCs nanowires into an intersecting grid pattern.

It was discovered that NiNS-BCNCs with random particle orientations could be uniformly deposited onto a substrate by allowing the deposited suspension to dry in the presence of a rotating magnetic field (i.e., on a laboratory stir plate). An example of this is shown in **Figure 67**. These examples demonstrate the ability to control the self-assembly of NiNS-BCNCs using simple process parameters (i.e., magnetic field strength/orientation and suspension concentration).

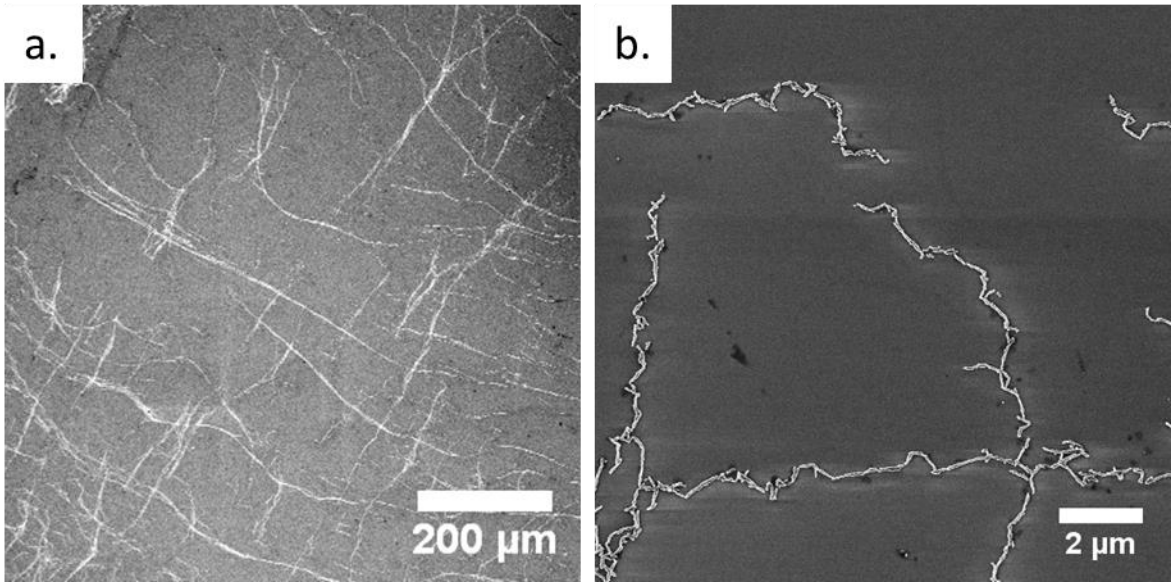

Figure 66. SEM images of an intersecting grid pattern produced by depositing NiNS-BCNCs on a substrate, which was rotated 90° between two sequential depositions. (a) Low magnification image showing long range arrangement (b) High magnification image showing details of intersecting self-assembled nanowires.

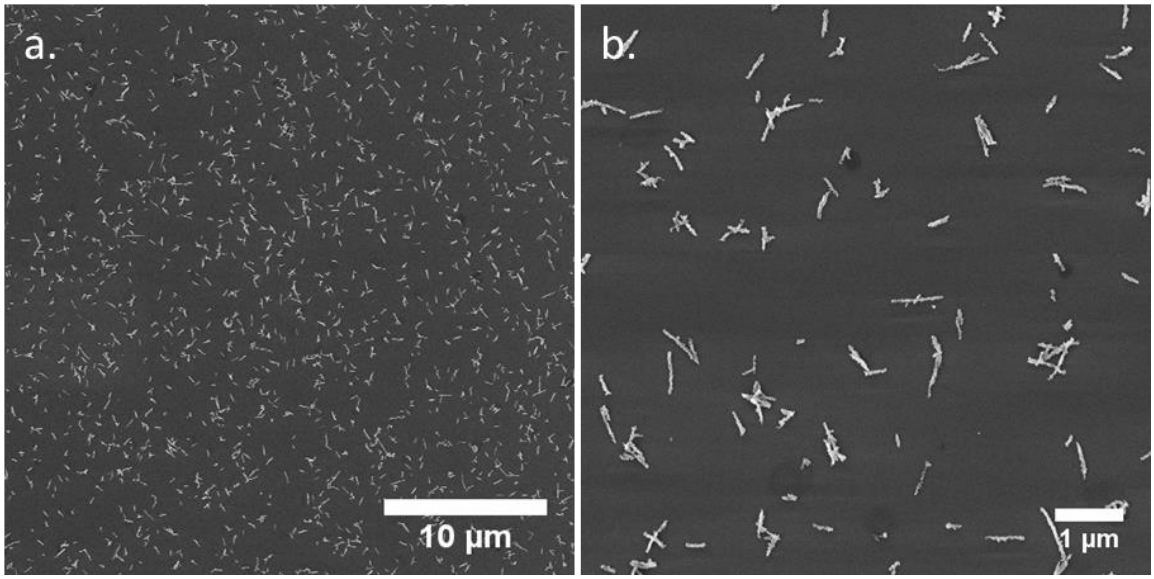

Figure 67. SEM images of randomly oriented NiNS-BCNCs deposited from suspension onto a Si substrate in the presence of a rotating magnetic field generated by the magnet of a laboratory stir plate.

4.5 Conclusions

In this chapter, the knowledge gained from learning how to functionalize, disperse, and coat CNCs with gold was applied to a new material system to generate magnetic nickel nanoshell-bearing BCNCs, demonstrating the versatility of the developed methods. Small platinum nanoparticles (<3 nm) were synthesised and uniformly attached to aminated BCNCs via a sequential incubation process. The adsorption of Pt nanoparticles onto BCNC surfaces was monitored using UV-vis spectroscopy. Saturation of the aminated BCNC surfaces was indicated by the lack of change in the absorbance spectrum after the 4^{th} incubation cycle and by the appearance of an absorption shoulder at 280 nm in the Pt-decorated BCNC suspensions, which is associated with the increase in Pt nanoparticle size. TEM analysis of the Pt-decorated BCNCs did not indicate Pt nanoparticle agglomeration, but instead revealed dense and uniform assemblies of individual Pt particles on the surface of BCNCs. This uniform coverage was a testament to the surface functionalization protocol developed in **Chapter 1**, as it demonstrated the level of uniformity and completeness with which the developed functionalization process was able to modify the BCNCs surfaces. Ni coatings were then deposited onto Pt-decorated BCNCs by electroless deposition, using a Ni-hydrazine plating bath. Electroless deposition trials coupled with SEM analysis revealed the need for stabilizing agents and strong agitation during electroless deposition. Otherwise, large Ni-BCNCs agglomerates was were found to form. Analysis of the Ni coatings with HRTEM revealed that they were composed of interconnected nanocrystalline Ni particles. Lattice spacing analysis indicated the presence of Ni and NiO, the latter of which was likely formed during washing cycles that exposed the particles to water and air. The magnetic properties of NiNS-BCNCs were studied with SQUID magnetometry, which

indicated that NiNS-BCNCs were ferromagnetic, with a M_s value of 42 emu/g at 5 K, which was comparable to Ni nanoparticles of similar morphology. However, NiNS-BCNCs showed greatly enhanced coercivity (H_c = 703 Oe), which was nearly double that of values reported in the literature for nickel nanorods and nanowires. This enhancement was attributed to the anisotropic geometry of NiNS-BCNCs and the nanosized grain structure of the Ni coatings, both of which have been shown to favor the establishment of single magnetic domains. Magnetic field-induced self-assembly was investigated by depositing NiNS-BCNC suspensions onto Si substrates in the presence of an external magnetic field established by two neodymium magnets, with their opposite poles separated by a fixed distance. Upon exposure to the magnetic field, NiNS-BCNCs formed long chains resembling Ni nanowires. The diameter of the self-assembled nanowires could be tuned by changing the magnetic field strength or the concentration of NiNS-BCNCs suspensions. Stronger magnetic fields and higher concentration suspensions resulted in larger diameter self-assembled nanowires. However, at high particle concentrations (>1 mg/ml) interparticle interactions hindered the alignment of individual NiNS-BCNCs and caused the deposition of particle networks of reduced alignment. As a demonstration of control over the self-assembly process, grid-like patterns of NiNS-BCNC nanowires were constructed through simple sequential deposition using magnetic fields of varied orientation. In contrast, uniform deposition of randomly oriented particles was achieved through the use of a rotating magnetic field (i.e., laboratory stir plate).

While this chapter has been focused on the conformal coating of BCNCs with nickel, the knowledge gained is applicable across a wide range of material systems. The demonstrated ability to generate BCNCs with highly uniform and dense coverage of metal

nanoparticles is likely to be highly attractive for catalysis applications, where stabilization of fine catalytic particles against agglomeration is paramount, as it preserves the benefits of using nanoparticles (i.e., high surface area and catalytic activity). The sequential incubation methodology developed here is not limited to a single type of nanoparticle and can be expanded to include other metals, which could be advantageous for generating bimetallic catalysts, which are being actively researched for their synergistic effects on catalytic performance.[29] The unique ability for NiNS-BCNCs to self-assemble into well aligned nanowires in the presence of external magnetic fields may be useful in the future manufacture of transparent conductive electrodes, as has been recently demonstrated in literature reports.[40-41] Additional work is needed to investigate the possibility of using NiNS-BCNCs in applications such as functional nanocomposites[42-43] and smart-materials.[44-45]

4.6 References

[1] Cordente, N.; Respaud, M.; Senocq, F.; Casanove, M.-J.; Amiens, C.; Chaudret, B., Synthesis and Magnetic Properties of Nickel Nanorods. *Nano Letters* **2001,** *1* (10), 565-568.

[2] Sanles-Sobrido, M.; Banobre-Lopez, M.; Salgueirino, V.; Correa-Duarte, M. A.; Rodriguez-Gonzalez, B.; Rivas, J.; Liz-Marzan, L. M., Tailoring the magnetic properties of nickel nanoshells through controlled chemical growth. *Journal of Materials Chemistry* **2010,** *20* (35), 7360-7365.

[3] Terris, B. D.; Thomson, T., Nanofabricated and self-assembled magnetic structures as data storage media. *Journal of Physics D: Applied Physics* **2005,** *38* (12), R199.

[4] Reiss, G.; Hütten, A., Applications beyond data storage. *Nature Materials* **2005,** *4*, 725.

[5] Bruce, I. J.; Sen, T., Surface Modification of Magnetic Nanoparticles with Alkoxysilanes and Their Application in Magnetic Bioseparations. *Langmuir* **2005,** *21* (15), 7029-7035.

[6] Bao, F.; Yao, J.-L.; Gu, R.-A., Synthesis of Magnetic Fe2O3/Au Core/Shell Nanoparticles for Bioseparation and Immunoassay Based on Surface-Enhanced Raman Spectroscopy. *Langmuir* **2009,** *25* (18), 10782-10787.

[7] Zhang, D.; Wei, S.; Kaila, C.; Su, X.; Wu, J.; Karki, A. B.; Young, D. P.; Guo, Z., Carbon-stabilized iron nanoparticles for environmental remediation. *Nanoscale* **2010,** *2* (6), 917-919.

[8] Tang, S. C. N.; Lo, I. M. C., Magnetic nanoparticles: Essential factors for sustainable environmental applications. *Water Research* **2013,** *47* (8), 2613-2632.

[9] Arruebo, M.; Fernández-Pacheco, R.; Ibarra, M. R.; Santamaría, J., Magnetic nanoparticles for drug delivery. *Nano Today* **2007,** *2* (3), 22-32.

[10] Na, H. B.; Song, I. C.; Hyeon, T., Inorganic Nanoparticles for MRI Contrast Agents. *Adv. Mater.* **2009,** *21* (21), 2133-2148.

[11] Hoffelner, D.; Kundt, M.; Schmidt, A. M.; Kentzinger, E.; Bender, P.; Disch, S., Directing the orientational alignment of anisotropic magnetic nanoparticles using dynamic magnetic fields. *Faraday Discussions* **2015,** *181* (0), 449-461.

[12] Grzelczak, M.; Rodríguez-González, B.; Pérez-Juste, J.; Liz-Marzán, L. M., Quasi-Epitaxial Growth of Ni Nanoshells on Au Nanorods. *Adv. Mater.* **2007,** *19* (17), 2262-2266.

[13] Searson, L. S. a. Y. H. a. C.-C. a. P. C., Tuning the properties of magnetic nanowires. *IBM Journal of Research and Development* **2005,** *49* (1), 79-102.

[14] Whitney, T. M.; Jiang, J. S.; Searson, P. C.; Chien, C. L., Fabrication and Magnetic Properties of Arrays of Metallic Nanowires. *Science* **1993,** *261* (5126), 1316-1319.

[15] Tian, F.; Chen, J.; Zhu, J.; Wei, D., Magnetism of thin polycrystalline nickel nanowires. *Journal of Applied Physics* **2008,** *103* (1), 013901.

[16] Rioux, R. M.; Song, H.; Hoefelmeyer, J. D.; Yang, P.; Somorjai, G. A., High-Surface-Area Catalyst Design: Synthesis, Characterization, and Reaction Studies of Platinum Nanoparticles in Mesoporous SBA-15 Silica. *The Journal of Physical Chemistry B* **2005,** *109* (6), 2192-2202.

[17] Cohen, R. L.; West, K. W., Generative and Stabilizing Processes in Tin-Palladium Sols and Palladium Sol Sensitizers. *Journal of The Electrochemical Society* **1973,** *120* (4), 502-508.

[18] E. Matijević, A. M. P. a. P. Z., The Characterization of the Stannous Chloride/ Palladium Chloride Catalysts for Electroless Plating. *Plating and Surface Finishing* **1975,** *61* (10), 958-965.

[19] Osaka, T.; Takematsu, H.; Nihei, K., A Study on Activation and Acceleration by Mixed PdCl2 / SnCl2 Catalysts for Electroless Metal Deposition. *Journal of The Electrochemical Society* **1980,** *127* (5), 1021-1029.

[20] Brandow, S. L.; Chen, M. S.; Wang, T.; Dulcey, C. S.; Calvert, J. M.; Bohland, J. F.; Calabrese, G. S.; Dressick, W. J., Size-Controlled Colloidal Pd(II) Catalysts for Electroless Ni Deposition in Nanolithography Applications. *Journal of The Electrochemical Society* **1997,** *144* (10), 3425-3434.

[21] Gharibshahi, E.; Saion, E., Influence of Dose on Particle Size and Optical Properties of Colloidal Platinum Nanoparticles. *International Journal of Molecular Sciences* **2012,** *13* (11), 14723.

[22] Gharibshahi, E.; Saion, E.; Ashraf, A.; Gharibshahi, L., Size-Controlled and Optical Properties of Platinum Nanoparticles by Gamma Radiolytic Synthesis. *Applied Radiation and Isotopes* **2017,** *130*, 211-217.

[23] Chen, D.-H.; Hsieh, C.-H., Synthesis of nickel nanoparticles in aqueous cationic surfactant solutions. *Journal of Materials Chemistry* **2002,** *12* (8), 2412-2415.

[24] Eluri, R.; Paul, B., Synthesis of nickel nanoparticles by hydrazine reduction: mechanistic study and continuous flow synthesis. *J Nanopart Res* **2012,** *14* (4), 800.

[25] Wu, S.-H.; Chen, D.-H., Synthesis and characterization of nickel nanoparticles by hydrazine reduction in ethylene glycol. *Journal of Colloid and Interface Science* **2003,** *259* (2), 282-286.

[26] Park, J. W.; Chae, E. H.; Kim, S. H.; Lee, J. H.; Kim, J. W.; Yoon, S. M.; Choi, J.-Y., Preparation of fine Ni powders from nickel hydrazine complex. *Materials Chemistry and Physics* **2006,** *97* (2), 371-378.

[27] Wiley, B.; Sun, Y.; Mayers, B.; Xia, Y., Shape-Controlled Synthesis of Metal Nanostructures: The Case of Silver. *Chemistry – A European Journal* **2005,** *11* (2), 454-463.

[28] Jiang, P.; Li, S.-Y.; Xie, S.-S.; Gao, Y.; Song, L., Machinable Long PVP-Stabilized Silver Nanowires. *Chemistry – A European Journal* **2004,** *10* (19), 4817-4821.

[29] Yu, W.; Porosoff, M. D.; Chen, J. G., Review of Pt-Based Bimetallic Catalysis: From Model Surfaces to Supported Catalysts. *Chemical Reviews* **2012,** *112* (11), 5780-5817.

[30] Yu, Y.; Chen, C.-H.; Shui, J.-L.; Xie, S., Nickel-Foam-Supported Reticular CoO–Li2O Composite Anode Materials for Lithium Ion Batteries. *Angewandte Chemie International Edition* **2005,** *44* (43), 7085-7089.

[31] Kong, W.; Lu, C.; Zhang, W.; Pu, J.; Wang, Z., Homogeneous core–shell NiCo2S4 nanostructures supported on nickel foam for supercapacitors. *Journal of Materials Chemistry A* **2015,** *3* (23), 12452-12460.

[32] Lin, H.; Wangzhi, Z.; Wei, Z.; Honglin, D.; Chinping, C.; Lin, G., Size-dependent magnetic properties of nickel nanochains. *Journal of Physics: Condensed Matter* **2007,** *19* (3), 036216.

[33] Tang, S.; Vongehr, S.; Ren, H.; Meng, X., Diameter-controlled synthesis of polycrystalline nickel nanowires and their size dependent magnetic properties. *CrystEngComm* **2012,** *14* (21), 7209-7216.

[34] Chien, C. L., Granular magnetic solids (invited). *Journal of Applied Physics* **1991,** *69* (8), 5267-5272.

[35] Zheng, M.; Menon, L.; Zeng, H.; Liu, Y.; Bandyopadhyay, S.; Kirby, R. D.; Sellmyer, D. J., Magnetic properties of Ni nanowires in self-assembled arrays. *Physical Review B* **2000,** *62* (18), 12282-12286.

[36] Carlos, M. H.; Youngwoo, R.; Bongyoung, Y.; Eui-Hyeok, Y.; Nosang, V. M., Hierarchical magnetic assembly of nanowires. *Nanotechnology* **2007,** *18* (20), 205305.

[37] Hangarter, C. M.; Myung, N. V., Magnetic Alignment of Nanowires. *Chemistry of Materials* **2005,** *17* (6), 1320-1324.

[38] Zhou, Z. F.; Zhou, Y. C.; Pan, Y.; Wang, X. G., Growth of the nickel nanorod arrays fabricated using electrochemical deposition on anodized Al templates. *Materials Letters* **2008,** *62* (19), 3419-3421.

[39] De, S.; Higgins, T. M.; Lyons, P. E.; Doherty, E. M.; Nirmalraj, P. N.; Blau, W. J.; Boland, J. J.; Coleman, J. N., Silver Nanowire Networks as Flexible, Transparent, Conducting Films: Extremely High DC to Optical Conductivity Ratios. *ACS Nano* **2009,** *3* (7), 1767-1774.

[40] Rathmell, A. R.; Nguyen, M.; Chi, M.; Wiley, B. J., Synthesis of Oxidation-Resistant Cupronickel Nanowires for Transparent Conducting Nanowire Networks. *Nano Letters* **2012,** *12* (6), 3193-3199.

[41] Kim, J.; da Silva, W. J.; bin Mohd Yusoff, A. R.; Jang, J., Organic devices based on nickel nanowires transparent electrode. *Scientific Reports* **2016,** *6*, 19813.

[42] Burke, N. A. D.; Stöver, H. D. H.; Dawson, F. P., Magnetic Nanocomposites: Preparation and Characterization of Polymer-Coated Iron Nanoparticles. *Chemistry of Materials* **2002,** *14* (11), 4752-4761.

[43] Kao, J.; Thorkelsson, K.; Bai, P.; Rancatore, B. J.; Xu, T., Toward functional nanocomposites: taking the best of nanoparticles, polymers, and small molecules. *Chemical Society Reviews* **2013,** *42* (7), 2654-2678.

[44] Yoshida, M.; Lahann, J., Smart Nanomaterials. *ACS Nano* **2008,** *2* (6), 1101-1107.

[45] Ramanujan, R. V.; Lao, L. L., The mechanical behavior of smart magnet–hydrogel composites. *Smart Materials and Structures* **2006,** *15* (4), 952.

CHAPTER 5: SYNTHESIS OF ELECTICALLY CONDUCTIVE SILVER-COATED BACTERIAL CELLULOSE NANOCRYSTALS

5.1 Summary

BCNCs with thin, conformal, and continuous silver coatings have been generated. It was discovered that a critical gold nanoparticle/seed size was required to initiate heterogeneous nucleation of silver. Decorating BCNCs with the appropriately-sized gold nanoparticles resulted in uniformly deposited silver coatings. The resulting particles had optical properties reminiscent of AuNS-BCNCs with two surface plasmon resonance extinction bands centered at 450 nm and >1800 nm. The position of these bands was found to be sensitive to the silver coating thickness and could be tuned by adjusting the volume of electroless silver plating solution. The electroless silver deposition reaction was found to be scalable, which allowed for enough material to be generated for deposition of an electrically conductive coating on a polymeric filtration membrane.

5.2 Introduction

With the advent of portable electronics, thin, transparent, flexible, and conductive electronic substrates are a growing necessity. Recent advances in cellulosic nanomaterial production, characterization, and processing techniques have enabled researchers to investigate cellulose-based conductive composites as alternatives to traditional glass and polymer substrates.[1-4] Cellulose composites offer several advantages over traditional substrates because they are highly flexible, durable, lightweight, biodegradable, and renewable. The techniques for manufacturing conductive cellulosic nanocomposites

typically involve mixing cellulosic nanomaterials (i.e. nanocrystals or nanofibrils) with conductive materials such as metal nanoparticles, semiconducting metal oxides, or conductive polymers.[1, 5-6] The electrical conductivity of the resulting composites strongly depends on the nature of the conductive material as well as the morphology and alignment of the conductive phase. The ability of a conductive filler to impart electrical conductivity to a composite can be compared across materials and particle morphologies by analyzing the percolation threshold, which represents the volume loading at which a conductive filler forms an interconnected network throughout the matrix. This point is characterized by a rapid increase in the overall conductivity of the composite. It has been shown that by increasing the aspect ratio of a conductive nanofiller, the percolation threshold shifts to lower and lower volume fractions.[7-8] Using simulations, Kwon, et al. have shown that nanospheres must be present in excess of 20 volume percent to form percolated networks, while high aspect ratio nanoplates require less than a 10 percent loading.[7] However, high aspect ratio nanorods show the best performance and typically require less than a couple of volume percent to reach the percolation threshold, suggesting that nanofiller shape is one of the most important parameters when considering the electrical conductivity of nanocomposites.[7] It is for this reason carbon nanotubes[9] (CNTs) and silver nanowires[10] (AgNWs) are commonly studied conductive nanofillers today. Low percolation thresholds offer the additional benefit of enabling the fabrication of composites with high optical transparency. Although CNTs strongly absorb visible light, the amount of CNTs needed to form a conductive network allows for thin composite films to remain largely transparent.[11] On the other hand, the optical extinction bands of AgNWs, which lie at the limits of the

visible wavelength range, make AgNWs ideal for fabricating conductive composites with optical transparencies greater than 90%.[10, 12-13]

In a recent report, Koga, et al. have shown that the combination of cellulose nanofibrils and silver nanowires can produce optically transparent composites with conductivities of $\approx 10^3$ S cm^-, demonstrating the feasibility of paper based electronics.[14] The work detailed below aims to demonstrate that cellulosic nanomaterials can not only be used as the composite matrix, but can also be used as templates for synthesis of conductive 1-D nanoparticles because of their high aspect ratios. In a recent report by Meulendijks, et al., dip coating and photonic sintering were used to fabricate highly conductive films, consisting of silver nanoparticle-decorated cellulose nanocrystals.[5] However, the Ag coated CNC particles tended to form large agglomerated bundles, making them less than ideal for dispersal in polymeric matrices and eliminated the possibility of producing optically transparent coatings/composites. Thus, the goal of this work was to produce individually dispersed, silver-coated BCNCs, so that they could be easily incorporated into conductive nanocomposites and transparent electrodes.

5.3 Experimental Procedures

5.3.1 Synthesis of Gold Nanoparticles

A suspension of small gold nanoparticles was prepared using the procedure described in section **2.3.3**, with one minor modification: the amount of aged $HAuCl_4$ solution was increased to 2.0 mL (previously 1.9 mL) to produce gold nanoparticles with a slightly larger size ($\leq$ 5 nm). The THCP-NaOH solution quickly turned reddish-brown after the introduction of the Au ions, indicating the formation of gold nanoparticles with a

plasmon resonance absorption band around 520 nm. The synthesized gold particles were passed through a 0.1 μm syringe filter and stored at 4°C for a minimum of two weeks before use. The synthesized particles have an approximate shelf-life of 2 months, after which particle agglomeration becomes apparent.

5.3.2 Preparation of Gold Nanoparticle-Decorated BCNCs

Aminated bacterial cellulose nanocrystals were decorated with small gold nanoparticles (≤ 5 nm) using the sequential incubation procedure described in section **4.3.2**. This ensured the surfaces of the aminated BCNCs were saturated with gold nanoparticles. The gold decorated BCNCs were then diluted to an optical density of 0.12 as measured by a UV-vis spectrometer (UV-3101PC, Shimadzu, Kyoto, Japan) at 490 nm through a 1 cm optical path length. The dilute suspension of gold decorated BCNCs was sonicated (Branson 2510 ultrasonic bath, Branson Ultrasonic Corp., St. Louis, MO) for 1 hour to disperse any agglomerates that may have formed during previous centrifugation cycles.

5.3.3 Synthesis of Ag-Coated BCNCs

In a typical procedure, 200 μL of gold-decorated BCNC suspensions were mixed with an aqueous silver nitrate solution (0.15 mM, 5-10 mL) and 25 μL of formaldehyde (37 wt.% aqueous solution) in a 50 mL Erlenmeyer flask. The mixture was placed onto a magnetic stir plate and stirred at 1200 rpm. After a strong vortex was established, 50 μL of concentrated ammonium hydroxide (28 wt.%) was quickly added. The solution immediately took on a pale yellow color and was stirred for an additional 5 minutes before being centrifuged (3000 RCF, 10 minutes) and washed with DI water three times.

5.3.4 UV-Vis-NIR Spectroscopy

UV-visible-near-infrared extinction analyses were conducted with a spectrophotometer (UV-3101PC, Shimadzu, Kyoto, Japan) operating in the range of 300 nm to 1800 nm. Silver coated BCNCs were solvent exchanged from H_2O into deuterium oxide (D_2O) by centrifugation and dispersion. The use of D_2O red-shifted the strong absorbance bands of water further towards the infrared, extending the measurable NIR wavelength range from 1300 nm to 1800 nm. Spectra of suspensions were collected over a 1 cm path length using quartz cuvettes (108-QS, Hellma Analytics, Muellheim Germany).

5.3.5 Morphology and Composition Analyses

Scanning electron microscopy (SEM) was used to analyze the morphology of the synthesized silver coated BCNCs. Analysis was conducted with a scanning electron microscope equipped with a field emission gun (Ultra 60 FE-SEM, Carl Ziess, Oberkochen, Germany). Images were collected at an accelerating voltage of 5 kV with a typical working distance of 3-4.5 mm. Samples were prepared for imaging by depositing ~2 μL of dilute silver coated BCNC suspensions onto plasma cleaned platinum-coated silicon wafer substrates. The deposited suspensions were dried at room temperature.

Electron dispersive spectroscopy (EDS) analysis was conducted to quantify the ratio of silver to gold in the sample of silver-coated BCNCs. A sample was prepared by depositing several drops of a silver-coated BCNCs suspension onto a graphite substrate. Multiple depositions were required to create a thick (≈50 μm) layer of silver-coated BCNCs, which insured that the X-ray signal would originate from the coated BCNCs and not the graphite substrate.

5.3.6 Deposition of a Conductive Film of Ag-coated BCNCs onto a Flexible Substrate

A conductive layer of Ag-coated BCNCs was deposited onto a polyether sulfone membrane (25 mm diameter with 20 nm pore size, STERLITECH, Kent, WA, USA) by vacuum filtration. In a typical procedure the membrane was masked off with scotch tape (Magic Tape, 3M, Maplewood, MN, USA) to produce a rectangular (5mm x 25 mm) section of membrane that was not covered by tape. Next the masked off membrane was placed onto a 25 mm fritted glass filtration funnel and 2 mL (.002 wt.%) of Ag-coated BCNC suspension was filtered through the masked membrane using a vacuum gauge pressure of -10 in. Hg. The silver coated membrane was allowed to dry at room temperature for 24 hours before being used to conduct electricity.

5.4 Results and Discussion

To further demonstrate the flexibility and compatibility of the previously developed methods across material systems, silver metal coatings were deposited onto BCNCs. This was accomplished by using the developed approach of first decorating the BCNC surfaces with heterogeneous nucleation sites (i.e. gold nanoparticles) and then using electroless deposition to create continuous and conformal silver coatings around the BCNCs. Although gold is commonly deposited onto silver objects through a galvanic reaction, in which the surface silver atoms are spontaneously replaced by gold, it is also possible to preferentially deposit silver onto gold by using an external reducing agent (e.g., formaldehyde, ascorbic acid, etc.). Interestingly, in the course of this work it was discovered that there is a critical size of gold nuclei below which heterogeneous silver nucleation did not occur, and above which nucleation proceeded as expected. An example

of this specificity for heterogeneous nucleation is shown in **Figure 68**. The spots of bright contrast (highlighted by red rectangles) seen along the length of the uncoated BCNC sections, indicated the presence of small gold nanoparticles evenly distributed along the BCNC surfaces; however, the silver deposition was limited to only a few select areas along the gold-decorated BCNCs. This resulted in the formation of a limited amount of silver particles that grew into large spheres surrounding sections of the gold decorated BCNCs. This peculiar nucleation and growth behavior were hypothesized to be caused by the presence of different diameter gold nanoparticles.

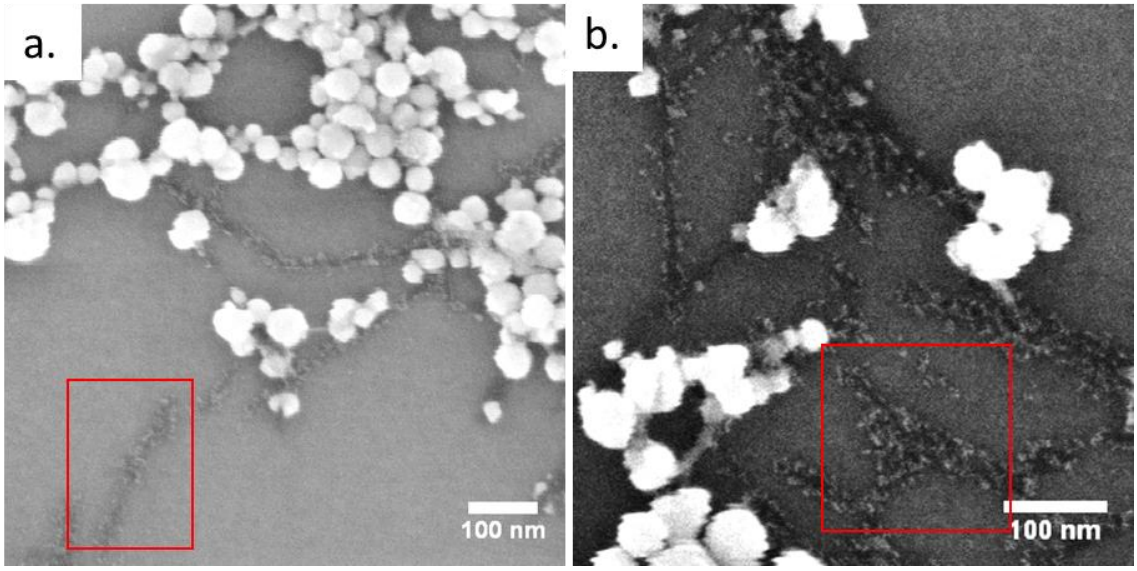

Figure 68. SEM images of non-uniform silver deposition onto BCNCs decorated with small/standard gold nanoparticles (≤ 3 nm). Red rectangles in (a and b) highlight the small enhancement in contrast along the same BCNC, which is a result of the presence of small gold nanoparticles.

The typical size of the standard THCP (Tetrakis(hydroxymethyl)phosphonium chloride) reduced gold nanoparticles is < 3 nm. Such fine gold nanoparticles do not exhibit surface plasmon resonance behavior and have an extinction spectrum characterized by a monotonically decaying curve. However, after aging suspensions of THCP gold for a few

weeks, their extinction spectrum develops a slight plasmon resonance shoulder at 520 nm, which is indicative of particle ripening. This shoulder was present in the extinction spectrum of gold decorated BCNCs, as shown in **Figure 69**, which indicated that the suspension contained a small population of particles larger than 3 nm. This distribution in particle size could have been the cause of the non-uniform heterogeneous nucleation observed during silver deposition. If a critical size of gold nanoparticles does exist, then only the small number of larger particles would initiate heterogeneous nucleation, resulting in a sparse deposition of silver like what was observed. To test this hypothesis, the small gold particles decorating the BCNCs were slightly enlarged by electroless gold deposition. This caused the small gold particles on the BCNCs to grow, creating BCNCs with partial gold coatings, as shown in **Figure 70**. These partially gold coated BCNCs were then exposed to the electroless silver plating solution.

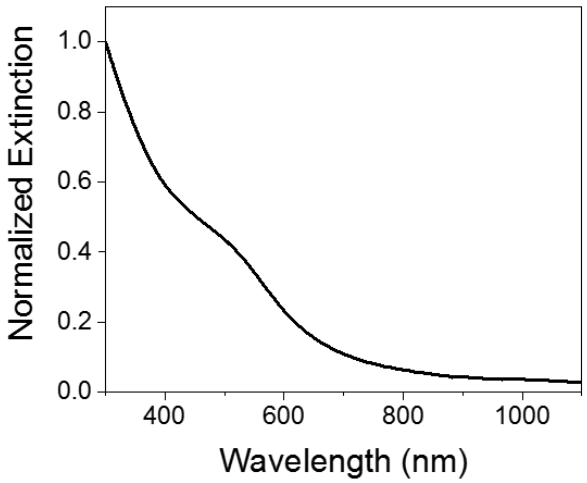

Figure 69. Extinction spectrum of BCNCs decorated with standard THCP reduced gold nanoparticles, which have an average diameter < 3 nm.

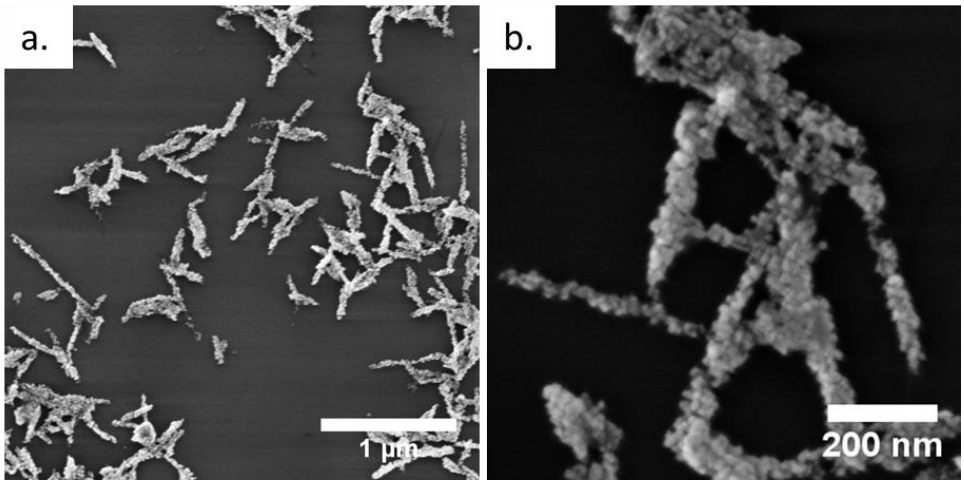

Figure 70. SEM images of BCNCs with partial gold coatings that resulted from the enlargement the standard THCP gold nanoparticles by electroless deposition.

Representative images of the resulting Ag coated BCNCs are presented in **Figure 71**. Unlike the previous attempt, complete and continuous coatings were formed on the partially gold coated BCNCs. It was found that increasing the volume of 0.15 mM $AgNO_3$ solution caused a predictable increase in the silver coating thickness (i.e., final particle diameter). The use of 5 mL, 7 mL, and 10 mL of $AgNO_3$ solutions produced particles with average diameters of ≈71 nm, ≈84 nm, and ≈90 nm, respectively.

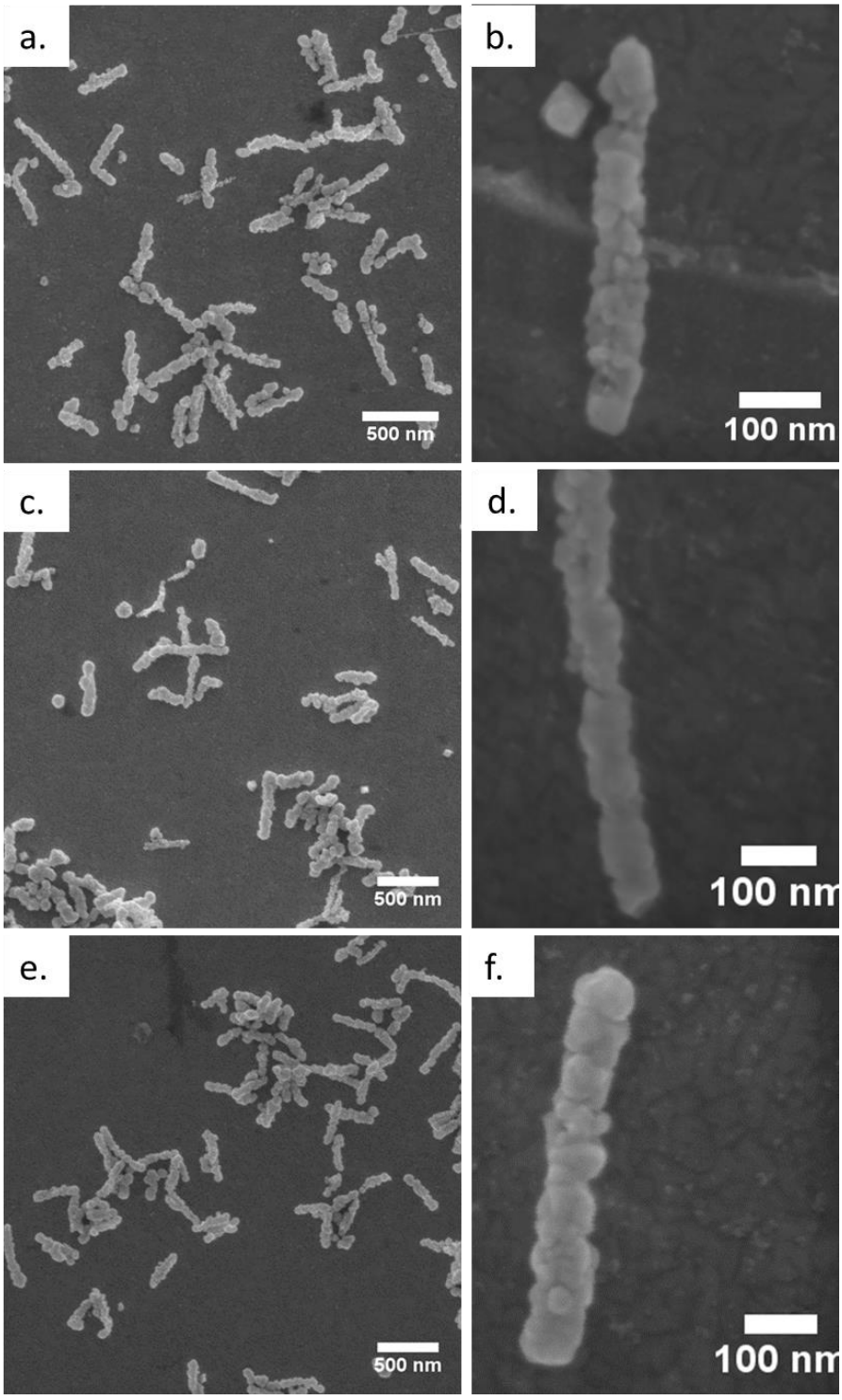

Figure 71. SEM images of BCNCs with increasingly thicker silver coatings. Final particle diameter was controlled by adjusting the amount of 0.15 mM $AgNO_3$ solution used in electroless deposition: (a-b) 5 mL, (c-d) 7 mL, (e-f) 10 mL. The average diameters of particles in (b, d, and f) were 71 nm, 84 nm, and 90 nm, respectively.

The optical extinction of each sample was measured by suspending the particles in D_2O. Two distinct extinction bands were observed in the silver-coated BCNC spectra (**Figure 72**) and were attributed to the plasmon resonance in the transverse and longitudinal directions, similar to AuNS-BCNCs. The transverse band was centered around 450 nm while the longitudinal band was around 1700 nm. Increasing the amount of $AgNO_3$ solution to 10 mL caused a red-shift in the transverse plasmon resonance band to 565 nm, which was accompanied with significant broadening. This was likely the result of a large increase in coating thickness. It was difficult to determine the effect that increasing the $AgNO_3$ volume had on the longitudinal plasmon resonance band because it extended beyond the measurable range (>1800 nm). However, the positions of the two plasmon resonance bands were found to occur at the edges of the visible wavelength range (400-800 nm), which is consistent with literature reports for silver nanowires.[15]

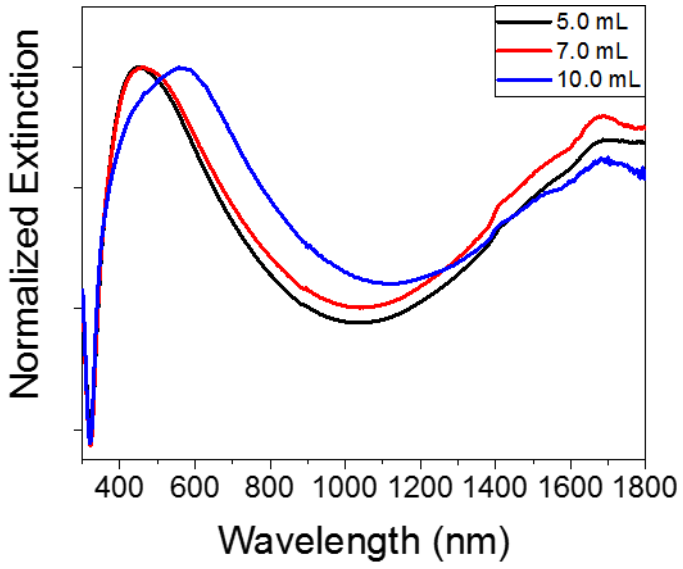

Figure 72. Extinction spectra of silver coated BCNCs grown with increasingly larger amounts of 0.15 mM $AgNO_3$ solution.

The successful deposition of silver coatings onto BCNCs decorated with enlarged gold nanoparticles reinforced the hypothesis of a minimum required gold nuclei size, which was needed for initiating heterogeneous nucleation of silver from the formaldehyde containing electroless plating solution. Perhaps an understanding of this observation can be obtained by considering the concept of r^*, as proposed in classical nucleation theory.[16] Classical nucleation theory suggests that there exists a critical nuclei radius r^*, which is associated with a maximum in excess free energy of formation for a new particle volume, and nucleation of new particles is only favored for nuclei with $r > r^*$, as this will result in a decrease in the free energy (ΔG_r). The value of r^* is a function of the solid-liquid interfacial energy (γ_{SL}) and the nucleation driving force (ΔG_v), as shown in **Equation 9**.

$$r^* = \frac{2\gamma_{SL}}{\Delta G_v} \tag{9}$$

The nucleation driving force for electroless silver deposition can be considered as the strength of the reducing agent (i.e. formaldehyde), and thus, is fixed. Additionally, nucleation theory states that the energy barrier for heterogeneous nucleation is typically lower due to a reduction in the nucleating particle's surface area/interfacial energy, as demonstrated by the schematic in **Figure 73**. The amount of surface area/interfacial energy reduction is a function of the wetting angle (θ) between the nucleating solid and the heterogeneous nucleation site/surface, and its contribution to the activation energy barrier for nucleation on a flat surface is described by **Equation 10**.

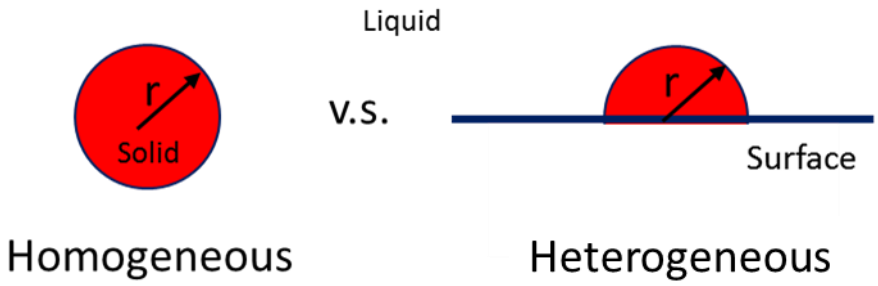

Figure 73. Schematic illustrating the difference in solid-liquid area/interfacial energy (γ_{SL}) for homogeneous and heterogeneous nucleation of a particle with a radius r.

$$\Delta G^*_{het} = S(\theta) G^*_{hom} \tag{10}$$

Where S(θ) is a factor (**Equation 11**) that has a numerical value ≤ 1and depends only on the wetting angle.[16] Thus, sites/surfaces that create a low wetting angle with the nucleating solid would strongly favor heterogeneous nucleation.

$$S(\theta) = \frac{(2 + \cos\theta)(1 - \cos\theta)^2}{4} \tag{11}$$

Gold and silver have similar crystal structures (FCC) and have been shown to have good epitaxy[17-18], and thus, gold particles should be good heterogeneous nucleation sites for Ag and *vice versa*. The above equations (**10&11**), which were derived for heterogenous nucleation on a flat surface, indicate that heterogenous nucleation always requires less energy than homogenous nucleation and will occur preferentially. By extension these results suggest that any foreign surface with favorable surface energy should serve as preferential nucleating site, however, it was observed that there is a clear preference for silver particles to nucleate on larger gold particles and not on the smaller ones. This observed preference cannot be explained by the classical heterogenous nucleation theory.

This observation is not surprising since the nucleating surface in this case is not flat but is spherical particle instead, thus a more detailed consideration of nucleating surface geometry is required.

The case of heterogenous nucleation of a spherical cap on a convex spherical particle was first studied by Fletcher[19] in 1958 and has recently been revisited in more detail by Qian and Ma.[20] A representation of the geometry associated with a spherical cap nucleating on a convex spherical particle is demonstrated in **Figure 74**. Referring to **Figure 74**, Fletcher defined the parent phase by the subscript **1**, the embryo by **2**, and the nucleus/nucleating particle by **3**. In an identical manner to classical nucleation theory Fletcher defines the free energy of formation of an embryo as shown in **Equation 12**, where the volume is denoted by V, surface area by S, free energy difference between two states of matter by ΔG_v, and the surface energy of the interfaces between phases is denoted by σ_{ij}. Fletcher then proceeded to define the volume (V), surface area (S) and angles (ψ,φ) found in equation 12 in terms of the geometrical variables presented in **Figure 74**.

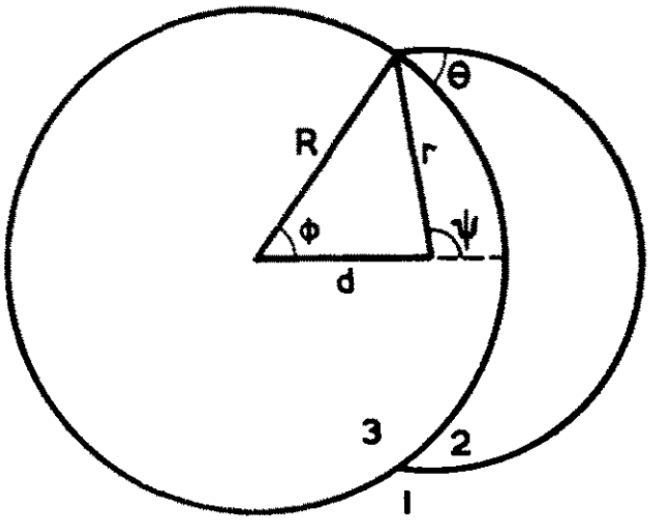

Figure 74. Schematic demonstrating the heterogeneous nucleation of embryo 2 with a radius equal to r on the nucleating particle 3 with a radius equal to R. Reproduced from Fletcher.[19]

Fletcher pointed out that the critical embryo radius r^*, should be the same as that for homogenous nucleation, and is equal to the expression shown in **Equation 9**.

$$\Delta G = \Delta G_v V_2 + \sigma_{12} S_{12} + (\sigma_{23} - \sigma_{13}) S_{23} \tag{12}$$

By rearranging equation 12 with the newly defined terms and defining a new variable

$$x = \frac{R}{r^*}, \tag{13}$$

Fletcher wrote the free energy of formation of a critical embryo as

$$\Delta G^* = \frac{8\pi\sigma_{12}^3}{3(\Delta G_v)^2} f(m, x) \tag{14}$$

where f(m,x) is a geometrical factor analogous to the shape factor (S(θ)) in the flat surface case. Fletcher defines the contact angle (θ) as

$$m = \cos(\theta) = \frac{\sigma_{13} - \sigma_{23}}{\sigma_{12}}, \tag{15}$$

and the geometrical factor as

$$f(m,x) = 1 + \left(\frac{1 - mx}{g}\right)^3 + x^3\left[2 - 3\left(\frac{x - m}{g}\right) + \left(\frac{x - m}{g}\right)^3\right] + 3mx^2\left(\frac{x - m}{g} - 1\right). \tag{16}$$

The term g in Equation **16**) is defined as

$$g = (1 + x^2 - 2mx)^{0.5}\,. \tag{17}$$

By plotting the geometrical factor (f(m,x)) as a function of x with m as a parameter (**Figure 75**) the critical energy of embryo formation (ΔG^*) can be calculated for any nucleation process. Thus, by substituting ΔG^* into the embryo rate formation equation

$$J = K \exp\left(\frac{-\Delta G^*}{kT}\right), \tag{18}$$

(where the kinetic coefficient K and is estimated to be equal to $4\pi 10^{25} R^2$, k is the Boltzman Constant and T is in Kelvin) Fletcher was able to identify the critical motive free energy ΔG_v (**Equation 19**) at which nucleation becomes appreciable.

$$\Delta G_v^2 = \frac{\left[\frac{8\pi}{3}\right]\sigma_{12}^3 f(m,x)}{kT[60.1 + 4.604\log_{10} R]} \tag{19}$$

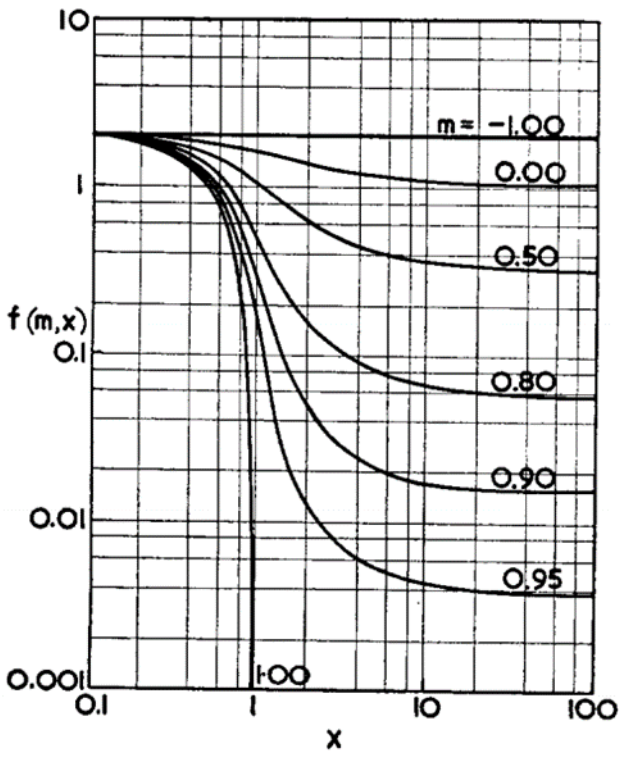

Figure 75. The geometrical factor f(m,x) in terms of the ratio x=R/r*, where m is shown as a parameter. Reproduced from Fletcher.[19]

Using the expression in **Equation 19**, Fletcher examined the cases of water freezing and condensing by calculating the amount of driving force (supercooling, supersaturation, etc.) needed for an embryo of r^* to nucleate on a spherical particle of size R (**Figure 76**). His analysis revealed that nucleation is always easier on a flat surface than on a spherical one and that as the nucleating particle size (R) gets smaller the energy barrier to nucleate an embryo of size r^* increases as can be seen in the graphs in **Figure 76**. The increase in the energy barrier to nucleation becomes more dramatic for particles ranging in size from about

1 nm to 10 nm, suggesting that for particles in this size regime even a small increase in size can drastically reduce the barrier to nucleation.

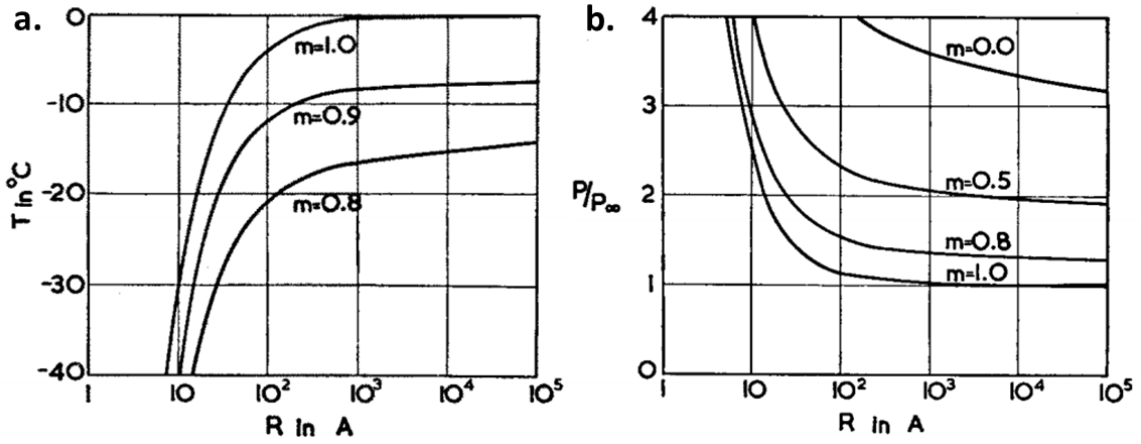

Figure 76. (a) Temperature T at which freezing occurs on a spherical particle of radius R (in Ångstroms) suspended in water. (b) Supersaturation (P/P_∞) at which condensation occurs on a spherical particle radius R at a temperature of 0°C. Parameter is $m=\cos\theta$ in both (a) and (b). Reproduced from Fletcher.[19]

Considering now the results obtained from the electroless deposition of silver onto gold nanoparticle decorated BCNCs, it becomes clear why there was a preference for silver to nucleate on the slightly larger gold particles and not the smaller ones. Drawing from Fletcher's conclusions, it is obvious that for a fixed driving force the slightly larger particles will always serve as the more potent nucleating sites and heterogenous nucleation will preferentially occur at these sites first. This also explains why enlarging the gold nanoparticles through an electroless gold deposition step beforehand was so effective at promoting uniform silver nucleation during subsequent silver deposition. The takeaway from this analysis is that to force nucleation of silver onto the smallest of gold nanoparticles would require a much stronger driving force (i.e. stronger reducing agent). However, since the driving force for electroless silver deposition is fixed by the bath composition (i.e.,

formaldehyde), the way to ensure uniform silver nucleation is to use gold nanoparticles with a size that reduces the nucleation barrier to a level compatible with the reducing agent's chemical activity.

Thus, to avoid using a secondary pre-growth step for gold nuclei enlargement, larger diameter gold nanoparticles were synthesized and directly attached to BCNCs. These larger gold nanoparticles were synthesized by increasing the amount of $HAuCl_4$ used in the standard THCP gold synthesis protocol. The extinction spectrum of BCNCs decorated with the larger gold nanoparticles revealed an enhanced surface plasmon resonance shoulder at 520 nm in comparison to BCNCs decorated with standard gold nanoparticles as demonstrated in **Figure 77**.

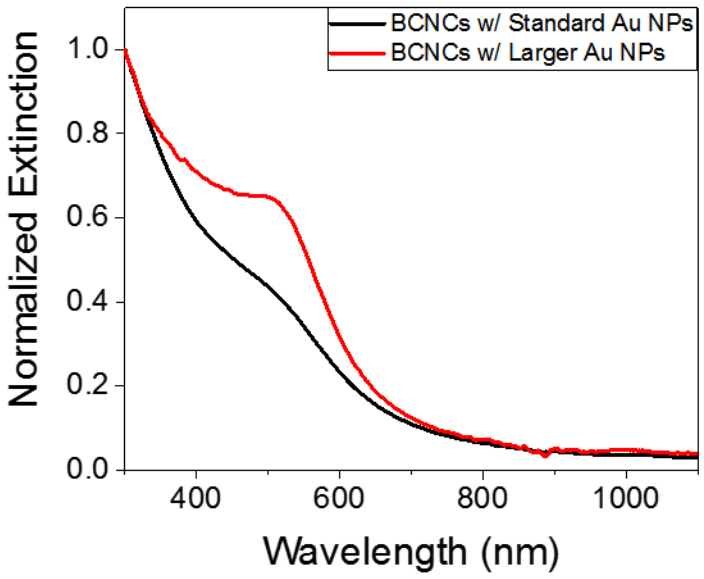

Figure 77. Extinction spectra of BCNCs decorated with standard gold nanoparticles (diam. ≤ 3 nm) and with larger gold nanoparticles (diam. ≤ 5 nm)

TEM imaging was used to analyze the particle size distribution of both the standard and larger THCP gold particles, the result of this analysis is presented in **Figure 78**. Spectral

and TEM data confirmed that a slight increase (0.1 mL) in $HAuCl_4$ resulted in a moderate increase of the average gold nanoparticle size, from 1.8 nm to 2.6 nm. Additionally, the particle size distribution of the larger nanoparticles was found to be broader and extended to ≈ 4.5 nm.

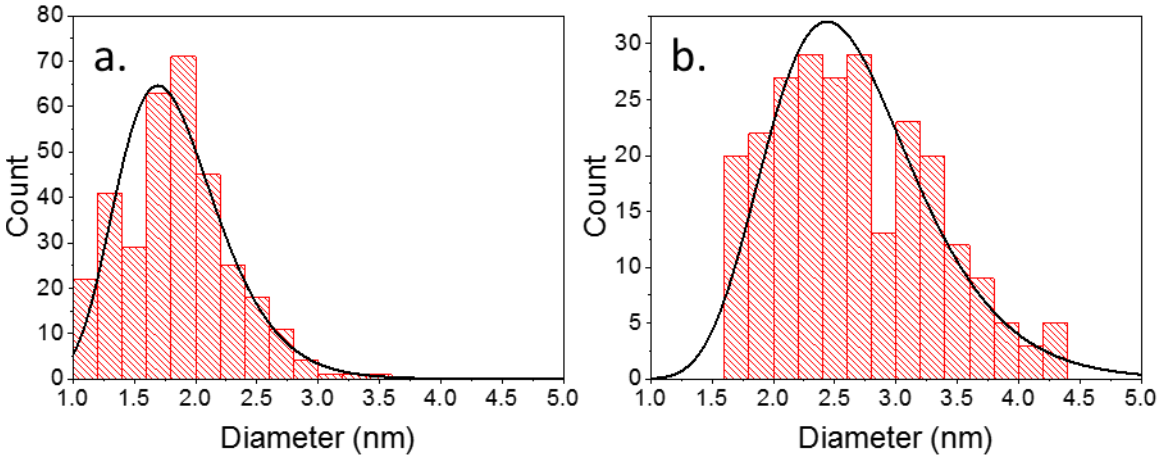

Figure 78. Particle size analysis of standard (a) and larger (b) gold nanoparticles showed that an avg. diam. = 1.8 nm, SD = 0.43 and avg. diam. = 2.6 nm, SD = 0.65, respectively.

Silver coatings were deposited onto the BCNCs decorated with the larger gold nanoparticles in the same manner as described previously. Representative SEM images of the silver-coated particles are presented in **Figure 79**. Even though the gold nanoparticles in this trial were only slightly larger than in the first trial, this his time, silver was uniformly deposited onto the BCNC surfaces, forming conformal Ag/Au coatings. The resulting silver coatings were similar to the ones deposited onto BCNCs with electrolessly enlarged gold nuclei. This result reaffirmed the fact that even a slight increase in nucleating particle size can significantly reduce the barrier to nucleation. This shows that when using nanoparticles as nucleating agents a consideration of the driving force and critical nucleus size needs to be made to ensure nucleation will occur uniformly.

As before, the diameter of these newly Ag-coated BCNCs was controlled by adjusting the volume of $AgNO_3$ solution. UV-vis-NIR spectroscopy was conducted to analyze the optical extinction of these Ag coated BCNCs, and the spectra of the samples grown with 3.0 mL and 7.0 mL of 0.15 mM $AgNO_3$ solution are presented in **Figure 80**.

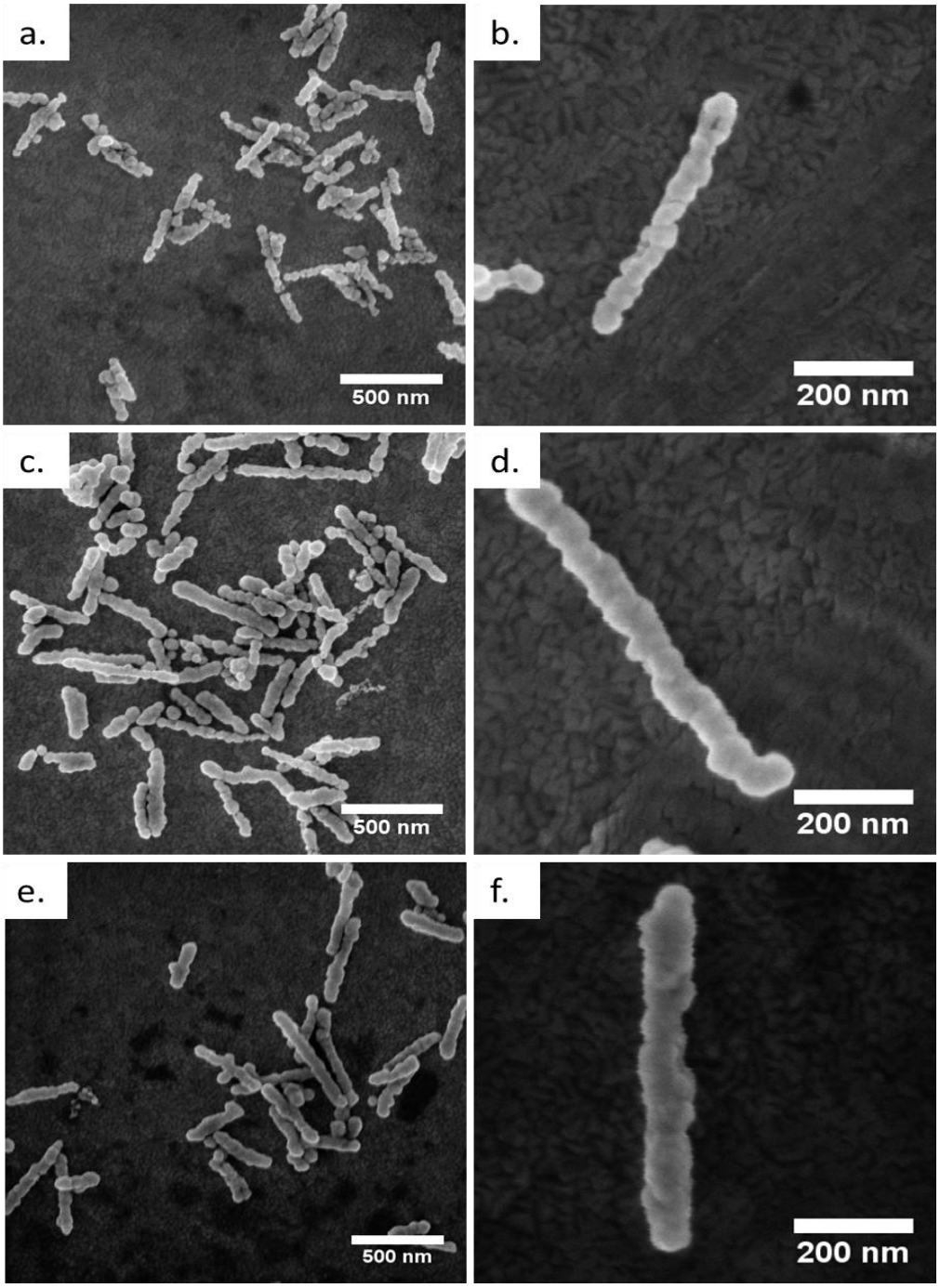

Figure 79. SEM images of silver coated BCNCs with increasingly thicker coatings. Coatings were grown on BCNCs decorated with larger (≤ 5) Au nanoparticles. Ag coated BCNC diameter was controlled by adjusting the amount of $AgNO_3$ solution used in electroless deposition: (a-b) 3 mL, (c-d) 5 mL, (e-f) 7 mL. The average diameter of particles in (b, d, f) were 59 nm, 84 nm, 93 nm, respectively.

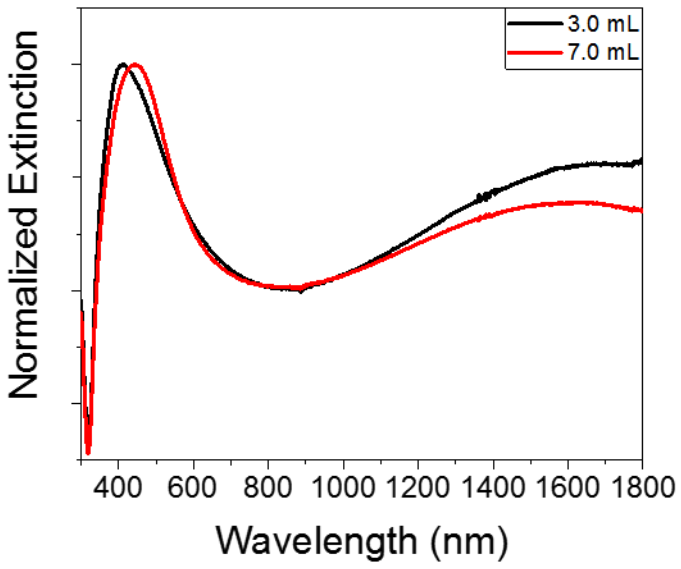

Figure 80. Extinction spectra of Ag coated BCNCs synthesized with 3.0 mL and 7.0 mL of 0.15 mM $AgNO_3$ solution. Particles were suspended in D_2O for measurement.

As before, their extinction spectra consisted of two plasmon resonance bands associated with the dimensions of the synthesized particles. A slight red-shift of the transverse plasmon resonance band (413 nm to 445 nm) was observed and correlated with an increase in particle diameter. The effect of size increase on the longitudinal band was again difficult to ascertain, as the extinction band extended beyond the measurable range (limited by the strong absorbance of D_2O above 1800 nm) but may have a slight blueshift with increasing coating thickness, as was previously observed for Au coated CNCs. Additionally, the linewidth of the transverse extinction bands was narrower for these samples, which suggested that the deposited silver coatings were more uniform in thickness, than those grown on BCNC decorated with electrolessly enlarged gold particles.

To produce a larger quantity of silver coated BCNCs, the 5 mL electroless deposition reaction was scaled 10-fold. Representative SEM images of the particles resulting from

this scaled-up synthesis are shown in **Figure 81**. The obtained particles were identical in coating quality as compared to the previous smaller scale trial (**Figure 79c, d**).

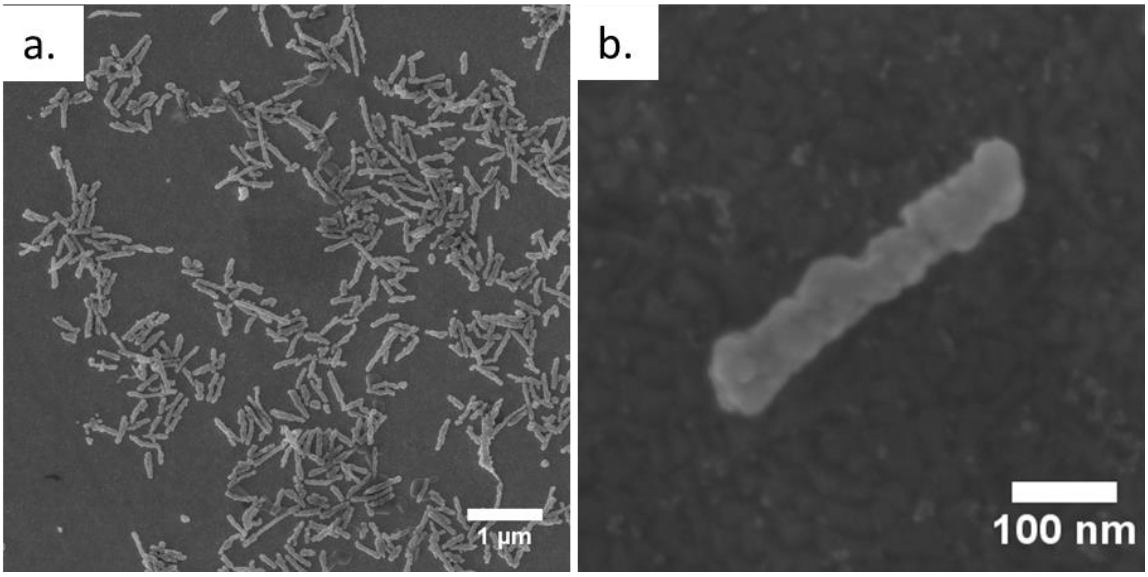

Figure 81. SEM images of Ag coated BCNCs synthesized by scaling the 5 mL electroless deposition reaction 10-fold.

Electron dispersive spectroscopy (EDS) analysis (**Figure 82**) revealed an Ag/Au weight ratio of $\approx 5 \pm 0.6$. This ratio is 2.6 times lower than the Ni/Pt ratio attained in the previous chapter but is likely the result of the use of larger gold nanoparticles, which were required to initiate heterogeneous nucleation. If a reliable synthesis method for small (< 3 nm) silver nanoparticles is developed, it may be possible to eliminate the need for gold by decorating BCNCs with the small silver particles instead, which may lead to thinner coatings and more defined surface plasmon resonance bands.

Several milliliters of a dilute suspension of silver-coated BCNCs from the scaled-up reaction were deposited onto a polyethersulfone (PES) filtration membrane, by vacuum filtration. A strip of the Ag BCNC coated PES membrane was cut and used as a conductive

trace in a simple circuit as shown in **Figure 83**. After completing the circuit, the LED lit up, indicating that the deposited Ag BCNCs were able to conduct electrical current. The conductive trace had a measured resistance of 1kΩ as measured by a multimeter.

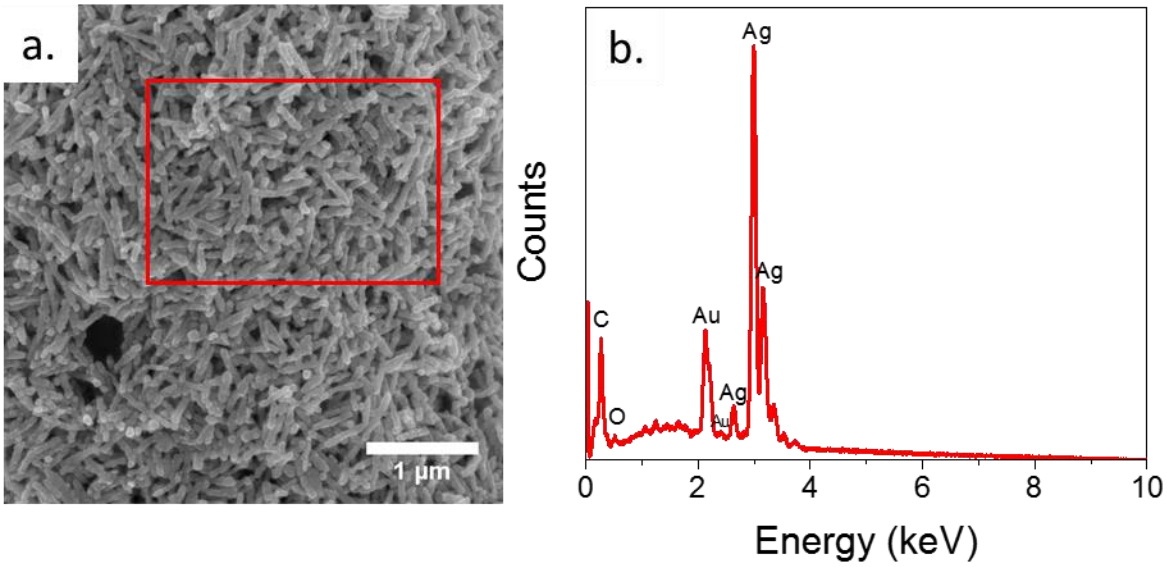

Figure 82. SEM image (a) and EDS spectrum (b) of Ag coated BCNCs synthesized by a scaled-up reaction using 50 mL of 0.15 mM $AgNO_3$. Note: spectrum collected from the area outlined by the red rectangle.

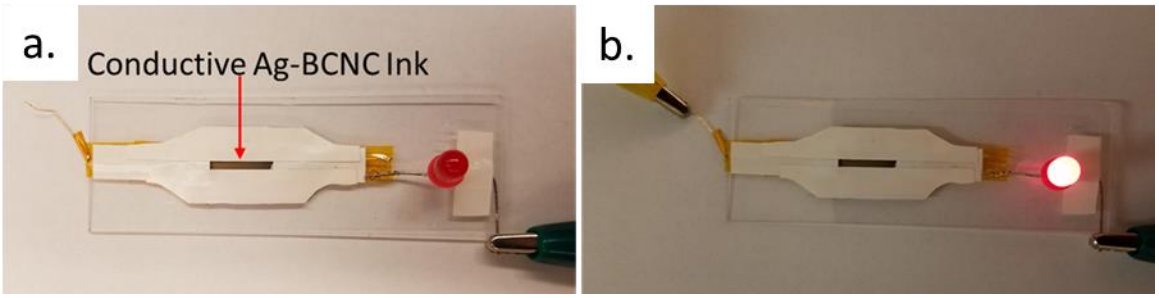

Figure 83. Electrical circuit used to demonstrate the electrical conductivity of silver coated BCNCs. Before (a) and after (b) completing the circuit.

SEM analysis (**Figure 84a)** of the deposited trace revealed that the membrane surface was uniformly covered and consisted of a silver-coated BCNC mat with some larger particle agglomerates interspersed throughout.

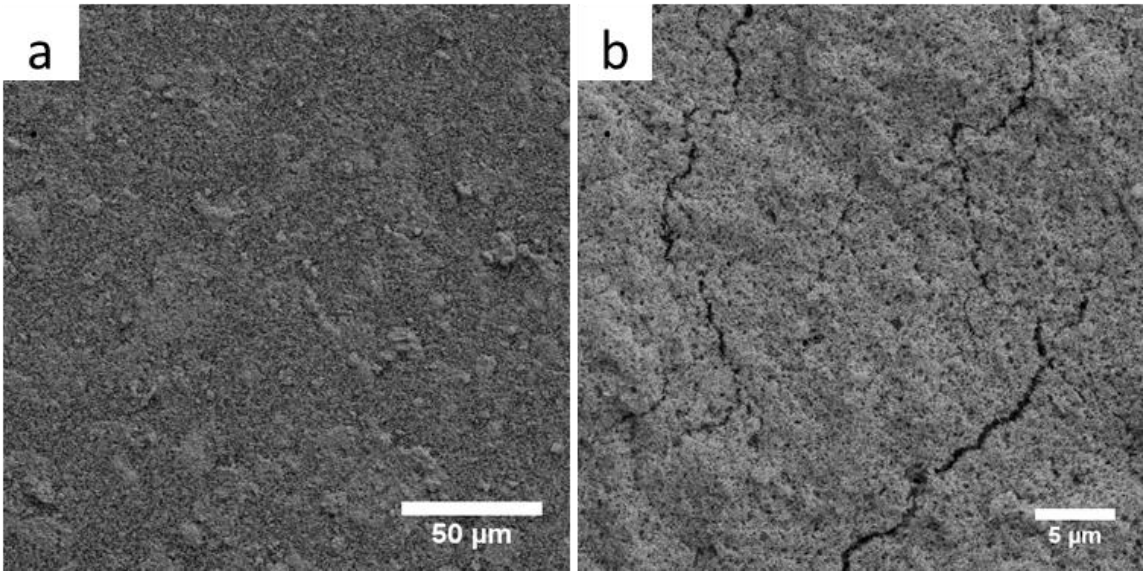

Figure 84. SEM images of Ag coated BCNCs deposited from suspension onto a polymer filtration membrane. Image in (a) shows the deposited layer is uniform across the surface and reveals the presence of particle agglomerates. Higher magnification image in (b) is a representation of cracks that were observed in some regions of the deposited layer.

Upon examination, regions containing a cracked coating were identified (**Figure 84b**), which may have been caused by depositing too thick of a layer (≈50 µm). Additional work is needed to determine the optimum concentration and volume of silver-coated BCNCs suspensions needed to form thin conductive traces. Nevertheless, this simple experiment demonstrated the potential of these materials to be used in conductive ink formulations, flexible electrodes, and conductive nanocomposites.

5.5 Conclusions

For the first time, individual BCNCs coated with conformal, continuous, and electrically conductive layers of metallic silver have been generated using a scalable wet chemical electroless deposition process. It was found that heterogeneous nucleation of silver did not occur on gold nanoparticles below a critical size (≈ 3 nm). It was then

demonstrated that heterogeneous nucleation of silver could be stimulated by decorating BCNCs with slightly larger gold nanoparticles (≤ 5 nm), which resulted in the deposition of uniform silver coatings. The thickness of such coatings was shown to be sensitive to the volume of $AgNO_3$ in the electroless plating solution and could be controlled by manipulating the plating solution volume. Optical extinction measurements revealed that silver coated BCNCs contained two surface plasmon resonance bands, like their all-gold counterparts. However, the positions of the transverse and longitudinal resonance bands were shifted closer to UV and further into the NIR wavelengths, respectively. The scalability of the electroless deposition process was demonstrated by scaling the electroless deposition reaction 10-fold, which did not degrade the quality of the silver coatings. EDS analysis of silver-coated BCNCs from the scaled-up reaction revealed that the coatings contained about 5 times more silver than gold. Finally, the deposition of silver coated BCNCs onto a flexible PES filtration membrane yielded an electrically conductive coating, which could be used to supply electrical current to power an LED.

Additional work is needed to further characterize the electrical properties of the generated silver coated BCNCs and their performance in conductive ink formulations, conductive composites, and flexible electrodes should be evaluated. Future work should explore applying silver coatings onto cellulose nanofibrils (CNFs) as their long lengths and thin cross-sections could provide even lower volume requirements for formation of percolated conductive networks. Additionally, conductive copper coatings should be investigated due to their expected high conductivity but reduced material costs.

5.6 References

[1] Du, X.; Zhang, Z.; Liu, W.; Deng, Y., Nanocellulose-based conductive materials and their emerging applications in energy devices - A review. *Nano Energy* **2017,** *35* (Supplement C), 299-320.

[2] Agate, S.; Joyce, M.; Lucia, L.; Pal, L., Cellulose and nanocellulose-based flexible-hybrid printed electronics and conductive composites – A review. *Carbohydrate Polymers* **2018,** *198*, 249-260.

[3] Feng, Y.; Zhang, X.; Shen, Y.; Yoshino, K.; Feng, W., A mechanically strong, flexible and conductive film based on bacterial cellulose/graphene nanocomposite. *Carbohydrate Polymers* **2012,** *87* (1), 644-649.

[4] Hu, W.; Chen, S.; Yang, Z.; Liu, L.; Wang, H., Flexible Electrically Conductive Nanocomposite Membrane Based on Bacterial Cellulose and Polyaniline. *The Journal of Physical Chemistry B* **2011,** *115* (26), 8453-8457.

[5] Meulendijks, N.; Burghoorn, M.; van Ee, R.; Mourad, M.; Mann, D.; Keul, H.; Bex, G.; van Veldhoven, E.; Verheijen, M.; Buskens, P., Electrically conductive coatings consisting of Ag-decorated cellulose nanocrystals. *Cellulose* **2017,** *24* (5), 2191-2204.

[6] Wang, Y.; Ren, K.; Sun, J.; Li, W.; Zhao, S.; Chen, Z.; Guan, J., Ultralow content silver densely-coated glass microsphere for high performance conducting polymer-matrix composites. *Composites Science and Technology* **2017,** *140* (Supplement C), 89-98.

[7] Kwon, S.; Cho, H. W.; Gwon, G.; Kim, H.; Sung, B. J., Effects of shape and flexibility of conductive fillers in nanocomposites on percolating network formation and electrical conductivity. *Physical Review E* **2016,** *93* (3), 032501.

[8] Lux, F., Models proposed to explain the electrical conductivity of mixtures made of conductive and insulating materials. *Journal of Materials Science* **1993,** *28* (2), 285-301.

[9] Bauhofer, W.; Kovacs, J. Z., A review and analysis of electrical percolation in carbon nanotube polymer composites. *Composites Science and Technology* **2009,** *69* (10), 1486-1498.

[10] De, S.; Higgins, T. M.; Lyons, P. E.; Doherty, E. M.; Nirmalraj, P. N.; Blau, W. J.; Boland, J. J.; Coleman, J. N., Silver Nanowire Networks as Flexible, Transparent, Conducting Films: Extremely High DC to Optical Conductivity Ratios. *ACS Nano* **2009,** *3* (7), 1767-1774.

[11] Wu, Z.; Chen, Z.; Du, X.; Logan, J. M.; Sippel, J.; Nikolou, M.; Kamaras, K.; Reynolds, J. R.; Tanner, D. B.; Hebard, A. F.; Rinzler, A. G., Transparent, Conductive Carbon Nanotube Films. *Science* **2004,** *305* (5688), 1273-1276.

[12] Ahn, B. Y.; Lorang, D. J.; Lewis, J. A., Transparent conductive grids via direct writing of silver nanoparticle inks. *Nanoscale* **2011,** *3* (7), 2700-2702.

[13] Cheng, T.; Zhang, Y.; Lai, W.; Chen, Y.; Huang, W., A Rapid Synthesis of High Aspect Ratio Silver Nanowires for High-Performance Transparent Electrodes. *Chinese Journal of Chemistry* **2015,** *33* (1), 147-151.

[14] Koga, H.; Nogi, M.; Komoda, N.; Nge, T. T.; Sugahara, T.; Suganuma, K., Uniformly connected conductive networks on cellulose nanofiber paper for transparent paper electronics. *Npg Asia Materials* **2014,** *6*, e93.

[15] Luu, Q. N.; Doorn, J. M.; Berry, M. T.; Jiang, C.; Lin, C.; May, P. S., Preparation and optical properties of silver nanowires and silver-nanowire thin films. *Journal of Colloid and Interface Science* **2011,** *356* (1), 151-158.

[16] Porter, D. A., Easterling, K. E., *Phase transformations in metals and alloys*. 2 ed.; Chapman & Hall: London, UK, 1992.

[17] Yang, Y.; Liu, J.; Fu, Z.-W.; Qin, D., Galvanic Replacement-Free Deposition of Au on Ag for Core–Shell Nanocubes with Enhanced Chemical Stability and SERS Activity. *Journal of the American Chemical Society* **2014,** *136* (23), 8153-8156.

[18] Aherne, D.; Charles, D. E.; Brennan-Fournet, M. E.; Kelly, J. M.; Gun'ko, Y. K., Etching-Resistant Silver Nanoprisms by Epitaxial Deposition of a Protecting Layer of Gold at the Edges. *Langmuir* **2009,** *25* (17), 10165-10173.

[19] Fletcher, N. H., Size Effect in Heterogeneous Nucleation. *The Journal of Chemical Physics* **1958,** *29* (3), 572-576.

[20] Qian, M.; Ma, J., Heterogeneous nucleation on convex spherical substrate surfaces: A rigorous thermodynamic formulation of Fletcher's classical model and the new perspectives derived. *The Journal of Chemical Physics* **2009,** *130* (21), 214709.

APPENDIX A: CONSTRUCTION AND USE OF A CARBON MONOXIDE GENERATOR

A.1 Overview

Carbon monoxide (CO) was used as the reducing agent during the synthesis of gold nanoshell-bearing CNCs. Carbon monoxide is a colorless, odorless, and tasteless gas that is highly toxic and should only be handled with proper safety measures in place. Carbon monoxide should never be released into open lab space and its use must be restricted to properly ventilated fume hoods. Properly maintained carbon monoxide detectors should be located near the areas where carbon monoxide gas is generated and used. Due to the serious risks involved in handling carbon monoxide gas in the laboratory, small quantities of CO were generated in the fume hood using a simple gas generator. This avoided the need to purchase and house CO cylinders in the laboratory which can raise the risk for accidental exposure.

A simple gas generator was constructed using common laboratory glassware. An image of the constructed CO generator is presented in **Figure 85**. The generator consisted of four main components: 1) a flask for gas generation, 2) a 3-way gas flow valve, 3) a 3-neck round bottom flask (RBF) for gas storage, and 4) an overflow/bubbler flask. These components were connected to each other using silicone tubing. The collection flask was the main component of this apparatus as it was used to collect and store a small volume of CO gas that could be metered and used in gold reduction experiments. The collection flask was constructed from a three-neck 500 mL round bottom flask. The right neck of the flask was fitted with a fritted gas bubbler that lead CO gas into the flask. The center neck was fitted with a rubber stopper containing a glass pipet that extended down into the flask,

approximately 5 mm from the bottom; this allowed water in the collection flask to be displaced, by the generated CO gas, into the overflow flask. The left neck was fitted with a rubber septum which allowed small quantities of CO gas to be extracted with a syringe.

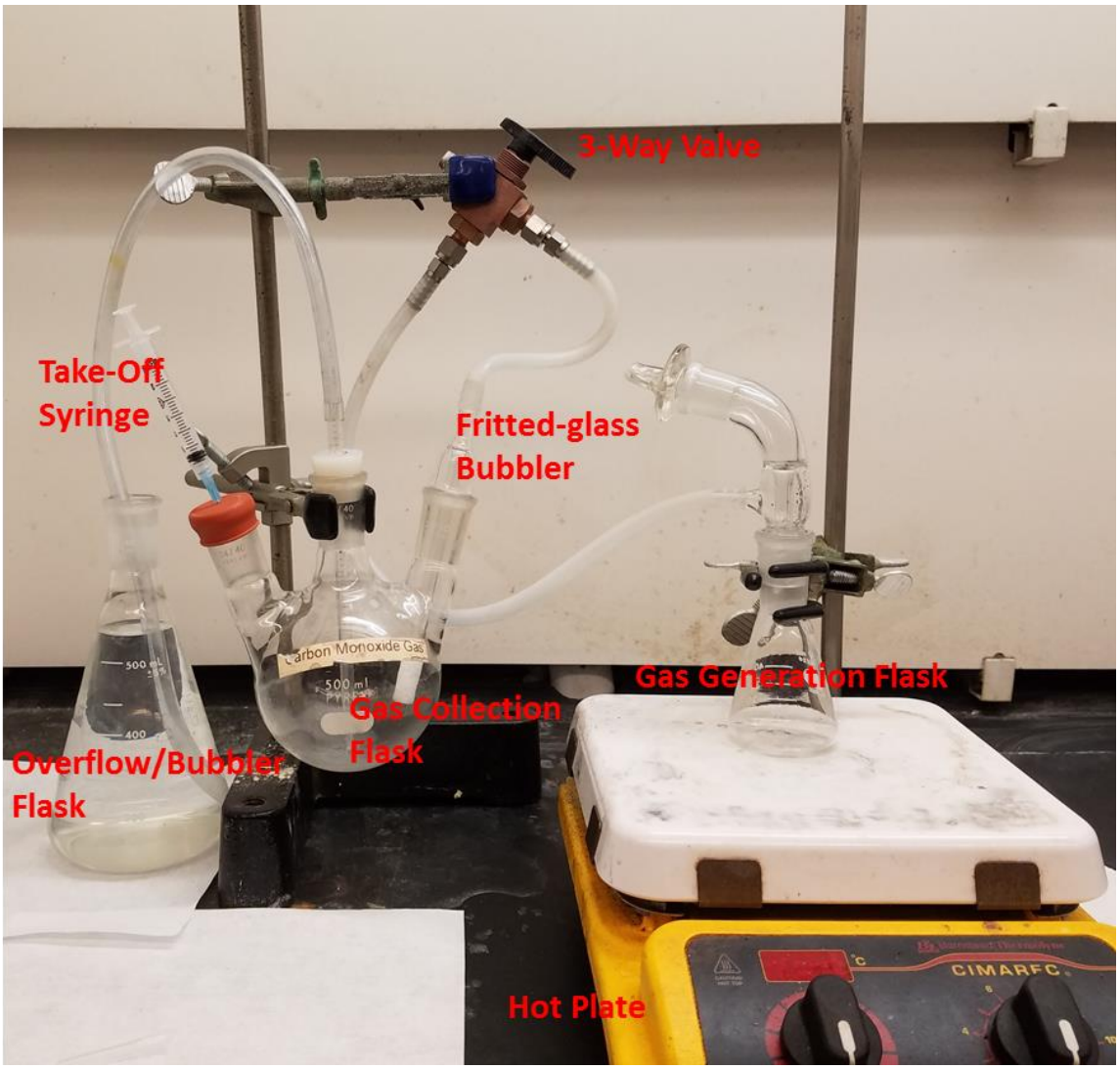

Figure 85. Optical image of the constructed carbon monoxide generator.

A.1 Gas Generator Operation

Before the start of gas generation, the center collection flask (500 mL RBF) was first filled completely with DI water. Next the fritted-glass bubbler was installed making sure

that the ground glass joint was lubricated with a small amount of vacuum grease. Next the center rubber stopper containing the long pipet was installed making sure it was securely seated in the neck opening. Finally, a rubber septum was installed in the remaining open neck of the round bottom flask. Silicone tubbing was connected to the pipet extending from the centrally located rubber stopper and was led to an empty 500 mL Erlenmeyer flask. This overflow flask was used to collect water displaced from the collection flask by the generated CO gas. Next silicone tubing was used to connect the fritted bubbler to one of the inputs of the 3-way gas valve as shown in **Figure 85**. The second input of the 3-way valve was then connected to a gas take off adapter. Carbon monoxide gas was generated in a 50 mL Erlenmeyer, which was fitted with the gas take off adapter.

Carbon monoxide was produced by the dehydration of formic acid with concentrated sulfuric acid. The corresponding chemical reaction is presented in **Equation 20**).

$$HCOOH_{(aq)} \xrightarrow{H_2SO_4} CO_{(g)} + H_2O_{(l)} \quad (20)$$

Cold (5°C) formic acid (≥95%, Sigma Aldrich, St. Louis, MO) (5 mL) was added to the 50 mL flask and was followed by careful addition of cold (5°C) concentrated sulfuric acid (95-98%, Sigma Aldrich) (10 mL). Acids were cooled before mixing to prevent a drastic increase in temperature and minimize the possibility of a runaway reaction, which can cause concentrated acid to froth out of the flask due to a high rate of gas generation. Once the acids were mixed, the glass take off adapter was fitted to the flask and the three-way valve was opened to allow gas to flow into the collection chamber. The reaction proceeded slowly and controllably at room temperature. The reaction rate was increased slightly, by

gently heating the gas generation flask to 50°C. Care must be taken not to heat the flask strongly as strong heating can cause a sudden spike in gas pressure, which could cause the apparatus to come apart at the joints. Once a steady rate of gas generation was achieved, the reaction was allowed to continue until most of the water was displaced from the collection flask. Once the collection flask was full of CO gas, the three-way valve was switched to divert the gas into the fume hood and the gas generation flask was cooled to room temperature. After cooling the gas generation flask was disconnected from the apparatus and its contents were slowly poured into 200 mL of ice-cold water. This diluted the reactants and halted the gas generation reaction. The resulting waste was discarded in a properly label acid waste container.

To use the generated CO gas, a syringe fitted with a hypodermic needle was inserted into the rubber septum of the collection flask and a small volume of gas was extracted by filling the syringe (**Figure 85**). The needle was then quickly inserted and into a vial filled with electroless gold solution, which was also fitted with a rubber septum. Once the syringe was emptied, and the reaction was complete, the vial was uncapped, and its contents were extracted. The vial was left to vent in the fume hood before being discarded. The gas generator was vented at the end of each day by removing the rubber septum and fritted-glass bubbler from the left and right necks, respectively. The collection flask was then filled with DI water to displace the CO gas from the flask. Operation was resumed by simply emptying the overflow flask and replacing the rubber septum and fritted-gas bubbler before connecting the gas generating flask once again.

APPENDIX B: RECOMMENDATIONS FOR IMAGING CELLULOSE NANOMATERIALS WITH SCANNING ELECTRON MICROSCOPY

B.1 Introduction

A major challenge associated with cellulose nanomaterials (CNs) research is the inherent difficulty of obtaining detailed images of individual particles. This difficulty arises from the extremely small cross-sections and low density of CNs. Transmission electron microscopy (TEM) is the current state-of-the-art characterization technique, but still struggles with capturing detailed images of these materials, simply because the high energy electron beams (> 100 kV) used in TEM penetrate these CNs without considerable attenuation. This results in no discernable contrast and the collected images provide little to no useful information. Methods for improving contrast have been developed and employ heavy metal stains (e.g. uranyl acetate) to create a dark background around the electron transparent CNs. However, the difficulty in perfecting staining protocols and the use of toxic heavy metal stains is prohibitive for most researchers. Additionally, the price associated with TEM characterization is typically much higher than for other microscopy techniques (e.g. scanning electron microscope).

In the course of this thesis work, a method to image cellulose nanomaterials with scanning electron microscopy was developed. This method allowed for quick and easy qualitative analysis of cellulose nanocrystal size and dispersion state. Details of the developed imaging methodology and general recommendations for imaging various CNs are given below.

B.2 Sample and Substrate Preparation

It was found that ideal substrates for imaging CNs needed to have nanometer scale roughness as flat surfaces allowed the extremely thin materials to lay flat making their true size more readily apparent. Additionally, it was found the substrate needed to be made of a material that would provide a good contrast against the dark CNs. Contrast observed in SEM images usually stems from the atomic mass differences (Z-contrast), materials with high atomic mass scatter more electrons and appear bright, while materials with lower atomic mass appear dark. Thus, an appropriate substrate for imaging CNs needed to have a high atomic mass and be electrically conductive, which would provide a bright background for the dark CNs and reduce charging artifacts, respectively.

Due to their unparalleled flatness and wide availability, silicon wafers were found to be good substrate candidates. However, silicon's low atomic number (14) is only slightly higher than carbon (12) and was found to give poor contrast for CNs. Thus, to overcome this limitation, a thin conformal layer of a noble metal (Pt) was sputtered onto a 100 mm Si wafer (thank you Carmen Deng, Bassiri-Gharb Group, Georgia Tech). Noble metals such as Au and Pt make an ideal substrate for enhancing contrast due to their high atomic mass and excellent oxidation resistance. After metal deposition the wafer was cut down into smaller pieces (typically 5 mm x 5 mm). This was done either by simply scoring the wafer with a diamond scribe and snapping as demonstrated in **Figure 86** A single 100 mm diameter Si wafer provided hundreds of usable substrates.

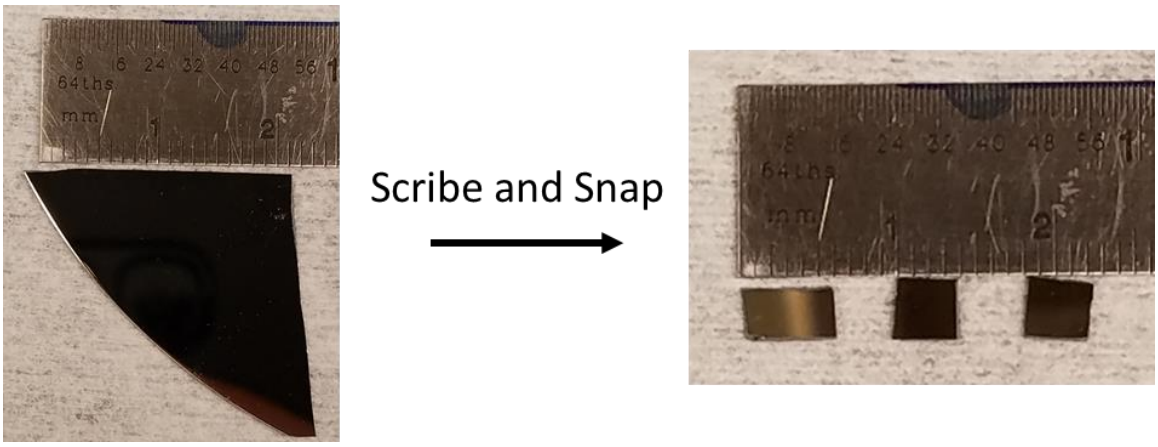

Figure 86. Pt coated wafer cut down into smaller ≈5 mm by ≈5 mm pieces by scoring with a diamond scribe and snapping.

Once the smaller substrates were cut, they were thoroughly cleaned to remove any organic residues. An SC-1 cleaning solution was used to chemically oxidize any organics present on the substrate surface. The SC-1 solution was prepared by mixing 5-parts DI water, 1-part ammonium hydroxide (28 wt.%), and 1-part hydrogen peroxide (30%). The diced substrate pieces were submerged in this mixture and heated to 80°C for 10 minutes. After heating the substrates were thoroughly rinsed with DI water to ensure no residue remained on the surface. These cleaned substrates were then stored in ethanol/DI water (20 vol.% to 80 vol.%) mixture until needed (Note: ethanol is required for long-term storage to discourage the growth of bacterial colonies). Before use, the substrates were cleaned with a 10-minute plasma cleaning cycle (Harrick Plasma, Ithaca, NY). This removed any remaining organic molecules and produced a highly hydrophilic surface that allowed for uniform deposition of CN particles. Comparisons of properly and improperly prepared substrates are shown in **Figure 87** and **Figure 46**.

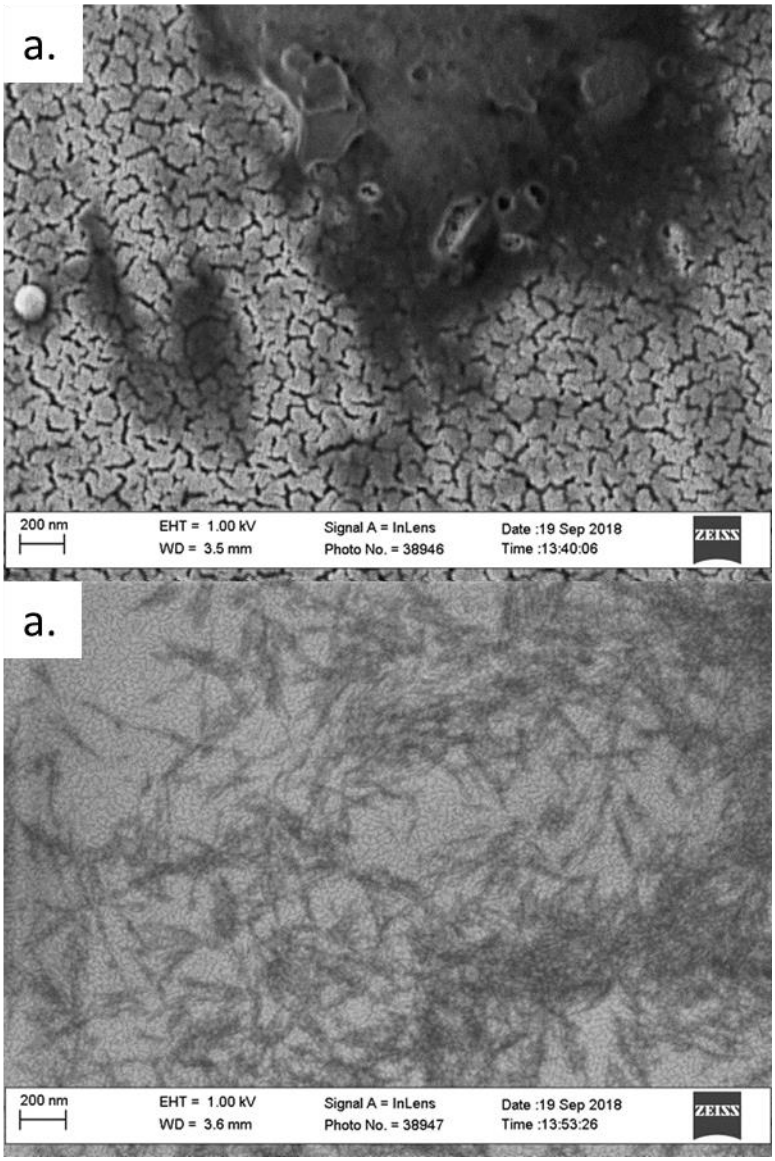

Figure 87. (a) SEM image of a poorly prepared substrate, having large cracks in the thin metallic film and lots of organic residue on the surface. (b) SEM image of BCNCs on a well-prepared substrate, having a continuous and uniform metallic thin film and no evidence of unwanted organic residue.

Cellulose nanomaterials were deposited onto these cleaned substrates from dilute suspensions. Low concentration CN suspensions were necessary to achieve uniform particle dispersion and to prevent the formation of a continuous cellulose layer. Typical concentrations of CN materials ranged from 0.01 wt.% to 0.001 wt.%. Occasionally, it took

several dilution trials to determine the optimum concentration for a CN material, but the stated range typically provided a good starting point. Examples of CNC samples deposited from concentrated and dilute suspension are shown in **Figure 88**.

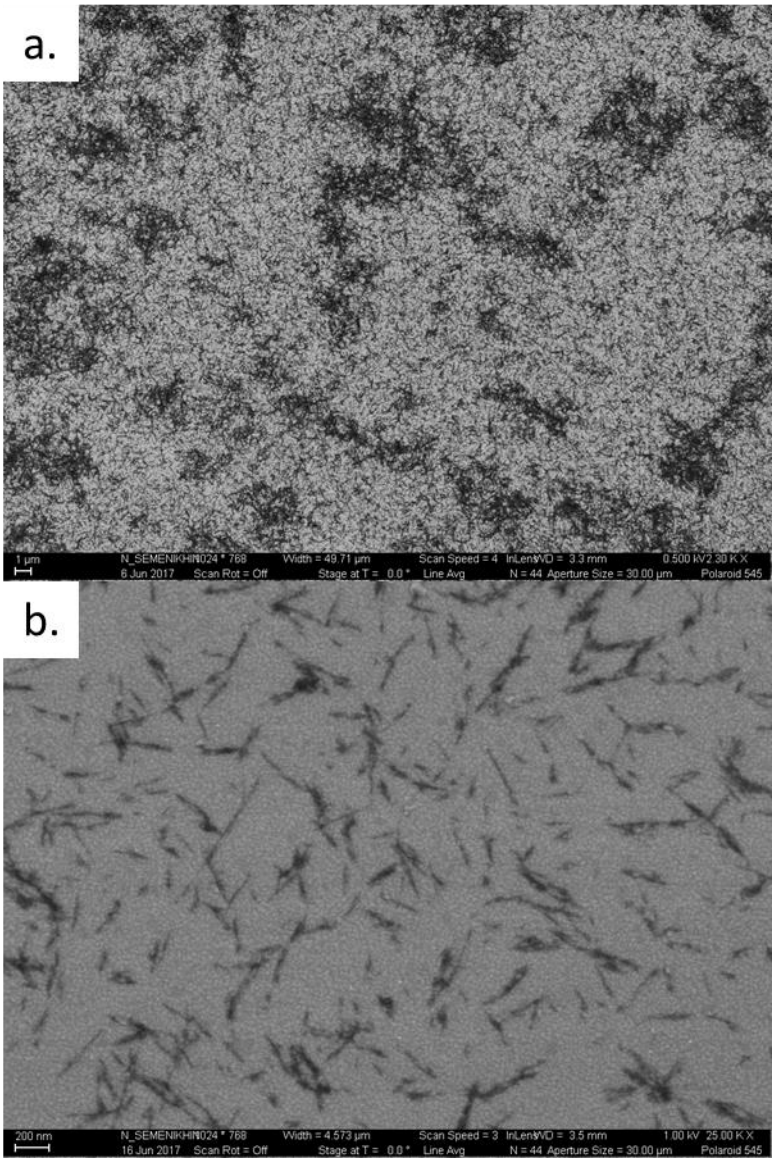

Figure 88. SEM images of CNCs deposited onto Pt coated Si wafer substrates from concentrated (a) and dilute (b) suspensions. (In-lens detector, 0.5 kV(a), 1.0 kV(b), 3.5 mm working distance)

For a 5 mm by 5 mm substrate it was found that 0.5-2 µL of the dilute CN suspension was enough to provide many well dispersed particles for observation (**Figure 88b**). The deposited suspensions were air dried before SEM analysis.

B.3 Imaging Parameters

As mentioned previously, due to their thin cross-sections and low atomic mass (i.e. electron density) cellulose nanomaterials do not scatter electrons strongly. Thus, to attain a noticeable contrast when imaging these materials in SEM a low electron beam acceleration voltage was used (0.5-5 kV). Lower accelerating voltages reduced the penetrating power of the electron beam and improved image contrast; an example of such contrast improvement is shown in **Figure 89.** However, reducing the accelerating voltage negatively affects the resolving power of the microscope, and thus, to observe the thin cross-sections of CNs a short working distance (3-4 mm) along with an in-lens detector was used. Microscope adjustment (focus, stigmation, aperture alignment) was found to be easier at higher accelerating voltages, so a 5 kV accelerating voltage was used to initially dial in the microscope settings. Once good images of the substrate were acquired, the voltage was reduced to 1-3 kV range and images of CNs were acquired. Additionally, it was found that further improvement of contrast and image quality could be realized by adjusting the microscope contrast/brightness settings as demonstrated in **Figure 90**.

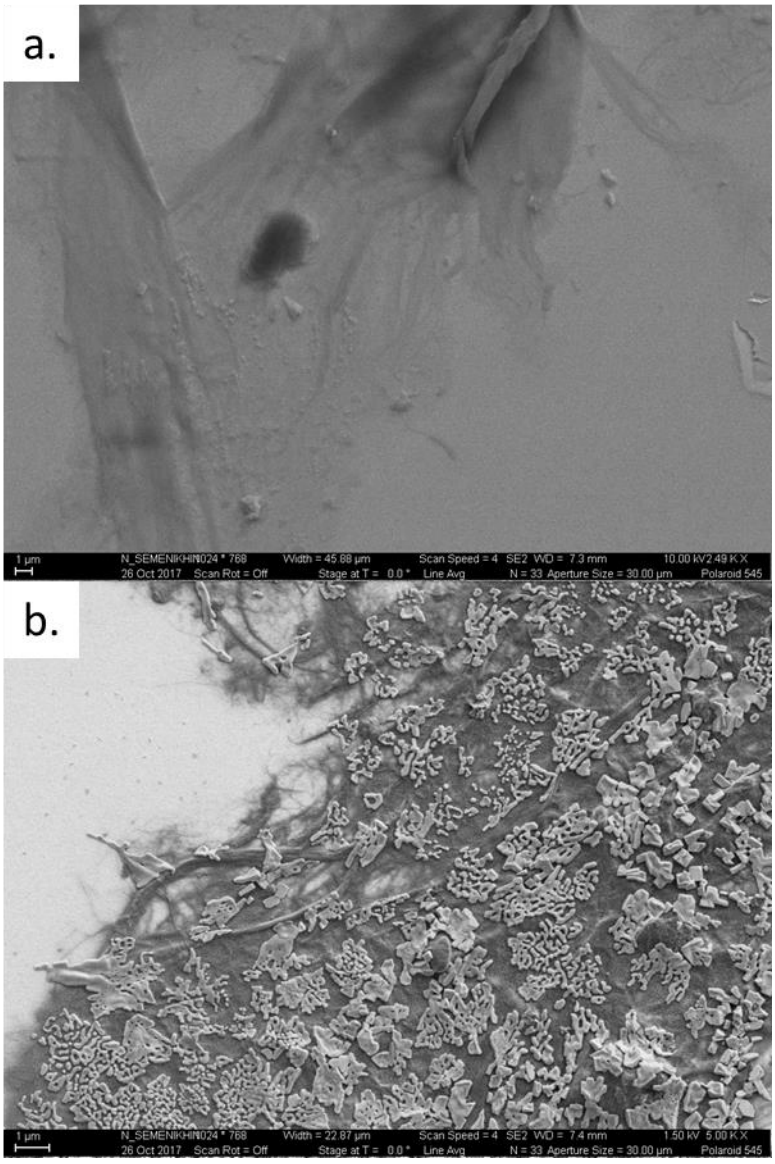

Figure 89. SEM images of recycled paper cellulose fibrils taken at different accelerating voltages using the SE detector, showing the improvement in contrast with lower voltage. Accelerating voltage for (a) was 10 kV and 1.5 kV for (b). (SE detector at working distance of 7.4 mm)

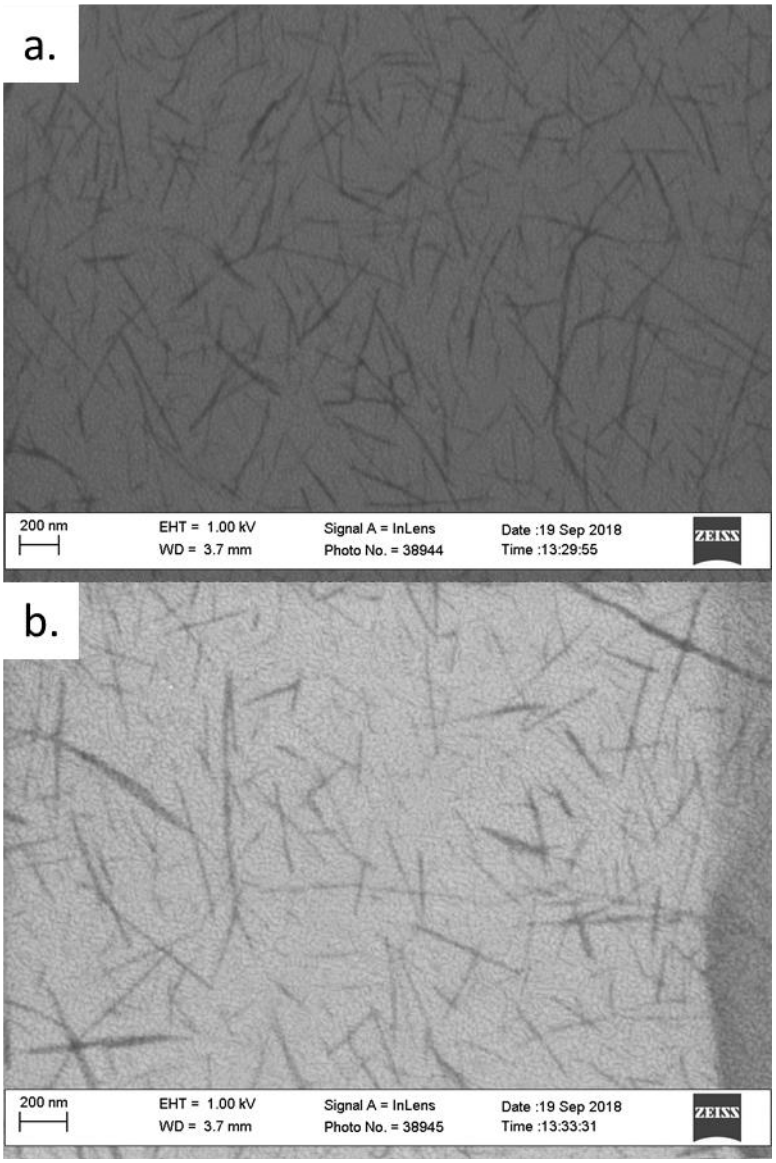

Figure 90. SEM images of BCNCs taken with 1 kV accelerating voltage at a working distance of 3.7 mm. (a) Before contrast/brightness adjustment and (b) after microscope contrast/brightness adjustment.

B.4 Recommendations

The following proposed recommendations are aimed at helping accelerate cellulose nanomaterial research by providing researchers with a method that allows for quick and easy visualization of their cellulosic products and one that can be used to inform research

decisions. A suitable substrate can be made by sputtering or evaporating a thin film of a noble metal (Au, Pt) onto a clean Si wafer. Deposited films not need be thick but should be continuous and uniform. Small pieces of the wafer should be scrupulously cleaned either as described above or by some other method, but the resulting substrate surface should be free of organic contaminants and hydrophilic (deposited aqueous suspensions should spread across the surface with a low angle of contact). CN suspensions should be diluted to 0.01 to 0.001 wt.% and a small volume (2 μL) should be deposited onto the cleaned substrates. The suspension should be allowed to air dry as heat can promote particle agglomeration through convective motion. SEM observation should be conducted with low accelerating voltages ranging from 0.5 kV to 5 kV, with short working distances ranging from the minimum allowed to about 4 mm (images presented above were taken in the range of 3-4 mm). Microscope contrast and brightness settings should be adjusted to produce a sharp contrast difference between the CNs and the substrate. These recommendations should provide a good starting point but can be adjusted to suit the researchers needs.

At the present, the proposed techniques yield mostly qualitative results, but with additional improvements it should be possible to integrate these techniques with automated image analysis software, that would provide statistically significant morphology/size data. Areas in need of improvement include but are not limited to are substrate preparation and uniform deposition of cellulose nanomaterials. Further improvement in image contrast may be achieved by implementing noble metal substrates with large grain sizes. It is anticipated that larger grain sizes will reduce the number of dark lines arising from grain boundaries, which can cause thresholding difficulties in automated image analysis. Better dispersion of cellulose nanomaterials can likely be achieved by functionalization of the substrate. It

was found that aminated cellulose nanomaterials strongly attached to metallic substrates and remained undisturbed even after rinsing with DI water. Thus, the use of substrates with having surface chemistries that complement that of the cellulose nanomaterials can provide a means for depositing individually dispersed cellulose nanomaterials, which would make quantitative the analysis of their size possible.

APPENDIX C: A NOTE ON THE USE OF PLASMONC GOLD COATINGS FOR CELLULOSE NANOCRYSTAL SIZE ANALYSIS

C.1 Introduction

Due to the current inability to quickly evaluate cellulose nanocrystal morphologies/sizes in an easy, inexpensive, and reliable industrial manner applicable to a wide range of particle sizes, a new optical characterization approach based on the anisotropic surface plasmon resonance induced within thin metal (Au) coatings quickly deposited on CNCs was proposed. To allow for such analyses, methods to functionalize CNCs so as to be able to apply conformal metal coatings of controlled thickness were developed. The resulting gold coated CNC were found to have size dependent optical properties, which could be related to the physical dimensions of the coated CNCs. Although the methods developed in the course of this research proved that thin plasmonic metal coatings can be used to glean insight into particle morphology/size, the complexity of the current synthesis and analysis methods would likely prohibit the adaptation of the developed approach in an industrial setting.

C.2 Surface Functionalization of CNCs

The initially proposed one-step alkoxysilane CNCs functionalization method was found to be compatible with larger microscrystalline cellulose (MCC) particles, which did not have a native surface charge and did not form colloidal suspensions. However, application of this method to CNCs resulted in irreversible particle agglomeration. This

was caused by the neutralization of surface charge as the grafted primary cationic amines counteracted the native anionic surface sulfate half-ester groups. An alternative functionalization method was developed to overcome this complication. Unfortunately, this new surface functionalization method was multistep in nature requiring: 1st) the removal of native sulfate half-ester groups through acid hydrolysis, 2nd) oxidation of the uncharged CNCs with sodium periodate, and 3rd) reductive amination of oxidized CNCs. Each step required many hours for reaction and was accompanied by lengthy purification steps. In total, several days were required to produce CNCs ready for gold coating deposition

C.3 Gold Coating of CNCs

Gold coating deposition was found to require the least amount of time and could be completed within a day. However, several issues made this process difficult to reproduce. First, the process of decorating CNCs with small gold nuclei required extensive high-speed centrifugation cycles to separate the highly stable gold decorated CNCs from the unbound gold nuclei. The amount of time required for this process was reduced to several hours by reducing the working sample size to several milliliters. However, this led to an additional issue, to deposit gold coatings of known thickness, the ratio of gold atoms to CNC quantity must be fixed. To achieve this, one must know the precise number concentration of CNCs and their approximate dimensions. The extremely small sample sizes (μg), eliminated the possibility of using simple thermogravimetric analyses for determining CNC suspension concentration. This made the deposition of gold coatings with precise thickness across different experimental batches difficult. Scanning electron microscopy analysis of several

coating trials for each batch was required to establish optimal gold ion to CNC suspension ratios.

C.4 Optical Properties of Gold Coated CNCs

The plasmonic extinction bands exhibited by gold coated CNCs were found to be sensitive to particle dimensions. Specifically, the longitudinal surface plasmon resonance (LSPR) band maximum was found to correlate well with particle length. However, this analysis was limited to particles with similar gold coating thickness. Additionally, correlated single-particle spectroscopy revealed that the plasmonic properties were highly sensitive to coating morphology. Particles of similar dimension, but with different gold coating roughness were found to have different maximum LSPR extinction wavelengths. Such surface roughness effects contributed to inhomogeneous plasmon band broadening, making an estimation of particle length and length distribution from the extinction spectrum difficult (if not impossible).

C.5 Concluding Remarks

The results presented in this thesis demonstrate that thin plasmonic coatings can potentially be used to interrogate the size of templated particles, but the developed technology is far from being mature enough for industrial implementation. Firstly, improvements in surface modification techniques are needed to reduce the amount of time required to prepare particles for gold coating. Only a limited number of possible surface modification techniques were explored in this work. However, future efforts and further analysis of the existing body of work on cellulose modification is sure to yield functionalization methodologies that are better suited for industrial settings. Secondly, the

difficulty in separating gold decorated CNCs from unattached gold nuclei could be improved by exploring alternative methods such as hollow-fiber filtration and selective precipitation. Such improvements are need for the larger scale synthesis of gold decorated CNCs and precise concentration measurements. Finally, improvements in gold coating morphology and thickness control are needed to generate particles possessing an optical response dominated by a single variable (particle length). This would make the estimation of the size and size distribution of coated particles from optical extinction spectra possible. In the meantime, it is the authors opinion that dynamic light scattering (DLS) and scanning electron microscopy (SEM) (as described in **Appendix B**) represent the most readily available and reliable methods for characterizing cellulose nanocrystal morphology/size.

APPENDIX D: CHAPTER 3 SUPPLEMENTARY INFORMATION

Table 9. Complete table of values for the comparison of experimentally measured and predicted LSPR $\lambda_{max,dipole}$ values for AuNS-BCNCs with varying diameters and aspect ratios.

Aspect Ratio	Length (nm)	Diam. (nm)	$\lambda_{max,exp}$	$\lambda_{max,Encina}$	% Diff.
2.23	156	70	1008	849	-16%
2.34	159	68	976	861	-12%
2.49	172	69	1014	898	-11%
3.09	204	66	1103	1005	-9%
2.70	205	76	1081	986	-9%
3.46	287	83	1356	1237	-9%
2.35	183	78	1001	915	-9%
2.72	201	74	1065	977	-8%
2.71	176	65	1001	918	-8%
3.39	224	66	1163	1071	-8%
3.74	254	68	1262	1166	-8%
3.47	298	86	1366	1267	-7%
2.75	209	76	1074	998	-7%
4.16	279	67	1351	1257	-7%
3.88	295	76	1375	1282	-7%
3.04	204	67	1074	1002	-7%

Table 9. Continued

3.36	232	69	1167	1089	-7%
2.56	192	75	1014	947	-7%
3.19	214	67	1107	1035	-6%
4.21	261	62	1297	1214	-6%
3.99	275	69	1319	1236	-6%
2.98	173	58	991	928	-6%
3.03	182	60	1014	951	-6%
2.56	210	82	1056	991	-6%
3.91	223	57	1174	1102	-6%
3.54	230	65	1163	1095	-6%
3.03	179	59	1003	944	-6%
3.89	272	70	1297	1222	-6%
3.50	273	78	1275	1202	-6%
3.64	309	85	1385	1307	-6%
3.16	193	61	1041	984	-6%
4.23	279	66	1333	1261	-5%
3.87	302	78	1370	1301	-5%
3.77	260	69	1245	1184	-5%
3.52	310	88	1370	1303	-5%
2.97	187	63	1003	958	-4%
3.86	309	80	1380	1319	-4%
3.88	229	59	1163	1114	-4%
3.84	215	56	1124	1078	-4%
3.40	231	68	1134	1088	-4%
4.16	266	64	1271	1223	-4%
4.04	283	70	1306	1260	-4%
4.06	288	71	1319	1274	-3%
3.91	219	56	1131	1092	-3%
3.87	317	82	1375	1341	-2%
3.90	285	73	1284	1257	-2%
4.18	297	71	1333	1305	-2%
3.75	225	60	1117	1096	-2%
4.35	287	66	1306	1290	-1%
4.54	277	61	1288	1277	-1%
3.97	262	66	1209	1201	-1%
4.83	290	60	1337	1330	-1%

Table 10. Comparison of the LSPR peak position, FWHM, and % Difference between observed LSPR max wavelength and one predicted by equation 6 for similar sized particles with different surface roughness (e_R) values. Comparison shows general redshift in LSPR peak wavelength, an increase in FWHM, and an increase in the % Difference for particles with larger surface roughness values.

Length (nm)	Diam. (nm)	e_R	$\lambda_{max,exp}$	FWHM	% Diff.
204	63	-0.231	1074	154	-6.7%
204	66	-0.239	1103	168	-8.9%
219	56	-0.280	1351	220	-3.4%
223	52	-0.304	1333	292	-6.7%
231	68	-0.211	1803	192	-0.17%
231	70	-0.246	1098	214	-1.9%
231	68	-0.274	1127	250	-4.0%
279	66	-0.315	1333	232	-5.4%
279	67	-0.333	1351	192	-7.0%